Support Effects in Heterogeneous Catalysis

Dragereffecten in Heterogene Katalyse

Support Effects in Heterogeneous Catalysis

Dragereffecten in Heterogene Katalyse

met een samenvatting in het Nederlands

Proefschrift

ter verkijging van de graad van doctor aan de
Universiteit Utrecht op gezag van de
Rector Magnificus, Prof. Dr. W. H. Gispen,
ingevolge het besluit van het College voor Promoties
in het openbaar te verdedigen op
woensdag 19 juni 2002 des middags te 12:45 uur
door Michiel Karel Oudenhuijzen,
geboren op 12 juni 1975, te Gouda.

Promotoren: Prof. Dr. Ir. D. C. Koningsberger
Faculteit Scheikunde, Universiteit Utrecht.

Prof. Dr. D. E. Ramaker
Faculty of Chemistry, George Washington University.

Copromotor: Dr. J. A. van Bokhoven
Faculteit Scheikunde, Universiteit Utrecht.

The research described in this thesis was supported by NWO.

ISBN 90-393-3062-X

Drukkerij Ponsen & Looijen, Wageningen

Voor papa en mama

Contents

Chapter 1	Introduction	1
Chapter 2	Understanding the Influence of the Pretreatment Procedure on the Platinum Particle Size and Particle Size Distribution for SiO_2 Impregnated with $[Pt^{2+}(NH_3)_4](NO_3^-)_2$ *A combination of HRTEM, mass spectrometry and Quick EXAFS*	11
Chapter 3	The Kinetics of H/D Exchange in Cyclopentane	33
Chapter 4	Support Induced Compensation Effects in H/D Exchange of Cyclopentane	57
Chapter 5	The Nature of the Pt-H Bonding for Strongly and Weakly Bonded Hydrogen on Platinum *A XAFS spectroscopy study of the Pt-H antibonding shaperesonance and Pt-H EXAFS*	87
Chapter 6	Influence of the Support Properties on the Adsorption Site and Strength of Hydrogen Chemisorption on Supported Pt Particles	101
Chapter 7	Observation of Strong Support Effects on the Insulator to Metal Transition of Supported Metal Clusters as Observed by X-Ray Absorption Spectroscopy	125
Chapter 8	Influence of the Support Acid/Base Properties on the Density of States of Pt Particles *Theory versus Experiment*	141
Chapter 9	Influence of Support Alkalinity on Pt Particle Adsorbate Bonding *Implcations for alkane hydrogenolysis*	169
Summary		187
Samenvatting		191
List of publications and presentations		195
Dankwoord		197
Curriculum Vitae		199

1

General Introduction

Introduction

Crude oil still is the most important energy source in the world, and will continue to be so for many years. It is used in power plants and in the propulsion of cars, ships and airplanes. A second important use of crude oil is the use as a building block in the synthesis of products like plastics. However, crude oil is mainly constituted from paraffins which are unreactive. Therefore, the crude oil has to be converted into more suitable molecules. Currently, this is done via a wide variety of mainly heterogeneously catalyzed reactions. In heterogeneous catalysis, reaction rates are generally accelerated by using a solid catalyst and reactants in the fluid or gas phase. Reactants chemisorb on the catalytically active surface, where they are activated and consequently react easily. Supported noble metal catalysts are among the most important solid catalysts, and are used in, for example, hydroisomerization, hydrogenolysis and (de)hydrogenation reactions. In general, the metal functions as the catalyst, and the function of the support is to keep the metal particles highly dispersed. The advantage of highly dispersed metal particles is that a large fraction of the metal is located at the surface of the particle, and therefore it is accessible for the reactants to adsorb. In some instances both the supported metal and the support itself function as a catalyst, for example in hydroisomerization reactions. However, in most applications, only the metal particles are catalytically active. Nevertheless, even in these metal-catalyzed reactions the support can have a large influence on the performance of the catalyst[1,2]. For example, platinum particles deposited on acidic supports show higher turnover frequencies and higher stability against sulfur poisoning in the hydrogenation of aromatics compared to platinum on basic support materials[3,4].

Although the concepts of acidity and basicity are widely known for aqueous systems, these concepts are less trivial when applied to solid systems. In the research described in this thesis, only oxidic supports are used. The Lewis definition of acidity/basicity is used, and thus an oxidic support is regarded as acidic when the surface oxygen atoms are electron-poor and basic when they are electron rich.

A lot of work has been devoted to the understanding of the origin of the effect of the support acid/base properties on the catalytic properties of the metal. The explanations have involved the formation of metal-proton adducts[5,6] on Brønsted acidic supports, a rehybridization of the orbitals within the metal particle induced by the bonding to the support, resulting in an electron transfer between the support and metal[7], and a polarization of the metal particle by the electric field of the support[8] or nearby cations[9] which influences the valence electron distribution within the metal particle. However, the relation between changes in the electronic properties of the metal particle on the one hand and the catalytic properties of the same particle on the other hand is poorly understood.

The goal of the Ph.D. research described in this thesis is to understand the nature of the metal-support interaction in supported metal catalysts and to relate support-induced changes in catalytic properties of the metal particles to changes in electronic properties. A wide variety of

techniques has been used for this research. Two of the most important techniques used are X-ray absorption fine structure spectroscopy (XAFS) and density functional theory (DFT). The XAFS experiments were performed to determine experimentally the electronic properties of supported Pt particles. The DFT calculations were carried out to calculate the electronic properties and to create an understanding of the experimentally observed effects leading to insights in metal-support interaction. These two techniques are explained in the following paragraphs.

Techniques used in this thesis

X-Ray Absorption Fine Structure Spectroscopy (XAFS)

Only an intuitive and general description of XAFS is given here. It is not the intention to provide a full physical background of XAFS, nor to give a detailed description of the data analysis. For a detailed description of XAFS, the overview given by Koningsberger *et al.*[10] is recommended.

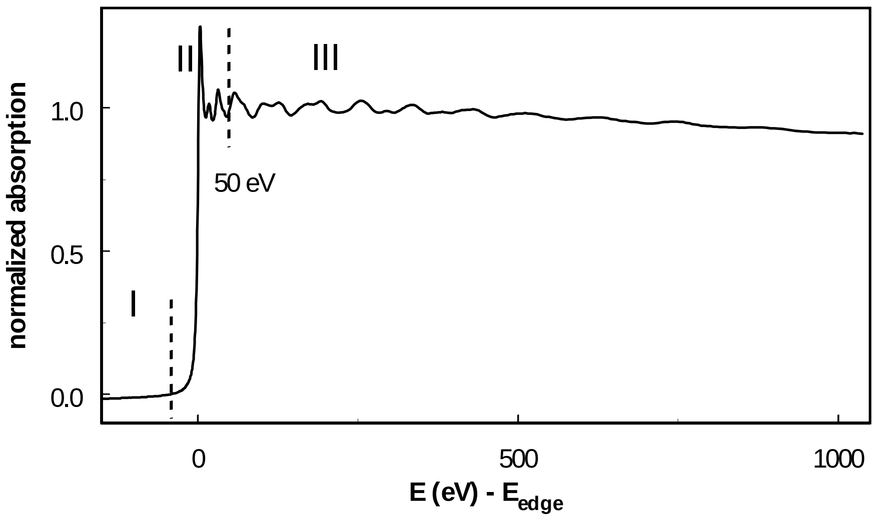

Figure 1: The L_3 X-ray absorption spectrum of a Pt foil. Region I: the pre-edge, II: the X-ray absorption edge and near-edge structure (XANES) and III: the extended X-ray absorption fine structure (EXAFS).

In Figure 1, the L_3 X-ray absorption spectrum of a Pt foil is shown. An X-ray absorption spectrum is generally divided in three regions: I) the pre-edge region, II) the absorption edge and the structure in the near-edge region (XANES) and III) the extended fine structure (EXAFS). During X-ray absorption experiments, which are performed on synchrotrons, a core electron is ejected into energy levels above the Fermi-level. The energy at which this occurs depends on the binding energy of the core-level; therefore the X-ray absorption edge is element specific. The transition has to obey selection rules. For example, when a Pt $2p_{3/2}$ core electron is excited (the L_3 edge), it is excited into the $5d_{5/2}$ level, and a $2p_{1/2}$ electron is excited into the $5d_{3/2}$ level (the L_2 edge). The edges are named after the origin of the electron.

Because in the case of the L_3 edge the electron is excited from the 2^{nd} electron shell (the L-shell), the transition is called the L-edge. Since the $2p_{3/2}$ level is the third level going from low to high energy in the L-shell (the 2s and $2p_{1/2}$ orbitals lie a few thousand eV lower in energy), the subscript 3 in L_3 is added to refer to this transition: the L_3 edge. These transitions are schematically shown in Figure 2.

Due to spin-orbit coupling, the $5d_{5/2}$ band lies a few eV higher in energy than the $5d_{3/2}$ band (as shown in Figure 2). As a result, part of the $5d_{5/2}$ band lies above the Fermi level and is empty. An electron can easily be excited into this band, and due to the amount of empty $5d_{5/2}$ states the L_3 edge (excitation to the $5d_{5/2}$ band) has a *whiteline* (defined as the 1^{st}, most intense peak in the spectrum shown in region II, Figure 1), whereas the L_2 edge (excitation to the filled $5d_{3/2}$ band) for bulk Pt has no whiteline.

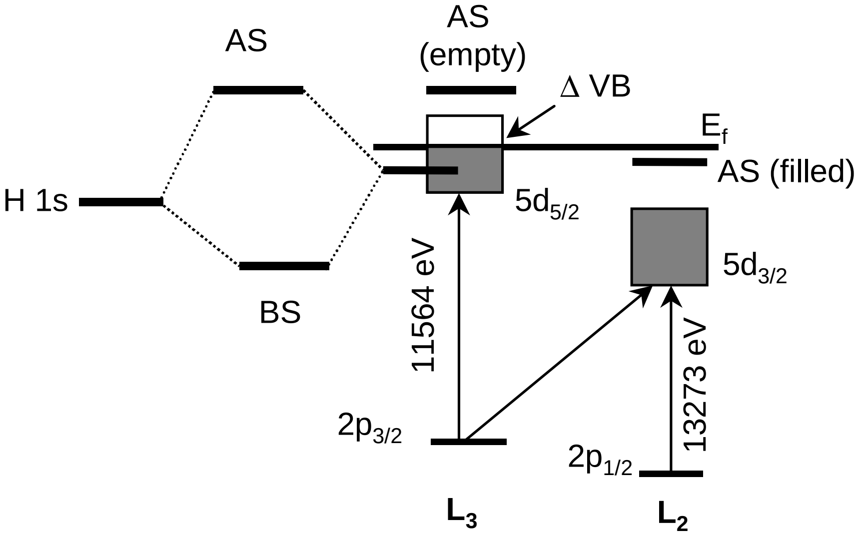

Figure 2: The Pt L_2 and L_3 X-ray absorption edges. The L_2 edge is the transition of the $2p_{1/2}$ level to the $5d_{3/2}$ level, the L_3 edge represents the excitation from the $2p_{3/2}$ level to the $5d_{5/2}$ level and, with a 6-fold smaller probability, to the $5d_{3/2}$ level. When hydrogen is chemisorbed, a bonding (BS) and anti-bonding (AS) state is formed. The overlap of H 1s with the Pt $5d_{3/2}$ (completely filled) leads to a filled AS, the overlap with the $5d_{5/2}$ (partly empty) leads to an empty AS.

Thus, the X-ray absorption edge is very sensitive to the empty $5d_{5/2}$ states, and therefore to the electronic properties of the absorber atom. Moreover, when the core-electron is excited, a core-hole remains behind. This core-hole attracts the higher-lying valence electrons, and it is screened via various processes, distorting the density of states (DOS) around the Fermi level.

This distorted DOS, and therefore the screening processes, are reflected in the whiteline. By taking the difference of the L_2 and L_3 edge in vacuum, the difference in the empty valence band (ΔVB) between the L_2 and L_3 edge, and the effect of the screening processes on the empty $5d_{5/2}$ states can be isolated.

When an adsorbate is chemisorbed on the Pt surface, the overlap between the orbitals of Pt and the adsorbate leads to the presence of empty anti-bonding states (AS). The AS of

chemisorbed hydrogen is empty on the L_3 edge, but filled on the L_2 edge. When an electron is excited to the $5d_{5/2}$ edge, this electron is also excited into the AS. The different contributions to the L_2 and L_3 edge are summarized in Table 1. When the difference between the L_3 spectra with and without adsorbate is taken, the influence of the adsorbate on the X-ray absorption spectrum can be isolated. In early work, it was assumed that this difference was totally determined by the AS, and that the difference spectrum therefore represents a shape resonance describing the anti-bonding state[11]. Based on this idea, a paper was published in J. Phys. Chem. B. The results as published in this paper[12] are described in chapter 5 of this thesis. Later it was pointed out by Ankudinov et al.[13] that in some configuration of the hydrogen adsorption site, hydrogen can influence the Pt-Pt multiple scattering significantly. This is also reflected in the L_2 and the L_3 X-ray absorption edges. The basic outcome of chapter 5 is not changed by these new findings. However, using this more refined interpretation it was possible to show that the L_3 difference spectrum (L_3 edge with H minus L_3 edge clean) is sensitive to the mode of hydrogen adsorption on Pt. A crucial finding as described in chapter 6 is that the mode of hydrogen adsorption is strongly influenced by the acid/base properties of the support.

Table 1: The differences between the L_2 and L_3 edges with and without chemisorbed hydrogen.

	L_3	L_2
H on Pt	REF + ΔVB + influence of H_2 on L_3 edge	REF + influence of H_2 on L_2 edge
clean Pt	REF + ΔVB	reference spectrum (REF)

The third region in the XAFS spectrum (region III in Figure 1) shows oscillations in the absorption coefficient. If the energy of the X-ray photon is higher than the energy that is required for ejecting the core-electron, the surplus of energy is converted into kinetic energy of the excited electron. With this kinetic energy, the electron moves more or less freely in the neighborhood of the absorber atom (the atom from which the excited electron originates) and it can encounter a neighboring atom. This atom has some electron density as well, and thus the ejected electron is repelled by the neighboring electrons – a process called scattering. At high kinetic energies, the ejected electron only scatters against heavy Z elements (*e.g.* Pt). Low Z elements like H have only a measurable cross section for scattering at very low kinetic energies of the outgoing electron (‘An electron with high energy passes right through a low Z element’).The result of the scattering process is an oscillatory behavior of the X-ray absorption coefficient, which is related to the local structure around the absorber atom. This part of the spectrum is called the EXAFS region (region III, Figure 1). A detailed analysis of the oscillations in the EXAFS region gives the type and number of neighboring atoms of the absorber, the distance to that neighbor and the disorder in the structure. In addition to scattering against the electrons of neighbors, the ejected electron can also scatter against the

valence electrons of the atom from which it is ejected. This scattering is called atomic XAFS (AXAFS)[14,15].

Density Functional Theory

Density Functional Theory, or DFT, is a very popular and powerful computational method of quantum chemistry. Here, it is tried to create an understanding of DFT for chemists, without going into too much detail. For a good review, the paper by Nagy is recommended[16].
The most important equation in quantum chemistry is the Schrödinger equation,

$$\hat{H}\Psi = E\Psi \qquad (1)$$

and the energies and the wavefunctions describing the system can be obtained when the Schrödinger equation is solved.
DFT is based on the proof of Hohenberg and Kohn that the total energy of a system is a function of the electron density only. In order to obtain the ground-state energy of a system one has to determine the ground-state electron distribution. Unfortunately, this is far from trivial.
However, the idea is simple: in an atom, the electrons move around the core. Since the electrons move, they have a kinetic energy T_K. The negative electrons move around a positive core, so they have a Coulomb interaction with the nucleus. Moreover, there can be several electrons that move around the core, and they repel each other. The sum of all coulomb interactions is given by the term V_C in equation 2. This term depends on the total electron density. So far, determining the energy of all electrons would be easy. However, in the case of a one-electron system, according to the Coulomb term that single electron would have interaction with itself, which is of course unrealistic. So, a correction for this self-interaction must be added. This can be done – for example – by adding 1 positron with exactly the same density as a certain electron in an orbital. Moreover, in reality electrons do not move freely, but their motions are correlated. Both effects are added in a so-called ‘exchange-correlation’ term V_{xc}. Now, the Hamiltonian can be written as:

$$\hat{H} = \hat{T}_K + \hat{V}_C + \hat{V}_{xc} \qquad (2)$$

The problem is that the dependence of the exchange-correlation V_{xc} on the electron density is not exactly known. Therefore, it has to be approximated. The simplest approximation is called the local density approximation (LDA). The LDA description makes use of a homogeneous electron-gas. Since within atoms and molecules the electrons are not distributed homogeneously, the LDA approximation can be improved by adding a gradient in the electron density. This is called the generalized gradient approximation (GGA). DFT calculations with the LDA – GGA approximation give very acceptable results for a wide variety of systems like the chemisorption of gases on surfaces, as applied in this thesis.
DFT makes use of so-called basissets: a series of functions that describe each occupied atomic orbital in the groundstate. If one function is used for each atomic orbital, the basisset is called ‘minimal’, if *e.g.* three functions are used to describe each orbital the basisset is called ‘triple

ζ'. In general, the more functions are used to describe each atomic orbital, the higher the accuracy is. The flexibility of a basisset can be increased by including functions for higher, unoccupied orbitals like the p-orbital for a hydrogen atom. These functions are referred to as 'polarization functions'. Heavy atoms like Pt have a large number of core levels that are virtually unaffected by bonds or an electric field. Therefore, it is a waste of computer-time to include these orbitals in the calculations of larger systems. Thus, these core-orbitals are kept fixed and they are not allowed to overlap with other orbitals: the core is 'frozen'.

In addition, in heavy elements the electrons close to the nucleus have to move very fast in order to overcome the large attraction by the core and maintain their position[17]. For example, the 1s electrons in tin (element 50) move with speeds of about 60% of light. The energy of these electrons is high enough to become relativistic and the mass of the electrons increases accordingly. Due to the higher mass of its electrons, the 1s orbital contracts. Also the electrons in the outer s orbitals spent some time close to the core, and they have to contract along with the 1s orbital. The geometry of the outer d-orbitals is such that their electrons don't spend much time near the core and these orbitals hardly contract at all. The relativistic contraction of the outer s orbitals has a large impact on the physical and chemical properties of the atom, and these relativistic effects have to be included for heavier elements (containing 5d, 6s and/or 6p electrons). In the case of ADF[18], the DFT code that is used in this thesis, the ZORA approach[19] is used to include relativistic effects[20].

This thesis

The goal of this thesis is to investigate the influence of the acid/base properties of the support on the electronic structure of the metal particles, and to relate these effects to the catalytic properties. A prerequisite of performing such a research is to have well-defined supported metal catalysts. Although this may seem straightforward, the synthesis of such catalysts is rather an art than science. In literature, many trial-and-error reports are given on the synthesis of supported noble-metal catalysts. It is (almost) inevitable that one ends up with a particle-size distribution: some metal particles are very small and may contain only 5 atoms, whereas others are very large and may contain as many as 1000-5000 atoms. Since also the particle size has a large influence on the catalytic and electronic properties, a large particle size distribution obscures the support effect. This particle-size distribution is often already present directly after synthesis. One starts with a metal precursor (in this case $Pt(NH_3)_4(NO_3)_2$) on a support (SiO_2), and in a series of temperature and gas treatments the ligands of the metal precursor are removed and one ends up with a supported metal catalyst (Pt/SiO_2).

During these temperature and gas treatments, processes like reduction, oxidation and sintering take place. In **Chapter 2** it is clarified what processes are responsible for the final metal particle size and particle size distribution. This is done using a combination time resolved extended X-ray absorption fine structure spectroscopy (quick EXAFS) and mass spectrometry.

The catalytic properties of the supported Pt particles have been investigated using the hydrogen – deuterium (H/D) exchange of cyclopentane (C_5H_{10}, CP) as a test reaction. With H/D exchange of CP, the hydrogen atoms (H) are exchanged for deuterium (D). Since a full understanding of the mechanism of the H/D exchange of cyclopentane was missing in literature, the attention was first focused on unraveling the mechanisms responsible for the H/D exchange reaction. In **Chapter 3** a Monte-Carlo model is presented explaining the observed selectivities observed in the H/D exchange reaction. In addition, a model describing the kinetics is presented. Using this Monte-Carlo model in **Chapter 4** it was possible to investigate the influence of the support acid/base properties on the H/D exchange of CP catalyzed by the supported Pt particles.

One of the primary reactants in hydrogenolysis and hydrogenation reactions is hydrogen (H_2). Since enhanced reaction rates induced by the support acidity are observed for a wide variety of hydrogenolysis and hydrogenation reactions for all kinds of hydrocarbons, it is very important to investigate and understand the influence of the support acid/base properties on the strength and mode of hydrogen chemisorption on the catalytically active Pt surface. In **Chapter 5**, the influence of the temperature on the hydrogen chemisorption is investigated using the XAFS technique (analysis of L_3 and L_2 near edge spectra and EXAFS). In **Chapter 6**, the influence of the temperature and the support acid/base properties on the preferred adsorption site and adsorption strength of hydrogen is investigated using a combination of the analysis of the L_3 near edge spectra and density functional theory (DFT).

In addition to the catalytic and hydrogen adsorption properties of the supported Pt catalysts, also the general influence of the support acid/base properties on the electronic structure of the Pt particles has to be investigated. One of the large differences in electronic properties of bulk platinum and highly dispersed Pt particles is that bulk platinum is a conductor, whereas small particles are insulators. Hence, with increasing particle size there must be a transition from insulator-to-conductor. In **Chapter 7** it is shown that taking the difference of the Pt L_2 and L_3 edge in vacuum (ΔVB, Figure 2), the influence of the support acid/base properties and the influence of particle size on the screening processes on the empty $5d_{5/2}$ states can be isolated. The support induced differences in the insulator-to-conductor transition are caused by different electronic properties of the Pt valence band. In order to understand in more detail the type of interaction of the support with the Pt particles, the influence of the acid/base properties of the support on the density of states of the Pt particles is determined in **Chapter 8** using a very powerful combination of theory (DFT calculations) and experiments (XAFS spectroscopy).

In **Chapter 9** DFT calculations are performed in order to obtain further insight in the support induced differences in electronic properties relate to differences in the chemisorption properties of adsorbates like H, CH_3 and CH_2. The influence of the support acid/base

properties on the chemisorption behavior of these adsorbates on Pt is correlated with the kinetic data obtained for the hydrogenolysis of alkanes .

Reference list

1. R. A. Dalla Betta and M. Boudart, *Proc 5th Int Con Cat* (1973), 1329-1341.
2. A. Yu. Stakheev and L. M. Kustov, *Appl. Catal. A: General*, **188** (1999), 3-35.
3. H. Yasuda and S. Y. Y. Sato, *Catal. Today,* **50** (1999), 63-71.
4. A. de Mallmann and D. Barthomeuf, *J. Chim. Phys.*, **87** (1990), 535-538.
5. Z. Karpinski, S. N. Gandhi and W. M. H. Sachtler, *J. Catal.*, **141** (1993), 337-346.
6. Z. Zhang, T. T. Wong and W. M. H. Sachtler, *J. Catal.*, **128** (1991), 13-22.
7. G. Larsen and G. L. Haller, *Catal. Lett.*, **3** (1989), 103-110.
8. B. L. Mojet, J. T. Miller, D. E. Ramaker and D. C. Koningsberger, *J. Catal.*, **186** (1999), 373-386.
9. A. P. J. Jansen and R. A. van Santen, *J. Chem. Phys.*, **94** (1990), 6764.
10. D. C. Koningsberger, B. L. Mojet, G. E. van Dorssen and D. E. Ramaker, *Top. Catal.,* **10** (2000), 143-155.
11. D. E. Ramaker, B. L. Mojet, M. T. Garriga Oostenbrink, J. T. Miller and D. C. Koningsberger, *Phys. Chem. Chem. Phys.*, **1** (1999), 2293-2302.
12. M. K. Oudenhuijzen, J. H. Bitter and D. C. Koningsberger, *J. Phys. Chem. B,* **105** (2001), 4616-4622.
13. A. L. Ankudinov, J. J. Rehr, J. Low and S. R. Bare, *Phys. Rev. Letters,* **86** (2001), 1642-1645.
14. D. E. Ramaker, B. L. Mojet, D. C. Koningsberger and W. E. O'Grady, *J. Phys.: Condens. Matter,* **10** (1998), 8753-8770.
15. Rehr, J. J.; Zabinsky, S. I.; Ankudinov, A. L.; Albers, R. C. *Physica B* **1995**, *208&209*23-26.
16. Á. Nagy, *Physics Reports,* **298** (1998), 1-79.
17. G. C. Bond, *Platinum Metals Rev.,* **44** (2000), 146-155.
18. Amsterdam Density Functional Package ADF 2000.02, Department of Theoretical Chemistry, Vrije Universiteit, Amsterdam. http://www.scm.com.
19. P. H. T. Philipsen, E. Van Lenthe, J. G. Snijders and E. J. Baerends, *Phys. Rev. B,* **56** (1997), 13556.
20. E. Van Lenthe, E. J. Baerends and J. G. Snijders, *J. Chem. Phys.*, **101** (1994), 9783.

2

Understanding the Influence of the Pretreatment Procedure on the Platinum Particle Size and Particle Size Distribution for SiO_2 Impregnated with $[Pt^{2+}(NH_3)_4](NO_3^-)_2$

A combination of HRTEM, mass spectrometry and Quick EXAFS

Abstract

Using the combination of mass spectrometry, *in situ* QEXAFS, HRTEM and hydrogen chemisorption, the reactions taking place during different pretreatments of the catalyst precursor $[Pt^{2+}(NH_3)_4](NO_3^-)_2$ impregnated on a high surface area SiO_2 (400 m^2/g) were elucidated. Direct reduction in hydrogen leads to the formation of Pt metal particles in the temperature range of 150-200°C in a fast process. The reduction is accompanied by sintering of the platinum particles, leading to relatively large particles with an average particle size of approximately 14-16 Å. Autoreduction in helium leads to multiple steps in the reduction. Around 210°C and 240°C, NO_x released due to the decomposition of NH_4NO_3, formed during heating up to 180-200°C, reduce the catalyst precursor at a high rate. At higher temperatures, the reduction continues slowly through an autoreduction of the $Pt(NH_3)_x^{2+}$ complex. The slow reduction rate suggests a non-mobile species. Accordingly, the final metal-particle size is small with particles of 10-12 Å. The particle size distribution after autoreduction is considerably smaller than after direct reduction. Calcination proceeds via a similar decomposition of NH_4NO_3 as autoreduction, but the atoms are immediately oxidized to Pt-O. Reduction following the calcination results in large particles. The key to obtain small particles with a relatively narrow size distribution is to avoid the formation of mobile species. With impregnated $[Pt^{2+}(NH_3)_4](NO_3^-)_2$, this is best achieved by autoreduction.

Introduction

A straightforward method to load a metal precursor of a supported heterogeneous transition-metal catalyst is incipient wetness impregnation[1,2]. Typically, a metal-precursor is dissolved in an aqueous solution and brought into the pores of the support. To remove all ligands and obtain metal particles, the impregnated support has to be pretreated. Generally, a pretreatment consists of several temperature-programmed steps in different gaseous environments (for example H_2, He or O_2). This pretreatment process is crucial for the final metal particle size and particle size distribution[3]. Since catalysis is a surface process, small particle sizes are crucial to have a high fraction of catalytically active surface atoms. Also, small particles are in general more active in catalysis. In addition, it has been reported repeatedly that the support largely influences the catalytic properties of supported catalysts[4-7]. If this metal-support interaction is well understood, this promises the possibility for tailor-made catalysts. In order to understand these metal-support effects it is crucial to be able to prepare different particle sizes on a support with a narrow particle size distribution. This can only be done when the pretreatment processes leading to certain metal particle sizes and distributions are well understood.

The metal precursor can be one of a variety of complexes. Commonly used precursors for Pt are H_2PtCl_6[8-13], $Pt(NH_3)_4(NO_3)_2$[14] and $Pt(acac)_2$[12,15,16]. Each precursor has its own unique properties. The choice of precursor therefore depends on parameters like the support properties and the requirements for the final metal particle size. A disadvantage of H_2PtCl_6 can be the presence of chlorine since chlorine alters the acidity of the support material[17] and can poison the catalyst. Platinum acetylacetonate ($Pt(acac)_2$) is reported to result in highly dispersed particles[12]. A disadvantage of this precursor can be the use of organic solvents during the exchange or impregnation procedure. $Pt(NH_3)_4(NO_3)_2$ overcomes these disadvantages. It can be used in aqueous solutions and all ligands can be removed by heating the sample. For these reasons, the $Pt(NH_3)_4(NO_3)_2$ on SiO_2 precursor is used in this study.

Typical studies on the pretreatment of $Pt(NH_3)_4(NO_3)_2$ deal with a trial-and-error variation of the pretreatment resulting in different metal particle sizes (*e.g.* ref. 3). For pretreatments involving zeolitic supports, generally it is found that slow heating rates (*e.g.* 0.2°C/min) are crucial for small particle sizes[18,19]. This is caused by the microporous structure of zeolites which adsorbs water strongly. H_2O present during pretreatment steps generally results in large particles[18]. For macroporous supports such as SiO_2, this is much less of a problem. Water desorbs easily at relatively low temperatures. Therefore, the heating rate during a pretreatment involving macroporous supports can be high compared to zeolites (*e.g.* ref. 3).

Several studies that already gave some insight onto the chemical processes taking place during the pretreatment processes have been performed[18,20]. Kinoshita *et al.*[20] studied the thermal stability of several metal precursors, including $[Pt^{2+}(NH_3)_4](NO_3^-)_2$, in air and hydrogen. It was found for all precursors that the thermal stability in air is higher than in hydrogen.

Dalla Betta and Boudart[21] studied the pretreatment of $Pt(NH_3)_4^{2+}$ exchanged on zeolite Y. They report that direct reduction in H_2 leads to the formation of neutral $Pt(NH_3)_2H_2$ hydride in the temperature range of 80-100°C, ultimately resulting in agglomeration and thus large particles. They conclude that decomposition of the complex in O_2 should be carried out prior to the reduction.

Van den Broek *et al.*[18] studied the pretreatment of ion-exchanged $Pt(NH_3)_4^{2+}$ on zeolite HZSM-5 in He and O_2 with UV-Vis spectroscopy and mass spectrometry. For the pretreatment in He, autoreduction was found to occur via to the formation of H_2 and N_2 from the NH_3 ligands. Calcination in O_2 led to the production of NO_x in several different steps. The presence of H_2O was found to play a crucial role in the pretreatment, replacing NH_3 as a ligand on the Pt^{2+} complex.

Keegan *et al.*[22] studied the calcination and reduction of the same $Pt(NH_3)_4^{2+}$ on HZSM-5 system with energy dispersive Extended X-ray Absorption Fine Structure (EXAFS). They showed that during calcination the Pt-Pt coordination rises, indicating agglomeration. The final metal particle size obtained after direct reduction (no calcination prior to the reduction) was smaller than the particle size obtained after calcination prior to the reduction. The authors did not clarify the chemistry of the pretreatment process.

All of these literature reports mainly deal with exchanged $Pt(NH_3)_4^{2+}$ on zeolite. The main difference between exchanged and impregnated $[Pt^{2+}(NH_3)_4](NO_3^-)_2$ is the presence of nitric groups (NO_3^-) on the support in the impregnated case. As will be shown, these groups play a vital role in the pretreatment of the impregnated catalyst precursor.

An example of a study that deals with impregnated $[Pt^{2+}(NH_3)_4](NO_3^-)_2$ on silica is the study of Zou and Gonzalez[23]. Using *in situ* UV reflectance spectroscopy, they establish the presence of the same mobile $Pt(NH_3)_2H_2$ hydride in the same temperature range as Boudart[21] suggested.

Muñoz-Páez and Koningsberger[24] use a combination of TPR, MS and EXAFS to study the decomposition of $[Pt^{2+}(NH_3)_4](OH^-)_2$ impregnated on γ-Al_2O_3. They report the decomposition of the precursor to $Pt(NH_3)_2O$ during drying in He at 120°C and a partial reduction of the precursor to metallic Pt when reduced at 180 and 200°C.

All in all, little has been reported on the reactions taking place for impregnated $[Pt^{2+}(NH_3)_4](NO_3^-)_2$ on macroporous supports. Moreover, the relation of the pretreatment to the final particle size distribution is rarely investigated. In our view, knowledge of the reactions occurring during pretreatment is a crucial step towards the development of a process leading to uniform small particle sizes.

In this study, a powerful combination of high resolution transmission electron microscopy (HRTEM), mass spectrometry (MS) and Quick EXAFS (QEXAFS) is used to study the reactions of $[Pt^{2+}(NH_3)_4](NO_3^-)_2$ impregnated on SiO_2 during different pretreatment processes.

MS is used to monitor which gases are produced during the pretreatment. QEXAFS is used to study the local structure of the Pt complex during the pretreatment. The timescale of

QEXAFS scans (30-90 seconds per scan) is suitable to study reactions like pretreatment processes. The whiteline area gives information concerning the oxidation state[25]. The EXAFS region represents the geometrical structure of the Pt atom. The final metal particle size was obtained from the Pt-Pt first shell coordination number, H_2 chemisorption[26] as well as HRTEM.

$[Pt^{2+}(NH_3)_4](NO_3^-)_2$ impregnated SiO_2 was heated in three different gases: an inert gas (Ar or He), H_2 and O_2. As mentioned above, heating in an inert gas leads to autoreduction of the $[Pt^{2+}(NH_3)_4](NO_3^-)_2$ complex. Heating in H_2 leads to a direct reduction of the complex. Heating in O_2 (calcination), generally performed to decompose the complex before reducing the metal, results in the formation of PtO_x.

Experimental

Catalyst precursor preparation

5 g vacuum-dried SiO_2 (Engelhard, BET surface area 400 m^2/g, pore volume 1.1 ml/g) was impregnated with 5.5 ml of an aqueous solution of $[Pt^{2+}(NH_3)_4](NO_3^-)_2$ (Aldrich, 18.0 mg/ml, resulting in 1 wt.% Pt/SiO_2) using the incipient wetness method. The impregnated support was dried in a water-free nitrogen flow for 1 hour at room temperature and for 18 hours at 80°C.

Pretreatments

Three different pretreatments were performed and studied by both Quick EXAFS and MS. During each pretreatment the impregnated support was heated in one gas with a ramp of 2°C/min from room temperature to 400°C. The gases used were 1) either He (QEXAFS) or Ar (MS) (this sample is called 'Pt[Ar/He]'), 2) O_2 ('Pt[O_2]') and 3) H_2 ('Pt[H_2]').

Mass spectrometry

A continuous downflow fixed bed reactor (inner diameter 0.8 cm) was loaded with 1 gram of a sieve fraction (212 μm < d_p < 425 μm) of the impregnated SiO_2. The outlet of the reactor was connected to a quadrupole mass spectrometer (Balzers QMS 420) via a capillary. The monitored masses (ions) were 2 (H_2^+), 16 (NH_2^+, O^+), 17 (NH_3^+, OH^+), 18 (H_2O^+), 28 (N_2^+), 30 (NO^+), 32 (O_2^+), 40(Ar^+), 44 (N_2O^+) and 46 (NO_2^+) a.m.u. With these masses, all likely reaction products can be monitored. Mass 16 was used to identify NH_3 since the contribution of the O^+ fragment ion of H_2O is limited for this mass and can easily be corrected for.

Quick EXAFS

120 mg of the impregnated SiO_2 was pressed in a self-supporting wafer and mounted in a stainless steel *in situ* cell[27]. This cell was attached to a series of flow controllers and to a temperature controller. It was checked that differences between the layout of the *in situ* EXAFS cell and the downflow reactor used for the MS experiments do not result in differences in temperature profiles and reactions of the catalyst precursor.

Quick EXAFS measurements were performed at the HASYLAB synchrotron (station X1.1) in Hamburg, Germany. The measurements were done in transmission mode using ion chambers filled with a mixture of Ar and N_2 to have an absorption of 20% in the first and of 80% in the second ion chamber. The monochromator (a double Si-111 crystal) was detuned to 50% at maximum intensity to avoid the presence of higher harmonics in the X-ray beam. In QEXAFS mode, the monochromator is in continuous motion.

The QEXAFS scans were performed at the Pt L_3 edge (11564 eV) and were taken from 11500 – 12000 eV with steps of 1 eV. Each 60 seconds 1 scan was taken.

The absorption data was background-subtracted using standard procedures[28,29]. The spectra were normalized on the height of the edge-step at 50 eV over the edge. The whiteline intensity was determined by the height of the whiteline after normalization. Data analysis was performed by multiple shell fitting in R-space ($1.3<R<3.2$ Å, $2.5<k<9.5$ Å^{-1}). k-weightings of 1 and 2 were used. Experimentally calibrated theoretical references[30] obtained with FEFF7[31] were used as references. The references can be used for $k>2.5$ Å^{-1}. The variances in imaginary and absolute parts were used to determine the fit quality[29]. Different backscatterers were identified by applying the difference-file technique[32] using phase-corrected Fourier transforms.

Transferability of the phase shift and amplitude among the nearest neighbors for the whole periodic table is generally assumed[25]. Using EXAFS no distinction between nitrogen and oxygen neighbors can therefore be made and nitrogen neighbors are analyzed with a Pt-O reference compound.

Hydrogen chemisorption

Experimental details of H_2 chemisorption measurements are described elsewhere[33]. Typically, the reduced samples are evacuated at 200°C and the H_2 uptake is measured at 35°C.

The samples were prepared *in situ* from the starting material using the same pretreatments as described above. The sample heated in He (Pt[Ar/He]) was measured twice: once directly after the pretreatment and once after the sample had been flushed with H_2 at 400°C for 30 minutes following the autoreduction before it was cooled down to measure the H_2 chemisorption. This was done to check whether all platinum was reduced after autoreduction. The sample heated in O_2 (Pt[O_2]) was also flushed at 400°C with subsequently He and H_2 to reduce the Pt particles prior to the chemisorption measurement.

Transmission electron microscopy

For samples Pt[Ar/He] and Pt[H_2] several pictures were recorded. For both samples the size of over 230 Pt particles on the pictures were measured. This was used to determine the average metal particle size and distribution in particle size. The limit in particle size for detection with HRTEM of the Pt particles is 5-10 Å (*i.e.* smaller particles are invisible).

High resolution transmission electron microscopy (HRTEM) was performed by the Dutch National Center for high resolution electron microscopy. The microscope was a Philips

CM30T transmission electron microscope with a LaB_6 filament operating at 300 kV. Samples were mounted on a microgrid carbon polymer supported on a copper grid by placing a few droplets of a suspension of ground sample in ethanol on the grid, followed by drying at ambient conditions.

Results

Direct Reduction, Pt[H_2]

Table 1 summarizes the results for H_2 chemisorption, HRTEM and EXAFS analysis for all samples.

In Figure 1, the development of the normalized near-edge region of the Pt L_3 edge during heating is shown. A sharp decrease in the whiteline intensity between 150 and 200°C is observed.

The EXAFS region of the QEXAFS spectra was analyzed. In Figure 2, an example is given of the Fourier transform and its best R-space fit of the spectrum taken at 50°C. The fit was performed with a Pt-O reference. It is noted again that no distinction between O and N neighbors can be made. The fit and experiment are in good agreement. This quality of the experimental data and of the fit is representative for all spectra. This spectrum represents the freshly impregnated $[Pt^{2+}(NH_3)_4](NO_3^-)_2/SiO_2$. The Pt-Pt coordination number is 0, as expected, and the fitted Pt-N coordination number is 5.1.

In Figure 3, the whiteline intensity, Pt-Pt and Pt-N coordination numbers as a function of temperature are shown. All fit parameters are given in Table 2. From Figure 3, it is obvious that the whiteline intensity sharply decreases for 150°C < T < 200°C, in a temperature range of only 50°C. This is accompanied by a simultaneous decrease in Pt-N coordination number and increase in Pt-Pt coordination number. The Pt-Pt coordination number rises from 0 at 150° to 8.0 at 200°C. The final Pt-Pt coordination number at 400°C is 9.5. The Pt-N coordination number drops from 4.6 at 150°C to 0.5 at 200°C.

Table 1: Sample properties.

Sample	H/Pt[a]		HRTEM diameter (Å)	Final[b] coordination number	
	total	strong		Pt-O	Pt-Pt
Pt(H_2)	0.89	0.36	18	0.2	9.5
Pt(He/Ar) I [c]	0.99	0.39	14	0.0	7.8
Pt(He/Ar) II [d]	1.09	0.53			
Pt(O_2) [d]	0.80[e]	0.30	n.d.	3.7	0

[a] The error margin in the H/Pt value is approximately ±0.03

[b] The final coordination numbers were derived from the QEXAFS spectrum at 400°C. The initial (at 50°C) Pt-O(N) coordination number was in all cases 5.0-5.4. The initial Pt-Pt coordination number was in all cases 0.

[c] Hydrogen chemisorption was measured directly after autoreduction.

[d] The autoreduction (or calcination) was followed by reduction for 30 min. in H_2 at 400°C.

Table 2: Fit parameters[a] of QEXAFS spectra during heating in H_2 and variances of fits. (R-space fit, 2.5 < k < 9.5 Å^{-1}, 1.3 < R <3.2 Å, k^2 weighted).

	O shell				Pt shell				variances (%)	
T(°C)	R(Å)	N	$\Delta\sigma^2$ [b]	E_0	R(Å)	N	$\Delta\sigma^2$ [b]	E_0	im.	abs.
51[c]	2.01	5.1	4.6	3.4	-[d]	-	-	-	0.595	0.319
143	2.01	4.6	4.3	4.0	-[d]	-	-	-	0.318	0.139
156	2.0	3.3	1.8	4.2	2.71	3.7	14.2	10.0	1.01	0.490
165	1.98	2.2	2.6	6.1	2.68	5.2	11.5	9.0	1.07	0.250
180	1.99	1.6	3.6	4.3	2.70	5.6	9.6	4.9	0.661	0.348
185	1.95	1.0	5.6	10.0	2.70	7.2	10.4	3.9	0.690	0.318
200	1.97	0.5	8.0	10.0	2.70	8.0	10.3	3.4	0.501	0.106
300	-[d]	-	-	-	2.70	8.7	11.8	2.6	0.904	0.605
400	-[d]	-	-	-	2.67	9.5	15.6	2.9	1.25	0.323

[a] errors in fits: $R \pm 1\%$, $N \pm 20\%$, $\Delta\sigma^2 \pm 5\%$, $E_0 \pm 10\%$
[b] Debye-Waller factor *10^{-3}
[c] fit with k^1 weighting, 1.3 < R < 2.5 Å
[d] No contribution of this shell present

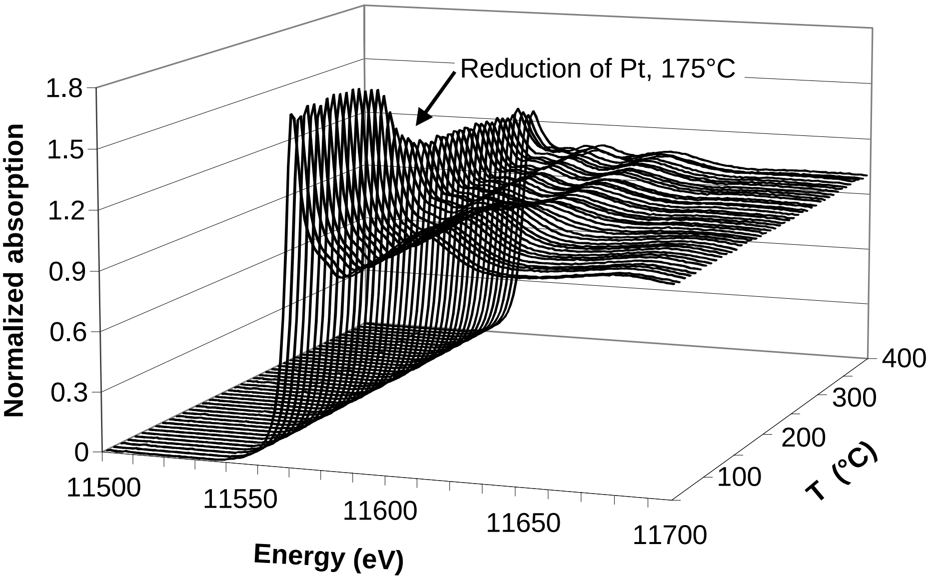

Figure 1: The near-edge region of the Pt L_3 edge during heating of $[Pt^{2+}(NH_3)_4](NO_3^-)_2$ on SiO_2 in H_2. The sharp decrease between 150 and 200°C indicates reduction of the Pt.

Figure 4 shows the intensity of masses 16 (ions NH_2^+, O^+), 17 (NH_3^+, OH^+) and 18 (H_2O^+) during heating of the catalyst precursor in H_2. No other gases are produced.
Below 100°C, the desorption of physisorbed H_2O is observed. Around 210°C a clear maximum in the desorption of H_2O and NH_3 is observed. Although mass 16 is caused by fragment ions of H_2O and NH_3, the intensity of mass 16 is too high to be explained by the

desorption of H_2O only. Therefore, it must be concluded that NH_3 desorbs simultaneously. A strong shoulder in the desorption of H_2O is observed between 150 and 200°C.

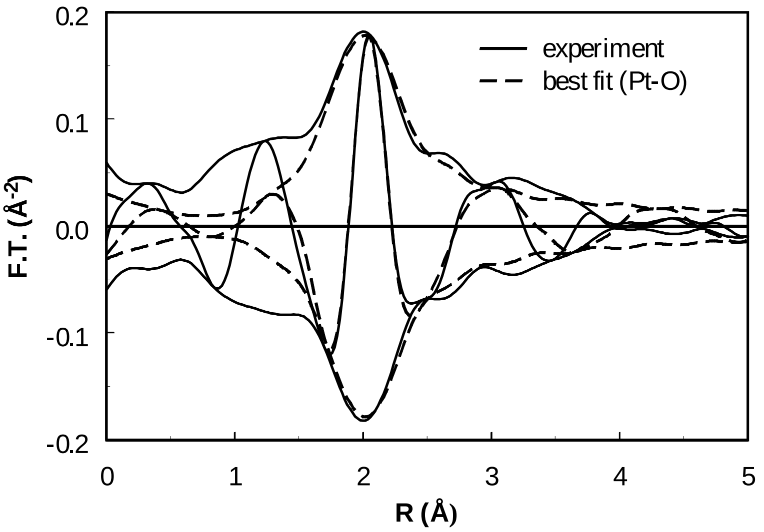

Figure 2: An example of a Fourier Transform and best-fit (R-space fit, single Pt-O shell, 1.3 < R < 2.6 Å, k^1 weighted, 2.5 < k < 9.5 $Å^{-1}$) based on a QEXAFS spectrum obtained during heating in H_2 at 50°C.

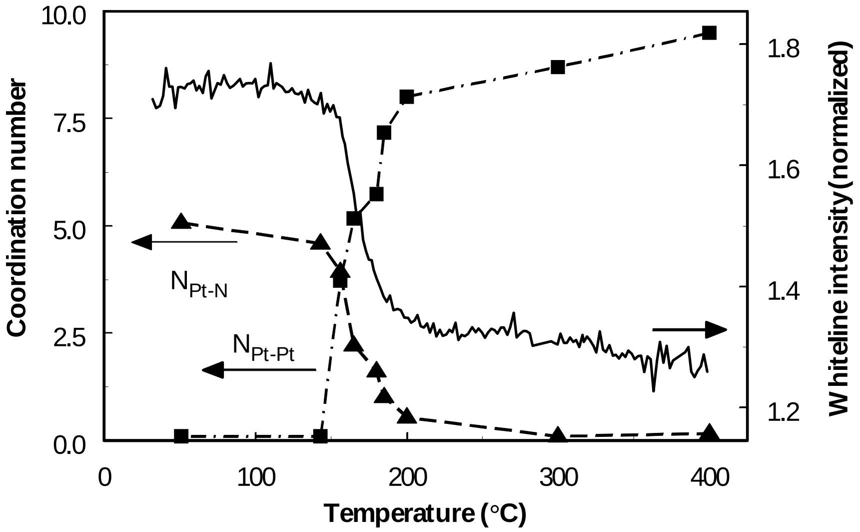

Figure 3: The normalized whiteline intensity (solid line), the Pt-N coordination number (dashed line, triangles) and the Pt-Pt coordination number (dashed-dotted line, boxes) as a function of temperature during heating of $Pt(NH_3)_4(NO_3)_2$ on SiO_2 in H_2.

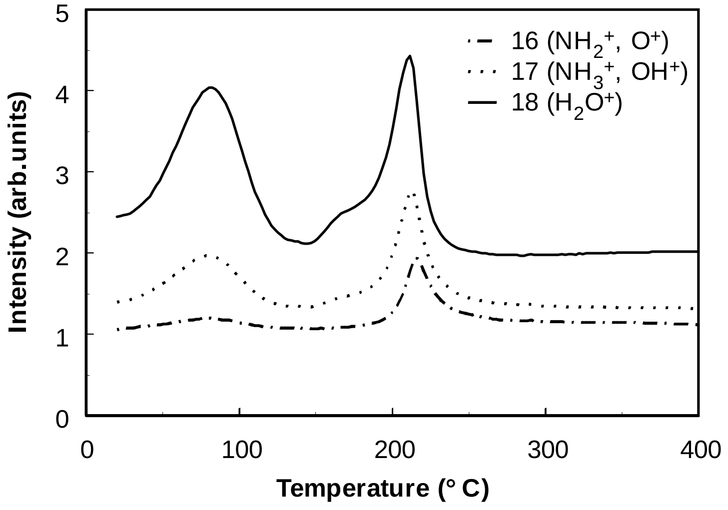

Figure 4: The intensity of (fragment)ions of desorbed gases vs. temperature during reduction in H_2.

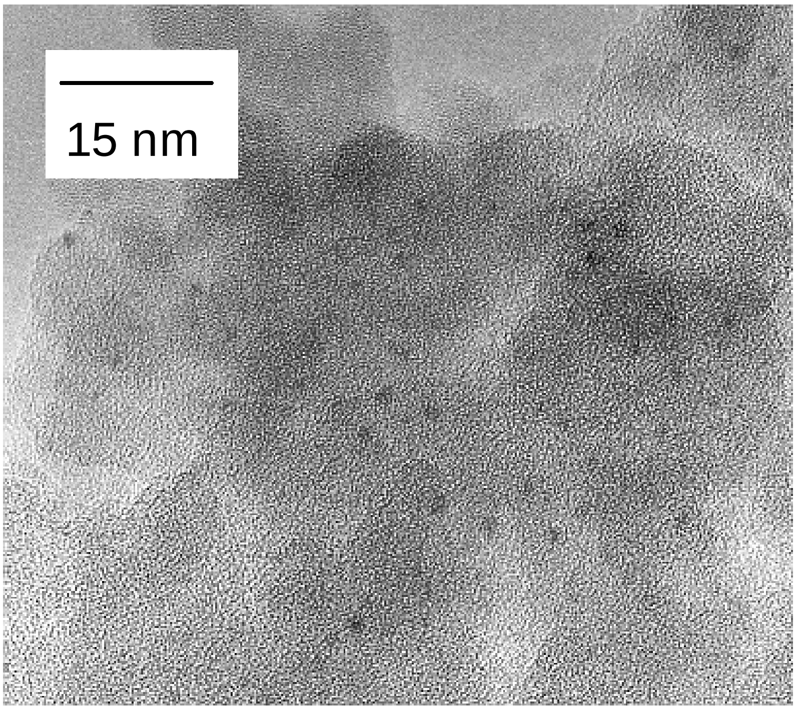

Figure 5: A representative HRTEM picture of the sample after direct reduction (Pt[H_2]). Dark spots: Pt-particles.

HRTEM was used to determine the final metal particle size. A representative photograph is shown in Figure 5. Multiple photographs were analyzed and the size of at least 230 particles was measured to determine the average particle size and the particle size distribution (Figure 6, grey). The particle size distribution appears to be bimodal, with maxima at 14 and 22 Å. The average particle size (as determined with HRTEM) for this sample is 18 Å.
Hydrogen chemisorption showed an average hydrogen coverage of H_{total}/Pt=0.89 (Table 1).

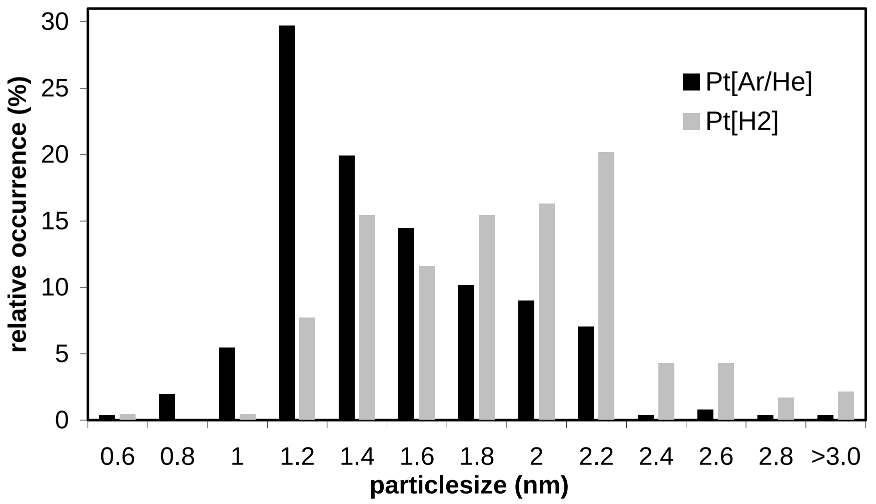

Figure 6: The particle size distribution as determined with HRTEM by measuring the size of >230 particles. Black bars: autoreduced sample (Pt[Ar/He]). Grey bars: directly reduced sample (Pt[H_2]).

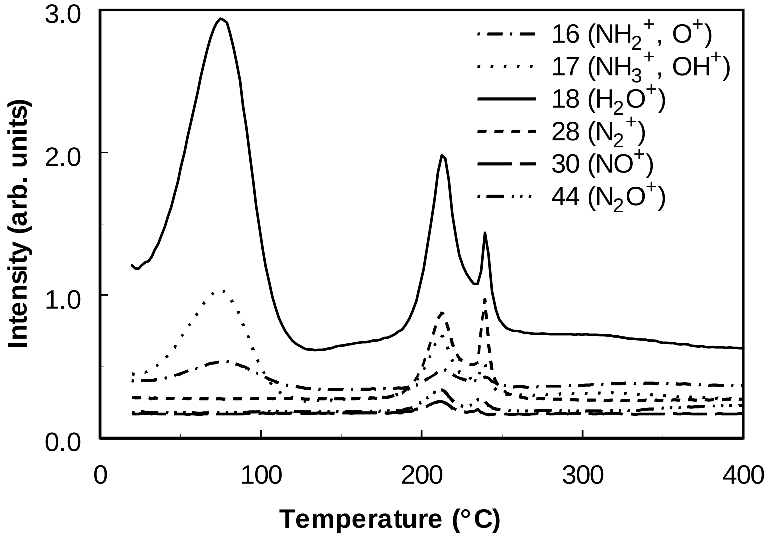

Figure 7: The intensity of (fragment)ions of desorbed gases vs. temperature during heating in Ar.

Autoreduction, Pt[Ar/He]

In Table 1, the results for H_2 chemisorption, HRTEM and EXAFS analysis are given.

Heating the sample in Ar led to the desorption of various gases which are probed with mass spectrometry (Figure 7). Below 100°C, physisorbed H_2O desorbs as shown by the desorption of masses 18, 17 and 16. Further heating leads to the desorption of NO_x, H_2O, NH_3 and N_2 in two temperature ranges. First, in a broad peak around 210°C the desorption of NO_x, H_2O, NH_3 and N_2 is observed. At a temperature of 240°C a second, sharper desorption peak for the

Table 3: Fit parameters[a] of QEXAFS spectra during heating in He and variances of fits. (R-space fit, 2.5 < k < 9.5 Å^{-1}, 1.3 < R <3.2 Å, k^2 weighted).

	O shell				Pt shell				variances (%)	
T (°C)	R (Å)	N	$\Delta\sigma^2$ [b]	E_0	R (Å)	N	$\Delta\sigma^2$ [b]	E_0	im.	abs.
50[c]	2.01	5.4	6.2	4.6	-[d]	-	-	-	0.044	0.012
150[c]	2.00	5.4	6.0	4.9	-	-	-	-	0.108	0.019
197[c]	1.99	4.4	3.3	5.3	-	-	-	-	0.371	0.095
209[c]	1.99	3.9	5.8	4.7	-	-	-	-	0.322	0.129
220	2.01	3.2	8.4	2.6	2.59	2.3	14.4	10.0	1.720	0.222
234	1.94	3.1	12.6	9.3	2.63	5.7	17.3	9.2	0.979	0.407
249	1.97	1.6	6.8	6.6	2.65	6.6	18.4	7.4	0.448	0.146
300	1.94	1.7	25.0	10.0	2.68	7.7	15.9	3.7	1.92	1.02
400	2.19	0.5	5.0	9.9	2.61	7.8	16.9	3.9	3.95	1.61

[a] errors in fits: $R \pm 1\%$, $N \pm 20\%$, $\Delta\sigma^2 \pm 5\%$, $E_0 \pm 10\%$

[b] Debye-Waller factor *10^{-3}

[c] Fit was done with k^1 weighting, with 1.3 < R < 2.5 Å

[d] No contribution of this shell present

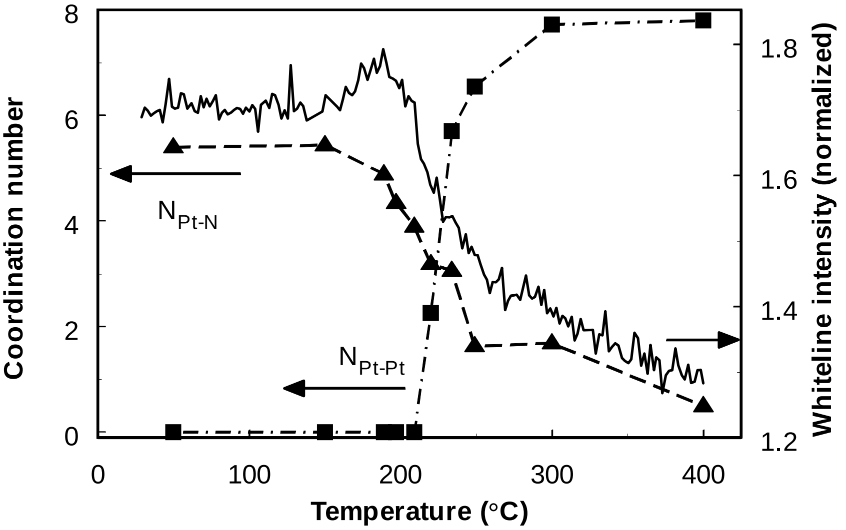

Figure 8: The normalized whiteline intensity (solid line), the Pt-N coordination number (dashed line, triangles) and the Pt-Pt coordination number (dashed-dotted line, boxes) as a function of temperature during heating of $[Pt^{2+}(NH_3)_4](NO_3^-)_2$ on SiO_2 in He.

same gases is observed. In the whole temperature range the desorption of NO_2, O_2 and H_2 was not detected.

The QEXAFS results are given in Figure 8 and Table 3. Heating the sample in He first shows a small increase in the whiteline from 180°C to 200°C, accompanied by a decrease in the Pt-N coordination number. A sharp decrease from 1.7 to 1.4 in the whiteline intensity starts at 200°C and continues up to approximately 260°C, after which the whiteline continues to

decrease slowly until the highest temperature measured (400°C). The sharp decrease of the whiteline between 200-260°C is accompanied by a sharp decrease in the Pt-N coordination number from approximately 4.5 to 2 and increase in the Pt-Pt coordination number from 0 to approximately 7. At higher temperatures, the nitrogen neighbors disappear slowly and the Pt-Pt coordination shows no significant changes.

Hydrogen chemisorption (Table 1) for this sample without an additional high temperature reduction showed a H_{total}/Pt value of 0.99. The additional high temperature reduction leads to an increase of H_{total}/Pt to 1.09.

In Figure 6 the particle size distribution for this sample as determined with HRTEM is shown (black bars). The average particle size for this sample is 14 Å. Compared to sample Pt[H_2], the particle size distribution is more uniform with only one maximum at 12Å and 50% of the particles in the range of 12-14Å.

Calcination, Pt[O_2]

Calcination of the impregnated sample in O_2 again shows the desorption of physisorbed H_2O below 100°C (Figure 9). Similar to heating the impregnated sample in Ar, heating the sample in O_2 leads to the desorption of NO_x, H_2O, NH_3 and N_2 at 2 temperatures, *viz.* at 210°C and at 240°C. NO_2 and H_2 were not detected. NH_3 could not be identified through its fragment ion NH_2^+ because the O_2 in the gas flow leads to high quantities of O^+ with mass 16.

QEXAFS (Figure 10) shows an increase in the whiteline intensity between 150°C and 325°C from 1.7 to 2.05. This increase is accompanied by a decrease in the Pt-O coordination number from 5.3 to 4.0 (see also Table 4). During the entire calcination procedure, no Pt-Pt neighbors are observed.

Hydrogen chemisorption after reduction following the calcination resulted in H_{total}/Pt=0.80 (Table 1).

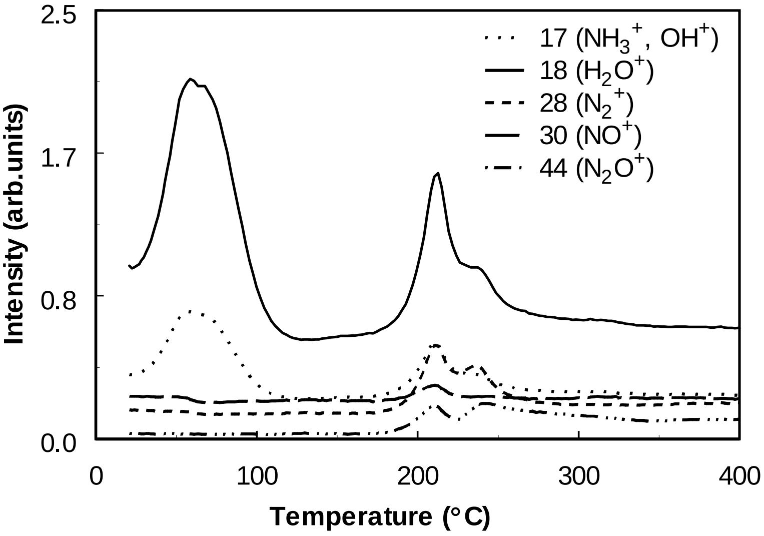

Figure 9: The intensity of (fragment)ions of the desorbed gases vs. temperature during calcination in O_2.

Table 4: Fit parameters[a] of QEXAFS spectra during heating in O_2 and variances of fits. (R-space fit, 2.5 < k <9.5 Å^{-1}, 1.3 < R < 2.5 Å, k^1 weighted).

	O shell				variances (%)	
T (°C)	R (Å)	N	$\Delta\sigma^2$(*10^{-3})	E_0	Im.	Abs.
51	2.00	5.0	3.8	4.6	0.197	0.159
100	2.00	5.3	5.2	5.0	0.111	0.106
149	2.01	5.3	5.3	4.5	0.346	0.254
200	1.99	5.3	6.3	5.5	0.277	0.227
208	1.97	5.4	7.9	6.3	0.110	0.075
212	1.98	5.1	7.1	6.0	0.158	0.060
216	1.98	4.9	7.5	5.4	0.116	0.037
224	1.98	4.4	6.5	4.6	0.122	0.016
244	1.98	4.0	5.0	5.4	0.259	0.125
260	1.98	4.0	4.3	5.8	0.238	0.068
272	1.99	4.0	3.7	4.8	0.268	0.119
296	1.98	4.2	4.9	5.1	0.932	0.588
346	1.98	4.4	4.4	5.5	0.508	0.268
400	2.01	3.7	3.0	1.7	0.898	0.749

[a] errors in fits: $R \pm 1\%$, $N \pm 20\%$, $\Delta\sigma^2 \pm 5\%$, $E_0 \pm 10\%$

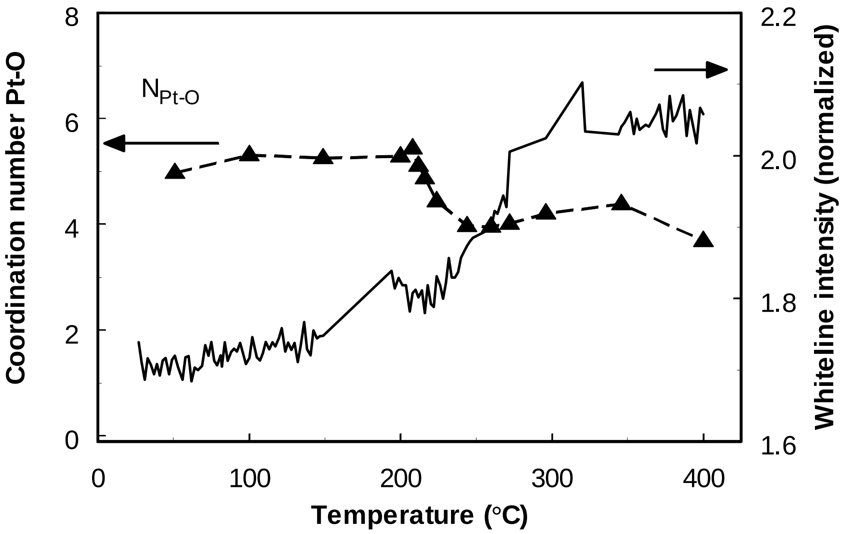

Figure 10: The normalized whiteline intensity (solid line) and the Pt-O coordination (dashed line, triangles) vs. temperature during heating of $[Pt^{2+}(NH_3)_4](NO_3^-)_2$ on SiO_2 in O_2. No Pt-Pt coordination was observed.

Discussion

Reliability of results from QEXAFS and HRTEM

In a QEXAFS experiment, the monochromator is in continuous motion. Accompanied by the low counting (120 ms) time per data-point, this gives a relatively low signal-to-noise ratio. Since the amplitude of the EXAFS-wiggles decreases at higher energies, this is most significant at higher energies. As a consequence, the measured QEXAFS spectra are considered only reliable up to k=9.5 Å^{-1}, in contrast to typical EXAFS spectra of Pt containing compounds which can be used up to k=15 Å^{-1}. Using the Nyquist theorem[29], the maximum number of free parameters that can be fitted doing a R-space fit of the data (1.3<R<2.9 Å, 2.5<k<9.5 Å^{-1}) is 9. With 9 free parameters 2 shells (N and Pt) can be fitted. Pt-Pt and Pt-O/N contributions have differences in backscattering-amplitudes, which are most prominent at higher energies. Therefore, fitting and discriminating between Pt and O/N backscatterers is less reliable using QEXAFS compared to normal EXAFS, where typically 3 spectra up to k=15 Å^{-1} of 30 minutes each are averaged. Moreover, the samples have temperatures between RT and 400°C. At high temperatures the thermal disorder is high. A high disorder leads to additional damping of the EXAFS wiggles at higher energies. This results in an additional error in the fitting of the QEXAFS spectra. The error in the fitted coordination number is estimated at approximately ± 2.

However, all samples are similar (all have the same starting material, loading and temperature range) and the differences in the sample between consecutive spectra are minimal. Therefore, the *differences* in the structural parameters as observed are reliable even though the absolute values may differ from the true physical parameters.

HRTEM allows the direct measurement of particle sizes larger than 5-10 Å. Depending on contrast, thickness of the sample and location of the Pt particle on the support, particles smaller then 5-10 Å are invisible. As these particles contain only a few atoms, they consist exclusively of surface atoms. Therefore, these small particles are extremely important in catalysis.

In addition, although these small particles are not probed by HRTEM, H_2 chemisorption is determined largely by these small particles. Extremely small (< 10 Å) Pt particles are known to adsorb more than 1 hydrogen atom per Pt[34]. This may result in discrepancies between the particle size as determined with HRTEM and H_2 chemisorption.

Direct reduction

The direct reduction is characterized by large changes in the Pt-complex between 150-200°C. The Pt-Pt coordination increases rapidly while both the Pt-N coordination and whiteline intensity decrease (Figure 3 and Table 2). These changes are characteristic for a reduction of the Pt^{2+} complex and the formation of metal particles. It is remarkable that in this temperature range only the desorption of a small amount of H_2O is observed (Figure 4). Only at higher temperatures (210°C) the desorption of NH_3 and large amounts of H_2O are observed. In this

region, QEXAFS shows that the reduction is nearly complete. This implies that the gases desorbing at 210°C must be produced by a mechanism independent of the reduction of the Pt^{2+} complex.

A proposed mechanism is shown in Scheme 1. Most likely, during the drying procedure following impregnation, $[Pt^{2+}(NH_3)_4](OH^-)_2$ and HNO_3 are formed in separate regions of the support. Although this may seem an unlikely reaction at first sight, this separation is very conceivable during impregnation. When the metal precursor is dissolved, the $[Pt^{2+}(NH_3)_4](NO_3^-)_2$ complex is dissociated into $Pt(NH_3)_4^{2+}$ and NO_3^-. Impregnation is followed by drying the impregnated support. During this drying, NO_3^- is transported to specific places on the support, where the capillary forces are greatest and, hence, water is evaporated latest. However, during drying the Pt^{2+} complex will remain behind on the SiO_2 surface and, hence, the homogeneous distribution of Pt^{2+} and NO_3^- is distorted and they will precipitate as $[Pt^{2+}(NH_3)_4](OH^-)_2$ and HNO_3.

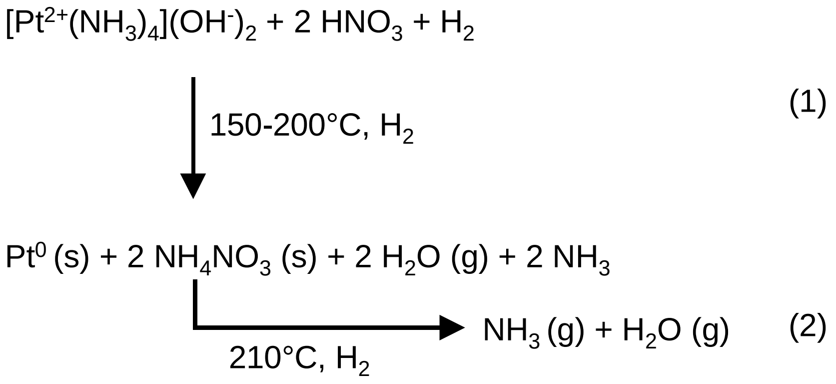

Scheme 1: Proposed mechanism for direct reduction.

During the reduction of the Pt complex, two of the ammonia ligands react with this HNO_3 to form ammoniumnitrate, NH_4NO_3. This complex is unstable at higher temperatures and has a boiling point of 211°C. When this complex decomposes, nitric oxides (NO_x) and H_2O are produced (Figure 11). In a H_2 atmosphere, NO_x can be reduced to NH_3 and H_2O in the presence of Pt. These gases are indeed observed.

The final particle size as determined with QEXAFS, H_2 chemisorption and HRTEM is quite large compared to the autoreduced sample (Table 1). Hydrogen chemisorption shows a H/Pt value of 0.89, with QEXAFS giving a Pt-Pt coordination number of 9.5. Normally, a coordination number of 9.5 would correlate to a H/Pt value of approximately 0.6[34]. However, as described before, the absolute Pt–Pt coordination number based on QEXAFS contains a large error margin (± 2). Based upon HRTEM and H_2 chemisorption, the average metal particle size is estimated at 14-16 Å.

In addition, the particle size distribution is broad (Figure 6). A broad particle size distribution is typically caused by a sintering process. Already directly after the reduction, at 200°C, a

high Pt-Pt coordination (~8) number is reached. Apparently, during the direct reduction sintering of the metal particles takes place. This is confirmed by the QEXAFS results.
The final metal particle size is determined by the ratio of two parameters, the growth and nucleation rate[35]. If the growth rate is high, the first nuclei will rapidly grow to large particles. Since the formation of metal-metal bonds adds significantly to the stability of Pt atoms[36,37], the reduction of the $Pt^{2+}(NH_3)_x$ complex must involve a migration and collision of the Pt^{2+} species with either an earlier formed metallic Pt nucleus or several other Pt^{2+} complexes and reduce at the same moment. The rapid reduction of the Pt^{2+} complex, high growth-rate of the Pt particles in the temperature range of 150-200°C, as observed with QEXAFS, and the low final dispersion therefore indicate the presence of a highly mobile species during the reduction, able to precipitate on the nucleus. It is very likely that this mobile species is similar to the $[Pt^{\delta+}(NH_3)_2H^{\delta-}{}_2]^0$ hydride, reported for direct reduction of $Pt(NH_3)_4{}^{2+}$ on zeolites[21] and SiO_2[23]. However, these hydrides were reported in the temperature range of 60-100°C. In this study, the MS results clearly show that the impregnated complex remains intact up to 150°C.

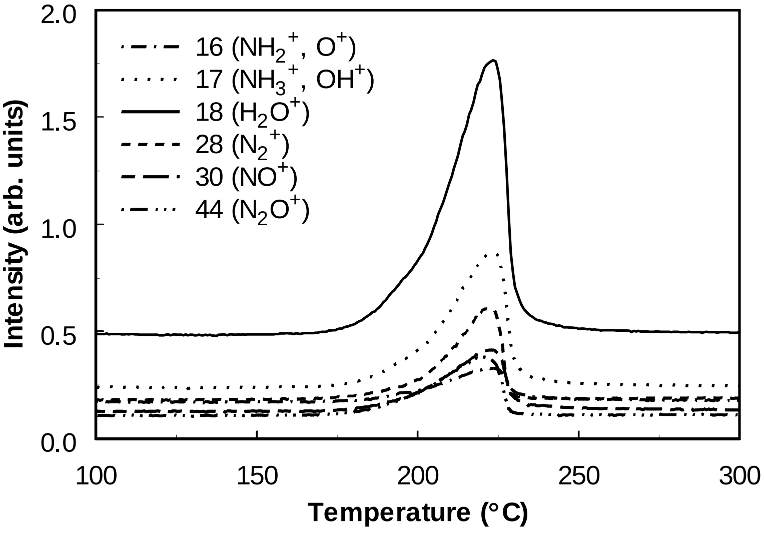

Figure 11: The decomposition of NH_4NO_3 during heating, followed by MS.

The sudden formation of large particles above 150°C is in agreement with observations made earlier[23,24]. Muñoz-Páez and Koningsberger[24] studied $[Pt^{2+}(NH_3)_4](OH^-)_2$ on γ-Al_2O_3 and observed a large Pt-Pt coordination number after heating the catalyst in H_2 to 200°C and cooling it down again to liquid nitrogen temperature to perform EXAFS measurements. They did not observe the characteristic H_2O/NH_3 desorption at 211°C, which was not to be expected since they used $[Pt^{2+}(NH_3)_4](OH^-)_2$ instead of $[Pt^{2+}(NH_3)_4](NO_3^-)_2$.
The results for the data analysis for the QEXAFS scans show some interesting features (Table 2). At lower temperatures, with a high amount of nitrogen neighbors, the E_0 for the Pt-N reference is 3.4 and the E_0 for the Pt-Pt reference is 10.0. At higher temperatures, with mainly metallic platinum particles, the situation is reversed: the E_0 for the Pt-N reference is high (10.0) and the E_0 for the Pt-Pt reference is low (2.9). This resembles a change in the edge

from Pt^{2+} to Pt^0. Furthermore, in the early stages of the reduction the Debye-Waller factor for the Pt-Pt coordination is large (14.2×10^{-3}) and this drops to 9.6×10^{-3}. Then, when the reduction is nearly complete, the Debye-Waller factor increases again (to 15.6×10^{-3}). The initial decrease of the Debye-Waller factor is caused by the formation of larger particles, which are structurally more ordered than smaller particles. The subsequent increase in the Debye-Waller factor is caused by the increase in temperature, which results in a higher thermal disorder.

In conclusion, the direct reduction is a fast process taking place between 150 and 200°C, resulting in relatively large particles with an average size of 14-16Å and a bimodal particle size distribution. The desorption of NH_3 and H_2O at 211°C is caused by the decomposition of NH_4NO_3 in an independent process of the reduction.

Autoreduction

The decrease in the whiteline when high temperatures are compared to low temperatures (QEXAFS, Figure 8) indicates a autoreduction of the Pt^{2+} complex. The observation that autoreduction takes place is in agreement with observations made in literature[18]. The process of autoreduction is characterized by the slow reduction of the Pt^{2+} complex (starting at 200°C) and the relatively low final metal particle size (Table 1) as the H/Pt number of 1.09 shows.

A peculiar observation is made with QEXAFS (Figure 8). The whiteline shows a small increase from 175-200°C. Simultaneously, the number of nitrogen neighbors decreases. This can be explained as follows: Each NH_3 ligand will donate some electron density to the Pt^{2+} ion via the lone pair of nitrogen. When a NH_3 ligand is desorbed, overall less electron density is donated to the Pt^{2+}. This results in an increase in the number of holes in the d-orbitals, which in turn results in a higher whiteline intensity. Therefore, the conclusion is that at least one ammonia group is desorbed from the Pt^{2+} between 175 and 200°C. However, mass spectrometry shows that no gases are produced until 200°C. This means that the desorbed NH_3 remains in the sample. It is likely that it reacts with HNO_3 to precipitate as NH_4NO_3 (reaction 3, Scheme 2). This mechanism is similar to the mechanism proposed for the direct reduction. NH_4NO_3 is unstable at higher temperatures, forming nitric oxides and H_2O. Indeed, mass spectrometry shows the production of N_2, O_2, NO_x, H_2O and some NH_3 between 200 and 250°C with maximum intensity at 211°C (Figure 7) and a second maximum at 240°C.

Simultaneous to the desorption of these gases, QEXAFS shows a large decrease in the whiteline in the temperature range of 200-250°C. In addition, the Pt-Pt coordination number increase from 0 to ~6 while to Pt-N coordination number decreases from 5 to 1.5. This implies that the Pt complex is reduced to a great extent in this temperature range. In the preceding paragraph (direct reduction), it was shown that production and decomposition of NH_4NO_3 is not necessarily coupled to the reduction of the Pt^{2+} complex. However, the gases produced during the decomposition might very well influence the Pt^{2+} complex. This is apparent when the 1st derivative of the whiteline as a function of temperature is compared with the desorption of H_2O (Figure 12). The decrease in the whiteline is maximal when the

highest amount of gases is produced, and vice versa, with the highest reduction rate at 210°C, and a second maximum at approximately 240-250°C. This confirms that reduction must be influenced by the gases produced during the decomposition of NH_4NO_3, either NH_3 or NO_x (reaction 4, Scheme 2). Since the Pt complex already has a high amount of NH_3 ligands, it is most likely that the NO_x influence the reduction. A mechanism for this reduction is proposed in reaction (5), Scheme 2.

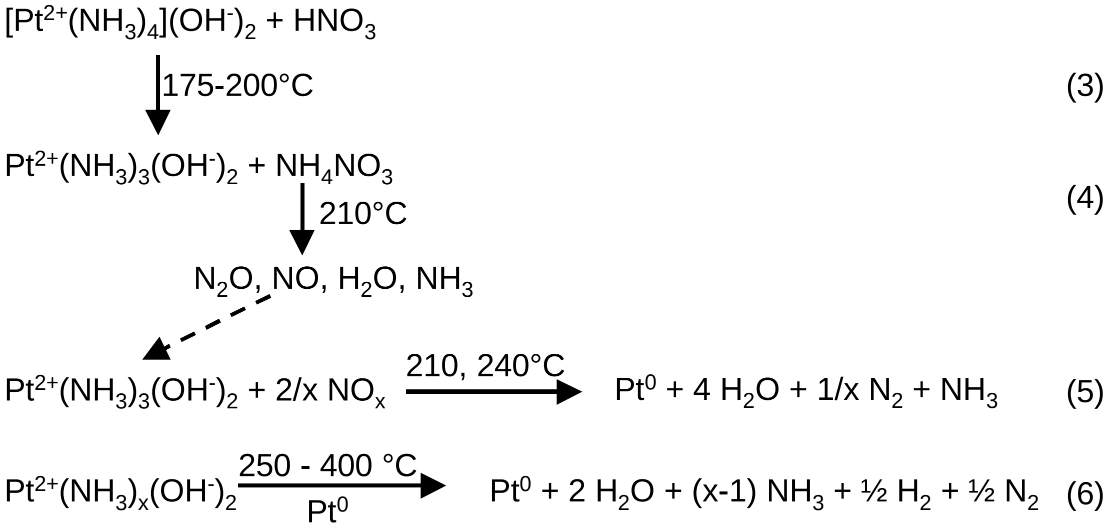

Scheme 2: Proposed mechanisms taking place during autoreduction.

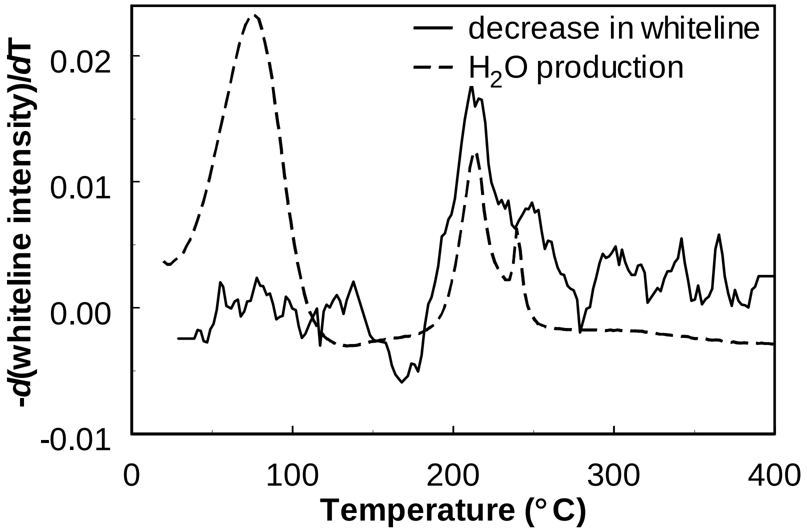

Figure 12: The decrease in the whiteline (1st derivative, solid line) and the production of H_2O (dashed line) vs. temperature during heating impregnated $[Pt^{2+}(NH_3)_4](NO_3^-)_2/SiO_2$.

At temperatures higher than 250°C, the reduction continues gradually as is indicated by the decrease in the whiteline (Figure 8). The Pt-O (N) coordination number (CN=1.5) at 250°C is still relatively high and decreases slowly. This indicates that not all Pt^{2+} complexes are

reduced by the NO_x and another reduction mechanism takes over: autoreduction. This autoreduction is characterized by the reduction of Pt^{2+} to Pt^0 accompanied by a loss of ligands. No other molecules are involved in the reduction. The proposed mechanism is given in reaction 6, Scheme 2. This reaction is similar to the one proposed by van den Broek *et al*[18]. A major difference between their study and the present is in the support material: they use the zeolite ZSM5, in this study SiO_2 is used. With this acidic zeolite, any NH_3 adsorbs strongly on the Brönsted acidic sites, whereas on SiO_2 NH_3 desorbs from the silanol surface groups below 100°C. The presence of NH_3 in zeolites at higher temperatures can lead to the formation of the highly mobile $Pt(NH_3)_2H_2$ hydrides, leading to sintering[18].
The slow rate of reduction of the complex is probably due to kinetic reasons. As discussed in the previous paragraph (direct reduction), the final particle size is governed by the ratio of the growth-rate and nucleation rate[35-38]. If the Pt^{2+} complex is not mobile, the reduction will be extremely slow and the final metal particle size is small.
At 400°C, the whiteline is still decreasing, indicating that reduction is still not complete. This is confirmed by the H_2 chemisorption experiments. The autoreduction followed by an additional reduction in H_2 for 30 min. at 400°C results in a higher hydrogen uptake (H/Pt = 1.09, Table 1) compared to the autoreduced sample without additional reduction (H/Pt = 0.99). The lower hydrogen uptake indicates that not all Pt is in the reduced state, since admission of H_2 at 35°C will not result in a reduction of the Pt complex.
All techniques reveal a smaller average particle size after autoreduction than after direct reduction. The high H/Pt number (1.09, Table 1) for the autoreduced sample shows that the final metal particle size is very small. According to Kip *et al.*[34], and assuming spherical particles, this H/Pt value corresponds to an average diameter of approximately 10-12 Å with particles consisting of approximately 20 Pt atoms. This is in agreement with the upper limit of the average particle size of 14Å as determined with HRTEM. The particle size distribution is significantly narrower than in the case of the directly reduced sample (see Figure 6). EXAFS gives a Pt-Pt coordination number of approximately 7.5.
In conclusion, heating the catalyst precursor in an inert atmosphere leads to a multiple step reduction, involving reduction by NO_x and autoreduction. The final metal particle size is approximately 10-12 Å and the metal particles are relatively uniform.

Calcination

In Table 1, the results of H_2 chemisorption, HRTEM and EXAFS analysis are given for this pretreatment.
QEXAFS during the calcination (Figure 10) shows a constant number of oxygen (or nitrogen) neighbors up to 200°C. This higher stability of $[Pt^{2+}(NH_3)_4](NO_3^-)_2$ in O_2 compared to the stability in H_2 is in agreement with the observations of Kinoshita *et al*[20]. As expected during calcination, no metallic Pt-Pt contribution was present for the whole temperature range. Already around 80°C, the whiteline starts to increase at a slow rate, although the number of direct Pt-O (N) neighbors remains nearly constant. At present, no clear explanation exists.

Since the oxygen containing atmosphere gives a large intensity for its fragment ion O^+ (m/z=16), it was impossible to identify desorbing ammonia by its fragment ion NH_2^+(m/z=16). However, it is likely that NH_3 desorbing from Pt^{2+} reacts similar as was observed during direct– and autoreduction: it reacts with HNO_3 on the support giving NH_4NO_3 (reaction 7, Scheme 3). The decomposition of NH_4NO_3 (reaction 8, Scheme 3) causes the characteristic broad desorption profile of nitric oxides and water (Figure 9) with maxima at 210°C and 240°C.

The sharp decrease in the Pt-N(O) coordination number and increase in the whiteline (Figure 10) between 200 and 250°C indicates a change in the ligands of the Pt. Probably, the formed NO_x will react with the Pt^{2+} complex to give Pt^0 (reaction 9, Scheme 3) in a similar manner as during the autoreduction. Naturally, the formed Pt^0 will immediately be oxidized to PtO (reaction 10, Scheme 3).

The final metal particle size, determined after reduction following the calcination, is large as is indicated by the H/Pt ratio of 0.80. It is uncertain whether the final dispersion is determined during the calcination or during the subsequent reduction. However, the fast rate of oxidation, as indicated by the sharp increase in the whiteline and sudden change to PtO_x around 200-250°C, suggests a large growth rate of PtO_x particles. Probably, the PtO_x particles have the ability to sinter and form large particles[39].

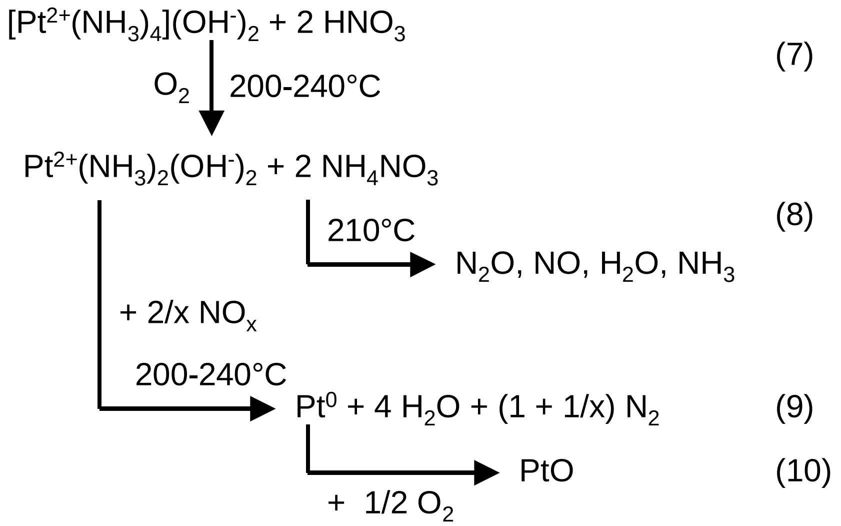

Scheme 3: Proposed mechanisms taking place during calcination

The final metal particle size. Processes leading to narrow particle size distributions.

Hydrogen chemisorption, HRTEM and QEXAFS all show that the final particle size is smallest after autoreduction. During autoreduction, the reduction proceeds in several steps. Two steps (at 210 and 240 °C) show a high reduction rate accompanied by sintering. During this sintering, metal particles in the range of 10-12 Å are formed. The reduction is caused by

the formation of NO_x species. A third step, at T>250°C, is the autoreduction of the $Pt^{2+}(NH_3)_x$ complex. This is a slow process, indicating that this species is not mobile. The size of the metal particles appears to be stable during this slow autoreduction.

During direct reduction, the creation of a mobile species at ~150 °C results in large Pt particles. In addition, calcination-reduction at higher temperatures leads to the formation of larger Pt particles. QEXAFS shows that PtO_x is formed after calcination. It is most likely that also PtO_x particles have the ability to sinter[39] and ultimately form larger Pt particles.

The key for making uniform small particles is to have a slow reduction process involving stable, immobile species. Analysis of the particle size distribution (Figure 6) shows that the Pt[Ar/He] sample, compared to Pt[H_2], has a narrow particle size distribution and small particles. The disadvantage during the autoreduction is the multiple-step reduction. If the presence of NO_x can be removed before pretreatment, the final metal particle size might be even smaller. One possibility to achieve this might be using $[Pt^{2+}(NH_3)_4](OH^-)_2$ as a precursor.

Conclusions

By combining mass spectrometry and *in situ* QEXAFS, it was possible to elucidate the mechanisms taking place during reduction, autoreduction and calcination of $[Pt^{2+}(NH_3)_4](NO_3^-)_2$ impregnated on SiO_2. The combination of mass spectrometry with QEXAFS showed that the production of gases can be an independent mechanism of the reduction of the $[Pt^{2+}(NH_3)_4](NO_3^-)_2$ precursor.

The smallest particles with the narrowest particle size distribution are obtained using autoreduction. The key to making small particles is to avoid the formation of mobile species that are able to precipitate as metal clusters.

Reference list

1. J.A. Schwarz, C. Contescu and A. Contescu, *Chem. Rev.*, **95** (1995), 477-510.
2. M. Komiyama, *Catal. Rev. - Sci. Eng.*, **27** (1985), 341-372.
3. W. Zou and R.D. Gonzalez, *Catal. Lett.*, **12** (1992), 73-86.
4. J.B.F. Anderson, R. Burch and J.A. Cairns, *J. Catal.*, **107** (1987), 351-363.
5. C. Besoukhanova, J. Guidot and D. Barthomeuf, *J. Chem. Soc. Faraday Trans. I*, **77** (1981), 1595-1604.
6. D.C. Koningsberger, J. de Graaf, B.L. Mojet, D.E. Ramaker and J.T. Miller, *Appl. Catal. A: General*, **191** (2000), 205-220.
7. B.L. Mojet, J.T. Miller, D.E. Ramaker and D.C. Koningsberger, *J. Catal.*, **186** (1999), 373-386.
8. G. Lietz, H. Lieske, H. Spindler, W. Hanke and J. Völter, *J. Catal.*, **81** (1983), 17-25.
9. B.N. Shelimov, J.-F. Lambert, M. Che and B. Didillon, *J. Catal.*, **185** (1999), 462-478.
10. B.N. Shelimov, J.-F. Lambert, M. Che and B. Didillon, *J. Mol. Catal. A*, **158** (2000), 91-99.
11. J.R. Regalbuto, A. Navada, S. Shadid, M.L. Bricker and Q. Chen, *J. Catal.*, **184** (1999), 335-348.
12. P. Reyes, M. Oportus, G. Pecchi, R. Frety and B. Moraweck, *Catal. Lett.*, **37** (1996), 193-197.
13. A.A. Bokhimi, O. Novaro, T. Lopez and R. Gomez, *J. Phys. Chem.*, **99** (1995), 14403-14406.

14. M.A. Aramendia, J.A. Benítez, V. Borau, C. Jimenez, J.M. Marinas, J.R. Ruiz and F. Urbano, *Langmuir,* **15** (1999), 1192-1197.
15. S.G. Fiddy, M.A. Newton, A.J. Dent, G. Salvini, J.M. Corker, S. Turin, T. Campbell and J. Evans, *Chem. Comm.* (1999), 851-852.
16. L. Persaud, A.J. Bard, A. Campion, M.A. Fox, T.E. Mallouk, S.E. Webber and J.M. White, *Inorg. Chem.*, **26** (1987), 3825-3827.
17. B.L. Mojet, D.E. Ramaker, J.T. Miller and D.C. Koningsberger, *Catal. Lett.*, **62** (1999), 15-20.
18. A.C.M. van den Broek, J. van Grondelle and R.A. van Santen, *J. Catal.*, **167** (1997), 417-424.
19. J. de Graaf, A.J. van Dillen, K.P. de Jong and D.C. Koningsberger, *J. Catal.*, **203** (2001), 307-321.
20. K. Kinoshita, K. Routsis and J.A.S. Bett, *Thermochim. Acta*, **10** (1974), 109-17.
21. R.A. Dalla Betta and M. Boudart, *Proc 5th Int Con Cat* (1973), 1329-1341.
22. M.B.T. Keegan, A.J. Dent, A.B. Blake, L. Conyers, R.B. Moyes, P.B. Wells and D.A. Whan, *Catal. Today,* **9** (1991), 183-188.
23. W. Zou and R.D. Gonzalez, *J. Catal.*, **133** (1992), 202-19.
24. A. Muñoz-Páez and D.C. Koningsberger, *J. Phys. Chem.*, **99** (1995), 4193-4204.
25. D.C. Koningsberger and R. Prins: *X-Ray Absorption. Principles, Applications, Techniq ues of EXAFS, SEXAFS and XANES;* John Wiley & Sons: New York, 1988.
26. J.J.F. Scholten, A.P. Pijpers and A.M.L. Hustings, *Catal. Rev. - Sci. Eng.*, **27** (1985), 151-206.
27. M. Vaarkamp, B.L. Mojet, F.S. Modica, J.T. Miller and D.C. Koningsberger, *J. Phys. Chem.*, **99** (1995), 16067.
28. D.E. Ramaker, B.L. Mojet, D.C. Koningsberger and W.E. O'Grady, *J. Phys.: Condens. Matter*, **10** (1998), 8753-8770.
29. D.C. Koningsberger, B.L. Mojet, G.E. van Dorssen and D.E. Ramaker, *Top. Catal.*, **10** (2000), 143-155.
30. G.E. van Dorssen, D.E. Ramaker and D.C. Koningsberger, *Phys. Rev. B,* **submitted**.
31. S.I. Zabinsky, J.J. Rehr, A. Ankudinov, R.C. Albers and M.J. Eller, *Phys. Rev. B*, **52** (1995), 2995-3009.
32. D.C. Koningsberger in: *Hercules Course. Neutron and Synchrotron Radiation for Condensed Matter Studies. Applications to Solid State Phys. and Chem.*; J. Baruchel, J.L. Hodeau, M.S. Lehmann, J.R. Regnard and C. Schlenker, eds., Springer Verlag: Berlin/New York, 1994; Vol. 2, pp 213-244.
33. M.K. Oudenhuijzen, J.H. Bitter and D.C. Koningsberger, *J. Phys. Chem. B,* **105** (2001), 4616-4622.
34. B.J. Kip, F.B.M. Duivenvoorden, D.C. Koningsberger and R. Prins, *J. Catal.*, **105** (1987), 26-38.
35. S.T. Homeyer and W.M.H. Sachtler, *J. Catal.*, **117** (1989), 91-101.
36. S.T. Homeyer and W.M.H. Sachtler in: *Zeolites*; P.A. Jacobs and R.A. van Santen, eds., Elsevier Science Publishers B.V.: Amsterdam, the Netherlands, 1989; pp 975-984.
37. D. Majumdar, D. Dai and K. Balasubramanian, *J. Chem. Phys.*, **113** (2000), 7928-7938.
38. S.T. Homeyer and W.M.H. Sachtler, *J. Catal.*, **118** (1989), 266-274.
39. A. Borgna, T.F. Garetto, C.R. Apesteguía, F. LeNormand and B. Moraweck, *J. Catal.*, **186** (1999), 433-441.

3

The Kinetics of H/D Exchange in Cyclopentane

Abstract

The exchange of hydrogen for deuterium (H/D exchange) in cyclopentane (CP) is a promising test reaction for studying support effects in heterogeneously metal catalyzed reactions. In order to employ this test reaction, a full understanding of the H/D exchange mechanism is essential. However, a clear insight in the observed kinetics and selectivities is lacking in the literature. In this paper, a kinetic model that adequately describes the observed activity and orders in CP and D_2 is developed. It is shown that the selectivity is determined in a series of reactions after the rate-determining step. To understand the observed selectivities a Monte-Carlo model is developed which accurately simulates the observed exchange patterns and reveals the relative contributions of four competitive intermediates. One intermediate (a π-bonded η^2-cyclopentene) can rotate in a non-activated mechanism via an allylic intermediate. The model reveals the number of rotations each intermediate experiences, and can be as high as ~20, even if only 5 D atoms are observed in the product. This number of rotations is a better measure of the H/D exchange than the conventional ‘multiplicity’. The H/D exchange of CP together with these insights can now be applied to investigate in detail the influence of the support on the catalytic properties of supported metal particles.

Introduction

Numerous reports have been made on the influence of the support material on the activity of supported metal catalysts. For example, the activity and selectivity in the benzene hydrogenation over zeolite supported Pt particles largely depends on the support material[1-5]. Another example is the large change in the activity of zeolite supported Pt catalysts in the hydrogenolysis with changing support acidity[6]. If the relation between support material and changes in activity/selectivity is well understood, it promises the prospect of tailor-made catalysts.

A large amount of work has been dedicated to relate changes in catalytic properties to changes in the electronic properties of the Pt particles[5,7-11]. Work by our group has shown that the support results in an electron rearrangement within the metal particle[12,13]. This rearrangement of electrons consists of a change in the ionization potential of the Pt particles and of a shift in the location of the electrons within the Pt particle.

One of the clearest examples where it is shown that the changes in the electronic properties influence the adsorption of reactants on the Pt particles is given by the chemisorption of CO followed by infrared spectroscopy. It is observed that CO adsorbs preferentially on an atop site when the Pt particles are supported by an acidic support, but it adsorbs in the bridged site when basic supports are used[14-18]. In addition, a number of catalytic experiments trying to correlate the changes in electronic properties to the catalytic performance have been published. For example, De Graaf *et al.*[19] speculated that the kinetics of neopentane hydrogenolysis depends on the degree of dehydrogenation during the adsorption of neopentane on Pt particles. On an acidic supports, neopentane adsorbs on the Pt particle via a single Pt-C bond, and the neopentane loses a single H atom. On a basic support, however, the neopentane adsorbs via a double or triple bond to the Pt clusters, losing an increased number of hydrogen atoms, which could explain the observed variations in the order in H_2 (-1.5 for acidic support and -2.5 for basic supports). Moreover, the activity of the neopentane conversion shows a compensation effect: an increase the activation energy E_{app} (which is observed when the basicity of the support is increased) is compensated by an increase of the pre-exponential factor $ln\ A_{app}$[20]. Bond *et al.* indicated that a likely cause of the compensation effect is related to different coverages of the reactants on the Pt surface[20]. This indicates that the adsorption properties of the reactants are influenced by the support acidity[19].

However, there is a lot of discussion on the relations between support material and electronic properties on one hand and the catalytic properties on the other. Thus, the need for a good test reaction is obvious. An important requirement for a proper test reaction is that it should be metal-catalyzed only. Among the possible reactions are the conversion of neopentane[6,19,21,22], neohexane[23-25] and the isotopic exchange of hydrogen with deuterium in hydrocarbons (H/D exchange)[26-29].

The selectivity of the H/D exchange of cyclopentane (CP) gives direct information about the different adsorption modes during the reaction. During the H/D exchange of CP, the hydrogen-atoms of cyclopentane are replaced by deuterium atoms. Typically, the H/D

exchange of cyclopentane shows several maxima in the product distribution. The products show maxima at 1, 5 or 10 exchanged deuterium atoms (the D1, D5 and D10 products), all resulting from different, competing exchange mechanisms. The resulting product distribution is reported to depend strongly on the support material[30]. Basic supports show a high selectivity towards the D10 product[29]. In contrast, neutral supports show mainly the D5 product[31] and acidic supports show a high amount of the D1 product[29]. The dependence of the product distribution on the support is explained by different influences on the different adsorption modes by changes in electronic properties[29]. In order to relate the electronic properties with the observed activities and selectivities for different catalysts, it is *crucial* to understand which processes lead to the different products.

The D1 product is produced by the exchange of a single hydrogen atom via a σ-bonded η^1-cyclopentyl (further referred to as σ-η^1, see Figure 1A). The involved reaction mechanism is proposed to be similar for all D2-D5 products and to proceed via a facile interconversion between the σ-η^1 intermediate and either a double σ-bonded α,β-η^2-cyclopentyl (di-σ-η^2, Figure 1B)[29,32,33] or a π-bonded η^2-cyclopentene (π-η^2, Figure 1C)[34]. With the D6-D10 products, the cyclopentane has rolled over from one side of the ring to the other, and also the atoms on the second side of the ring are exchanged. The reaction mechanism for this roll-over is proposed to proceed via a double σ-bonded η^1-cyclopentylidene (di-σ-η^1, Figure 1D)[35].

In the literature, a clear understanding of the H/D exchange of cyclopentane involving all possible exchange mechanisms, dependencies on D_2 and CP partial pressures, and temperature is missing. There still is debate in the literature regarding the D2-D5 products, which are believed to consist of cyclopentane with deuterium atoms all located on a single side of the ring. H/D exchange of CP results in maxima at D1 and D5. It is important to note that it is therefore impossible that the D5 product is produced via a mechanism which involves the same intermediate that results in the D1 product[36].

This paper will focus on understanding the observed activities and activities. A subsequent paper deals with an

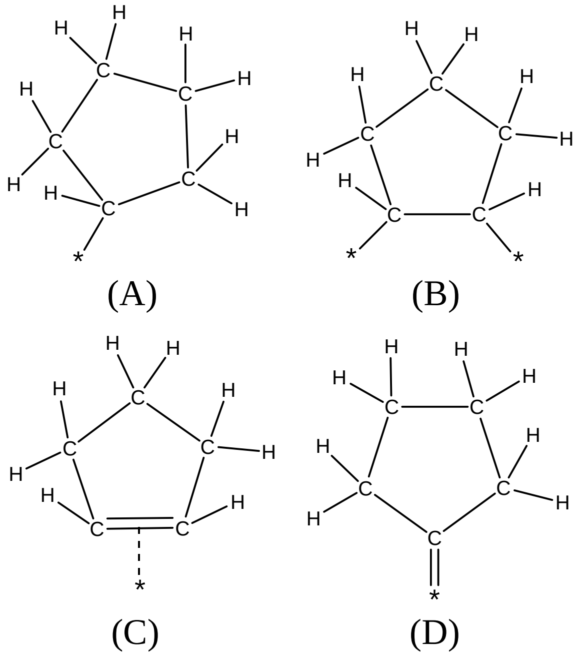

Figure 1: Different adsorbed intermediates, leading to different products (A) σ-bonded η^1-cyclopentyl (further referred to as σ-η^1), leading to D1, (B) a double σ-bonded α,β-η^2-cyclopentyl (di-σ-η^2) and (C) π-bonded η^2-cyclopentene (π-η^2) both leading to D2-D5 products and (D) double σ-bonded η^1-cyclopentylidene (di-σ-η^1) leading to roll-over.

understanding of support effects on the H/D exchange of CP. As will be shown in this paper, not all exchange mechanisms as proposed in the literature can explain the product distributions as observed for different Pt catalysts. A Monte-Carlo based method has been developed, which allows for the simulation of exchange patterns. In addition, a detailed kinetic model, that is able to explain the observed orders and activation energies for the H/D exchange of cyclopentane will be presented.

Experimental methods

Catalyst preparation

5 g vacuum-dried SiO_2 (Engelhard, BET surface area 400 m^2/g, pore volume 1.1 ml/g) was impregnated with 5.5 ml of an aqueous solution of $[Pt^{2+}(NH_3)_4](NO_3^-)_2$ (Aldrich, 18.0 mg/ml, resulting in 1 wt.% Pt/SiO_2) using the incipient wetness method. The impregnated support was dried in a water-free nitrogen flow for 1 hour at room temperature and for 18 hours at 80°C. The resulting catalyst precursor was dried in He for 1 hr at 150°C (ramp 5°C/min), calcined in 30% O_2/He at 250°C (ramp 1°C/min) for 2 hrs and reduced at 400°C for 30 min in H_2 (ramp 1°C/min) before the sample was cooled down in He and stored for further use in ambient atmosphere.

The resulting metal particles were analyzed using H_2 chemisorption, high resolution electron microscopy (HRTEM) and EXAFS. Details are given elsewhere[37,38]. All techniques indicated a similar dispersion. The H_2 chemisorption resulted in H/Pt_{total}= 0.87 and H/Pt_{strong}= 0.43. HRTEM revealed an upper limit of the metal particle size of 1.7 nm. EXAFS showed a Pt-Pt coordination number (1st shell) of 7.8.

H/D exchange of cyclopentane

A continuous down-flow fixed-bed microreactor (with a diameter of 4 mm) was loaded with 10 mg of the catalyst and dilluted with 60 mg of SiO_2, both with a sieve fraction of $90 < d_p < 150$ μm. The catalyst that was previously reduced and stored in ambient atmosphere was again dried at 150°C in Ar for 1 hr and pre-reduced for 1 hr at 400°C (ramp 5°C/min) in pure hydrogen. All flows were 30 ml/min, resulting in a gas-hourly space velocity of GHSV=7200 s^{-1} and a contact time of τ = 0.5 s. After the reduction at 400°C, the H_2 was switched to D_2 and the catalyst was cooled down in 50% D_2 in Ar to 75°C. Typical H/D experiments were performed at 75°C at atmospheric pressure, with P_{D2}=0.45 bar, P_{CP}=0.025 bar (resulting in a atomic ratio of D/H=20) and P_{Ar}=0.475 bar. The cyclopentane was brought into the feed by flowing part of the Ar through a saturator filled with cyclopentane. Conversions were kept below 10%. No side reactions were observed.

The products were analyzed online by a quadrupole mass spectrometer (Balzers QMS 420) that was connected via a capillary to the outlet of the reactor. The monitored intensities of CP were corrected for the natural abundance of ^{13}C.

Reaction orders in CP and D_2 were determined by varying the pressures ($0.022 < P_{CP} < 0.036$ and $0.33 < P_{D2} < 0.63$), while the total flow was kept constant. Activation energies were

determined by heating the catalyst over a range of 15°C with a ramp of 1°C/hour, followed by cooling down over (part of) the same temperature range.
The conversion is defined as the total amount of exchanged cyclopentane divided by the total amount of cyclopentane. Selectivity is defined as the amount of a specific product divided by all products:

$$C = 100 * \frac{\sum_{i=1}^{i=10} I_{Di}}{\sum_{i=0}^{i=10} I_{Di}} \quad (1)$$

$$S_{Di} = 100 * \frac{I_{Di}}{\sum_{i=1}^{10} I_{Di}} \quad (2)$$

with *i* : the amount of deuterium atoms in the product and i = 0 the unreacted product.
C : the conversion (in %)
I_{Di} : the amount of product *Di* (*e.g.* D3, CP containing 3 deuterium atoms) detected, after correction for the natural abundance of ^{13}C, and
S_{Di} : the selectivity (in %) towards product *Di.*

In literature, also the 'multiplicity' is commonly used to describe the product distribution. This multiplicity *M* is defined as the average deuterium content in the reacted cyclopentane species according to[35]:

$$M = 0.01 * \sum_{i=1}^{i=10} i * S_{Di} \quad (3)$$

with *M* : multiplicity,
i : number of exchanged deuterium atoms, and
S_{Di} : selectivity (%) towards product Di.

Results

Experiments

Influence of D_2 and CP partial pressures

A typical product distribution for the H/D exchange in cyclopentane over a Pt/SiO_2 catalyst, recorded at 73°C with 10.4 % conversion, is shown in Figure 2. Clearly, 3 distinct maxima are visible in the selectivity towards the D1, D5 and D10 products.

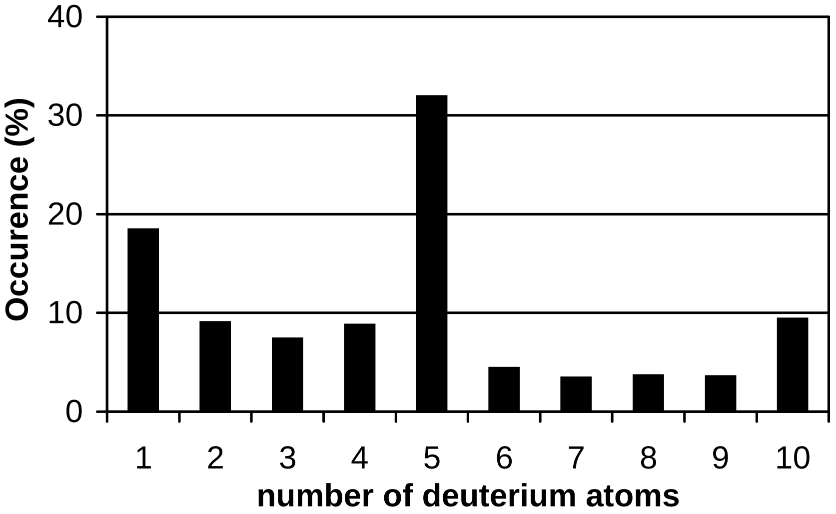

Figure 2: Typical exchange pattern for Pt/SiO_2 recorded at 73°C, with 10.4 % conversion.

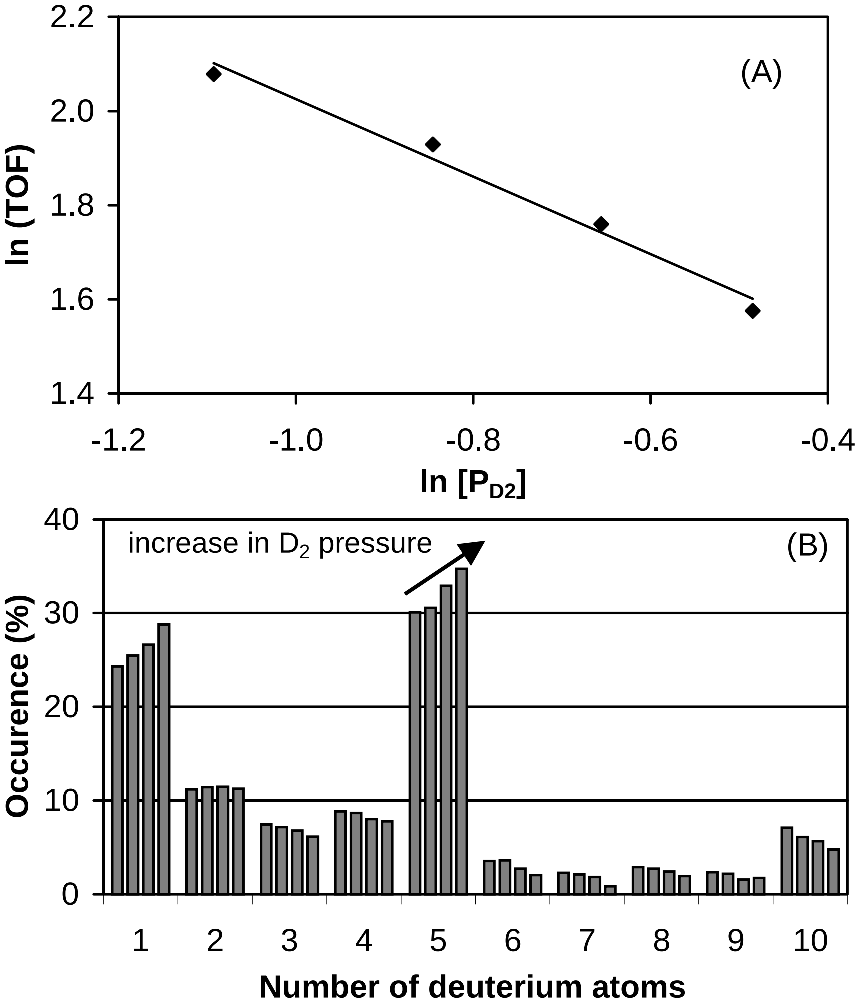

Figure 3: Influence of the D_2 partial pressure on (A) activity and (B) selectivity.

Figure 3 shows the influence of the D_2 partial pressure on activity and selectivity. The activity decreases when P_{D2} is increased (Figure 3A). Using the power rate law, $r = kP^{\alpha}_{CP}P^{\beta}_{D2}$, and keeping kP^{α}_{CP} constant, the order of the activity in D_2 was determined at β= -0.85.
In addition to the activity, also the selectivity depends on P_{D2} (Figure 3B). When P_{D2} was increased, the selectivity towards D1 and D5 increased. D2 was unaffected, and the selectivity towards D3-D4 decreased. The changes in selectivity are also reflected in the multiplicity. It decreases from M=4.1 at low D_2 pressure to M=3.7 at high D_2 pressure.
Figure 4 shows the influence of the CP partial pressure on the activity and product distribution. The reaction rate is increased by increasing P_{CP}, whereas the selectivity is almost unaffected. Keeping P^{β}_{D2} constant, and using the power rate law, the order of the activity in P_{CP} was determined at α = +0.87.

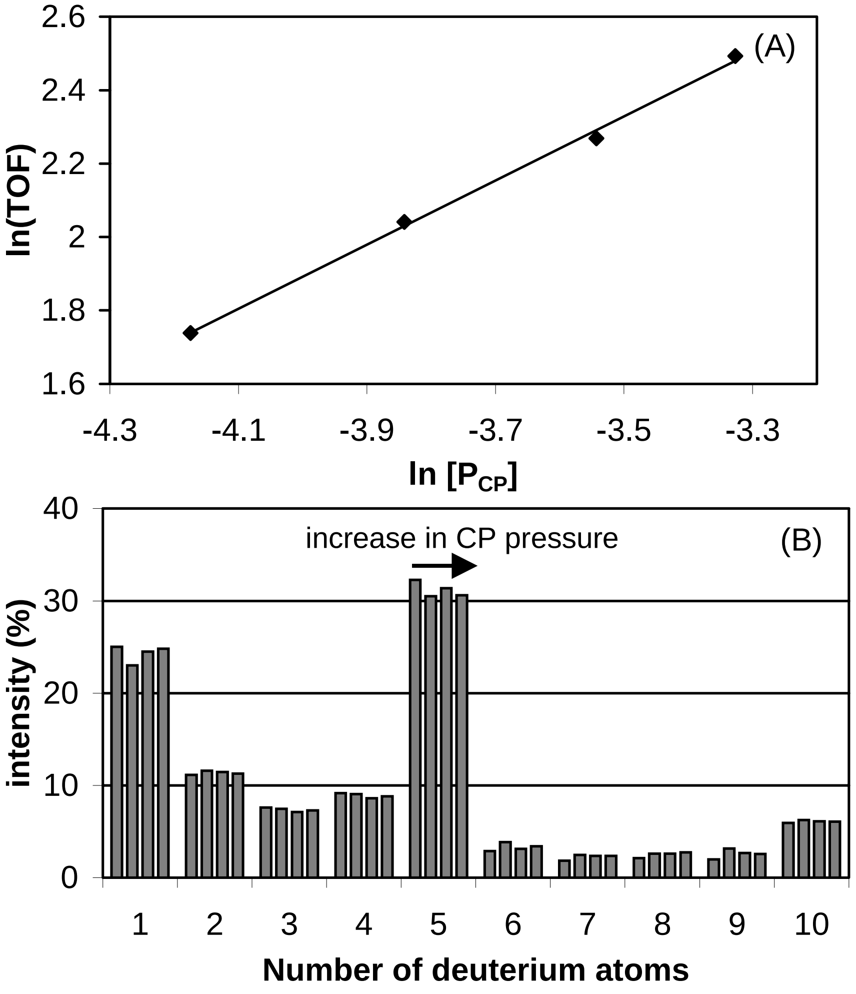

Figure 4: Influence of the CP partial pressure on (A) activity and (B) selectivity.

Effect of temperature

The activity is strongly influenced by the temperature. An Arrhenius plot of the activity as a function of temperature is given in Figure 5A. Using Arrhenius law[39], the (apparent) activation energy was determined at E_{app} = 55 kJ/mol.

Figure 5B shows the influence of the temperature on the selectivity. Increasing the temperature in steps of 1°C from 66°C to 81°C results in a decrease of the D1, D2 and D3 products and an increase for D6-D10. The selectivity towards D6-D10 increases from 19.1% at 66°C to 28.8% at 81°C. D4 and D5 are unaffected. In line with these observations, also the multiplicity increases from M=4.4 at 66°C to M=4.9 at 81°C.

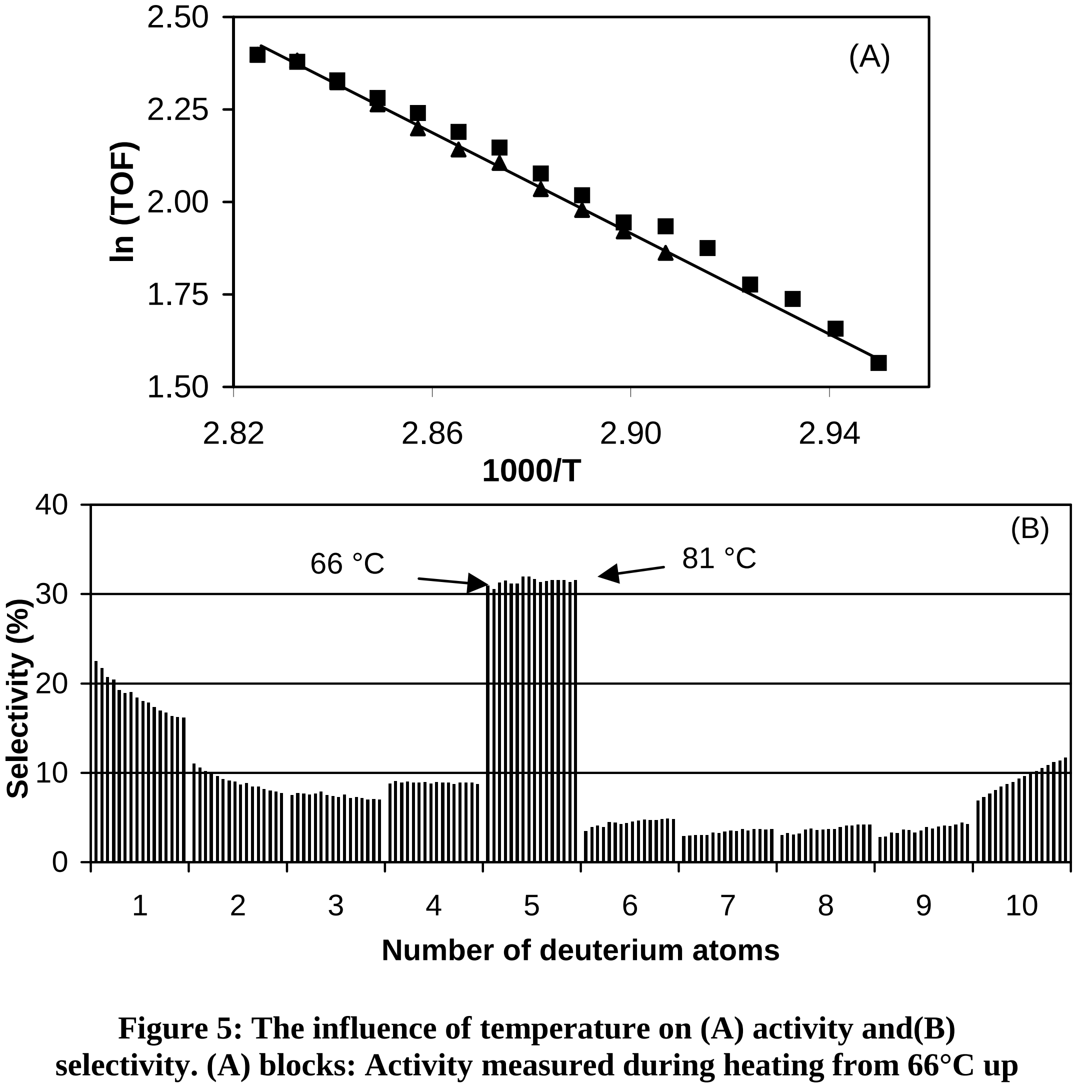

Figure 5: The influence of temperature on (A) activity and(B) selectivity. (A) blocks: Activity measured during heating from 66°C up to 81°C, triangles: during cooling down from 81°C down to 71°C. (B) distribution normalized for each T at 100%. Left bars: 66°C, each consecutive bar: + 1 °C up to 81°C.

The development of a Monte-Carlo model: understanding H/D exchange patterns.

As described in literature, a typical exchange pattern (as in Figure 2, with maxima for D1, D5 and D10) is the result of several competing mechanisms, each resulting in different products. The mechanisms, as proposed in literature, proceed via[29,32,35,40,41]:

1) a single σ-bonded η^1-cyclopentyl intermediate (σ-η^1, Figure 1A), leading to the D1-product,
2) a double σ-bonded α,β-η^2-cyclopentyl intermediate (di-σ-η^2, Figure 1B), leading to D2,
3) a π-bonded η^2-cyclopentene intermediate (π-η^2, Figure 1C), responsible for a rotation mechanism and leading to D2-D10, and
4) a double σ-bonded η^1-cyclopentylidene intermediate (di-σ-η^1, Figure 1D), responsible for roll-over and leading to D6-10.

The mechanism leading to D1

In the D1 product only one hydrogen atom is exchanged for a deuterium atom. Thus, only one C-H bond is dissociated during adsorption of CP on the Pt. After dissociation, a Pt-C and Pt-H bond are formed. The most likely form of this Pt-C species is the σ-η^1 intermediate (Figure 1A)[35,40]. In a competing mechanism, D_2 will be dissociatively chemisorbed on the Pt. This reaction is known to be an easy and fast reaction, with no activation energy[42-45]. Hence, the chemisorbed H-atom on the Pt surface, originating from the cyclopentane, will quickly recombine on the Pt surface with a chemisorbed D-atom to form HD(g). The σ-η^1 intermediate can then recombine with chemisorbed D on the Pt surface, and $C_5H_9D_1$ is formed. This is detected as the D1 product.

The mechanism leading to D2-D5

Literature

The D2 product itself can easily be formed via the di-σ-η^2 intermediate (Figure 1B). In addition, it is generally assumed that the D2-D5 products are formed by a stepwise exchange of the D-atoms. Therefore, any mechanism leading to these products must include an adsorption, followed by dissociation and a rotation mechanism, during which the probability of desorption is small compared to the probability of rotating to an adjacent C-C bond.

The mechanism for the rotation reaction has been proposed in literature to involve an alternation between the σ-η^1 intermediate (Figure 1A) and either a di-σ-η^1 (Figure 1D)[32,41] or a π-η^2 intermediate (Figure 1C). However, also D1 is believed to be formed via the σ-η^1 intermediate (Figure 1A), and thus the amount of D1 observed indicates the desorption probability of the σ-η^1 intermediate. Since generally a (local) maximum for D1 is observed, this desorption probability is relatively high. Therefore, a rotation mechanism involving this σ-η^1 intermediate should show intensities in the order D1>D2>D3>D4>D5. Since this is not the case, the rotation mechanism cannot include a σ-η^1 intermediate. In addition, since the

selectivity towards D5 is much higher than the selectivity to D4, the rotation mechanism must have a low activation energy.

Therefore, another process must be involved in the rotation mechanism which fits the requirements described above. We propose an allylic-like rotation mechanism of a π-bonded species (Figure 6). This would meet these requirements and is proposed as the mechanism for rotation. In this mechanism, the π-η^2 intermediate is the intermediate molecule which can rotate. The rotations proceed via the formation of an allylic intermediate, and this allylic intermediate breaks a C-H bond and forms a C-D bond on the other side of the allylic bond.

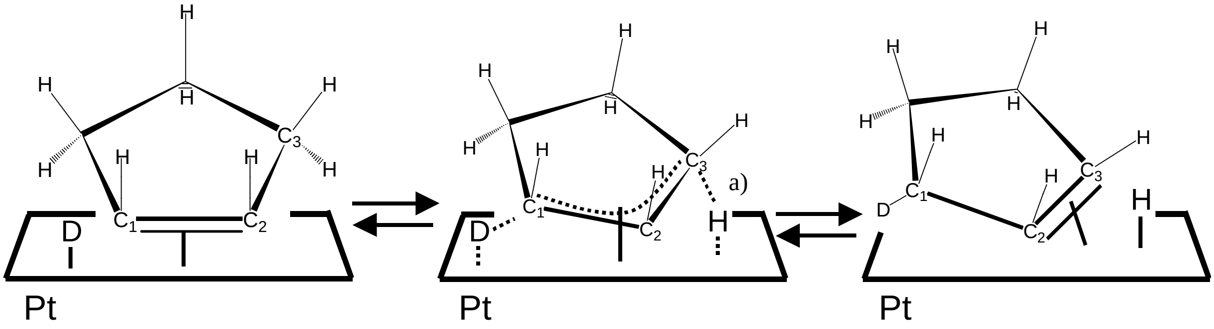

Figure 6: The rotation mechanism occurs via a allylic intermediate. [a)] The hydrogen attached to C3 can either bond to a surface Pt atom or recombine with a chemisorbed D atom to form gaseous HD.

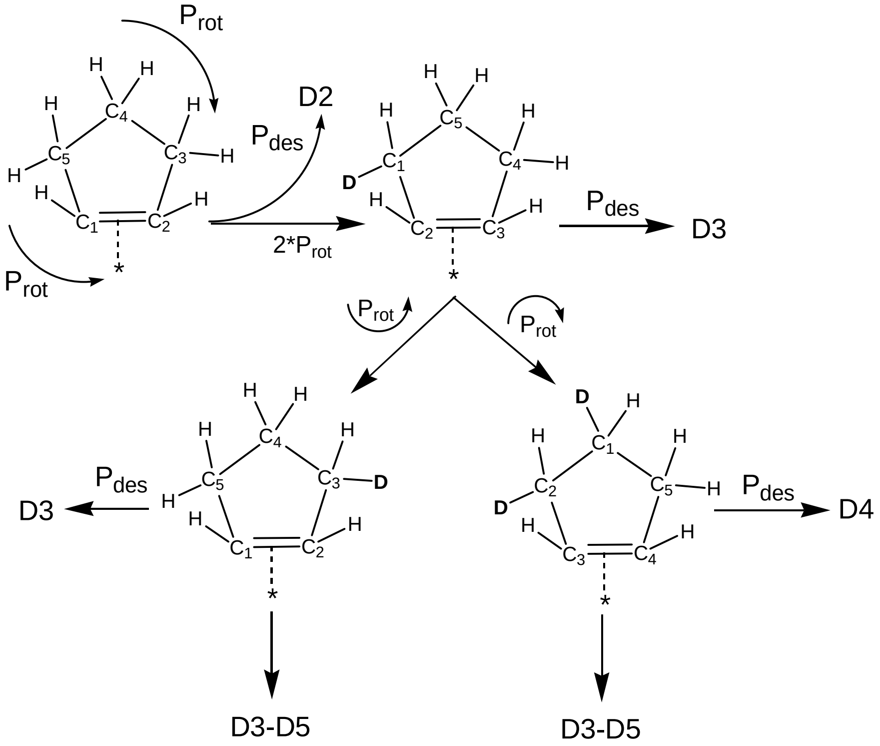

Figure 7: Schematic representation of the rotation mechanism leading to D3-D5. P_{rot}: probability to rotate either clock- or counterclockwise, and P_{des}: probability to desorb. After the 1st rotation, desorption would yield the D3 product. After the second rotation, desorption can yield both the D3 and D4 product.

Statistics of the rotation mechanism

During the initial formation of this rotating intermediate, with a surface coverage θ, two C-H bonds are broken (Figure 7). This molecule can either recombine with an adsorbed D atom and desorb, or rotate to an adjacent C-C bond. If the molecule would desorb, it would be detected as a D2 product. The desorption probability is given by P_{des}. Now the amount of D2 formed via this π-η^2 intermediate is given by $I_{D2} = \theta P_{des}$. If the molecule rotates, a D atom is attached to one of the C atoms (carbon atom #1 in Figure 7) and another C atom loses a H atom (C atom # 3). Again, the molecule can either desorb or rotate to an adjacent C-C bond. If the molecule desorbs, atoms C_1, C_2 and C_3 have a D atom attached to them and, hence, the molecule would be detected as the D3 product. The adsorbed molecule can also rotate, to either the next C-C bond (the bond between atoms C_3-C_4 in Figure 7) or the previous C-C bond (C_1-C_2). The rotation probability in each direction is given by $P_{rot} = ½ (1- P_{des})$. In the first case (adsorbed on the C_3-C_4 bond), desorption would lead to a CP molecule with D atoms attached to carbon atoms #1, 2, 3 and 4 and it would be detected as a D4 product. In the latter case (adsorption on the C_1-C_2 bond), however, the C_1-D bond is broken and a C_3-D bond is formed. Desorption then leads to the D3 product with D atoms bonded to C_1, C_2 and C_3. In this D3 molecule 4 times a C-H or C-D bond has been broken and formed: twice the C_1-H(D) and once the C_2-H and C_3-H bond. This example illustrates that the number of D atoms in the product (3) does not represent the number of times a C-H bond is broken and reconstructed (4 times), as is normally assumed in the literature.

A schematic representation of these concepts is shown in Scheme 1. First, a CP molecule is adsorbed as π-η^2 intermediate, containing 8 H atoms (species I in Scheme 1, adsorbed on C-C bond [A]) with a surface concentration θ. This species can either desorb (giving the D2 product) or rotate to an adjacent C-C bond (bonds [B] or [E] in Scheme 1). It is important to realize that after the 1st rotation, desorption of the adsorbed species would yield the D3 product regardless of the direction of rotation. This means that both adsorbed species are indistinguishable: adsorption via C-C bond [B] is indistinguishable from adsorption via C-C bond [E] and, therefore, after 1 rotation the surface concentration of this species II (Scheme 1) is $\boldsymbol{2 * \theta *} P_{rot}$.

After the first rotation, the adsorbed molecule goes through a similar mechanism with again the probability P_{des} on desorption (giving an intensity of $I_{D3} = 2 \theta P_{rot} P_{des}$) and probability P_{rot} on rotating to the next C-C bond (bond [C] giving species III in Scheme 1) or previous C-C (bond [A], species IV) bond. If the molecule would rotate to the previous bond in its second rotation, this molecule would exchange a D-atom for another D-atom, and is therefore still detected as a D3-product, although it has undergone 4 exchange steps. This species is depicted in Scheme 1 as species IV, which has undergone adsorption on C-C bond A → B → A. Species IV in Scheme 1 is comparable to the bottom left CP molecule in Figure 7. When this statistical analysis is followed through (part of which is shown in Scheme 1), it becomes clear that the intensity resulting from the rotation-mechanism for the D2 and D3 products are described by formulas (4) and (5):

$$I_{D2} = \theta * P_{des} \tag{4}$$

$$I_{D3} = 2\,\theta\, P_{des} \sum_{n=1}^{\infty} P_{rot}^{n} = 2\,\theta\, P_{des} \sum_{n=1}^{\infty} \left(\frac{1-P_{des}}{2} \right)^{n} \tag{5}$$

with I_{Di} : the intensity of Di,

θ : surface coverage (in %) of the rotating species,

P_{des} : fractional desorption probability,

P_{rot} = ½ * (1-P_{des}) : probability on rotation, either counter-clockwise or clockwise, and

n : number of rotations.

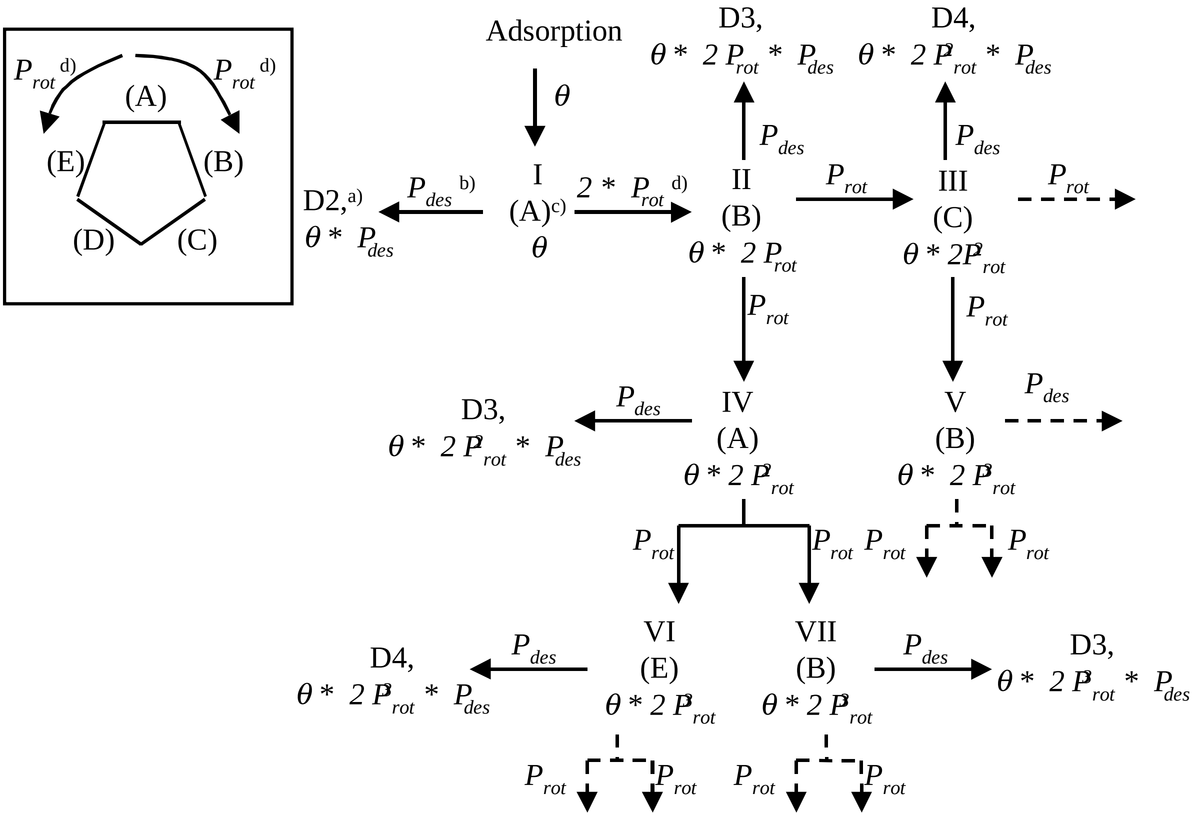

Scheme 1: Statistical approach of the formation of D2-D5 product. [a]: The product D2 is formed in a concentration I_{D2} = θ * P_{rot} with θ = surface concentration (in %) of the rotating species and [b]: P_{des} = fractional probability on desorption, [c]: Species I is bonded at C-C bond (A), [d]: Adsorbed species has a fractional probability P_{rot} of rotating right and an equal probability P_{rot} of rotating left; P_{rot}=(1-P_{des})/2. After the first rotation, the species rotated to the left and right are equal. Species VI has been through the following route: adsorption on bond A → B → A → E and desorption would result in the D4 product. The route for species VII has been: A → B → A → B.

The development of the Monte-Carlo model

Such formulas for the D4 and D5 product are very complicated to derive. Therefore, another approach is chosen: the use of Monte-Carlo techniques. Since the contribution of a molecule that has undergone a high amount (*e.g.* 20) of rotations is negligible to the formation of the D3 product, $\theta * P_{des}$ can be determined from a known intensity of D3 via formula (5). With the known value of $\theta * P_{des}$, both θ and P_{des} can be estimated separately. The estimation can be checked with the use of a computercode: in this code a CP molecule is virtually adsorbed and rotated randomly until it is desorbed again. With the use of this random generator, the molecule is rotated a number of times and the average number of rotations depends on the estimated value of P_{des}. When the adsorption of a high amount of molecules (> 10^6) is simulated, a complete exchange pattern can be simulated. In an iterative process towards best agreement between theory and experiment the best values of θ and P_{des} are determined. In Table 1, a comparison between experiment and theory is given. As becomes clear, even though a molecule might be detected as D5, the average number of rotations this molecule has experienced in this particular example is as high as 18.3. Since the adsorbed, unrotated π-η^2 intermediate already yields the D2 product, the average number of exchange steps (one exchange step is defined as a subsequent cleavage and formation of a C-H or C-D bond) is as high as 18.3+2=20.3. This gives a good measure for the exchange activity via the rotation.

Table 1: Comparison between theory and the results of the statistical simulation.

	D1	D2, di-σ-η^2 [a]	D2, π-η^2 [b]	D2 total	D3	D4	D5	>D5
Experiment	18.4[c]			9.0	7.4	8.8	31.9	24.4
Theory (# rotations)[d]	18.6	2.3	4.6	6.9	7.6 (3.9)	8.9 (6.6)	33.6 (18.3)	24.4

[a] The amount of D2 produced via the double σ-bonded α,β-cyclopentyl (Figure 1B)

[b] The amount of D2 produced via the π-bonded cyclopentenyl (Figure 1C)

[c] Selectivity in %

[d] The average number of rotations the molecule has experienced

The high amount of D5 product that is (generally) found, shows that rotating is easier than desorption. Therefore, P_{des} must be much smaller than P_{rot} ($P_{des} << P_{rot}$). From formulas (4) and (5) follows that in this case the contribution of this rotation-mechanism to the D2 product must be smaller than the total amount of the D3-product formed. Since it is generally found that D2>D3 (Figure 2), a second mechanism must contribute to the formation of D2. Such a mechanism must include the exchange of 2 hydrogen atoms and must exclude the possibility of a easy rotation. The di-σ-η^2 intermediate (Figure 1B) is such a species, and it is proposed that the second mechanism leading to the D2 product proceeds via this di-σ-η^2 intermediate.

In summary, the assumptions made in the development of the Monte-Carlo model are:

- The probability of rotating clockwise or counterclockwise is always equal.
- Already after the initial formation of the rotating species, 2 D-atoms are exchanged.

- The desorption probability is not influenced by the number of D-atoms in the product.

The mechanism leading to D6-D10

The products D6-D10 have exchanged deuterium atoms on both sides of the cyclopentane ring. These products must have undergone a roll-over mechanism which exposes both sides of the ring. The relative intensities D7-D10 and D3-D5 show a similar pattern. This suggests that the formation of the D6-D10 species involves the same intermediate that is responsible for the rotation: the π-η^2 intermediate. Thus, it is the π-η^2 intermediate that can roll-over. Therefore, the total amount of the mechanism that proceeds via the π-η^2 intermediate is given by the sum of all products D3-D10 and that part of the D2 product which is formed via the π-η^2 intermediate (Figure 1B) as calculated with the Monte-Carlo model. The activity $R_{roll\text{-}over}$ for this roll-over mechanism is than given by:

$$R_{roll-over} = \frac{\sum D6 - D10}{D2_{\pi-species} + \sum D3 - D10} \qquad (6)$$

The observation that D6 is more abundant than D7 gives important information on the roll-over mechanism[32]. When the intermediate adsorbed species is formed during the roll-over, the cyclopentane can either roll back to the same side of the ring, or forward to the next side of the ring. The relatively high abundance of D6 suggests that the formation of the intermediary involves the cleavage of 1 C-H bond on the unexchanged side of the ring: if it would roll back, than only one atome would be present on the second side of the ring. This indicates that the dominant mechanism for the roll-over is via a di-σ-η^1 intermediate (Figure 1D)[32]. The D7-D10 product distribution is similar to the D2-D5 distribution, which indicates that for the formation of the D6-D10 products the roll-over occurs starting from the π-η^2 (Figure 1C), via the di-σ-η^1 intermediate (Figure 1D) towards again the π-η^2 intermediate. Via this mechanism a large number of H atoms can be exchanged for D-atoms, leading to the D6-D10 products.

Implications for interpretation of the selectivity

In the literature, the multiplicity has been used to reflect the average number of exchange steps leading to a particular exchanged product. However, the multiplicity does not reflect the full magnitude of changes in the selectivity. It is an overall parameter which is most sensitive for the roll-over mechanism leading to D10 and, for example, it only reflects the *observed* number of exchange steps, not the *true* number of exchange steps leading to D5.

It is very likely that the different adsorption modes as shown in Figure 1 are influenced differently by changes in temperature and partial pressure of reactants. The same holds for the influence of support induced changes in the electronic properties of the metal on the adsorption of the various intermediates. Instead of using the multiplicity, one should carefully analyze the observed selectivities and extract the contribution of the different adsorption modes in the exchange reaction. D1 represents the contribution of the σ-η^1 intermediate. By using the developed Monte-Carlo model, the contribution to the formation of D2 of the di-σ-

η^2 intermediate can be calculated, as well as the total amount of the π-η^2 intermediate formed and the average number of rotations that each π-η^2 intermediate experiences. The contribution of the roll-over mechanism, with the di-σ-η^1 intermediate, follows from equation (6).

In order to further illustrate this very important point, the data presented in Table 2 are considered. By increasing the D_2 partial pressure, the multiplicity was decreased by 10 %, from 4.1 to 3.7. This is mainly caused by a strong decrease in the roll-over activity, from 18.1 % to 11.4 %. However, the average number of rotations each adsorbed π-η^2 intermediate undergoes is increased by 25 %, from 12.5 to 15.9.

Table 2: The influence of the D_2 partial pressure on the selectivity and on the average number of rotations, as calculated with the Monte-Carlo method.

P_{D2} [a]	Contribution (in %) of [b]				Average # rotations[c]	M[d]
	σ-η^1 (D1)	di-σ-η^2 (D2)	π-η^2 (D2-D10)	di-σ-η^1 (D6-D10)		
0.34	24.3	3.4	72.3	18.1	12.5	4.1
0.43	25.5	3.7	70.9	16.7	12.9	4.0
0.52	26.7	3.7	69.7	14.2	14.2	3.9
0.62	28.7	3.8	67.5	11.4	15.9	3.7

[a] Partial pressure of D_2

[b] For a description of the intermediate species, see figure 1

[c] The average number of rotations each π-η^2 intermediate experiences

[d] Multiplicity

Discussion

Orders in D_2 and cyclopentane

By varying the partial pressure of CP while keeping P_{D2} constant, and assuming the power rate law $r = kP^{\alpha}_{CP}P^{\beta}_{D2}$, our results show that the order in CP is α=0.87. Remarkably, the selectivity to a particular product is – within accuracy limits – hardly affected by P_{CP}. The observation that all D1-D10 products are unaffected by P_{CP}, suggests that all reaction mechanisms leading to the different products have a similar rate-determining step, and that the selectivity to the D1-D10 products is only determined *after* the rate-determining step. This argument, and the consideration that a molecule of CP can only be deuterated and observed after a dissociation step of a C-H bond in the CP molecule suggests that the rate determining step is a dissociation. The 1st step in a catalytic reaction is always an adsorption of the reactant on the catalytically active surface. This adsorption step might even preceed the rate-determining step. For the adsorption of a hydrocarbon adsorption like CP on a Pt surface, the 1st step adsorption can be either a dissociative or molecular adsorption.

A dissociative adsorption can proceed in different ways:

A dissociative adsorption during which both CP and a H atom are adsorbed on the catalytically active surface:

$C_5H_{10}(g) + 2 * \Leftrightarrow C_5H_9(*)+ H(*)$

and a dissociative adsorption on a site which is filled with a deuterium atom, during which immediately the gaseous HD is formed:

$C_5H_{10}(g) + D(*) \Leftrightarrow C_5H_9(*) + HD\ (g)$

During this dissociative adsorption atomically adsorbed D is also involved. If this reaction would take place, the presence of D_2 would be expected to be beneficial to the reaction rate. However, the order in D_2 for conversion of cyclopentane to any product was determined at $\beta = -0.85$ (see Figure 3A): the H/D exchange is inhibited by D_2. This is in agreement with reported literature values[46]. Because the order in D_2 is negative, a dissociative adsorption on a site containing D(*) can be excluded.
Also a molecular adsorption in the 1st step can take place:

$C_5H_{10}(g) + * \Leftrightarrow C_5H_{10}(*)$

This is in agreement with a study reported by Campbell[47], who showed that, initially, cyclopentane is molecularly adsorbed before it dissociates. The negative order for the activity in D_2 also indicates that both cyclopentane and deuterium adsorb on the same adsorption sites. Based on the molecular adsorption in the first step, a series of reactions can be postulated that can explain the observed kinetics:

(I) $C_5H_{10}(g) + * \xleftrightarrow{K_1} C_5H_{10}(*)$

(II) $D_2(g) + 2* \xleftrightarrow{K_2} 2D(*)$

(IIIA) $C_5H_{10}(*) + * \xrightarrow{k_{+3}} C_5H_9(*) + H(*)$

(IIIB) $C_5H_nD_{9-n}(*) + D(*) \xrightarrow{k_{-3}} C_5H_nD_{10-n}(*)$

As argued above, all exchange mechanisms, leading to D1-D10, are assumed to originate from the same, dissociatively adsorbed molecule via a series of exchange mechanisms. This is depicted in an energy scheme which is shown in Figure 8. The highest activation energy is in the rate determining step, the dissociation of CP. From this dissociated molecule the CP can further react to, for example, π-η^2 with a relatively low activation energy. The π-η^2 intermediate can than easily rotate with an even lower activation energy.
As shown in appendix A, reactions (I) – (III) lead to a reaction rate given by:

$$R = \frac{k_{-3}K_1K_3P_{CP}}{\left(1 + K_1P_{CP} + \frac{K_1K_3P_{CP}}{\sqrt{K_2P_{D_2}}} + \sqrt{K_2P_{D_2}}\right)^2} \qquad (7)$$

Reaction (II) involves the dissociation of deuterium on Pt. Since this reaction is known to be fast and non-activated[42], it is very likely that the equilibrium in this reaction is far to the right side. Moreover, since this reaction is fast, any adsorbed H(*) formed from the dissociation of

CP immediately recombines with D(*) to form HD(g). Also, H(*) and D(*) are chemically equal and thus H(*) in reaction (IIIA) can be substituted by D(*), and similarly $C_5H_nD_{9-n}$(*) can be substituted by C_5H_9(*). As a consequence, reactions (IIIA) and (IIIB) are in equilibrium and in a steady state $r_{+3} = r_{-3}$.

Reaction (I) only involves a non-dissociative adsorption. Therefore, it is expected that $K_2 >> K_1$, and the denominator in equation (7) is dominated by the term K_2P_{D2}. In that case, the observed order in deuterium will be near –1 and the order in CP will be close to +1. This is indeed observed in the experiment, with an order of –0.82 in D_2 and +0.87 in CP.

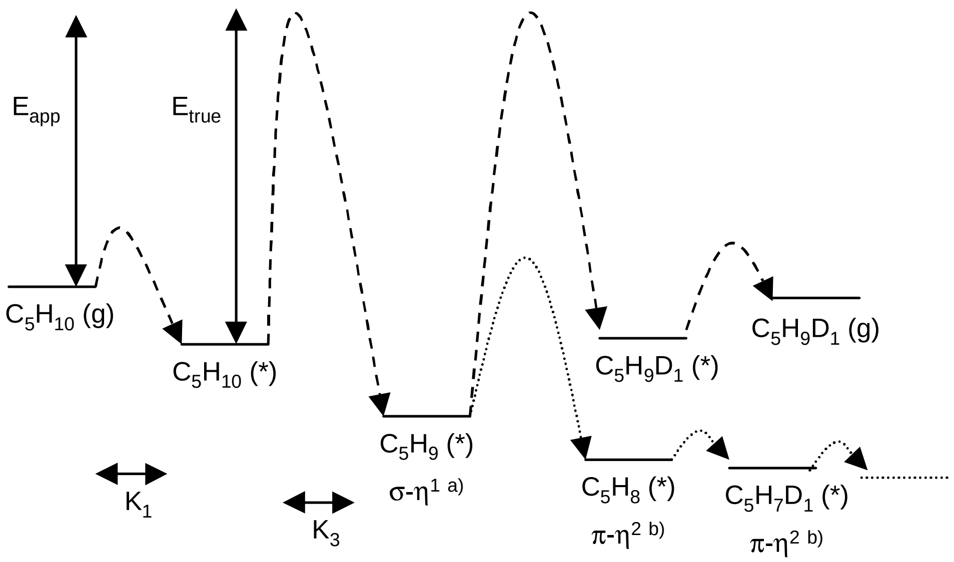

Figure 8: A schematic energy scheme for the HD exchange of CP. The rate determining step is K_3, the dissociation of molecularly adsorbed CP to C_5H_9(*), the [a] σ-bonded η^1-cyclopentyl intermediate. From this dissociated CP the other intermediates are formed, for example [b] π-bonded η^2-cyclopentene. This intermediate can easily rotate with a low activation energy. E_{app} is the apparent (or observed) activation energy, E_{true} the true activation energy.

In addition to the activity, the selectivity is also influenced by P_{D2} (Figure 3B). The selectivities to D1 and D5 increased, D2 was unaffected and D3,D4 and D6-D10 decreased in intensity by increasing P_{D2}. These selectivities were analyzed with the Monte-Carlo model, and the results are given in Table 2. The contribution of the σ-η^1 intermediate (Figure 1A) increased whereas the contribution of the π-η^2 intermediate (Figure 1C) decreased. In contrast, the average number of rotations which the π-η^2 intermediate experiences increases from 12.5 at low D_2 pressure to 15.9 at higher D_2 pressures. This increase in the average number of rotations suggests that the rotation mechanism is facilitated by an adsorbed D-atom. This is in agreement with the proposed allylic mechanism (Figure 6): in order to rotate via the resonant mechanism, a deuterium atom must be adsorbed on an adjacent adsorption site. With higher P_{D2} the coverage with deuterium is expected to be higher and, hence, the rotation is more facile.

The contribution of the di-σ-η^1 intermediate decreases from 18.1 to 11.3 % with increasing D_2 pressure. This means that the roll-over, which results in D6-D10, is strongly inhibited by D_2. With higher D_2 pressures, the surface coverage of D on the Pt will be higher and less empty sites will be available. The inhibition of the roll-over by D_2 therefore implies that an extra (empty) adsorption site is required for the roll-over mechanism.

In summary, a positive 1st order in CP and a negative order of –0.85 in D_2 were found. The selectivities were independent of the CP partial pressure, and a kinetic model with corresponding reaction rate was developed. Increasing D_2 pressures lead to an enhanced rotation of the π-η^2 intermediate, which is in agreement with the proposed rotation mechanism (Figure 6). In addition, a decreased roll-over selectivity is observed, which implies that the roll-over mechanism via the di-σ-η^1 intermediate requires an empty adsorption site.

Effect of temperature

The Arrhenius plot shown in Figure 5A represents a rate determining step during the H/D exchange with an apparent activation energy of E_{app}=55 kJ/mol. According to the mechanism proposed above, the selectivity is determined in the subsequent mechanisms following the adsorption.

As shown in Figure 5B, the effect of increasing the temperature on the selectivity is a decrease for D1 and D2 accompanied by an increase for D6-D10. The relative amounts of D3-D5 are unaffected. This is similar to what is observed in literature[33,40].

The high amount of rotations (~18 for the D5 product, Table 1) and the observation that the selectivity towards D3-D5 is unaffected by temperature, indicate that the rotation mechanism is virtually non-activated.

Table 3: The effect of temperature on the exchange selectivity. The data given are based upon the Monte-Carlo model. Only the two extreme temperatures are given, the other temperatures are shown in Figure 5B.

T (°C)	Selectivity (%) towards intermediate[a]						
	σ-η^1	di-σ-η^2	π-η^2				
	(D1)	(D2)	(D2)	(D3)	(D4)	(D5)	di-σ-η^1 (> D6)
66	22.6	3.3	4.8	8.0	9.1	33.1	19.1
81	16.2	1.9	4.3	7.3	8.4	33.2	28.8

[a] For a description of the intermediates: see Figure 1.

The selectivity for the roll-over, leading to D6-D10, increases from 19.1% at 66°C to 28.8% at 81°C (see Table 3 and Figure 5B). This increase shows that the roll-over mechanism is an activated mechanism. As explained earlier, it is the π-η^2 intermediate (Figure 1C) that rolls over via the di-σ-η^1 intermediate, and the activity is given by formula (6). Since this activity is as high as 28.8/81.2=35%, the activity for roll-over is no longer differential. This can be corrected by assuming that 35% of the rolled-over molecules rolls-over again and than the

activity is approximately (35% from 35%) + 35% = 47%. By constructing an Arrhenius plot of this corrected fraction as a function of temperature the activation energy for roll-over can be estimated (Figure 9). The apparent activation energy for roll-over was estimated at 24 kJ/mol.

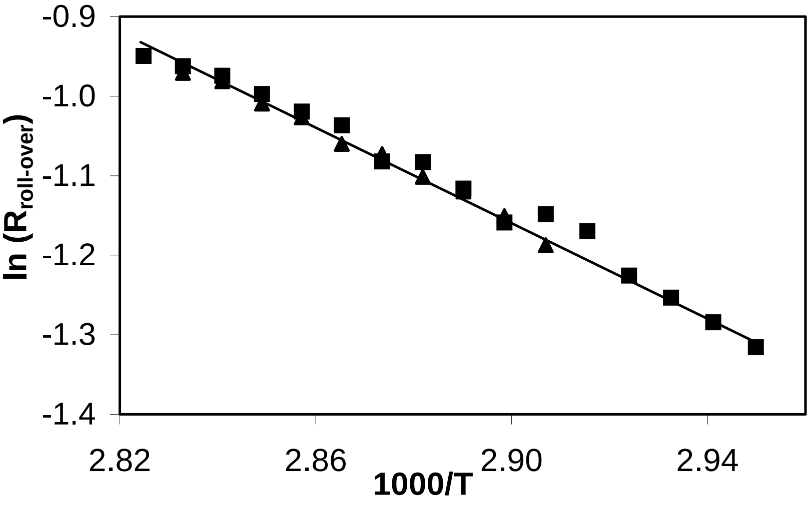

Figure 9: Arrhenius plot of the influence of temperature on the selectivity towards rollover.

Implications for the H/D exchange experiments

In the older literature, the selectivities as-measured were used to describe the experiments. It has been shown that this is not adequate. If one wants to investigate the relative contributions to the selectivity of the 4 competing exchange mechanisms, it is essential to carefully investigate the observed selectivity. For example, when a molecule containing 5 D atoms is observed, in reality it has undergone as much as ~20 exchange steps, 15 of which are D/D exchanges. The developed Monte-Carlo model is essential to calculate this true number of exchange steps based upon the observed selectivity. Each exchange step is associated with a rotation of the π-η^2 intermediate to an adjacent C-C bond in CP. This rotation mechanism can not proceed via an interconversion of the σ-η^1 intermediate (Figure 1A) on the one hand and di-σ-η^2 (Figure 1B) and π-η^2 (Figure 1C) intermediates on the other hand. Instead, the rotation mechanism is hardly activated and proceeds via an allylic-like mechanism (Figure 6). Also, two different exchange mechanisms proceeding via the a di-σ-η^2 (Figure 1B) and π-η^2 (Figure 1C) intermediates result in the D2 product. The relative contributions can only be calculated with this Monte-Carlo model. This Monte-Carlo model is also essential in determining the true roll-over activity.

Conclusions

The H/D exchange of CP leads to a product distribution with maxima for the D1, D5 and D10 products. The observed exchange patterns can be simulated by a newly developed, Monte-

Carlo based model. At least 4 different mechanisms lead to the observed product distributions. The Monte-Carlo model reveals that the real number for exchange steps can not be directly extracted from the measured exchange pattern. For example, the D5 product indicates that 5 exchange steps have occurred. In reality, however, the number of exchange steps can be as high as 15-20. The mechanism leading to the D5 product is proposed to proceed via a rotation mechanism involving a allylic mechanism and a π-η^2 intermediate. Careful considerations regarding the observed selectivity inevitably lead to the conclusion that D2 is produced via 2 different intermediates, whose relative contributions are given by the Monte-Carlo model. In addition, it is concluded that the roll-over leading to the D6-D10 products can only occur when the CP first is adsorbed as the π-η^2 intermediate, followed by a roll-over via the di-σ-η^1 intermediate. Again the Monte-Carlo model is essential to obtain the true activity for this roll over. In addition to an understanding of origins of the selectivity, also a kinetic model describing the activity and orders in reactants was developed. The exchange pattern, or selectivity, is determined in a series of reactions occurring *after* the rate determining step.

Reference list

1. T. M. Tri, J. Massardier, P. Gallezot and B. Imelik, *Stud. Surf. Sci. Catal.,* **11** (1982), 141-148.
2. W. C. Neikam and M. A. Vannice, *Proc. 5th Int. Con. Catal. Miami*, **1** (1972), 609-619.
3. D. Poondi and M. A. Vannice, *J. Catal.*, **161** (1996), 742-752.
4. V. N. Romannikov and K. G. Ione, *J. Catal.*, **66** (1980), 121-129.
5. A. de Mallmann and D. Barthomeuf, *J. Chim. Phys.*, **87** (1990), 535-538.
6. R. A. Dalla Betta and M. Boudart, *Proc 5th Int Con Cat* (1973), 1329-1341.
7. C. Besoukhanova, J. Guidot and D. Barthomeuf, *J. Chem. Soc. Faraday Trans. I,* **77** (1981), 1595-1604.
8. A. de Mallmann and D. Barthomeuf, *Stud. Surf. Sci. Catal.*, **46** (1989), 429.
9. Z. Zhang, T. T. Wong and W. M. H. Sachtler, *J. Catal.*, **128** (1991), 13-22.
10. B. L. Mojet, J. T. Miller, D. E. Ramaker and D. C. Koningsberger, *J. Catal.*, **186** (1999), 373-386.
11. D. C. Koningsberger, J. de Graaf, B. L. Mojet, D. E. Ramaker and J. T. Miller, *Appl. Catal. A: General*, **191** (2000), 205-220.
12. Chapter 8 of this thesis.
13. D. E. Ramaker, J. de Graaf, J. A. R. Van Veen and D. C. Koningsberger, *J. Catal.*, **203** (2001), 7-17.
14. C. Hippe, R. Lamber, G. Schulz-Ekloff and U. Schubert, *Catal. Lett.*, **43** (1997), 195-199.
15. V. B. Kazansky and V. Yu. Borovkov, *Stud. Surf. Sci. Catal.*, **92** (1995), 275-280.
16. M. T. M. Koper, R. A. van Santen, S. A. Wasileski and M. J. Weaver, *J. Chem. Phys.*, **113** (2000), 4392-4407.
17. A. Yu. Stakheev, E. S. Shapiro, N. I. Jaeger and G. Schulz-Ekloff, *Catal. Lett.*, **32** (1995), 147-158.
18. M. Vaarkamp, B. L. Mojet, F. S. Modica, J. T. Miller and D. C. Koningsberger, *J. Phys. Chem.*, **99** (1995), 16067.
19. J. de Graaf, Ph.D., Utrecht University, Ridderkerk, 2001.

20. G. C. Bond, M. A. Keane, H. Kral and J. A. Lercher, *Catal. Rev. - Sci. Eng.*, **42** (2000), 323-383.
21. K. Foger and J. R. Anderson, *J. Catal.*, **54** (1978), 318-335.
22. Z. Karpinski, S. N. Gandhi and W. M. H. Sachtler, *J. Catal.*, **141** (1993), 337-346.
23. R. Burch and Z. Paál, *Appl. Catal. A: General*, **114** (1994), 9-33.
24. R. Burch, *Catal. Today*, **10** (1997), 233-249.
25. M. J. P. Botman, K. de Vreugd, H. W. Zandbergen, R. de Block and V. Ponec, *J. Catal.*, **116** (1989), 467-479.
26. A. Khodakov, N. Barbouth, Y. Berthier, J. Oudar and P. Schulz, *J. Chem. Soc. Faraday Trans.*, **91** (1995), 569-573.
27. V. Eskinazi and R. L. Burwell, *J. Catal.*, **79** (1983), 118-131.
28. B. F. Hegarty and J. J. Rooney, *J. Chem. Soc. Faraday Trans. I*, **85** (1989), 1861-1871.
29. T. Baird, E. J. Kelly, W. R. Patterson and J. J. Rooney, *J. Chem. Soc. Chem. Comm.* (1992), 1431-1433.
30. A. da Costa Faro Jr. and C. Kemball, *J. Chem. Soc. Faraday Trans.*, **91** (1995), 741-748.
31. J. K. A. Clarke, B. F. Hegarty and J. J. Rooney, *J. Mol. Catal.*, **62** (1990), L39-L43.
32. Y. Inoue, J. M. Hermann, H. Schmidt, R. L. Burwell, J. B. Butt and J. B. Cohen, *J. Catal.*, **53** (1978), 401-413.
33. R. Pitchai, S. S. Wong, N. Takahashi, J. B. Butt, R. L. Burwell and J. B. Cohen, *J. Catal.*, **94** (1985), 478-490.
34. E. J. Kelly, W. R. Patterson and J. J. Rooney, *J. Mol. Catal.*, **89** (1994), 19-28.
35. C. Kemball, *Adv. Catal.*, **11** (1959), 223-262.
36. V. Ponec and G. C. Bond: *Catalysis by Metals and Alloys*, Studies in Surface Science and Catalysis, Elsevier Science, 1995, Vol. 95.
37. M. K. Oudenhuijzen, J. H. Bitter and D. C. Koningsberger, *J. Phys. Chem. B*, **105** (2001), 4616-4622.
38. M. K. Oudenhuijzen, P. J. Kooyman, B. Tappel, J. A. van Bokhoven and D. C. Koningsberger, *J. Catal.*, **205** (2002), 135-146.
39. R. A. van Santen, P. W. N. M. van Leeuwen, J. A. Moulijn and B. A. Averill: *Catalysis: an Integrated Approach*, 2nd ed., Studies in Surface Science and Catalysis, Elsevier Science, Amsterdam, 1999, Vol. 123.
40. V. Ponec and W. M. H. Sachtler, *J. Catal.*, **24** (1972), 250-261.
41. R. L. Burwell, *Acc. Chem. Res.*, **2** (1969), 289-296.
42. E. Poulain, V. Bertin, S. Castillo and A. Cruz, *J. Mol. Catal. A*, **116** (1997), 385-396.
43. B. Hammer and J. K. Nørskov, *Surf. Sci.*, **343** (1995), 211-220.
44. B. Hammer and J. K. Nørskov, *Nature*, **376** (1995), 238-240.
45. J. Barbier, E. Lamy-Pitara and P. Marecot, *Bull. Soc. Chim. Belg.*, **105** (1996), 99-105.
46. K. Schrage and R. L. Burwell, *J. Am. Chem. Soc.*, **88** (1966), 4549-4555.
47. J. T. Campbell and C. T. Campbell, *Surf. Sci.*, **210** (1989), 46-68.

Appendix A

The reactions considered are:

(III) $C_5H_{10}(g)+* \xleftrightarrow{K_1} C_5H_{10}(*)$

(IV) $D_2(g)+2* \xleftrightarrow{K_2} 2D(*)$

(IIIA) $C_5H_{10}(*)+* \xrightarrow{k_{+3}} C_5H_9(*)+H(*)$

(IIIB) $C_5H_nD_{9-n}(*)+D(*) \xrightarrow{k_{-3}} C_5H_nD_{10-n}(*)$

with *: an empty adsorption site and
D(*): an adsorbed atom of deuterium (D_2).

Since H_2 and D_2 are chemically similar, H(*) = D(*) and $C_5H_nD_{9-n}$(*) = C_5H_9 (*), and thus k_{+3} and k_{-3} are equal in a steady state. Between reaction (IIIA) and (IIIB), the cyclopentane can exchange a lot of D atoms.

The accompanying reactions rates are:

(a) $R_1 = r_{+1} - r_{-1} = k_{+1}P_{CP}\theta_* - k_{-1}\theta_{C_5H_{10}}$

(b) $R_2 = r_{+2} - r_{-2} = k_{+2}P_{D_2}\theta_*^2 - k_{-2}\theta_D^2$

(c) $R_3 = r_{+3} - r_{-3} = k_{+3}\theta_{C_5H_{10}}\theta_* - k_{-3}\theta_{C_5H_9}\theta_H$

with θ_x: the fractional coverage of species *X*.
k: the reaction constants with the equilibrium constant $K_n = \frac{k_{+n}}{k_{-n}}$

Since H_2 and D_2 are chemically similar, H(*)=D(*). Substituted in R_3, this gives:

(d) $R_3 = r_{+3} - r_{-3} = k_{+3}\theta_{C_5H_{10}}\theta_* - k_{-3}\theta_{C_5H_9}\theta_D$

Furthermore, the total coverage is 1:

(e) $1 = \theta_* + \theta_{C_5H_{10}} + \theta_{C_5H_9} + \theta_D$

Since all measurements are performed in steady state, the coverages are constant in time:

(f) $\frac{d\theta_{C_5H_9}}{dt} = 0 = k_{+3}\theta_{C_5H_{10}}\theta_* - k_{-3}\theta_{C_5H_9}\theta_D$

→ $$\theta_{C_5H_9} = \frac{k_{+3}\theta_{C_5H_{10}}\theta_*}{k_{-3}\theta_D} = \frac{K_3\theta_{C_5H_{10}}\theta_*}{\theta_D}$$

(g) $$\frac{d\theta_{C_5H_{10}}}{dt} = 0 = k_{+1}P_{CP}\theta_* - k_{-1}\theta_{C_5H_{10}} - k_{+3}\theta_{C_5H_{10}}\theta_* + k_{-3}\theta_{C_5H_9}\theta_D$$

(h) $$\frac{d\theta_D}{dt} = 0 = k_{+2}P_{D_2}\theta_*^2 - k_{-2}\theta_D^2 + k_{+3}\theta_*\theta_{C_5H_{10}} - k_{-3}\theta_{C_5H_9}\theta_D$$

substitution of (f) in (g) leads to

(i) $$\theta_{C_5H_{10}} = K_1 P_{CP}\theta_*$$

substitution of (g) and (i) into (h) leads to

(j) $$\theta_D = \theta_* * \sqrt{K_2 P_{D_2}}$$

and substitution of (f), (i) and (j) in (e) gives:

(k) $$\theta_* = \frac{1}{1 + K_1 P_{CP} + \frac{K_1 K_3 P_{CP}}{\sqrt{K_2 P_{D_2}}} + \sqrt{K_2 P_{D_2}}}$$

Since all cyclopentane which dissociates on the surface is detected as a D1-D10 product, the reaction rate is given by r_{+3} or r_{-3}:

$$R = r_{-3} = k_{-3}\theta_{C_5H_9}\theta_D = k_{-3}\frac{K_3\theta_{C_5H_{10}}\theta_*}{\theta_D}\theta_D = k_{-3}K_1K_3P_{CP}\theta_*^2 = \ldots$$

(l) $$\ldots\frac{k_{-3}K_1K_3P_{CP}}{\left(1 + K_1 P_{CP} + \frac{K_1 K_3 P_{CP}}{\sqrt{K_2 P_{D_2}}} + \sqrt{K_2 P_{D_2}}\right)^2}$$

Estimation of reaction constants:

1. Reaction (I) is easy and fast, with $K_1 = k_{+1}/k_{-1} > 1$
2. Reaction (II) is very fast, $K_2 >> 1$
3. Reaction (III) is the rate determining step, thus $(k_{-3}, k_{+3}) << (k_{+1}, k_{-1}, k_{+2})$

thus, if $K_2 >> K_1K_3$, equation (l) can be simplified by ignoring several terms:

(l) $$R = \frac{k_{-3}K_1K_3P_{CP}}{\left(1 + K_1 P_{CP} + \frac{K_1 K_3 P_{CP}}{\sqrt{K_2 P_{D_2}}} + \sqrt{K_2 P_{D_2}}\right)^2} \approx \frac{k_{-3}K_1K_3P_{CP}}{K_2 P_{D_2}}$$

4

Support Induced Compensation Effects in H/D Exchange of Cyclopentane

Abstract

The exchange of hydrogen for deuterium (H/D exchange) in cyclopentane was measured for Pt catalysts with supports of various acidity. With an earlier developed Monte-Carlo model the contributions of the various possible intermediates in the H/D exchange can directly be measured. It was shown that the activity and the selectivity in the H/D exchange over the supported Pt catalysts strongly depend on the support acid/base properties. The activities of the various catalysts show a compensation effect. The compensation effect can directly be correlated to the contribution of the various exchange mechanisms, which proceed via different intermediates. The contribution of each intermediate depends on the electronic properties of the Pt particles, which in turn depend on the support acidity. This shows that the compensation effect is caused by support induced changes in the adsorption modes of cyclopentane.

Introduction

The influence of the support acid/base properties on the catalytic properties of supported metal particles has been studied extensively[1,2]. It has been established that the rate of hydrogenolysis and hydrogenation over supported Pt particles increases with the acidity of oxidic supports[3,4]. A large amount of work has been dedicated to relate changes in catalytic properties to changes in the electronic properties of the Pt particles[5-10]. The support is believed to interact with the Pt particles via the oxygen atoms of the oxidic supports. In line with the definition of Lewis acidity, acidic supports are associated with a low electron-richness on the support oxygen atoms, whereas basic supports are associated with a high electron richness. Recently, based on the results of atomic X-ray absorption fine structure spectroscopy (AXAFS) and ab initio multiple scattering calculations, it was found that a lower electron richness of the support oxygen atoms leads to a higher ionization potential of the Pt particles. At the same time, a charge rearrangement from within the Pt particle towards the metal-support interface was observed for acidic supports[10-12]. If the relation between support material and changes in activity/selectivity is well understood, it promises the prospect of tailor-made catalysts. However, there is a lot of discussion on the relations between support material and electronic properties on one hand and the catalytic properties on the other. The direct relation between the changes electronic properties and its effect on the catalytic properties is not well understood.

Thus, the need for a good test reaction is obvious. An important feature for a proper test reaction is that it should be metal-catalyzed only. The isotopic exchange of hydrogen with deuterium in hydrocarbons (H/D exchange) is a typical metal-catalyzed reaction[13-16]. During H/D exchange, hydrogen atoms of a hydrocarbon are replaced by deuterium atoms. The advantage of H/D exchange of cyclopentane (CP) as a test reaction is that its product distribution gives direct information about the different modes of adsorption of the intermediates during the reaction. These adsorption modes are proposed to be dependent on the electronic properties of the metal[16-18].

In order to fully understand the H/D exchange mechanism of CP, the kinetics, selectivities and adsorption modes of CP in the H/D exchange were studied in detail in an earlier paper[19]. It was shown that the D1 product is produced by the exchange of a single hydrogen atom via a σ-bonded η^1-cyclopentyl intermediate (further called 'σ-η^1', Figure 1A). The D2-D5 products consist of cyclopentane with deuterium atoms all located on a single side of the ring, and is produced via a rotation mechanism of a π-bonded η^2-cyclopentene (further called 'π-η^2', Figure 1C)[16,20]. The D2 product can also be formed via a second intermediate, a double σ-bonded α,β-η^2-cyclopentyl ('di-σ-η^2', Figure 1B)[21]. With the D6-D10 products, the CP has to be rolled over from one side of the ring to the other, leading to the possibility that the atoms on the second side of the ring are also exchanged. The only species that can roll-over is the π-η^2 intermediate via a double σ-bonded η^1-cyclopentylidene ('di-σ-η^1', Figure 1D). A Monte-Carlo model was developed, which can be used to accurately determine the relative

contributions of the above mentioned intermediates. The Monte-Carlo model reveals that the multiplicity parameter as defined in literature does not represent the relative contribution of each intermediate, although it has been generally used for this purpose[22]. In addition to an understanding of the selectivity, also a kinetic model for the understanding of observed orders and reaction rates was developed[19].

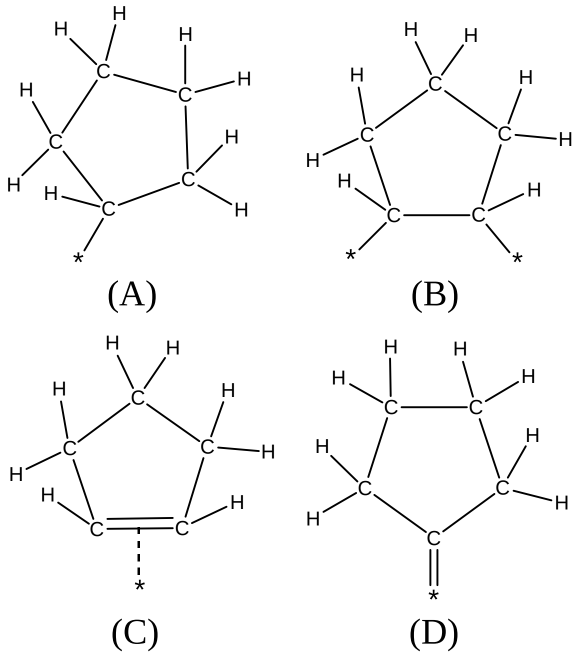

Figure 1: Different adsorbed intermediates, leading to different products (A) σ-bonded η¹-cyclopentyl (‘σ-η¹’), leading to D1, (B) a double σ-bonded α,β-η²-cyclopentyl (‘d-σ-η²’) and (C) π-bonded η²-cyclopentene (‘π-η²’) both leading to D2-D5 products and (D) double σ-bonded η¹-cyclopentylidene (‘di-σ-η¹’) leading to roll-over.

This paper focuses on the influence of the support on the H/D exchange of CP over supported Pt catalysts. It will be shown that kinetics and selectivities are largely affected by the support material. Particle size effects are separated from support effects. The activity shows a compensation effect, and the apparent activation energy and pre-exponential factor show an isokinetic relationship[23,24]. This can be explained by different adsorption modes of the CP on the metallic Pt surface. The change in adsorption modes is attributed to a change in the electronic structure of the Pt particles, which in turn is induced by changes in the acid/base properties of the support.

Methods

Catalyst preparation

Several supported Pt catalysts were prepared. The supports used are Mg hydrotalcite (HT), SiO_2, amorphous SiO_2-Al_2O_3 (ASA) and LTL zeolite. The support characteristics are shown in Table 1.

Table 1: The characteristics of the supports.

Support	Si/Al	# of acid sites (mmol/g)[a]	BET surface area (m^2/g)	pore volume (ml/g) total	pore volume (ml/g) micropore	average pore diameter (nm)[b]
SiO_2	n.a.	n.a.	405	1.10	0	25 (± 15 nm)
ASA [2.5]	2.5	1.2	355	0.59	0	7 (± 2 nm)
ASA [11.3]	11.3	0.28	321	0.50	0	5 (± 1 nm)
K-LTL	3.0	K/Al=0.47: 1.76 K/Al=0.82: 0.58 K/Al > 1: none		0.25	0.11	0.71[c] 1.30
Hydrotalcite	Mg/Al = 3.0	n.a.	105	0.57	0.00	18 (± 3 nm)

[a] The number of acid sites for the ASA was determined with the combined thermographic analysis and temperature programmed desorption of iso-propylamine. For the LTL zeolites is was calculated based upon crystallographic data[27].

[b] Determined from the N_2 desorption plot, according to the Broekhoff I method for CeO_2-3•H_2O. The values between brackets represent the distribution in pore-diameter.

[c] LTL zeolites have pores in a single direction along the [001] axis[27]. The pores are constructed of cages with a diameter of 13Å, and are interconnected with 12 membered rings with a diameter of 7.1 Å.

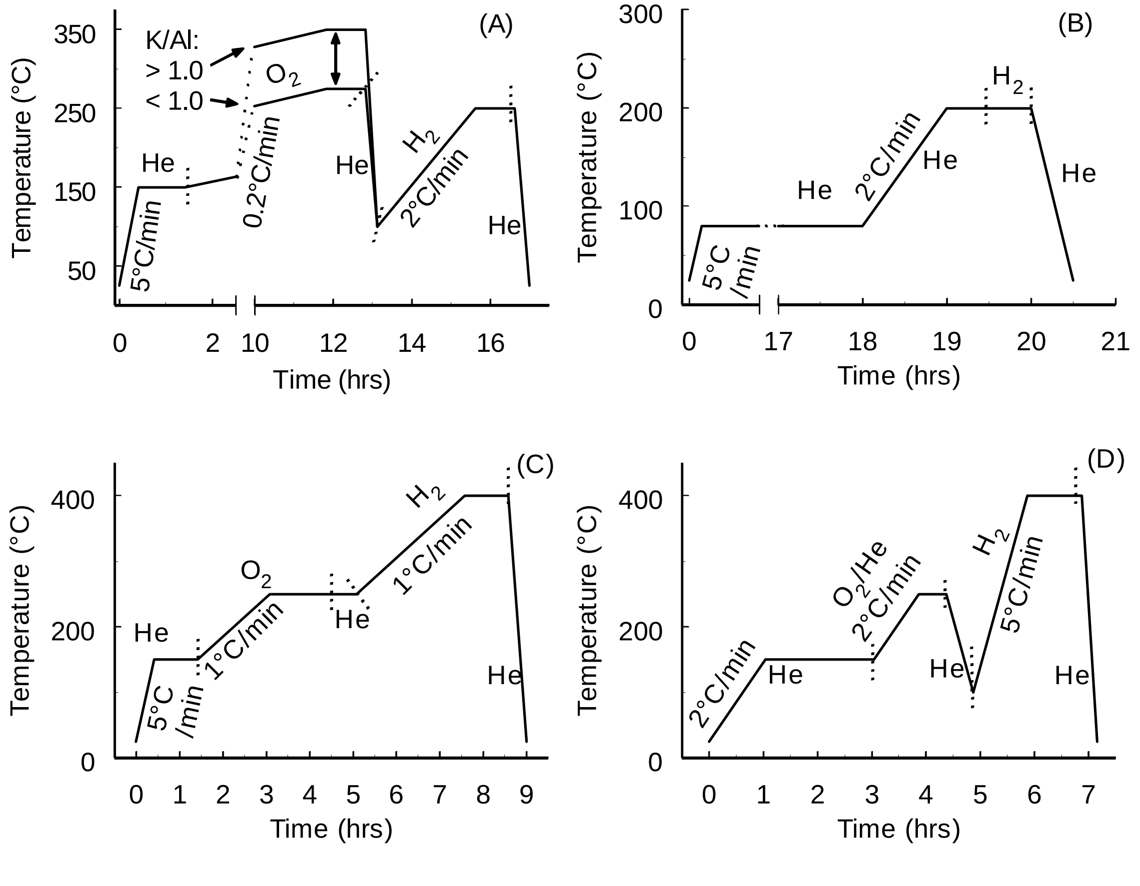

Figure 2: The calcination-reduction schemes for the various catalysts, (A): for the Pt/LTL catalysts, (B) for Pt/HT, (C) for Pt/SiO_2 [big] (D) Pt/SiO_2 [small] and Pt/ASA.

The catalysts were all calcined and prereduced. For the calcination/reduction, a sieve fraction ($225 < d_p < 450$ μm) was placed in a downflow fixed-bed reactor. The prereduced catalysts were stored in air. The Pt particle size was determined by H_2 chemisorption, high resolution transmission electron microscopy and EXAFS analysis. Details of H_2 chemisorption[25], HRTEM[26] and EXAFS[25] are given elsewhere.

Pt on LTL zeolites

The acidity of the LTL zeolite was varied by either impregnating a K-LTL zeolite with KNO_3(aq), or exchanging it with NH_4NO_3 to give K/Al ratios ranging from K/Al=0.47 to 1.53. The zeolites were calcined at 225°C and analyzed for K and Al contents. The catalysts are designated LTL [*.**] with *.** representing the K/Al ratio. High K/Al ratios are associated with basic supports (see the discussion section).

Platinum was added by incipient wetness impregnation of an aqueous $Pt(NH_3)_4(NO_3)_2$ solution, resulting in a 1 wt.% Pt/LTL catalyst. The impregnation was followed by drying the zeolite at 150°C for 1 hour in a high He flow. Subsequently, the catalyst was calcined in a high O_2 flow at 275°C (LTL [0.47], [0.82] and [1.04]) or 350°C (LTL [1.53]) with a slow heating rate of 0.2 °C/minute, cooled down to 100°C in He, and reduced in H_2 at 250°C (heating rate 1°C/min) (as shown in Figure 2A).

For one catalyst precursor, with a LTL [0.47] support, the drying procedure following the impregnation was performed under vigorous conditions (high heating rate, low flow rate). This resulted in a catalyst with a larger particle size. The two Pt/LTL [0.47] catalysts are coded Pt/LTL [0.47, small] when the regular drying and pretreatment procedure was used, and Pt/LTL [0.47, big] when the severe drying pretreatment was used.

Pt on hydrotalcite

The hydrotalcite (HT) support was prepared with a Mg/Al ratio of 3.0 and activated as described by Roelofs *et al*[28]. The activation procedure consists of a calcination in N_2 at 450°C, followed by a rehydration of the hydrotalcite in H_2O, during which the hydrotalcite structure is restored. During the rehydration procedure, H_2PtCl_6 was added to part of the hydrotalcite support. The now ion exchanged hydrotalcite was filtrated and dried in He at 80°C for 18 hours, followed by drying at 200°C (heating rate 2°C/min) for 1 hour and a reduction in H_2 at 200°C for 1 hour (Figure 2B). The resulting Pt/hydrotalcite is further designated as Pt/HT.

Pt on SiO_2

SiO_2 (Engelhard, BET surface area 400 m^2/g, pore volume 1.1 ml/g) was washed with 0.05 M HNO_3 to remove alkali ions from the surface.

5 g vacuum-dried SiO_2 was impregnated with 5.5 ml of an aqueous solution of $[Pt^{2+}(NH_3)_4](NO_3^-)_2$ (Aldrich, 18.0 mg/ml, resulting in 1 wt.% Pt/SiO_2) using the incipient wetness method. The impregnated support was dried in a water-free nitrogen flow for 1 hour at room temperature and for 18 hours at 80°C. The calcination-reduction scheme for this catalyst is given in Figure 2C. The resulting catalyst is further designated Pt/SiO_2 [big].

Another batch of the SiO_2 support was ion exchanged with $Pt(NH_3)_4(NO_3)_2$. 5 g of the support was suspended in a NH_3 solution with pH=9.0. This deprotonates a large part of the silanol surface groups. A $Pt(NH_3)_4(NO_3)_2$ solution was slowly added to the suspension under vigorous stirring and allowed to ion exchange with the SiO_2 surface for 12 hrs. Next, the catalyst precursor was washed twice and dried at 120°C overnight. Atomic Absorption Spectroscopy (AAS) revealed that nearly all Pt^{2+} complex is exchanged, resulting in a 1 wt.% Pt catalyst precursor. This catalyst precursor was pretreated according to the calcination-reduction shown in Figure 2D. This catalyst is coded Pt/SiO_2 [small].

Pt on SiO_2-Al_2O_3

Two amorphous SiO_2-Al_2O_3 (ASA) supports with different Si/Al-ratios were used. One ASA had a Si/Al ratio of 2.5 (Engelhard, BET surface area 320 m^2/g, pore volume 0.50 ml/g), the other of 11.3 (Ketjen, HA 100 5P, 355 m^2/g, 0.59 ml/g). The supports and corresponding catalysts are further coded ASA [*.**], where *.** represents the above mentioned Si/Al ratio. For both supports, the number of acid sites was determined with the combination of thermographic analysis and temperature programmed desorption of isopropylammine[29]. The number of acid sites was 1.2 mmol/g for ASA [2.5] and 0.28 mmol/g for ASA [11.3]. See Table 1.

The ASA [11.3] used in this study was a mesoporous ASA with an average pore diameter of 5 nm. 5 g of the ASA [11.3] was ion exchanged in an aqueous suspension with $Pt(NH_3)_4(NO_3)_2$ at 80°C for 24 hrs under vigorous stirring. This sample was washed twice at 80°C for 24 hrs. The filtrated catalyst precursor was dried in a nitrogen flow for 1 hr at 60°C, 2 hrs at 80°C and 12 hrs at 120°C (all heating rates 3°C/min). The sample was subsequently calcined and reduced according to the scheme given in Figure 2D.

The catalyst 1 wt.% Pt/ASA [2.5] was prepared with incipient wetness impregnation, using the same procedure as described for the Pt/SiO_2 [big] catalyst. The calcination-reduction scheme was similar to the Pt/ASA [11.3] catalyst (Figure 2D), with the exception that the calcination heating rate was 0.2°C/min.

H/D exchange of cyclopentane

Experiments

Details of the H/D exchange experiments are described elsewhere[19]. A downflow fixed-bed reactor (diameter of 4 mm) was loaded with ~5-10 mg of the catalyst and dilluted with 60 mg of SiO_2, both with a sieve fraction of $90 < d_p < 150$ µm. The basic catalysts (Pt/HT and Pt/LTL [K/Al>1] showed extremely low activities, and the reactor was loaded with 70-90 mg pure catalyst.

The catalyst was prereduced for 1 hr at 200°C (Pt/HT), 300°C (LTL [*.**]) or 400°C (Pt/SiO_2 [**] and Pt/ASA [*.**]) in hydrogen. The catalyst was cooled down in 50% D_2 in Ar to 75°C. Typical HD experiments were performed at 75°C at atmospheric pressure, with P_{D2}= 0.5 bar, P_{CP}=0.025 bar (resulting in D/H=20) and P_{Ar}=0.475 bar and conversions below 10% with no significant side reactions.

Analysis of the selectivity: the Monte-Carlo model

In an earlier paper[19] a Monte-Carlo model was developed, which was used to accurately determine the relative contributions of the various intermediates shown in Figure 1. This Monte-Carlo model also reveals the true number of rotations each π-η^2 intermediate experiences, giving the real number of exchange steps. For example, a CP molecule observed as $C_5H_5D_5$ has not only exchanged 5 H atoms for 5 D atoms, but the introduced D atoms can also be exchanged for other D atoms. This D-D exchange cannot be directly measured, but is determined by this Monte-Carlo model.

Analysis of reaction rates and orders

The turnover frequency (TOF) is defined as the number of molecules CP that is converted per Pt *surface* atom per second. The number of accessible Pt surface atoms is based on the total amount of hydrogen chemisorbed. Orders in CP and D_2 were determined by varying the applicable partial pressures while the total flow was kept constant.
Activation energies were determined by heating the catalyst multiple times from 65-90°C. The following form of Arrhenius formula was used:

$$TOF = A_{app} e^{\frac{-E_{act,app}}{RT}} \qquad (1)$$

with TOF : the turn over frequency, mol CP converted per mol surface Pt, per second,
$E_{act,app}$: the apparent activation energy (kJ/mol),
T : the reaction temperature (K), and
A_{app} : the pre-exponential factor.

It was shown that the reaction rate can be modeled with the following reactions and corresponding rates[19]:

(I) $C_5H_{10}(g) + * \xleftrightarrow{K_1} C_5H_{10}(*)$

(II) $D_2(g) + 2* \xleftrightarrow{K_2} 2D(*)$

(IIIA) $C_5H_{10}(*) + * \xrightarrow{k_{+3}} C_5H_9(*) + H(*)$

(IIIB) $C_5H_nD_{9-n}(*) + D(*) \xrightarrow{k_{-3}} C_5H_nD_{10-n}(*)$

leading to a reaction rate R given by

$$R = r_{-3} = \frac{k_{-3}K_1K_3P_{CP}}{\left(1 + K_1P_{CP} + \frac{K_1K_3P_{CP}}{\sqrt{K_2P_{D2}}} + \sqrt{K_2P_{D2}}\right)^2} \qquad (2)$$

where it assumed that H_2 and D_2 are chemically similar and thus H(*) is also similar to D(*) and $C_5H_nD_{9-n}(*)$ similar to C_5H_9 (*), and thus r_{+3} and r_{-3} are equal in a steady state reaction.

The observed orders in CP and D_2 depend on the equilibrium constants K_1, K_2 and K_3, and in principle can be anything between +1 and –1 for CP and between 0 and -1 for D_2. The selectivity in the H/D exchange is determined in a process *after* the rate-determining step.
The activation energy for the roll-over reaction was determined from the above mentioned Monte-Carlo based method[19]: the Monte-Carlo method was used to accurately determine the contribution of the π-η^2 intermediate leading to D2-D10 and the amount of this π-η^2 intermediate that rolls over, giving D6-D10. The ratio of the two intermediates indicates how much of the π-η^2 intermediate rolls over via the di-σ-η^1 intermediate. This roll-over is an activated mechanism, and by measuring the amount of roll-over as a function of temperature the activation energy for roll-over can be determined.

Results

Particle sizes of the reduced catalysts

In Table 2, the results from HRTEM, H_2 chemisorption, the final Pt-Pt and Pt-O coordination number and the estimated number of Pt atoms in the cluster are given. This average number of atoms was estimated with the help of a computer program. This program cuts spheres from a fcc bulk structure, and calculates the corresponding Pt-Pt coordination number and dispersion (the ratio of the amount of coordinatively unsaturated Pt atoms and the total amount of Pt atoms). A series of spheres with increasing radii was calculated. By comparing the with HRTEM, H_2 chemisorption and EXAFS observed particles sizes with the theoretical values of the calculated, spherical clusters an average number of atoms was estimated.

Table 2: The results of H_2 chemisorption, HRTEM and EXAFS analysis for the reduced Pt catalysts

catalyst, Pt/	H/Pt weak	H/Pt strong	H/Pt total	diameter (nm, ± 0.2) (HRTEM)	N_{PtPt}	$N_{Pt\text{-}O}$	estimated # atoms
LTL [0.47, small]	0.42	0.64	1.07	n.d.	5.2	1.0	10-15
LTL [0.47, big]	0.27	0.16	0.43	n.d.	10.1	0	500-1000
LTL [0.82]	0.41	0.76	1.17	n.d.	4.8	0.4	8-12
LTL [1.04]	0.47	0.59	1.06	n.d.	4.9	0.7	8-12
LTL [1.53]	0.18	0.78	0.97	n.d.	5.4	0.8	15-20
ASA [2.5]	0.52	0.58	1.10	n.d.	n.d.	n.d.	8-12
ASA [11.3]	0.58	0.36	0.94	1.5	4.8	0.5	8-12
SiO_2 [small]	0.65	0.61	1.26	1.2	6.9	0.4	30-50
SiO_2 [big]	0.44	0.43	0.87	1.7	7.8	0.2	60-80
HT	0.62	0.54	1.16	1.1	5.2	0.7	10-15

The Pt/LTL [0.47, small], the other Pt/LTL [*.**] catalysts, both Pt/ASA catalysts and the Pt/HT all show a high H/Pt number with $H_{total}/Pt \geq 1.0$ and a Pt-Pt coordination of approximately N_{PtPt}=5. The number of Pt atoms in these particles was estimated at approximately 8-15 atoms in all cases. For the Pt/ASA [11.3] catalyst, the particle size

determined with HRTEM (1.5 nm) is a little higher than the particle size that is expected based on the H_2 chemisorption or Pt-Pt coordination number.The Pt/SiO_2 catalysts all showed larger Pt-Pt coordination numbers (N_{PtPt} = 6.9 and 7.8). The Pt/SiO_2 [small] catalyst, prepared via ion exchange, shows a high H/Pt number (H_{total}/Pt =1.26) in combination with a small particle size as revealed with HRTEM (1.2 nm). The Pt/LTL [0.47, big] catalyst showed a large particle size, with H_{total}/Pt=0.43 and N_{PtPt}=10.1.

Particle size effects in H/D exchange

Activity as a function of particle size

The particle size effect on the activity was measured for two supports, LTL [0.47] and SiO_2. The results for these catalysts are given in Table 3. The TOF (turn over frequency) was of the same order of magnitude, irrespective to the particle size. However, the apparent activation energy is clearly smaller for the larger particles. This lower E_{app} is compensated by a smaller pre-exponential factor $ln\ A_{app}$.

Selectivity as a function of particle size

In Figure 3, the exchange patterns as measured for the catalysts with the different particle sizes is shown. The selectivity was analyzed using the Monte-Carlo model. The results are given in Table 4.

Table 3: The activity and orders for D_2 and CP in H/D exchange for the various catalysts. The TOF is defined as the number of converted CP atoms per *surface* Pt atom per second.

Catalyst, Pt/	TOF at 75°C [mol CP/(mol Pt*s)]	E_{app} (kJ/mol)	ln A_{app}	roll-over (via di-σ-η[1], based on Monte-Carlo method)		order	
				$E_{app,}$ (kJ/mol)	ln A_{app}	D_2	CP
LTL [0.47, small]	4.8	73.7	27.5	20.5	5.6	-0.32	0.18
LTL [0.47, big]	10.0	66.4	25.2	20.8	5.7	-0.79	0.49
LTL [0.82]	7.5	67.1	25.2	12.6	2.8	-0.46	0.28
LTL [1.04] [a]	0.2	n.d.	n.d.	n.d.	n.d.	n.d.	n.d.
LTL [1.53][a]	0.3	n.d.	n.d.	n.d.	n.d.	n.d.	n.d.
ASA [2.5]	7.9	56.2	21.6	5.5	8.7	n.d.	n.d.
ASA [11.3]	10.4	56.9	22.0	82.7	27.4	-0.82	0.69
SiO_2 [small]	7.5	64.7	24.4	29.9	8.9	-0.60	0.58
SiO_2 [big]	8.0	55.0	21.1	24.3	6.7	-0.82	0.87
HT [a]	1.6×10^{-3}	66.9	16.7	n.d.	n.d.	n.d.	n.d.

[a] Due to the low activity, E_{app}, $E_{app,roll-over}$, ln A_{app} and the orders in D_2 and CP could not be determined accurately

Table 4: The selectivities and activity for the rotation mechanism for the different catalysts, determined at 75°C, with P_{D2}=0.45 and P_{CP}=0.024 atm. For a description of the different intermediates, see Figure 1 and ref. [19]

Catalyst, Pt/	σ-η^1 (D1) (%, ± 1)	di-σ-η^2 (D2) (%, ± 1)	π-η^2 (D2-D10) selectivity (%, ± 1)	# rotations (±0.5)	desorption probability (%, ± 0.5)	di-σ-η^1 (D6-D10) (%, ± 1)
LTL [0.47, small]	33.6	5.7	60.8	9.4	11.9	9.9
LTL [0.47, big]	27.5	4.2	68.3	9.0	12.6	12.6
LTL [0.82]	30.7	4.8	64.5	8.6	13.2	12.5
ASA [2.5]	27.1	3.8	69.1	11.2	9.8	10.6
ASA [11.3]	28.1	3.7	68.3	9.5	9.3	9.5
SiO_2 [small]	21.5	3.0	75.4	13.1	8.3	15.4
SiO_2 [big]	17.8	2.3	79.9	12.6	8.6	25.5

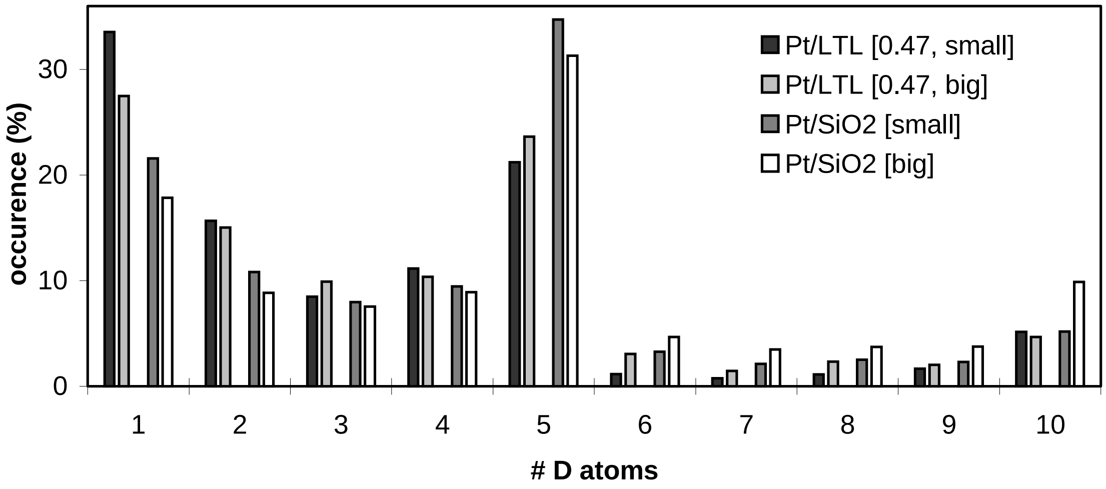

Figure 3: The influence of the particle size on the exchange pattern. Each first to bars represent the Pt/LTL catalysts, the last two bars the Pt/SiO_2 catalysts.

For both supports it was found that the average number of rotations for each π-η^2 intermediate, and, related to this, the desorption probability is unaffected by the particle size. Also for both supports, larger particles lead to an increased roll-over activity via the di-σ-η^1 intermediate, whereas the contribution of the di-σ-η^2 intermediate is unaffected within the limits of accuracy.

The effect of the particle size on the σ-η^1 intermediate (leading to D1) and the total contribution of the π-η^2 intermediate (D2-D10) is different for the two supports. With the LTL [0.47] support, larger particles do not affect these intermediates. With the SiO_2 support, however, larger particles lead to a decrease of the σ-η^1 intermediate accompanied by an increase of the π-η^2 intermediate.

Table 5: The selectivity as a function of partial pressures in CP.

Catalyst, Pt/	P_{CP}	P_{D2}	σ-η[1] (D1) (%, ± 1)	di-σ-η[2] (D2) (%, ± 1)	π-η[2] (D2-D10) Sel. (%, ± 1)	# rotations (±0.5)	desorption probability (%, ± 0.5)	di-σ-η[1] (D6-D10) (%, ± 1)
SiO_2 [big]	0.015	0.44	25.0	3.3	71.7	12.9	8.4	14.8
	0.021		23.0	3.7	73.3	12.5	8.7	18.4
	0.029		24.5	3.7	71.8	13.2	8.2	16.9
	0.036		24.8	3.6	71.6	12.7	8.5	17.2
SiO_2 [small]	0.016	0.46	18.8	2.6	78.7	13.6	7.9	17.3
	0.021		19.4	2.6	78.0	13.2	8.2	17.5
	0.027		20.4	2.9	76.7	13.2	8.2	17.2
	0.033		20.9	2.9	76.2	13.0	8.3	17.4
LTL [0.47, big]	0.017	0.46	28.4	4.2	67.4	9.7	11.5	12.4
	0.022		29.4	4.3	66.3	9.2	12.1	13.3
	0.027		31.9	4.7	63.4	9.6	11.7	11.8
	0.032		32.7	4.7	62.6	9.4	11.9	12.8
LTL [0.47, small]	0.014	0.45	21.8	3.2	75.1	10.2	10.9	18.5
	0.026		26.1	3.7	70.2	9.9	11.2	17.8
	0.037		28.5	4.2	67.2	9.4	11.8	16.8
	0.048		30.7	4.6	64.7	9.3	12.0	16.1

Table 6: The selectivity as a function of partial pressures of D_2.

Catalyst Pt/	P_{CP}	P_{D2}	σ-η[1] (D1) (%, ± 1)	di-σ-η[2] (D2) (%, ± 1)	π-η[2] (D2-D10) Sel. (%, ± 1)	# rotations (±0.5)	desorption probability (%, ± 0.5)	di-σ-η[1] (D6-D10) (%, ± 1)
SiO_2 [big]	0.023	0.34	24.3	3.4	72.4	12.5	8.7	18.1
		0.43	25.4	3.6	70.9	12.9	8.4	16.7
		0.52	26.6	3.7	69.7	14.2	7.6	14.2
		0.62	28.8	3.8	7.3	15.9	6.7	11.3
SiO_2 [small]	0.024	0.33	18.6	2.5	78.8	12.9	8.4	20.8
		0.42	19.8	2.8	77.4	13.4	8.1	17.7
		0.51	20.2	2.7	77.1	13.2	8.2	17.0
		0.55	21.0	2.9	76.0	13.3	8.1	16.6
LTL [0.47, big]	0.024	0.35	28.3	4.3	67.4	9.4	11.8	15.4
		0.41	30.3	4.6	65.2	9.4	11.9	12.8
		0.49	32.0	4.7	63.3	10.2	10.8	11.6
		0.55	32.7	5.3	62.0	10.3	10.7	9.9
LTL [0.47, small]	0.022	0.32	22.2	3.9	73.9	8.9	12.7	18.8
		0.43	22.4	3.9	73.7	9.5	11.7	17.9
		0.54	22.7	4.2	73.1	9.8	11.4	16.9
		0.65	23.1	3.8	73.0	10.2	10.9	15.7

Order in D_2 and CP for activity and selectivity as a function of particle size

In Table 3, the observed orders in CP and D_2 are given. For both the LTL [0.47] and SiO_2 support, an increase in particle size results in a significant increase of the positive order in CP and a more negative order in D_2.

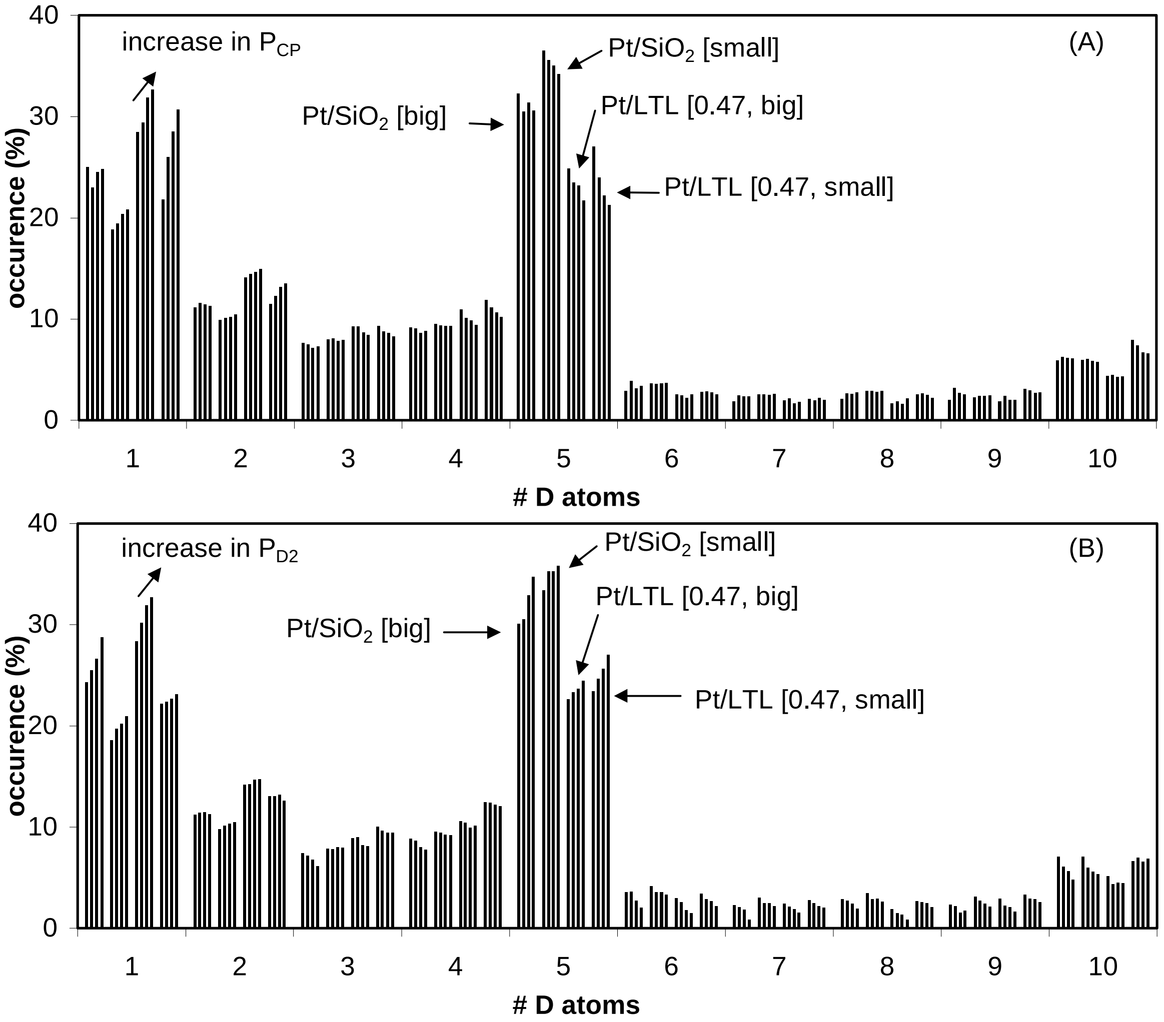

Figure 4: The influence of the partial pressure of (A) CP and (B) D_2 on the exchange pattern. Four catalysts are shown, Pt/SiO_2[big], Pt/SiO_2[small], Pt/LTL [0.47, big] and Pt/LTL [0.47, small]. From left to right for a single product and catalyst represents an increase in partial pressure.

The experimentally observed influence of the CP partial pressure on the selectivity as a function of particle size is shown in Figure 4A. The Pt/SiO_2 [big] catalyst showed no significant changes in the selectivity as a function of the CP partial pressure. For the other catalysts, Pt/SiO_2 [small] and both Pt/LTL [0.47, **] catalysts, an increase in the D1 and D2 product and a decrease in the D3-D5 products was observed for higher CP partial pressures. The observed selectivities were analyzed with the Monte-Carlo model. The results of this analysis are given in Table 5. Also from this analysis follows that for the Pt/SiO_2 [big]

catalyst the contributions of the various intermediates and the average number of rotations do not show a trend with the CP partial pressure. For the other catalysts, the Monte-Carlo analysis reveals that, in addition to the above mentioned changes, both the total contribution of the π-η^2 intermediate and the average number of rotations for this intermediate decrease with increasing CP partial pressure.

The influence of the D_2 partial pressure is similar for all catalysts as can be seen in Figure 4B. The Monte-Carlo analysis of this selectivity is given in Table 6. These analyses reveal that increasing the D_2 partial pressure resulted in an increased contribution of the σ-η^1 intermediate, whereas the amount of the di-σ-η^2 intermediate was unaffected. The contribution of the π-η^2 and di-σ-η^1 intermediates was decreased with increasing D_2 partial pressure, but the average number of rotations of the π-η^2 intermediate was increased with higher D_2 partial pressures.

Support effects in H/D exchange

Activity as a function of support

In Table 3, the turn-over frequency (TOF, mol CP * mol Pt^{-1} * s^{-1}) and apparent activation energies (kJ/mol) for the conversion of CP and the roll-over mechanism are given. With the exception of the basic catalysts (Pt/LTL [K/Al > 1.0] and Pt/HT), the TOF at 75°C for the different catalysts are all of the same magnitude, approximately 5-10 mol CP * mol Pt^{-1} * s^{-1}. The basic catalysts show activities that are up to 10^4 times smaller. The low activity of the basic catalysts prevented the accurate determination of selectivities, activation energies and orders in D_2 and CP for these catalysts.

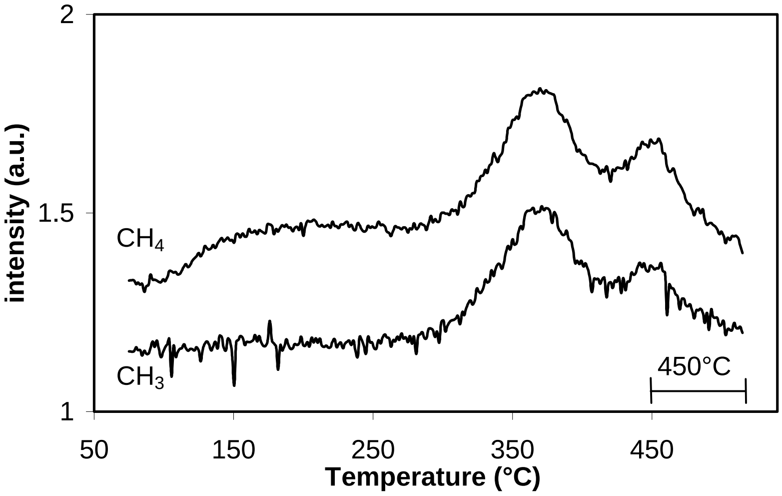

Figure 5: CH_4 and CH_3 are observed during heating the used, basic Pt/HT catalyst to 450°C in (ramp 5°C/min) in H_2, indicating the desorption of CH_4. The same desorption profile was observed for the other basic catalysts.

The basic catalysts do not only show a relatively low activity, but in addition they initially produce a large amount of HD (g) when CP is added to the gas mixture. When this used catalyst is heated to higher temperature (~450°C) in H_2, CH_4 and CH_3 is observed (Figure 5). This indicates the desorption of CH_4. These observations are representative for all basic catalysts.

Selectivity as a function of support

The experimental selectivity patterns are shown in Figure 6, the results of the Monte-Carlo analyses are given in Table 4. Going from acidic to neutral supports, the contribution of the π-η^2 intermediate is increased. This is accompanied by a decrease in the production of the D1 product via the σ-η^1 intermediate and by a decrease in the amount of D2 product formed via the di-σ-η^2 intermediate. Within the zeolites, the total number of exchange steps each π-bonded intermediate undergoes is considerably less then on the mesoporous supports.

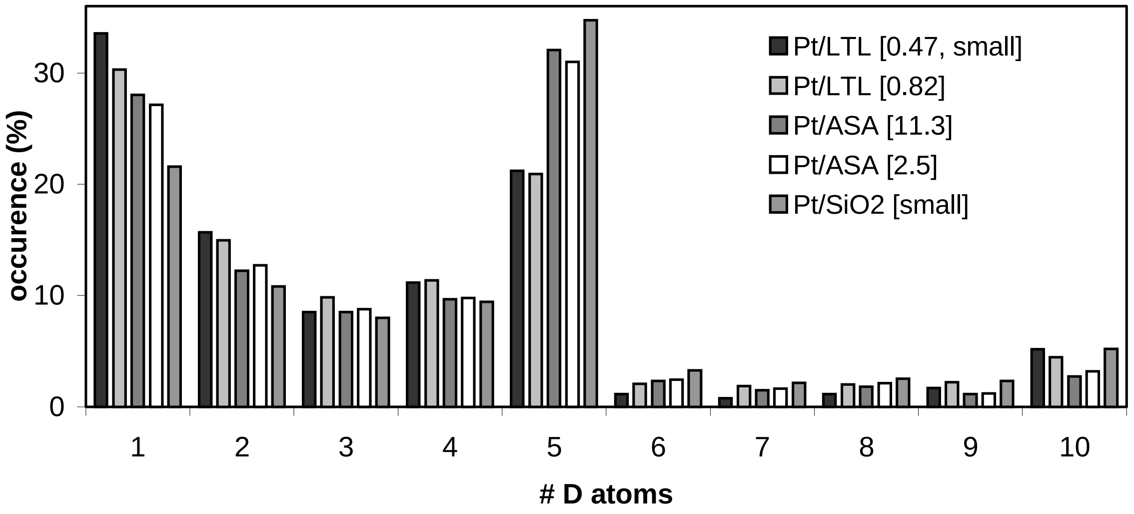

Figure 6: The influence of the support in the exchange pattern.

Orders in CP and D_2 as a function of support

The observed orders in D_2 and CP are given in Table 3. The order in D_2 increases from –0.82 for the H/D exchange over Pt/ASA [11.3] to –0.32 over Pt/LTL [0.47, small]. The latter catalyst contains the most acidic support. The increase in the order in D_2 is accompanied by a decrease in the order in CP from 0.69 (Pt/ASA [11.3]) to only 0.18 (Pt/LTL [0.47, small]). In Figure 4A, it is shown that increasing the CP partial pressure over catalyst Pt/LTL [0.47, small] results in large changes in the selectivity. In contrast, the catalyst with the highest order in CP (+0.87, catalyst Pt/SiO_2 [big]) shows no effect of the CP partial pressure on the selectivity.

Discussion

The acidity of the support materials

The two amorphous SiO_2-Al_2O_3 (ASA) supports were mesoporous supports with different Si/Al ratios, Si/Al=2.5 and 11.4 (see Table 1). The number of acid sites was determined with the combination of thermographic analysis and temperature programmed desorption of isopropylammine[29]. The number of Brønsted acid sites was 1.20 (ASA [2.5]) and 0.28 mmol/g (ASA [11.4]). Based upon the Si/Al ratio, the ASA [11.4] contains 1.275 mmol Al/g. This means that from all of the Al in the ASA [11.4], only about 20% results in acid sites. Only Al atoms incorporated into the tetrahedral SiO_2 framework will result in acid sites, the other 80% of the Al in the ASA is most likely contained in isles of the octahedral Al_2O_3 framework. For the ASA [2.5] support, about 30% of the Al results in Brønsted acid sites. That means that the Si/Al ratio in the SiO_2 framework is considerably higher than the bulk values. With a high Si/Al ratio, two Al atoms are far apart and it is unlikely that they influence each other. The result is that the acid sites are locally (within the distance of a few atoms) similar for both ASA supports, and the main difference between those two ASA support materials is the number of acid sites, not the intrinsic acidity of the site.

The LTL zeolites have a Si/Al ratio of 3.0[27]. Based upon the crystallographic formula of LTL ($[K_9(H_2O)_{21}][Al_9Si_{27}O_{72}]$), the number of Brønsted acid sites in the LTL with a K/Al = 0.47 is 1.76 mmol/g. In the case of the LTL [0.82], this is 0.57 mmol/g. The LTL zeolites with K/Al>1 have no Brønsted acid sites, and after calcination at elevated temperatures, the excess K is probably present as KOH or K_2O. Increased amounts of K results in a more basic support, with an increased electron-richness on the support oxygen atoms[30-32].

The number of Brønsted acidic sites is similar for the ASA and LTL [K/Al < 1.0] supports. However, the Pt particles are influenced rather by the electron-richness of the support oxygen than by the number of Brønsted acid sites[12], as has been shown earlier[9,10]. In the covalent zeolite framework, the electron richness on the oxygen atom is much lower than on a support like ASA[31,33,34]. In that sense, a zeolite is much more acidic.

One can ask if the number of acid sites is large enough to have an effect on the supported Pt particles. A 1 wt.% Pt catalyst contains 0.051 mmol Pt per gram. By using an aqueous solution of pH≈7 when the $Pt^{2+}(NH_3)_4$ complex is brought on the support (both for ion exchange and impregnation), the acid sites are deprotonated and the Pt^{2+}-complex is directed towards the acid sites. The number of acid sites is sufficiently large to have all Pt around the acid sites.

SiO_2 is a neutral material, and has no acid sites. The SiO_2 used was highly amorphous and contains a high surface area.

A hydrotalcite is regarded as a very basic support. It consists of platelets in a brucite structure, with Mg^{2+} ions octahedrally coordinated by O atoms. Part of the Mg^{2+} ions are isomorphically exchanged for Al^{3+} ions, creating a positive charge on the framework. Between the platelets, this positive charge is compensated with CO_3^- or OH^- ions. The OH^- ions located at the edge

of the platelets are active in basic catalysis. Also Pt particles are located at the edges of the platelets, near the OH^- ions, and they experience the support material as basic.

When all the mentioned support materials are compared, and if the electronrichness of the support oxygen atoms is taken as a measure of acidity, then the acidity for the applied support materials increases in the order HT < LTL [1.53] < LTL [1.04] < SiO_2 < ASA [11.4] = ASA [2.5] < LTL [0.82] < LTL [0.47].

Final metal particle sizes

For the SiO_2 support material, two different particle sizes were obtained. All techniques used reveal a smaller final metal particle size for the ion-exchanged catalysts compared to the impregnated catalyst. This is probably caused by a better anchoring of the Pt^{2+} complex during ion exchange than during impregnation. HRTEM, H_2 chemisorption and EXAFS showed somewhat contradicting results for the ion exchanged catalyst (Table 2). The high H_{total}/Pt ratio of 1.26 is in contrast with the diameter (1.2 nm) as revealed by HRTEM and Pt-Pt coordination number of 6.9. The latter two are in perfect agreement; based upon spherical particles with a diameter of 1.2 nm an average coordination number of 7.0 would be expected (see *e.g.* ref [35]). The origin of the discrepancy with H_2 chemisorption is unclear.

The particle sizes for both Pt/SiO_2 catalysts are higher than for the other catalysts. The larger particle size for the Pt/SiO_2 catalysts illustrates that it is very difficult to achieve highly dispersed metal particles on an inert support material. When no interaction between the support and the metal particles is present, the support material loses its primary function: to keep the metal particles highly dispersed.

The Pt/LTL [*.**], Pt/LTL [0.47, small], Pt/ASA and Pt/HT catalysts all have highly dispersed Pt particles. Based on the H_{total}/Pt and N_{PtPt} results, the average particle size for all these catalysts was estimated < 1 nm. The particle size for the Pt/ASA catalyst as revealed with HRTEM (1.5 nm) seems in contradiction with the other techniques. However, it has to be noted that with HRTEM the lower detection limit for Pt/ASA is approximately 8-10 Å, and that on the HRTEM pictures taken only a small amount of particles was visible. In other words, with HRTEM the smallest particles, which make up the majority of all Pt in the Pt/ASA catalyst, are invisible. The relation between particle sizes as determined with HRTEM, H_2 chemisorption and EXAFS was extensively described by de Graaf *et al*[35].

Mass transport limitations

The absence of external diffusion limitations (diffusion from the bulk to the surface of the support crystallite) was established by varying the space velocity with a constant catalyst volume. A twofold increase in the space velocity did not affect the TOF. This shows that external diffusion limitations are absent[36].

Establishing the presence of internal diffusion limitations is less trivial. An easy check would be to decrease the crystallite size. If internal diffusion limitations are absent, this would not affect the activity. However, the internal diffusion is related to the pore-size. The catalyst particles of the catalyst with the smallest pores, the LTL zeolite, are constructed of several

crystallites. The pores between these crystallites are macropores, and will not limit the diffusion of reactants. Scanning electron microscopy revealed that the size of these crystallites is extremely small, only 0.4 μm. As grinding will not result in a smaller crystallite size, it is nearly impossible to decrease this crystallite size. Therefore, the effectiveness and Thiele modulus were determined. An effectiveness indicates close to 1 indicates that internal diffusion limitations are absent. The effectiveness η is related to the Thiele modulus ϕ by[37]:

$$\eta = \frac{\tanh \phi}{\phi} \tag{3}$$

The Thiele modulus ϕ is defined as:

$$\phi = \frac{1}{a'_v}\sqrt{\frac{k_{v,p}}{D_{eA}}} \tag{4}$$

with $k_{v,p}$: the rate constant per unit catalyst volume (v),
D_{eA} : the effective diffusion of reactant A, and
a'_v : the ratio between the external surface of the particle and its volume.

For spherical particles, a'_v is given by:

$$a'_v = \frac{6}{d_p} \tag{5}$$

with d_p : the particle diameter.

The effective diffusion D_e is expressed as:

$$D_e = \frac{\varepsilon_p D}{\tau_p} \tag{6}$$

with D : the diffusion constant,
ε_p : the volume fraction that the pores occupy and
τ_p : the tortuosity (correction for the fact that the pores are not necessarily straight in the direction of diffusion).

Typical values for ε_p are between 0.3 and 0.6, and for τ_p between 2 and 5. So, a reasonable assumption for the effective diffusion D_e is that it is $^1/_{10}$ of the diffusivity D. This diffusivity D can be calculated from the Knudsen (corresponding to collisions with the wall) and molecular diffusivity (intramolecular collisions). The molecular diffusivity was estimated at 10^{-5} m^2/s, which is reasonable for the diffusion in gases. The Knudsen diffusivity depends on the pore diameter. The exact formulas for the molecular and Knudsen diffusion are given by Moulijn *et al*[37]. For zeolites, the determination of the diffusivity is more complicated. The microporous nature of zeolites strongly influences the diffusivity. Therefore, the diffusion

coefficient for CP in LTL zeolite was estimated from values for comparable molecules and zeolites. For example, the diffusivity of cyclohexane in the 12-membered ring zeolite (like LTL) NaX is reported between 1 x 10^{-11} and 4 x 10^{-9} m^2/s [38]. Therefore, the diffusivity of CP in LTL is estimated at 1 x 10^{-10} m^2/s.

The difficulty in determining the Thiele modulus is that the intrinsic rate constant (without diffusion limitations) is required, while the Thiele modulus is used to determine if diffusion limitations are present in the first place. This problem can be avoided by using the iterative procedure described by van Donk *et al.*[39], where the observed rate constant can be used for determination of the Thiele modulus and effectiveness.

In Table 7 the effectiveness and corresponding Thiele modulus for the different support materials is given. The particle size for the ASA, SiO_2 and HT supports was taken equal to the sieve fraction. This is a worst-case scenario, since it is far more likely that the particles in the sieve fraction are constructed of several crystallites which contain the relevant pores and Pt particles. Between those crystallites, the pore radii will be very large compared to the pore radius in the support material. Even in this worst case scenario, the effectiveness is still high, close to unity, for all catalysts. This demonstrates that the observed reaction kinetics reflect the intrinsic catalyst properties, since internal diffusion limitations are absent.

Table 7: the effective diffusion D_e, Thiele modulus ϕ and effectiveness η as a function of support at 75°C. For the observed rate constant k_{obs} the most active catalyst for each support material was taken.

support	pore radius (nm)	D_e (m^2/s)	particle diameter (μm)	k_{obs} (s^{-1})	ϕ	η
LTL	-	1 x 10^{-10}	0.4	0.6 x 10^3	0.16	0.99
ASA	2.5	5.1 x 10^{-7}	100	0.7 x 10^3	0.64	0.88
SiO_2	12.5	21.2 x 10^{-7}	100	10 x 10^3	0.37	0.96
HT	9.0	16.2 x 10^{-7}	100	0.1	0.004	1.0

Particle size effects

Activity as a function of metal particle size

For larger supported metal particles, the apparent activation energy for the H/D exchange is significantly higher (Table 3). This is observed with both support materials (SiO_2 and LTL [0.47]). However, with both support materials, the TOF at 75°C is of the same magnitude, irrespective of particle size. At first sight, this seems contra-intuitive as the apparent activation energy is approximately 15-20% higher for the smaller particles. However, as can be seen in Table 3, this increase in activation energy was compensated for by an increase in the pre-exponential factor. This suggests that a compensation effect is present, as will be discussed later[23,24].

Selectivity as a function of metal particle size

In Figure 3 (experiments) and Table 4 (results of Monte-Carlo analysis) give the selectivities in the H/D exchange of CP with the same two support materials. On the SiO_2 support, the

presence of larger particles leads to slightly decreased amounts of the σ-η^1 intermediate, the di-σ-η^2 intermediate is unaffected, whereas the total contribution of the π-η^2 intermediate is slightly increased. In contrast to the latter, the average number of rotations of the π-η^2 intermediate is insensitive to the particle size of the catalyst. Apparently, the formation of the π-η^2 intermediate is structure sensitive, but once the π-η^2 is formed it can rotate freely. On the LTL [0.47] support, larger particles do not affect the σ-η^1, di-σ-η^2 and π-η^2 intermediates. The influence of the particle size on these intermediates is minimal for both supports.

The particle-size effect is for both supports the largest for the selectivity towards the roll-over mechanism (via the di-σ-η^1 intermediate, Figure 1D), which is strongly increased with the larger particles. Hence, also the roll-over mechanism is a clearly structure-sensitive reaction. It is facilitated by large particles, and probably an ensemble of catalytically active, empty sites is needed for the formation of the di-σ-η^1 intermediate.

If the Pt/SiO_2 [big] is compared with LTL [0.47, big], than the particles are the largest on the LTL [0.47] support, but the roll-over mechanism is much more important on the Pt/SiO_2 support. Probably, the freedom of the CP is limited within the constraints of the pores in the LTL zeolite and rolling-over is sterically hindered.

Orders in CP and D_2 as a function of metal particle size

The orders in CP and D_2 for H/D exchange over the Pt/LTL [0.47] and Pt/SiO_2 [**] catalysts is given in Table 3. For both supports, the order in D_2 decreased (it was more negative) and the order in CP increased when a catalyst with a larger particle size was used. When these observations are correlated to equation (2) for the reaction rate, the lower order in D_2 indicates that for larger particles the ratio K_2/K_1 is increased for larger particles. In other words, for larger particles the surface of the Pt particles is mainly covered with (atomic) D_2, whereas for smaller particles, the surface contains more adsorbed CP. Although the particles were largest in the case of the Pt/LTL [0.47, big] catalyst, the order in CP was the highest for the Pt/SiO_2 [big] catalyst. Clearly, the orders also depend on the support material.

In general, a high order in CP (*e.g.* +0.87, as was found in the case of the Pt/SiO_2 [big] catalyst), indicates that the surface contains on average a very low concentration of CP: by doubling the amount of CP molecules in the gasphase, the surface concentration is doubled. This can only occur if during the adsorption process the CP molecule does not encounter another CP molecule which is already adsorbed. The surface is virtually covered with atomic D (indicated by the order in D_2 of –0.82 for Pt/SiO_2 [big]), and the surface concentration of D is unaffected by the CP partial pressure. The low surface concentration of CP also explains the observation that the exchange pattern of CP is unaffected by P_{CP} for this Pt/SiO_2 [big] catalyst: the surface contains only a small amount of CP and adsorbed CP molecules do not influence each other due to mutual (lateral) interactions.

However, decreased orders in CP and increased (less negative) orders in D_2 are found for smaller particles (*e.g.* when Pt/SiO_2 [big] and Pt/SiO_2 [small] or both Pt/LTL [0.47] catalysts are compared). When these orders are translated to the rate-expression (equation 2), it

indicates that the ratio K_2/K_1 is decreased, and the surface contains more CP. A high surface coverage of CP can result in lateral interactions which influences the selectivity pattern. These lateral interactions can consist of long range electronic interactions or of steric interactions between two adjacent, adsorbed CP molecules. Therefore, it is to be expected that a relatively low order in CP is accompanied by an increased amount of lateral interactions by increasing the CP partial pressure, which inhibit mainly the structure sensitive reactions (roll-over via the di-σ-η^1 intermediate). This is indeed observed in Figure 4A and Table 5.

In summary, the metal particle size has a distinct influence on the H/D exchange of CP. Smaller particles lead to a higher apparent activation energy, which is compensated by the pre-exponential factor. In terms of selectivity, the formation of the π-η^2 intermediate and roll-over via a di-σ-η^1 intermediate is inhibited by smaller particles, but the particle size has no effect on the rotation mechanism of the π-η^2 intermediate. Larger particles also lead to higher positive order in CP and lower, negative orders in D_2, indicating that for larger particles the surface concentration is very low. This low surface concentration of CP is also apparent from the exchange pattern: when a low order in CP is observed, lateral interactions of CP are absent and the selectivity is independent of the CP partial pressure. The opposite is observed for smaller particles, where the order in CP is lower and P_{CP} influences the selectivity.

Support effects

Activity as a function of support

As is shown in Table 3, the TOF at 75°C is several orders of in magnitude lower for the basic Pt/LTL [1.53] and Pt/HT catalysts compared to the acidic and neutral catalysts. In addition, the basic catalysts showed a consumption of D_2 in the initial stages of the H/D exchange without a production of CP. Moreover, a desorption of CH_4 was observed when these basic catalysts were heated in H_2 to high temperatures (see for example Pt/HT in Figure 5). These observations suggest an immediate deactivation of the basic catalysts due to coking. This indicates that the CP molecule is strongly bonded on the Pt particles supported by a basic material, and it does not desorb anymore. The deactivation prohibits a reliable determination of the observed activation energy, the pre-exponential factor and the selectivity.

The activation energies for the remaining acidic and neutral catalysts show a continuous decline for the apparent activation energies in the order Pt/LTL [0.47, small] > Pt/LTL [0.47, big] > Pt/LTL [0.82] > Pt/ASA ≈ Pt/SiO_2 [small] ≈ Pt/SiO_2 [big]. The pre-exponential factor increases in the opposite direction. These observations indicate an apparent compensation effect, as will be discussed later.

Selectivity as a function of support

As is shown in Figure 6 (experiments) and Table 4 (Monte-Carlo analysis), a general trend is that Pt catalysts with supports of higher acidity lead to a higher contribution of the σ-η^1 (D1) and di-σ-η^2 (D2) intermediates. As the ASA and LTL supports have similar metal particle sizes, this cannot be explained by particle size effects. Apparently, acidic supports enhance

the ability of Pt to form σ-bonded species, whereas π bonded species are preferred for Pt on neutral, and probably also on basic support materials. The latter is not only apparent from the increased selectivity towards D2-D10, but also from an increased number of exchange steps (or rotations) the π-η^2 intermediate experiences. This increased number of exchange steps indicates both the π-η^2 and the allylic intermediate adsorb strongly on the surface of Pt particles that are supported on neutral supports, and remain longer on this surface.

Orders in CP and D_2 as a function of support

As is shown in Table 3, the order in CP decreases from +0.87 to +0.18 going from Pt particels with neutral to acidic supports. This is accompanied by an increase in the order in D_2 from –0.82 to –0.32. In general, a low, positive order in a reactant indicates that the surface concentration of the reactant on the catalytic surface is relatively high. The low order in CP, in combination with the decreased inhibition by D_2 for H/D exchange of CP over Pt with the most acidic support (catalyst Pt/LTL [0.47, small]) shows that –compared to a Pt catalyst with a neutral support– the surface contains a relatively high concentration of CP and low concentration of D.

The surface concentrations are related to the bond energy of D and CP on the Pt surface, and apparently the ratio $E_{CP\text{-}Pt}/E_{D\text{-}Pt}$ is higher for Pt on the acidic support materials than it is for the neutral supports. It was shown earlier[19] (see also Table 6) that the rotation of the π-η^2 intermediate is facilitated by an increased surface coverage of D. Also, in agreement with this, the catalysts (Pt/SiO_2 [**]) which have the lowest $E_{CP\text{-}Pt}/E_{D\text{-}Pt}$ ratio and thus the highest surface coverage of D also have the highest number of average rotations per π-η^2 intermediate (Table 4).

Compensation phenomena

When the Arrhenius parameters E_{app} and $ln\ A_{app}$ of a variety of catalysts obey the Constable-Cremer isokinetic relation[23,24,40]:

$$\ln A_{app} = mE_{app} + c \qquad (7)$$

then an increase in E_{app} is compensated by an increase in $ln\ A_{app}$. This is called the compensation effect. In Figure 7, a Constable plot for all catalysts is shown. The observation that all Arrhenius parameters for all catalysts obey the Constable-Cremer relation, indeed suggests that compensation behavior is present. According to the standards set by Bond *et al.*[23] the range in E_{app} should ideally be at least 50% of the smallest E_{app} measure, which is close to our 35%.

If E_{app} and $ln\ A_{app}$ indeed obey to the Constable-Cremer relation, then there must be an isokinetic relation between all catalysts. At the isokinetic temperature, the activities for all catalysts are the same. However, it is very difficult to establish this isokinetic relation with statistical certainty. Therefore, a second, more reliable way to establish the presence of an isokinetic behavior is to plot all activity plots in one graph, and to check if there is an isokinetic temperature T_i where all activity plots intersect. Since the parameters in such a plot

(1/T and ln TOF) are measured independently, it is statistically more reliable than a Constable plot. Such a plot is constructed in Figure 8. All Arrhenius plots for the different catalysts appear to intersect, approximately around T_i = 90-100°C.

Both the Constable plot (Figure 7) and the intersecting Arrhenius plots (Figure 8) strongly suggests that indeed an isokinetic relation (IKR) between A_{app} and E_{app} exists. The errors in the determination of these Arrhenius plots and its derived variables prevent the establishment of this IKR with absolute certainty. According to Bond *et al.*[23], an IKR is most likely caused by changes in the surface coverage of the reactants, and the true activation energy is unaffected. The chemisorption of reactants (and inhibitors) can be incorporated in the reaction equation as follows:

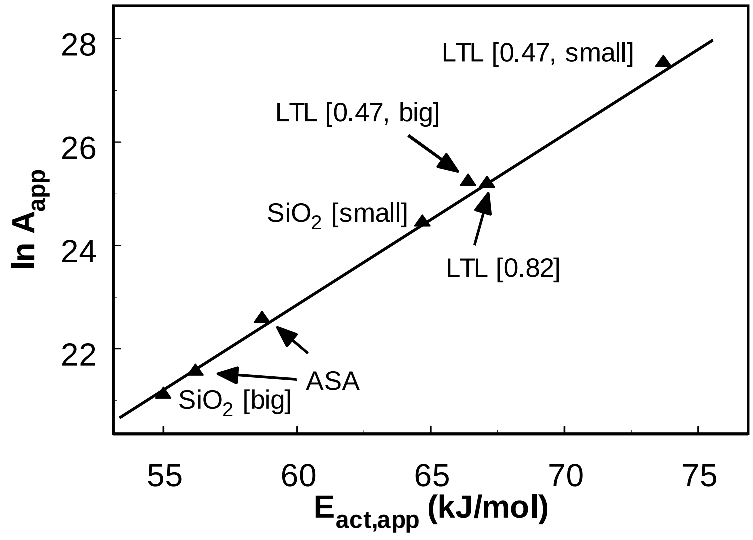

Figure 7: A constable plot for the HD exchange. The estimated errors are approximately ± 2 kJ/mol for $E_{act,app}$ and ±0.5 for ln A_{app}.

For the simplified case of a reaction which is first order in CP and inhibited by D_2 the reaction rate can be modeled by:

$$R = k_{int} * [D]^{\alpha} * [CP]^{\beta} = k_{int} * \left(K_{ads,D} P_{D2}\right)^{\alpha} * \left(K_{ads,CP} P_{CP}\right)^{\beta} \qquad (8)$$

with R : the reaction rate per Pt surface site (TOF),
k_{int} : the intrinsic rate constant of the reaction over the catalyst,
α : the observed order in deuterium, which was negative in all cases, and
β : the observed order in CP, which is positive.

An equilibrium constant K (or rate constant k) is described with the following expression:

$$-RT \ln K = \Delta H - T\Delta S = \Delta G \quad \rightarrow \quad K = e^{\frac{\Delta S}{R}} * e^{\frac{-\Delta H}{RT}} \qquad (9)$$

When (8) is substituted in (9), this leads to

$$R = P_{D2}^{\alpha} P_{CP}^{\beta}\, e^{\frac{\Delta S_{\text{int}}^{\mp} + \alpha \Delta S_{ads,D} + \beta \Delta S_{ads,CP}}{R}} * e^{\frac{-\left(\Delta H_{\text{int}}^{\mp} + \alpha \Delta H_{ads,D} + \beta \Delta H_{ads,CP}\right)}{RT}} = A_{app} e^{\frac{-\Delta E_{app}}{RT}} \qquad (10)$$

with $E_{app} = \Delta H^{\pm}_{intrinsic} + \alpha \Delta H_{ads,D} + \beta\, \Delta H_{ads,CP}$ and

$$A_{app} = P_{D2}^{\alpha} P_{CP}^{\beta}\, e^{\frac{\Delta S_{\text{int}}^{\mp} + \alpha \Delta S_{ads,D} + \beta \Delta S_{ads,CP}}{R}}$$

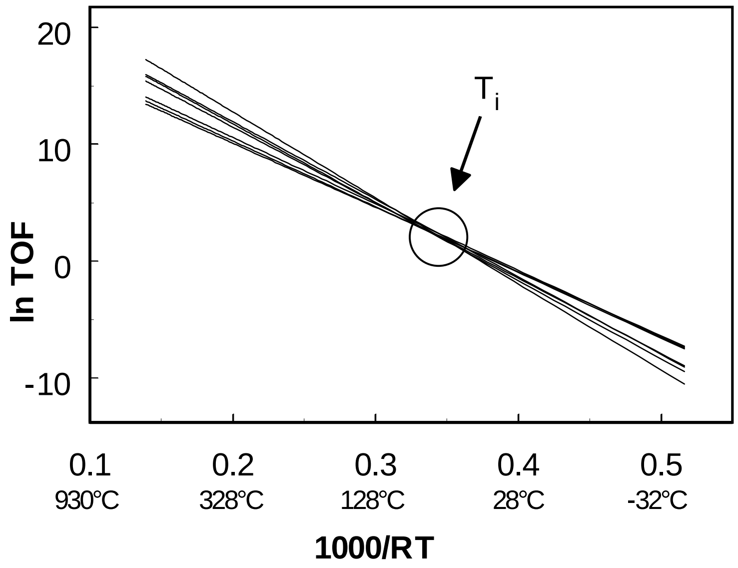

Figure 8: A series of extrapolated Arrhenius plots for the HD exchange of cyclopentane, intersecting at T_i: the isokinetic temperature.

Thus, changes in the pre-exponential factor A_{app} represent mainly changes in the adsorption entropy and in the order of the reactants. Molecules that chemisorb from the gasphase to the surface have a negative enthalpy (ΔH < 0), but also lose entropy (ΔS <0). Moreover, for a stronger adsorbed species, the adsorption enthalpy is even lower ($\Delta H_{strong} < \Delta H_{weak}$), but the molecules loses even more entropy ($\Delta S_{strong} < \Delta S_{weak}$). This would lead to a lower E_{app}, but also *ln* A_{app} will decrease. If ΔH and ΔS would vary independently from each other, this would not lead to obedience of the linearity in the Constable-Cremer relation (equation 7), but for many similar processes (like in this case chemisorption on a metal surface), ΔS and ΔH are correlated. The phenomenon that ΔS and ΔH are correlated is known as 'Linear Free-Energy Relations', LFER[41], and then *ln* A_{app} and E_{app} will obey the Constable-Cremer relation.

Changes in E_{app} reflect both changes in the adsorption energy and in the reaction orders. The adsorption energy has a large influence on the reaction order; if the adsorption energy of a reactant is high, the surface coverage will be high and nearly independent of temperature or pressure, which leads to a low order of this reactant.

Thus, different chemisorption strengths of the reactants on the catalyst's surface are most likely the origin of the observed isokinetic relationship. In the previous paper[19], it was shown

that the activity and selectivity are independent of each other: the selectivity is only determined *after* the rate determining step. The rate-determining step is the dissociation of molecularly adsorbed CP into H(*) and C_5H_9(*), leading to the σ-η^1 intermediate, and following steps include the formation of the other possible intermediates like π-η^2 (see the energy scheme in Figure 9). This means that the compensation effect is only correlated to the adsorption strength of molecularly adsorbed intermediate and the σ-η^1 intermediate, and not necessarily to the adsorption energies of *all* adsorbed intermediates. However, in the case of catalyst with similar particle sizes in combination with different supports, it is likely that if one adsorption mode is influenced by the acidity of the support, that also the other adsorption modes are influenced in a similar manner by the support and that some trend between selectivity and E_{app} should exist. If the particle sizes vary, other effects like the number of available ensembles of sites may start to play a role in the selectivity.

In Figure 10, the relation between the contribution of the different exchange mechanisms and the apparent activation energy for H/D exchange of CP over four catalysts with various acidities but similar particle sizes is shown. By choosing these four catalysts, particle size effects are eliminated. There is a clear correlation visible: a higher E_{app} is accompanied by a higher contribution of the exchange via the σ-η^1 and the di-σ-η^2 intermediate, and a lower contribution of the π-η^2 intermediate. This clearly illustrates that the metal-support interaction has a large influence on the Pt particles.

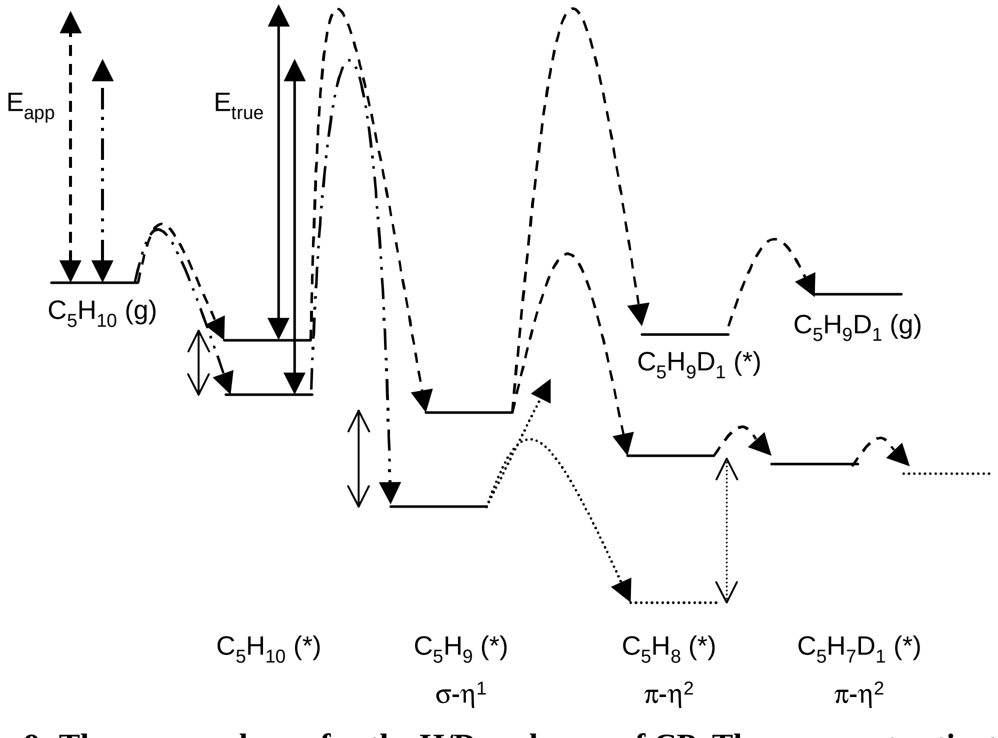

Figure 9: The energyscheme for the H/D exchange of CP. The apparent activation energy E_{app} is influenced by the bonding properties of CP. If CP is bonded strongly on the Pt surface (represented by the dashed-dotted lines), the E_{app} is small even though the true activation energy is unaffected.

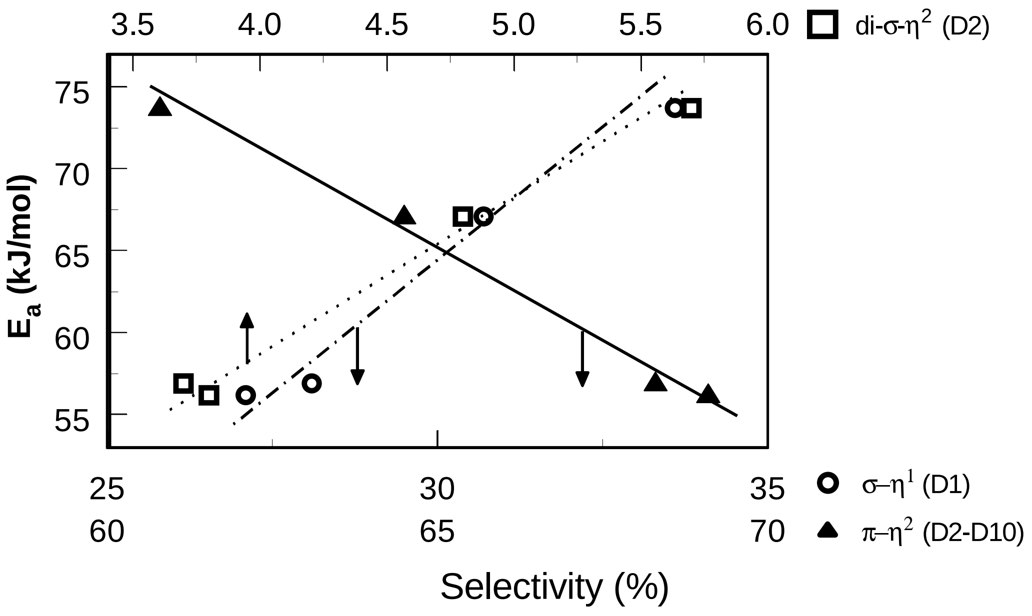

Figure 10: The relation between E_{app} and the exchange via the σ-η^1 intermediate (leading to D1, O symbol and dashed-dotted line), the di-σ-η^2 intermediate (D2, □ and dotted line) and the π-η^2 intermediate (D2-D10, ▲, solid line)

The influence of the metal-support interaction on the π-η^2 intermediate

The question that now rises is why the formation π-η^2 intermediate is preferred on Pt supported on neutral carriers and probably even more with basic supports. The chemisorption of a π containing molecule on a metal has been described extensively[42-44] by the Dewar-Chatt-Duncanson model[44-46]. This model was originally proposed for organometallic complexes, and involves electron backdonation from the metal to the π* orbitals of the adsorbate. This antibonding π* orbital lies relatively high in energy (otherwise it would not be antibonding), and therefore significant backdonation from the Pt 5d band can only occur if the valence band lies at a relatively high energy. A second requirement for 5d-π* backdonation is that the π*-orbital has the same symmetry as the interacting Pt valence orbital. This second requirement is probably easily met on small metal particles, which have irregular surface areas with all sorts of valence orbitals sticking out of the surface.

Thus, the enhanced formation of the π-η^2 intermediate going from acidic to basic support materials indicates more 5d-π* backdonation and therefore it indicates a shift of the Pt valence band towards higher energies. This shift of the valence band for Pt on basic support materials has been experimentally observed with atomic XAFS[9]. It has been attributed to a change in the Madelung potential of the support, charge transfer and rearrangement, and several other effects[2,12,16,47-49]. Density Functional Theory confirms that the Madelung Potential of the support can be responsible for such shifts of the Pt valence band[47]. The adsorption of the π-η^2 intermediate and the effect of the support material-induced shifts in the Pt valence band is

schematically illustrated in Figure 11, where an energyscheme of the density of states (DOS) of a Pt_4 cluster on a basic and acidic support and of a C_5H_8 molecule is shown. The depicted DOS of the basic and acidic support are both from a clean, tetrahedral Pt_4 cluster, and its DOS was shifted in energy according to earlier observed and calculated support induced shifts in the DOS[12,47]. These DOS were calculated with the density functional theory code ADF[50]. Details of these calculations are given elsewhere[47]. The calculated C_5H_8 molecule is cyclopentene, and therefore represents the adsorbed π-η^2 intermediate. Only the bonding between the π^* orbital and the Pt valence band is shown. If the support is basic, the valence band is shifted to higher energies and the overlap between π^* and the valence band is high. As a result, bonding combination is filled and the bond energy is high. Moreover, it is (almost) equally shared between the CP molecule and the Pt cluster, and the π^* is filled with a considerable amount of electron density, which weakens the CP π bond.

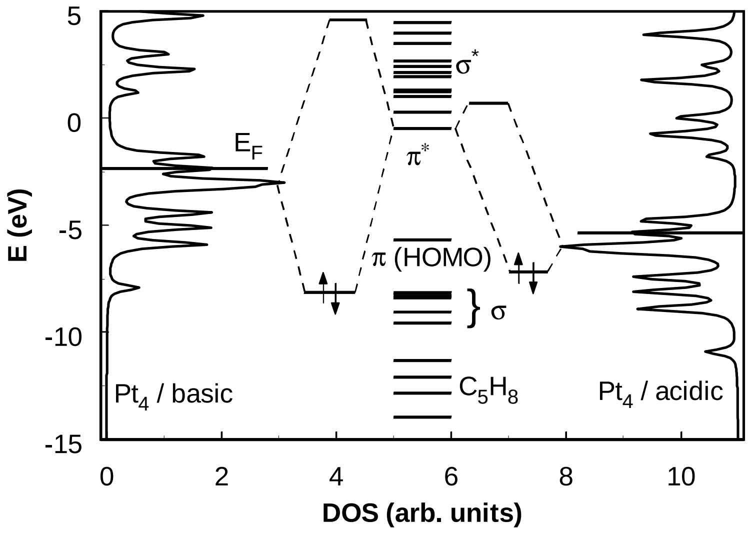

Figure 11: The valence density of states of a Pt_4 cluster and of cyclopentene. The Pt valence band is shifted to higher energies on a basic support (left side of the picture), and to lower energies on an acidic support (right side). On the acidic support, overlap between π^* (C_5H_8) and the Pt 5d band is minimal, and the bonding combination is located at the Pt cluster. For the basic support, the overlap is large and the bonding combination is equally shared between CP and Pt.

When placed on an acidic support, the valence band in the Pt particles is shifted to lower energy, resulting in less overlap between π^* and the Pt valence band and leading to a lower bond energy for the π-η^2 intermediate and less weakening of the π bond. Therefore, for Pt with basic versus acidic supports, the π-η^2 intermediate is favored basic support materials.

If the backdonation is very strong, as is the case for Pt with a very basic support, the π bond can dissociate and the CP molecule is dissociated into a highly unsaturated C5 molecule, bonded with multiple carbon atoms on the metal surface. This is the first step in coking of the

catalyst, and it gives a possible explanation for the coking that was observed for the Pt/HT and Pt/LTL [1.04 and 1.53] catalysts.Therefore, it is concluded that the observed compensation effect and IKR for various supported Pt catalysts is caused by changes in the chemisorption strengths of reactants. These changes cause a variation in activity and a variation in the selectivity in catalytic reactions.

Chemisorption of reactants on the Pt surface involves the donation and sharing of electrons between the Pt particles and the reactants. Therefore, changes in the chemisorption must be caused by changes in the electronic properties of either the Pt particles or the reactants. Since the reactants are always the same molecules, the changes in the chemisorption strengths must be caused by changes in the electronic properties of the supported Pt particles. This was illustrated above for the case of the bonding of the π-η^2 intermediate.

Conclusions

The influence of the support on the catalytic properties of supported Pt particles was investigated via a test reaction: the H/D exchange of cyclopentane. The acidity of the support largely influences the activity and selectivity of supported Pt particles in the H/D exchange of cyclopentane. The activities for the different catalysts show an iso-kinetic relation (IKR): the Arrhenius parameters A_{app} and E_{app} show a compensation, and at the isokinetic temperature of ~100°C all catalysts show similar activities. This IKR is caused by variations in the adsorption strengths of the reactants CP and D_2 on the Pt surface. The resulting ratios of the surface coverages CP(*)/D(*) are high for acidic supports and low for neutral and basic supports, as is apparent from the observed reaction orders. The variations in the chemisorption strengths of CP on the Pt is also apparent from changes in selectivity. When particle size effects are eliminated, the apparent activation energy E_{app} directly correlates with the selectivity. On Pt with acidic supports, the formation of the σ-bonded η^1-cyclopentyl intermediate is favored, whereas with neutral and basic supports the formation of a π-bonded η^2-cyclopentene intermediate is preferred. This intermediate is adsorbed via π backbonding, and this backbonding is very strong with basic supports. The result of this strong backbonding of Pt particles supported on basic supports is that the CP ring is broken, and the catalyst deactivates rapidly via coking. This strong backbonding is caused by a shift of the Pt valence band to higher energies on basic support materials.

Reference list

1. G. Blyholder, *J. Mol. Catal. A*, **119** (1997), 11-17.
2. A. Yu. Stakheev and L. M. Kustov, *Appl. Catal. A: General*, **188** (1999), 3-35.
3. R. A. Dalla Betta and M. Boudart, *Proc 5th Int Con Cat* (1973), 1329-1341.
4. T. M. Tri, J. Massardier, P. Gallezot and B. Imelik, *Stud. Surf. Sci. Catal.*, **11** (1982), 141-148.
5. C. Besoukhanova, J. Guidot and D. Barthomeuf, *J. Chem. Soc. Faraday Trans. I*, **77** (1981), 1595-1604.
6. A. de Mallmann and D. Barthomeuf, *Stud. Surf. Sci. Catal.*, **46** (1989), 429.
7. A. de Mallmann and D. Barthomeuf, *J. Chim. Phys.*, **87** (1990), 535-538.

8. Z. Zhang, T. T. Wong and W. M. H. Sachtler, *J. Catal.*, **128** (1991), 13-22.
9. B. L. Mojet, J. T. Miller, D. E. Ramaker and D. C. Koningsberger, *J. Catal.*, **186** (1999), 373-386.
10. D. C. Koningsberger, J. de Graaf, B. L. Mojet, D. E. Ramaker and J. T. Miller, *Appl. Catal. A: General,* **191** (2000), 205-220.
11. D. C. Koningsberger, M. K. Oudenhuijzen, D. E. Ramaker and J. T. Miller, *Stud. Surf. Sci. Catal.,* **130A** (2000), 317-322.
12. D. E. Ramaker, J. de Graaf, J. A. R. Van Veen and D. C. Koningsberger, *J. Catal.,* **203** (2001), 7-17.
13. A. Khodakov, N. Barbouth, Y. Berthier, J. Oudar and P. Schulz, *J. Chem. Soc. Faraday Trans.*, **91** (1995), 569-573.
14. V. Eskinazi and R. L. Burwell, *J. Catal.*, **79** (1983), 118-131.
15. B. F. Hegarty and J. J. Rooney, *J. Chem. Soc. Faraday Trans. I*, **85** (1989), 1861-1871.
16. T. Baird, E. J. Kelly, W. R. Patterson and J. J. Rooney, *J. Chem. Soc. Chem. Comm.* (1992), 1431-1433.
17. S. M. Augustine and W. M. H. Sachtler, *J. Catal.,* **106** (1987), 417-427.
18. G. Fitzsimons, C. Hardacre, W. R. Patterson, J. J. Rooney, J. K. A. Clarke, M. R. Smith and R. M. Ormerod, *Catal. Lett.,* **45** (1997), 187-191.
19. Chapter 3 of this thesis.
20. R. Pitchai, S. S. Wong, N. Takahashi, J. B. Butt, R. L. Burwell and J. B. Cohen, *J. Catal.,* **94** (1985), 478-490.
21. V. Ponec and G. C. Bond: *Catalysis by Metals and Alloys*, Studies in Surface Science and Catalysis, Elsevier Science, 1995, Vol. 95.
22. C. Kemball, *Adv. Catal.,* **11** (1959), 223-262.
23. G. C. Bond, M. A. Keane, H. Kral and J. A. Lercher, *Catal. Rev. - Sci. Eng.,* **42** (2000), 323-383.
24. A. K. Galwey, *Thermochim. Acta,* **294** (1997), 205-219.
25. M. K. Oudenhuijzen, J. H. Bitter and D. C. Koningsberger, *J. Phys. Chem. B,* **105** (2001), 4616-4622.
26. M. K. Oudenhuijzen, P. J. Kooyman, B. Tappel, J. A. van Bokhoven and D. C. Koningsberger, *J. Catal.,* **205** (2002), 135-146.
27. Baerlocher, Ch.; Meier, W. M.; Olson, D. H. *Atlas of Zeolite Framework Types*; Elsevier: Amsterdam, 2001.
28. J. C. A. A. Roelofs, A. J. van Dillen and K. P. de Jong, *Catal. Today,* **60** (2000), 297-303.
29. J. G. Tittensor, R. J. Gorte and D. M. Chapman, *J. Catal.,* **138** (1992), 714-720.
30. N. O. Gonzales, A. K. Chakraborty and A. T. Bell, *Catal. Lett.,* **50** (1998), 135-139.
31. G. N. Vayssilov and N. Rösch, *J. Catal.,* **186** (1999), 423-432.
32. R. J. Gorte, *Catal. Lett.,* **62** (1999), 1-13.
33. R. A. van Santen and G. J. Kramer, *Chem. Rev.,* **95** (1995), 637-660.
34. G. O. A. Janssens, B. G. Baekelandt, H. Toufar, W. J. Mortier and R. A. Schoonheydt, *J. Phys. Chem.,* **99** (1995), 3251-3258.
35. J. de Graaf, A. J. van Dillen, K. P. de Jong and D. C. Koningsberger, *J. Catal.,* **203** (2001), 307-321.
36. F. M. Dautzenberg in: *Characterization and Catalyst Development: An Interactive Approach*; S. A. Bradley, M. J. Gattuso and R. J. Bertolacini, eds., American Chemical Society: Los Angeles,

1989; Vol. 411, pp 99-119.
37. R. A. van Santen, P. W. N. M. van Leeuwen, J. A. Moulijn and B. A. Averill: *Catalysis: an Integrated Approach*, 2nd ed., Studies in Surface Science and Catalysis, Elsevier Science, Amsterdam, 1999, Vol. 123.
38. J. Kärger and D. M. Ruthven: *Diffusion in Zeolites*, 1st ed., John Wiley & Sons, New York, 1992.
39. S. van Donk, A. Broersma, O. L. J. Gijzeman, J. A. van Bokhoven and K. P. de Jong, *J. Catal.* (2001).
40. F. H. Constable, *Proc. Roy. Soc. (London) A*, **108** (1925), 355.
41. W. Linert and R. F. Jameson, *Chem. Soc. Rev.*, **26** (1989), 4977.
42. A. Föhlisch, M. Nyberg, J. Hasselström, O. Karis, Petterson. L. G. M. and A. Nilsson, *Phys. Rev. Letters*, **85** (2000), 3309-3312.
43. C. G. P. M. Bernardo and J. A. N. F. Gomes, *Theochem,* **542** (2001), 263-271.
44. G. Frenking, *J. Organomet. Chem.,* **635** (2001), 9-23.
45. M. J. S. Dewar, *Bull. Soc. Chim. Fr.*, **18** (1951), C79.
46. D. M. P. Mingos, *J. Organomet. Chem.,* **635** (2001), 1-8.
47. Chapter 8 of this thesis.
48. M. T. M. Koper, R. A. van Santen, S. A. Wasileski and M. J. Weaver, *J. Chem. Phys.*, **113** (2000), 4392-4407.
49. N. López, *J. Chem. Phys.*, **114** (2001), 2355-2361.
50. Amsterdam Density Functional Package ADF 2000.02, Department of Theoretical Chemistry, Vrije Universiteit, Amsterdam. http://www.scm.com.

5

The Nature of the Pt-H Bonding for Strongly and Weakly Bonded Hydrogen on Platinum

A XAFS spectroscopy study of the Pt-H antibonding state shaperesonance and Pt-H EXAFS

Abstract

A long-standing problem in the research of hydrogen chemisorption on supported Pt catalysts is the unclarity about the difference in nature of the Pt-H bonding for weakly and strongly bonded hydrogen. Based on Pt-Pt EXAFS and a newly developed XANES analysis of the Pt L_2 and L_3 edges it will be shown that both types of hydrogen are truly chemisorbed species. The EXAFS analysis shows a similar contraction of the Pt-Pt bond irrespective of the removal of weakly or strongly bound hydrogen indicating a similar nature for both interactions. Moreover, the analysis of the L_2 and L_3 X-ray absorption edges shows unambiguously the presence of a Pt-H anti-bonding state for both the weakly and strongly bonded hydrogen. This is a clear indication for chemisorption of hydrogen for both types of hydrogen. The Pt-H EXAFS shows a smaller Pt-H bond-length in the case of strongly adsorbed, which is in correlation with the expected strength of the Pt-H bond.

Introduction

The chemisorption of hydrogen has been a well-known standard tool to study the metal surface area, average particle size and dispersion of the metal (*e.g.* Pt) in noble metal catalysts[1]. Generally two types of hydrogen are observed, weakly and strongly bonded to the metal[2-10]. Weakly (or reversibly) adsorbed hydrogen is defined as hydrogen which can easily be desorbed, for example by evacuating for 10 minutes at low temperatures[11]. Strongly (or irreversibly) adsorbed hydrogen is defined as hydrogen that remains on the metal surface after evacuation at room temperature. However, the term irreversible as used in literature is confusing. Namely, this so-called irreversible adsorbed hydrogen can be removed by evacuation at higher temperatures (>150°C) or prolonged evacuation at low temperature[12]. Therefore, only the terms weakly and strongly adsorbed hydrogen will be further used in this work.

Three types of adsorption can be considered: (i) molecularly chemisorbed, (ii) atomically chemisorbed and (iii) molecularly physisorbed. In the case hydrogen is chemisorbed on platinum, a real bond between Pt and atomic H is formed, *i.e.* two electrons are located in a bonding orbital between Pt and H or H_2. In the case hydrogen is molecularly physisorbed, the interaction between Pt and molecular H_2 is electrostatic, *i.e.* no electrons are shared in a Pt-H bond and no dissociation takes place.

As shown in literature[13,14], molecularly chemisorbed H_2 is very unlikely. When a H_2 molecule chemisorbs on a Pt surface, the antibonding σ^* orbital of H_2 is completely filled by electrons from platinum. In addition to this, it has been shown theoretically[13,15,16] and experimentally[17] that dissociative chemisorption of H_2 is non-activated, *i.e.* it is not kinetically hindered. Consequently, chemisorbed H_2 will immediately dissociate on the platinum surface and thus chemisorption of H_2 on Pt can only be atomic. Therefore, in this paper only atomic (dissociative) chemisorption and molecular physisorption are considered.

It is generally accepted in the literature that the strongly adsorbed H_2 found in a H_2 adsorption isotherm is dissociatively chemisorbed. However, the nature of the weakly adsorbed H_2 is still unclear: physisorbed as molecular H_2 or chemisorbed as atomic H. Generally, this weakly adsorbed H_2 is considered to be chemisorbed. The main argument to call this species chemisorbed rather than physisorbed is the higher energy of adsorption compared to condensation (~20 and 8 kJ/mole respectively)[1]. However, no experimental evidence is given yet to decide upon the nature of the weakly adsorbed H[8].

In this paper the nature of the Pt-H bond for both the weakly and the strongly adsorbed H is further investigated. A new analysis method[18,19] of the L_2 and L_3 absorption edges of small supported platinum particles both with and without chemisorbed H_2 is used[20]. This analysis method allows the isolation of the Pt-H anti-bonding state shape resonance present above the Fermi level at the L_3 edge. This anti-bonding state originates from the chemisorption of H on the surface atoms of the Pt particles.

This paper will show that an Pt-H anti-bonding state shape resonance is present for both strongly and weakly adsorbed hydrogen. Both types of hydrogen are thus atomically

chemisorbed. Moreover, the difference in energy for the Pt-H anti-bonding state with respect to the Fermi-level of both types of hydrogen suggests a weaker Pt-H bond for the weakly adsorbed hydrogen. It was also possible to isolate the Pt-H EXAFS. The differences in Pt-H EXAFS suggest a longer Pt-H bond for the weaker chemisorbed hydrogen, which correlates with the expected bond strengths.

Experimental

Catalyst preparation

The studied Pt/Al_2O_3 catalyst was prepared by incipient wetness impregnation with an aqueous solution of $Pt(NH_3)_4(NO_3)_2$ on an Al_2O_3 support (pseudobohemite, Criterion). The metal loading was 2% by weight. The sample was taken from a series of catalysts prepared to study the influence of the alkalinity on the support on the Pt particles. Therefore, the Al_2O_3 was made alkaline by impregnation of the Al_2O_3 with KOH solution to yield a support with 0.25 wt.% K.

The impregnated catalyst was calcined at 100°C (1°C/min, 60 min) and subsequently reduced at 350°C(5°C/min, 60 min).

Hydrogen chemisorption

Hydrogen chemisorption measurements were performed in a conventional static volume apparatus (Micrometrics ASAP 2010). The samples were subsequently dried in He at 150°C for 1 hour (heating rate 10°C/min), reduced in pure H_2 at 400°C for 1 hour (5°C/min) and evacuated at 200°C until a equilibrium pressure was reached (cooling rate 5°C/min). H_2 adsorption isotherms were taken at 35°C. The absolute amount of adsorbed H_2 is determined by adding a fixed volume of H_2 to a known volume containing a known amount of catalyst. From the decrease in pressure the amount of adsorbed H_2 can be calculated. After the first H_2 adsorption isotherm was taken, the sample was evacuated for 10 min. at 35°C (to remove weakly adsorbed H_2) and a second H_2 adsorption isotherm was taken. The second adsorption isotherm is determined by the weakly adsorbed H_2, whereas the difference between both isotherms gives the amount of strongly adsorbed H_2. The H_2 uptake per Pt atom was calculated using the method described by Wilson and Hall[21]. It was confirmed that the bare support did not show any H_2 uptake.

XAFS data collection

XAFS measurements were performed at the HASYLAB synchrotron (beamline X1.1) in Hamburg, Germany, and at the European Synchrotron Radiation Facility (beamline BM 29) in Grenoble, France. The measurements were done in transmission mode using ion chambers filled with a mixture of Ar and N_2 to have a μx of 20% in the first and a μx of 80% in the second ion chamber. The monochromator was detuned to 50% of maximum intensity to avoid higher harmonics present in the X-ray beam.

The catalyst sample (approximately 130 mg, resulting in a total absorption of 2.5 after the Pt L_2 edge) was pressed in a self-supporting wafer and mounted in a stainless steel *in situ* cell equipped with Be-windows[22]. Both the Pt L_2 and L_3 edge XAFS spectra were recorded at liquid nitrogen temperature in transmission mode.

The sample was *in situ* dried at 150°C for 1 hour (heating rate 10°C/min) in He and subsequently reduced at 400°C for 1 hour (5°C/min) in flowing H_2 and cooled down in a H_2 atmosphere. This sample is considered to be fully covered with H, further denoted by RED400. Next, the first EXAFS data for both the L_2 and L_3 edge were collected (T= -196°C). Subsequently, the sample was evacuated at 50°C, 100°C, 150°C and 200°C (all heating rates were 5°C/min) for 30 min. After each evacuation the $L_{2/3}$ EXAFS data were collected maintaining a vacuum better then 10^{-3} Pa at T=-196°C). The sample after evacuation at 50°C is considered to be covered with strongly adsorbed H only (further denoted by VAC50), while the sample after evacuation at 200°C is H-free (further denoted by VAC200).

EXAFS data analysis

The absorption data was background-subtracted using standard procedures[23,24]. Data analysis was performed by multiple shell fitting in R-space (1.6<R<3.2 Å, 2.5<k<14 $Å^{-1}$, k-weighting 2) using the commercially available data analysis package XDAP[25]. The variances in imaginary and absolute parts were used to determine the fit quality[24]. Different backscatterers were identified by applying the difference-file technique[26] using phase-corrected Fourier transforms. Data for the phase shifts and backscattering amplitudes were obtained form reference compounds. The references were theoretical Pt-Pt and Pt-O references[27] generated by the FEFF7 code[28] and calibrated with experimental spectra of Pt-foil and $Na_2Pt(OH)_6$[27]. The references can be used for k>2.5 $Å^{-1}$.

Near-edge analysis of the Pt L_2 and L_3 absorption edges

The L_2 and L_3 whiteline areas with and without H adsorbed change dramatically[19]. A special alignment- and subtraction procedure has been developed to isolate the Pt-H antibonding state shaperesonance and Pt-H EXAFS. Details are given elsewhere[19,29].

The difference in XAFS scattering due to the geometric changes of the Pt cluster is dominated at low energies by Pt-H scattering[19]. The Pt-H EXAFS can be approximated with a theoretical Pt-H EXAFS function (calculated with the FEFF7 code[28]). This allows a determination of the Pt-H bond-length.

Based upon the earlier developed methods, the Pt-H shaperesonance and Pt-H EXAFS for weakly and strongly adsorbed H can be isolated from the experimental data as follows:

Starting with three samples (the fully-covered, the sample with strongly adsorbed H and the H-free sample), two models for H adsorption can be considered. The first model is that in the fully covered sample (RED400) both weakly and strongly adsorbed H are present at different sites. The weakly adsorbed H can then be isolated by subtracting the XAFS data of the sample with the strongly adsorbed H (VAC50) from data of the fully-covered sample (weakly adsorbed=RED400-VAC50). The second model is that in the fully covered sample all H is

present as weakly adsorbed H and that after desorption of part of the H the remaining H is stronger bonded. This can be due to a change in electronic properties of the Pt particles while desorbing H_2 or due to a movement of the remaining H to strongly-adsorbing sites (*e.g.* from atop sites to 3-fold sites which were formerly inaccessible). In this case, the weakly adsorbed H can be isolated by subtracting the XAFS data of the H-free sample from the fully-covered sample (Weakly adsorbed = RED400-VAC200). For both models, the strongly adsorbed H can be isolated by subtracting the XAFS data of the H-free sample from the sample covered with strongly adsorbed H (strongly adsorbed = VAC50-VAC200).

Both models were tested in this paper. To the best of our knowledge, in the literature the validity of the two models has not yet been investigated. The shape resonances and Pt-H EXAFS for the weakly adsorbed H (using both models) and the strongly adsorbed H were isolated and analyzed.

Results

Hydrogen adsorption

The adsorption isotherms for the Pt/Al_2O_3 sample are given in Figure 1. The H_2 uptakes were determined by extrapolating the linear parts of the adsorption isotherms to P=0 mm Hg. The total amount of adsorbed H_2 was determined by the first adsorption isotherm (solid line) and resulted in $H_{total}/Pt=0.70$. The amount of weakly adsorbed H_2 is given by the second adsorption isotherm (dotted line), the amount of strongly adsorbed H_2 by the difference (dashed-dotted line) between to the two adsorption isotherms. This resulted in $H_{strong}/Pt=0.36$ and $H_{weak}/Pt=0.34$.

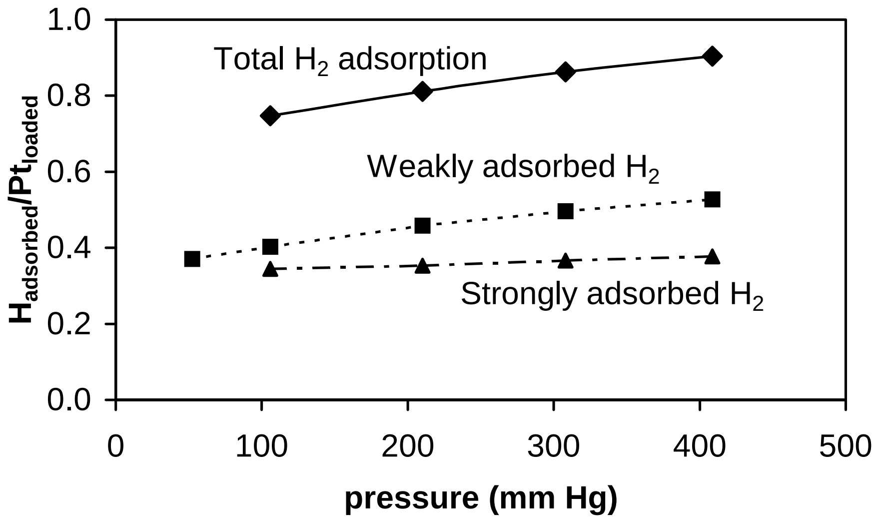

Figure 1: The first H_2 adsorption isotherm (total H_2 adsorption; solid line with diamonds) and second H_2 adsorption isotherm (weakly adsorbed H; the dotted line with squares) of Pt/Al_2O_3. The difference between these two adsorption isotherms is the strongly adsorbed H (dashed-dotted line, triangles).

EXAFS data analysis

In Figure 2a the raw EXAFS data is shown after reduction (RED400, solid line), after evacuation at 50°C (VAC50, dotted line) and after evacuation at 200°C (VAC200, dashed-dotted line). It is clearly shown that the evacuation treatment changed the nodes of the oscillations. The distance between the nodes increases in the order RED400<VAC50<VAC200. This indicates a decrease in the Pt-Pt bond distance in the order RED400>VAC50>VAC200.

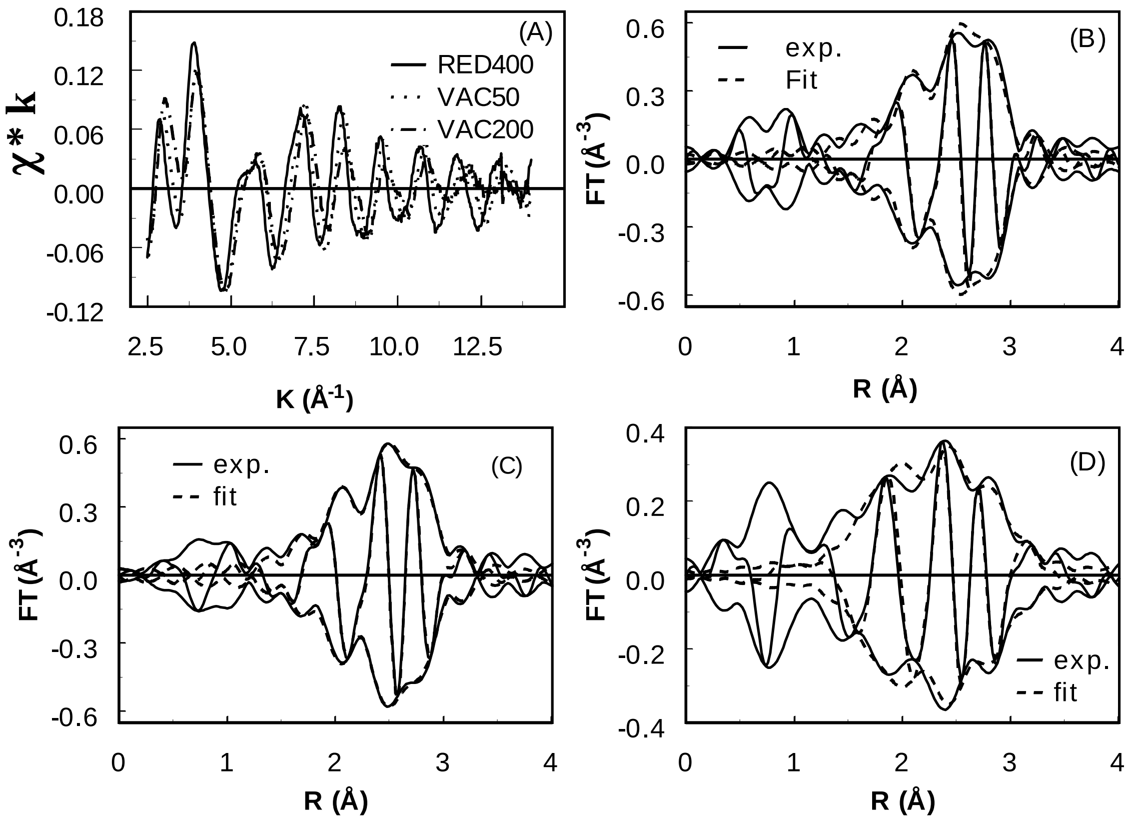

Figure 2: A) k^1 weighted EXAFS spectra of Pt/Al_2O_3 L_3 edge after reduction (solid line), after evacuation at 50°C(dotted line) and after evacuation at 200°C (dashed line) and corresponding Fourier transforms (solid line) with best total fit (dashed line) (R-space fit, 1.6 Å < R < 3.2 Å, k^2 weighted, 2.5 < k < 14 $Å^{-1}$) B) after reduction, C) after evacuation at 50°C and D) after evacuation at 200°C.

In Figure 2B-D the corresponding Fourier-transforms (k^2, Δk=2.5-14 $Å^{-1}$) and best-fits are shown. Data-analysis has been performed by multiple-shell fitting in R-space (1.6 < R < 3.2 Å). The O and Pt backscatterers were identified using the difference-file technique. It has been shown earlier that the oxygen backscatterers originate from the metal-support interface[30-32]. The variances in imaginary and absolute parts were used to determine the fit quality. The best-fit results are given in Table 1. It can be seen (Figure 3) that after the desorption of H_2 at low temperature, the first metal-shell distance (Pt-Pt distance) decreases with 1-2 % compared to the sample in a H_2 atmosphere. After evacuation at 150°C and 200°C a further decrease of

again 1-2% was observed. This is in agreement with the observation of the decrease in the distance between the nodes as seen in the raw EXAFS data.

The Pt-Pt first-shell coordination number decreased slightly while the coordination number of he Pt-$O_{support}$ coordination increased after evacuation at 150 °C. After evacuation at 200°C the Pt-Pt coordination number increased again. The Pt-$O_{support}$ coordination number remained relatively high at this temperature.

Table 1: Fit results for all samples. Fits were done in R-space, k^2 weighting, 1.6 Å < R < 3.2 Å, and Δk=2.5-14 $Å^{-1}$. The Debye-Waller factors are relative to the theoretical references. Accuracy limits[37] between brackets.

Sample	Scatterer	N (±10%)	R(Å) (±0.02 Å)	$\Delta\sigma^2$ ($Å^2$) (±5%)	E_0(eV) (±10%)	Variance	
						Imaginary	Absolute
Reduced 400°C	Pt	6.5	2.75	0.0041	1.2	0.868	0.308
	O	0.3	2.10	0.0020	-8.0		
Evacuation 50°C	Pt	6.5	2.71	0.0056	-0.3	0.414	0.135
	O	0.3	2.10	0.0040	-7.3		
Evacuation 100°C	Pt	6.5	2.71	0.0050	-0.2	0.700	0.321
	O	0.4	2.10	0.0040	-7.0		
Evacuation 150°C	Pt	5.7	2.69	0.0050	0.1	1.59	0.993
	O	0.5	2.10	0.0040	-7.0		
Evacuation 200°C	Pt	5.4	2.68	0.0066	-0.6	2.07	0.632
	O	0.7	2.10	0.0040	-2.6		

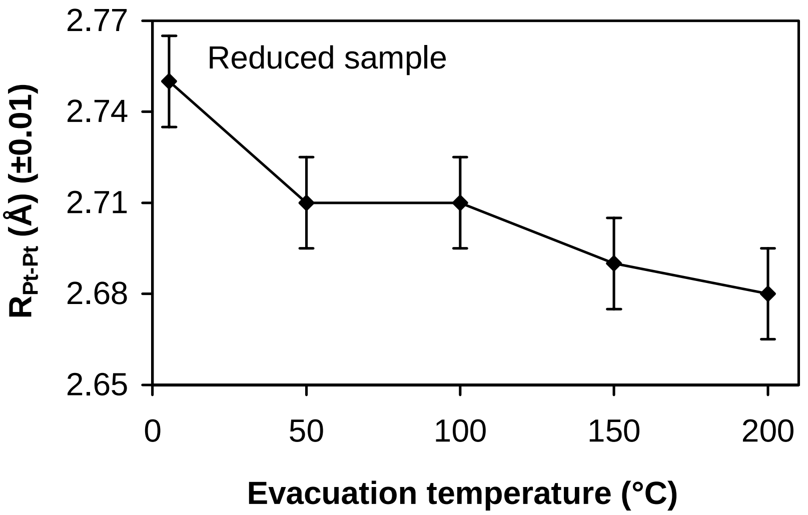

Figure 3: The Pt-Pt coordination distance as a function of the treatment of the sample.

Isolation of the Pt-H antibonding state shaperesonance

In Figure 4 the near-edge spectra of the L_2 and L_3 edge of the samples RED400, VAC50 and VAC200 after the alignment procedure as described in ref. 19 are shown. The L_2 spectra are aligned at a step-height of 0.6. The L_3 edges are aligned at their corresponding L_2 edges by fitting the EXAFS wiggles at 100-500 eV over the edge using the least-squares method. The region below 100 eV can not be used for alignment since all differences in the L_2 and L_3 edges are present in this energy-window. The region higher than 500 eV was not used since the noise-level is too high at these energies. It can be seen that after evacuation the intensity of the L_2 whiteline decreases, while the L_3 whitelines sharpen and start at lower energies after evacuation. Clearly, the influence of chemisorption of H is different for L_2 than for L_3 edges.

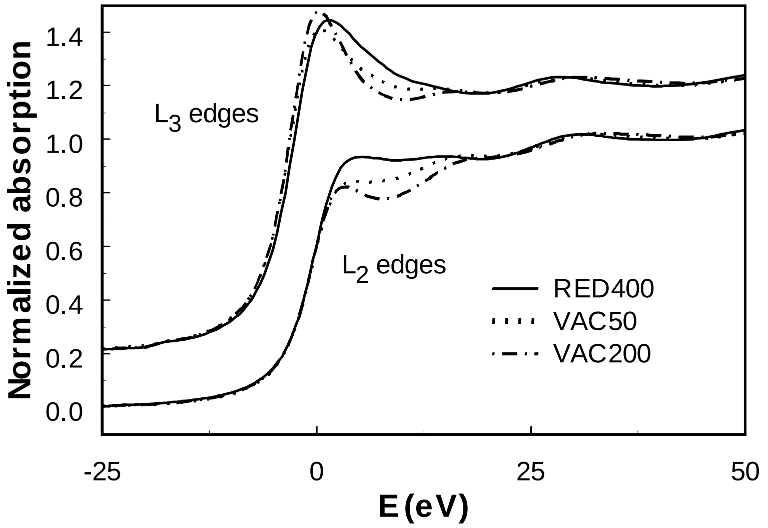

Figure 4: L_2 and L_3 edges after H_2 chemisorption, evacuation at 50°C and at 200°C.

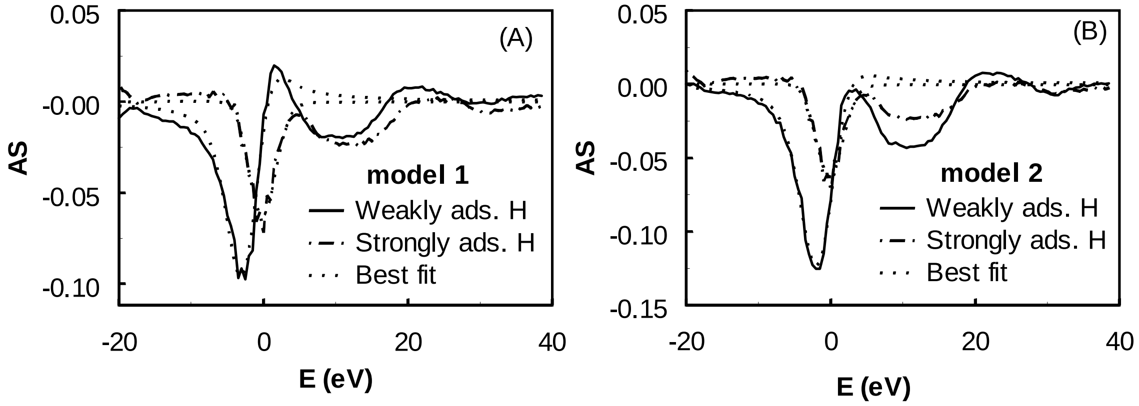

Figure 5: The shaperesonance of the Pt-H anti-bonding state for the weakly (solid line) and strongly (broken-dotted line) adsorbed H in (A) model 1 (simultaneous adsorption) and (B) model 2 (rearrangement of Pt) with the corresponding fits (dotted line).

By taking the difference VAC50-VAC200 (as described in the experimental section and in ref. 19) the Pt-H AS shaperesonance (Figure 5) for the strongly adsorbed H were isolated. Also, RED400 was used to subtract VAC50 (giving weakly adsorbed H according to model 1) and VAC200 (giving weakly adsorbed H in model 2), giving an Pt-H EXAFS and Pt-H AS.
The position and shape of the shaperesonance depends on multiple parameters[19]: the amplitude A, energy E_{res}, width Γ and phase Φ. Φ can be calculated as described in ref. 29. A, E_{res} and Γ can be obtained by fitting the lineshape with the Fano-expression[19]. The best fit was determined by the least-squares method. The shaperesonance was fitted in the energy-range of –20 to 5 eV. The region 5-20 eV was not taken into account, since the bumps present in this region can be attributed to differences in Atomic XAFS between the L_2 and L_3 edge for the bare sample and the H-covered samples. The different parameters describing both Pt-H AS shaperesonance lineshapes are compiled in Table 2. The best fit for the strongly adsorbed H gives an energy of the anti-bonding state of –0.3 eV. The energy of the AS for the weakly adsorbed H in model 2 (RED400-VAC200) was found to be –1.7 eV. In the case of model 1 the AS of the weakly adsorbed H (RED400-VAC50) has an energy of –2.5 eV.

Table 2: Fit parameters for the isolated shaperesonances. Parameters obtained from non-linear least-squares fit of Fano-profile to the hydrogen-induced shape-resonance in experimental spectra. Applied experimental width: Gaussian, 5 eV.

Isolated AS	Amplitude	Energy (eV, relative to E_F)	Width (eV)
RED400-VAC50 (model 1 for weakly adsorbed H)	0.22	-2.5	1.7
RED400-VAC200 (model 2 for weakly adsorbed H)	0.16	-1.7	2.5
VAC200-VAC50 (Strongly adsorbed)	0.28	-0.3	0.3

Isolation of Pt-H EXAFS

In Figure 6 the difference in XAFS obtained for the strongly adsorbed H, the weakly adsorbed H according to model 1 (simultaneous adsorption) and the weakly adsorbed H according to model 2 (rearrangement of H) are shown. This difference in XAFS is dominated by Pt-H EXAFS[19]. The amplitude of H scattering is near zero above k=2 $Å^{-1}$, since H has a cross-section for scattering which decreases stongly with increasing values of k. A consequence is that no experimental Pt-H reference is available to do normal EXAFS analysis on the isolated Pt-H EXAFS. However, since the distance of the nodes in oscillations is different, it is expected that the Pt-H distance in the two samples is different. In order to quantify these differences, FEFF7[28] was used to calculate the Pt-H XAFS for different Pt-H distances. An atop adsorption site for H was assumed. The input parameters are given in Table 3. The only input-parameter that was varied was the Pt-H distance. The calculated Pt-H EXAFS was used to fit the experimentally observed ΔXAFS. To obtain a good fit, the theoretical data was

shifted in energy until the onset of the theoretical Pt-H EXAFS spectrum was aligned with the experimental data. Then the theoretical spectrum was scaled until the theoretical and experimental maxima were in agreement. The quality of the fit was then judged on the right part of the Pt-H first wiggle, since the left part of the theoretical spectrum was fixed at perfect alignment with the experimental spectrum. The best fits are shown in Figure 6 (dotted lines). For strongly adsorbed H it was found that the Pt-H bond is 1.89 Å whereas weakly adsorbed H was found at 1.94 Å from Pt in model 1 and at 1.92 Å in model 2. The small bumps around 25-30 eV in the experimental curve that cannot be reproduced by the theoretical curve are caused by the differences in Pt-Pt EXAFS. These differences are due to the decrease in Pt-Pt bond-length after the evacuation treatments.

Table 3: Input parameters for FEFF7 calculations. *: This parameter (the Pt-H distance) was varied.

Parameter	Value(s)	Parameter	Value(s)
Control	1 1 1 1	Exchange	1 4 3
Print	0 0 0 0	Potentials	0 78 Pt
Hole	3 0.82		1 1 H
Criteria	2.0 1.25	Atoms	0 0 0 0
Nleg	6		1.94* 0 0 1
Rmax	8.3		

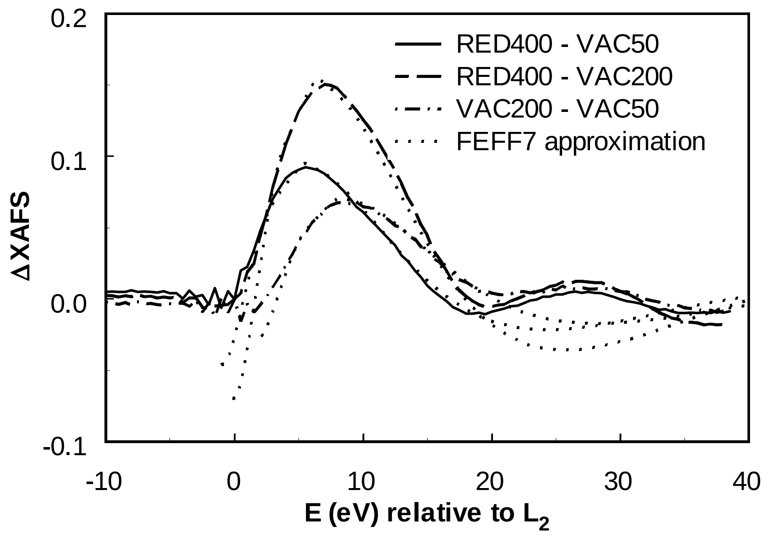

Figure 6: The difference (L_2 in vacuum-L_2 in hydrogen) spectra with Pt-H EXAFS for weakly adsorbed H in model 1 (solid line), model 2 (dashed line), strongly adsorbed H (dashed-dotted line) and the FEFF7[28] Pt-H calculation (dotted line) with Pt-H=1.89Å (strongly adsorbed H_2), Pt-H=1.92Å (weakly adsorbed H_2 in model 2) and Pt-H=1.94Å (weakly adsorbed H_2 in model 1).

Discussion

Pt-Pt coordination distance

Figure 3 shows a decrease in Pt-Pt bond length of ca. 1-2% after desorption of weakly adsorbed H and again a decrease of 1-2% after desorption of strongly adsorbed H.

A decrease of the metal-metal coordination distance is expected going from bulk to very small metal-particles, owing to a softening of the phonon spectrum caused by the dehybridisation of the spd metal orbitals[33]. The dehybridisation results in increased electron density between the atoms in the small particle, which in turn results in a contraction in the inter-atomic distance. However, for small particles covered with chemisorbed H, EXAFS results show bulk-like coordination distances[22,34]. This is caused by the electron-withdrawing properties of H chemisorbed on Pt[35], leading to a decrease in electron-density between the atoms[33]. This is illustrated in Figure 7. A longer Pt-Pt bond length is observed going from the H free sample to the sample covered with strongly adsorbed H and again going from the latter species to the fully covered sample (Table 1). This is a strong indication that both types of H are chemisorbed.

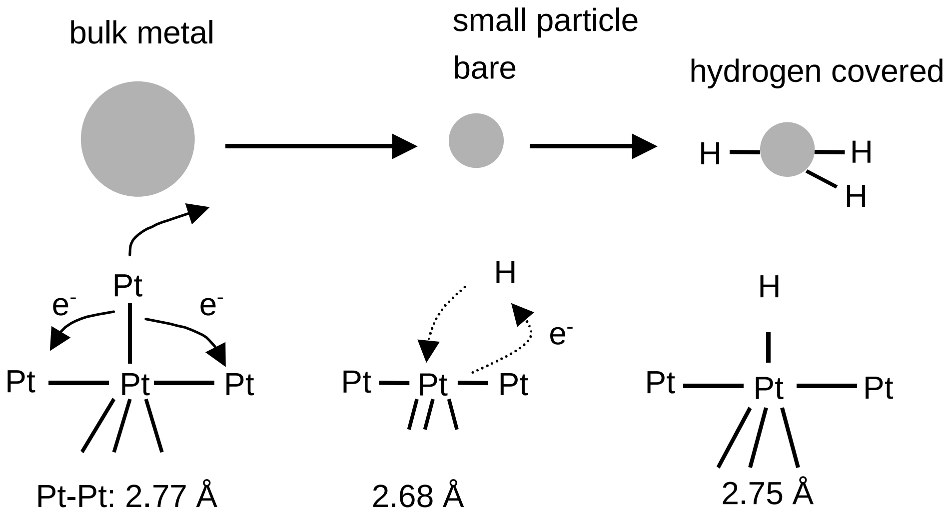

Figure 7: The Pt-Pt bond length is shortened going from bulk-metal to small particles and enlarged by chemisorbing H.

Pt-H antibonding state shaperesonance

Regardless of the methods used (model 1 or model 2) to determine the weakly adsorbed hydrogen, a Pt-H anti-bonding state shaperesonance is present for both the weakly and the strongly adsorbed hydrogen (shown in Figure 5). Moreover, the value of the energy of the antibonding state is larger for the strongly adsorbed species. The sheer presence of an anti-bonding state for the weakly chemisorbed hydrogen in itself is evidence that the weakly adsorbed hydrogen is indeed chemisorbed on the Pt cluster. Physisorption of molecular H_2 on the Pt clusters or sorption of the H_2 on the support would not result in a Pt-H anti-bonding state.

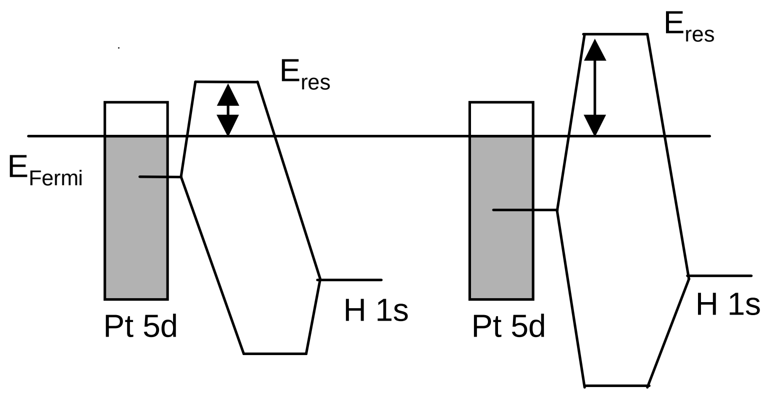

Figure 8: Molecular Orbital (MO) scheme of Pt-H interaction showing the effect of differences in orbital-overlap on the strength of the Pt-H bond-strength.

The lower energy of the anti-bonding state of the weakly adsorbed H compared to that of the strongly adsorbed H (-0.3 eV) shows that the weakly adsorbed H indeed has a weaker Pt-H bond than the strongly adsorbed H, since a lower energy of the anti-bonding state is the result of a weaker Pt-H bond (Figure 8).

Pt-H EXAFS

Normally, the starting point of the EXAFS region is taken at about k=2.5 $Å^{-1}$. As discussed earlier, at this energy a H atom does not contribute to the EXAFS as a backscatterer due to the small absorption cross section of H. However, the procedure described in this paper and by Ramaker *et al.*[19] isolates the Pt-H EXAFS for $0 < k < 2.5$ $Å^{-1}$. The isolated Pt-H EXAFS could be analyzed using theoretical spectra generated by the FEFF7[28] code. For the calculations a single Pt atom was considered to be bonded to a single H atom at varying distances. Multiple scattering was not taken into account.

The experimental Pt-H EXAFS (Figure 6) showed a smaller bond length for the strongly adsorbed H. Generally, a longer bond is the result of a weaker bonding. This is another indication that the weakly adsorbed H is indeed weaker bonded on the Pt particles.

Pt-H bond strength

Differences in Pt-H bond strength may result from several reasons. First, the metal clusters in a heterogeneous catalyst are small and therefore contain only small crystal surfaces and many edges and corners. The atoms on the corners and edges are coordinatively highly unsaturated and therefore will bond strongly to H atoms. So the strongest bonded H atoms may be the H atoms that are chemisorbed on the corners of the clusters. After saturation of the cluster with a monolayer of H, these corner-atoms will still be relatively unsaturated and can bond to yet another H atom. This H however will be bonded rather weakly.

Tsuchiya *et al.*[36] performed temperature-programmed desorption experiments of H_2 chemisorbed on platinum. This gave rise to several desorption maxima. To explain different

desorption maxima, Tsuchiya *et al.*[36] proposed linear chemisorbed H for the weakly bonded species and bridged H for the strongly sorbed species.
Structurally different adsorption sites are also proposed by Giannantonio *et al*[8]. They claim that adsorption energies as determined by TPD for the weakly adsorbed species are in agreement with theoretical calculations for the adsorption of H at an atop or bridged position. The adsorption energy for the strongly adsorbed H is in agreement with calculations for adsorption of H at three- and four-fold symmetry surface sites.
Normally, in literature H_2 chemisorption is used to determine the metal dispersion, and in relation to this the accessible metal surface area for reactants during reactions. Now the question rises which H_2 chemisorption values should be used to determine the metal dispersion and accessible surface area: the weakly, strongly or total H_2 chemisorption. In literature generally only strong adsorption is used (see *e.g.* ref. 6 and 10). Whatever the nature of the different adsorption sites is, both weakly and strongly adsorbed H_2 are chemisorbed on the Pt surface and all sites are accessible to H and thus all these sites might be important during reactions. Therefore, this study shows that H/M values should be based on the total amount of H_2 adsorption. Of course the adsorption sites for reactants other than H_2 might be different than that for H_2 adsorption.

Conclusions

Pt EXAFS in the presence in the presence and absence of hydrogen was used to determine the nature of hydrogen adsorbed on Al_2O_3 supported Pt particles.
Pt EXAFS analysis during evacuation at different temperatures results in a contraction of the Pt-Pt distance with 1-2% after desorption of weakly and strongly adsorbed hydrogen. This is the result of an increased electron density between the Pt clusters after removal of the electron withdrawing hydrogen atoms, indicating that both types of hydrogen are chemisorbed.
A Pt-H anti-bonding state for both weakly and strongly adsorbed hydrogen could be isolated using the analysis of the Pt L_2 and L_3 X-ray absorption edges. The presence of a anti-bonding state for both types of hydrogen proofs that all hydrogen is chemisorbed on the Pt clusters. The lower energy of the antibonding state for the weakly adsorbed hydrogen compared to the strongly adsorbed hydrogen shows that this strongly adsorbed hydrogen indeed has a stronger Pt-H bond. Since hydrogen is chemisorbed in all cases, the H/Pt values used to determine the accessible metal surface area should be based on the total amount hydrogen adsorption.
Finally, the weakly adsorbed hydrogen shows a Pt-H EXAFS. The Pt-H bond-length is longer for weakly adsorbed hydrogen compared to strongly adsorbed hydrogen. This again is the result of a weaker bond strength.

Acknowledgements

The European Union program for Large Scale Facilities (contract nr. ERBFMGECT950059) is acknowledged for financial support.

Reference list

1. J.J.F. Scholten, A.P. Pijpers and A.M.L. Hustings, *Catal. Rev. - Sci. Eng.*, **27** (1985), 151-206.
2. G.B. McVicker, R.T.K. Baker, R.L. Garten and E.L. Kugler, *J. Catal.*, **65** (1980), 207-220.
3. Z. Paál, P.G. Menon, *Catal. Rev. - Sci. Eng.*, **25** (1983), 229-324.
4. H. Ahlafi, M. Nawdali, A.K. Bencheikh and D. Bianchi, *Bull. Soc. Chim. Fr.*, **133** (1996), 461-469.
5. J.H. Sinfelt, Y.L. Lam, J.A. Cusumano and A.E. Barnett, *J. Catal.*, **42** (1976), 227-237.
6. J.H. Sinfelt, G.H. Via, *J. Catal.*, **56** (1979), 1-11.
7. C.H. Yang, J.G. Goodwin jr., *J. Catal.*, **78** (1982), 182-187.
8. R. Giannantonio, V. Ragaini and P. Magni, *J. Catal.*, **146** (1994), 103-115.
9. J.M. Guil, A. Pérez Masiá, A. Ruiz Paniego and J.M. Trejo Menayo, *Thermochim. Acta*, **312** (1998), 115-124.
10. D.O. Uner, M. Pruski and T.S. King, *J. Catal.*, **156** (1995), 60-64.
11. A. Sayari, H.T. Wang and J.G. Goodwin jr., *J. Catal.*, **93** (1985), 368-374.
12. L.H. Germer, A.U. MacRae, *J. Chem. Phys.*, **37** (1962), 1382-1386.
13. E. Poulain, V. Bertin, S. Castillo and A. Cruz, *J. Mol. Catal. A*, **116** (1997), 385-396.
14. J. Andzelm, *Surf. Sci.*, **108** (1981), 561-577.
15. B. Hammer, J.K. Nørskov, *Surf. Sci.*, **343** (1995), 211-220.
16. B. Hammer, J.K. Nørskov, *Nature*, **376** (1995), 238-240.
17. J. Barbier, E. Lamy-Pitara and P. Marecot, *Bull. Soc. Chim. Belg.*, **105** (1996), 99-105.
18. D.C. Koningsberger, J. de Graaf, B.L. Mojet, D.E. Ramaker and J.T. Miller, *Appl. Catal. A: General*, **191** (2000), 205-220.
19. D.E. Ramaker, B.L. Mojet, M.T. Garriga Oostenbrink, J.T. Miller and D.C. Koningsberger, *Phys. Chem. Chem. Phys.*, **1** (1999), 2293-2302.
20. D.C. Koningsberger, B.L. Mojet, J.T. Miller and D.E. Ramaker, *J. Synchr. Rad.*, **6** (1999), 135-141.
21. G.R. Wilson, W.K. Hall, *J. Catal.*, **17** (1970), 190-206.
22. M. Vaarkamp, B.L. Mojet, F.S. Modica, J.T. Miller and D.C. Koningsberger, *J. Phys. Chem.*, **99** (1995), 16067.
23. D.E. Ramaker, B.L. Mojet, D.C. Koningsberger, W.E. O'Grady, *J. Phys.: Condens. Matter* **1998**, *10*8753-8770.
24. D.C. Koningsberger, B.L. Mojet, G.E. van Dorssen and D.E. Ramaker, *Top. Catal.*, **10** (2000), 143-155.
25. M. Vaarkamp, J.C. Linders and D.C. Koningsberger, *Physica B*, **208** (1995), 159-160.
26. D.C. Koningsberger, *Hercules Course. Neutron and Synchrotron Radiation for Condensed Matter Studies. Applications to Solid State Phys. and Chem.*; J. Baruchel, J.L. Hodeau, M.S. Lehmann, J.R. Regnard, C. Schlenker, eds., Springer Verlag: Vol. 2, pp 213-244.
27. G.E. van Dorssen, D.E. Ramaker and D.C. Koningsberger, *Phys. Rev. B*, **submitted**.
28. S.I. Zabinsky, J.J. Rehr, A. Ankudinov, R.C. Albers and M.J. Eller, *Phys. Rev. B*, **52** (1995), 2995-3009.
29. D.C. Koningsberger, M.K. Oudenhuijzen, J.H. Bitter and D.E. Ramaker, *Top. Catal.*, **10** (2000), 167-177.
30. J.B.A.D. Van Zon, D.C. Koningsberger, H.F.J. Van 't Blik, R. Prins and D.E. Sayers, *J. Chem. Phys.*, **80** (1984), 3914.
31. M. Vaarkamp, F.S. Modica, J.T. Miller and D.C. Koningsberger, *J. Catal.*, **144** (1993), 611-626.
32. M. Vaarkamp, J.T. Miller, F.S. Modica and D.C. Koningsberger, *J. Catal.*, **163** (1996), 294-305.
33. B. Delley, D.E. Ellis, A.J. Freeman, E.J. Baerends and D. Post, *Phys. Rev. B*, **27** (1983), 2132-2144.
34. F.W.H. Kampers, D.C. Koningsberger, *Faraday Discuss. Chem. Soc.*, **89** (1990), 137-141.
35. E. Sanchez Marcos, A.P.J. Jansen and R.A. van Santen, *Chem. Phys. Lett.*, **167** (1990), 399-406.
36. S. Tsuchiya, Y. Amenomiya and R.J. Cvetanovic, *J. Catal.*, **19** (1970), 245-255.
37. G.G. Li, F. Bridges and C.H. Booth, *Phys. Rev. B*, **52** (1995), 6332.

6

Influence of the Support Properties on the Adsorption Site and Strength of Hydrogen Chemisorption on Supported Platinum Particles

Abstract

Hydrogen chemisorption on supported Pt catalysts has been studied utilizing Pt L_3 XANES data. The Pt L_3 edge is sensitive to the H adsorption position. Both hydrogen coverage and support effects were investigated. It is found for Pt on basic supports that H is adsorbed in the Pt 3-fold hollow sites near cluster edges at high temperatures. However, in the case of acidic supports, the H appears to adsorb at the Pt cluster edge atop sites. This difference in adsorption site is supported by density functional theory (DFT) calculations on H_n/Pt_4 clusters, which show that at low coverage, H prefers the atop sites. However, the adsorption energy in this atop position is much lower for Pt on acidic supports compared to basic supports. At higher coverage, the H prefers the 3-fold hollow sites with approximately equal bond strength on both acidic and basic supports. The DFT calculations therefore suggest that the fraction of strongly bonded H is much larger in basic supports. Due to the higher coverage this H exists in the 3-fold sites. On basic supports a greater fraction of strongly bonded H is found with the DFT calculations. This is confirmed by H_2 chemisorption experiments involving a series of Pt/LTL catalysts with different support acidities. This report is the first report that hydrogen, at high temperature catalytic reaction conditions, changes its dominant adsorption site as the support acidity is varied.

Introduction

It has been well established that the rate of heterogeneously catalyzed hydrogenation or hydrogenolysis reactions on supported noble metal catalysts is strongly influenced by the alkalinity or acidity of the support material[1,2]. Moreover, the resistance to sulfur poisoning of these supported metal catalysts is dramatically increased with increasing support acidity[3]. The reasons for this support effect have been highly debated. Since atomically adsorbed H is one of the primary reactants in these hydrogenation and hydrogenolysis reactions, it is important to elucidate the nature (*e.g.* bond strength and adsorption site) of chemisorbed H on the supported metal particles and the influence of the support acid/base properties on this chemisorption.

In an earlier paper[4], we focused on elucidating the nature of the chemisorbed H found at different temperatures, namely in understanding the common H_2 chemisorption conditions that routinely exist when determining the dispersion of the supported metal particles[5]. In such H_2 chemisorption experiments, H_2 is adsorbed at the metal surface at room temperature, followed by an evacuation at this temperature. The H_2 that desorbs at low temperatures (typically T< 323 K) is commonly called 'weakly' adsorbed hydrogen, whereas the H_2 that desorbs at higher temperatures (T > 323 K) is referred to as 'strongly' adsorbed hydrogen[6-8]. Using X-ray absorption spectroscopy near edge structure (XANES) experiments, it was shown that both types of H are atomically chemisorbed on the metal surface of a supported Pt catalyst.

The terms 'weakly' and 'strongly' adsorbed H may not be fully adequate to describe the difference between the two types of H. Adsorbed H has been shown to exist in various sites, and at low coverage H is even delocalized on the surface[9]. Temperature programmed desorption (TPD) experiments have been most helpful in sorting out the different H adsorption sites. The results of these TPD studies are summarized in Figure 1 and Figure 2. TPD studies on Pt(111) single crystals show that all H_2 desorbs at temperatures lower than 323 K[10-13], which is the temperature regime that is referred to as the weak H adsorption region. When steps and kinks are introduced on this single crystal surface, a second desorption peak in the TPD at T > 323 K is observed[10], which we refer to as the region of strongly adsorbed H[12,14,15]. This single crystal data suggest that the strongly chemisorbed H can be attributed to H that is adsorbed on the low-coordinated metal atoms at the edges. Since these edge metal atoms are coordinatively unsaturated, they apparently adsorb H stronger than the metal atoms on a perfect (111) flat surface. However, infrared (IR) and high resolution electron energy loss spectroscopy (HREELS) data show for reasonably high H coverage that H both near the edges and on the flat (111) surfaces is bound in the 3-fold Pt hollow sites. The 3-fold sites on the flat surfaces vs. near the edges are apparently sufficiently different to make a difference in the Pt-H bond strength. In the case of our supported catalysts, the very small

(Pt-Pt coordination number N = 4-6) Pt particles have many edges, so there are significant amounts of both types of H. Thus it is likely that the so-called 'weakly' adsorbed H corresponds to H adsorbed on the flat faces of the cluster, and that the 'strongly' adsorbed H is chemisorbed near the edges and corners of the metal particles.

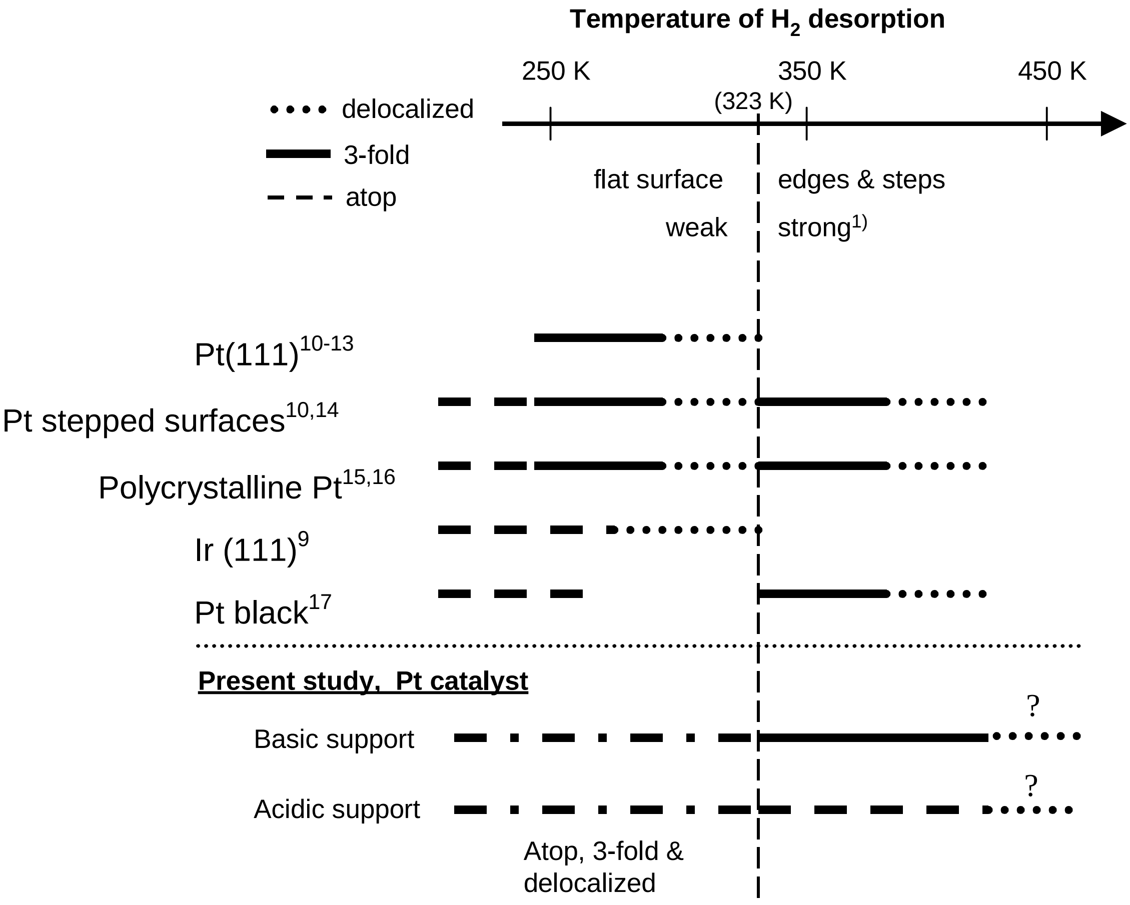

Figure 1: Summary of reported H TPD data, and proposed H binding sites as indicated by spectroscopic data. [1)]: Weak hydrogen is defined as the H that is desorbed during evacuation below 323 K (the vertical line), strongly adsorbed H is the H that remains on the surface after this evacuation. Also indicated are the proposed results for supported Pt clusters as suggested from this work.

It is known from single crystal studies that at low coverage H becomes delocalized: it hops from fcc to hcp sites via the bridge sites at relatively high rates[9,18]. This delocalized H apparently can exist on both the flat faces and the edge sites, and is more strongly bound than the localized H at higher coverage. This delocalized H produces either shoulders or barely

resolved TPD peaks at higher temperature in the weakly and strongly H-bonded regions. We have indicated these regions by the dotted lines in Figure 1. Finally, at very high coverage, H can also adsorb in the atop sites[9,19]. These sites apparently exist on the edge atoms, since atop chemisorbed H is not observed on flat single crystal (111) faces. This is the weakest bound H_2 producing TPD peaks around 250 K.

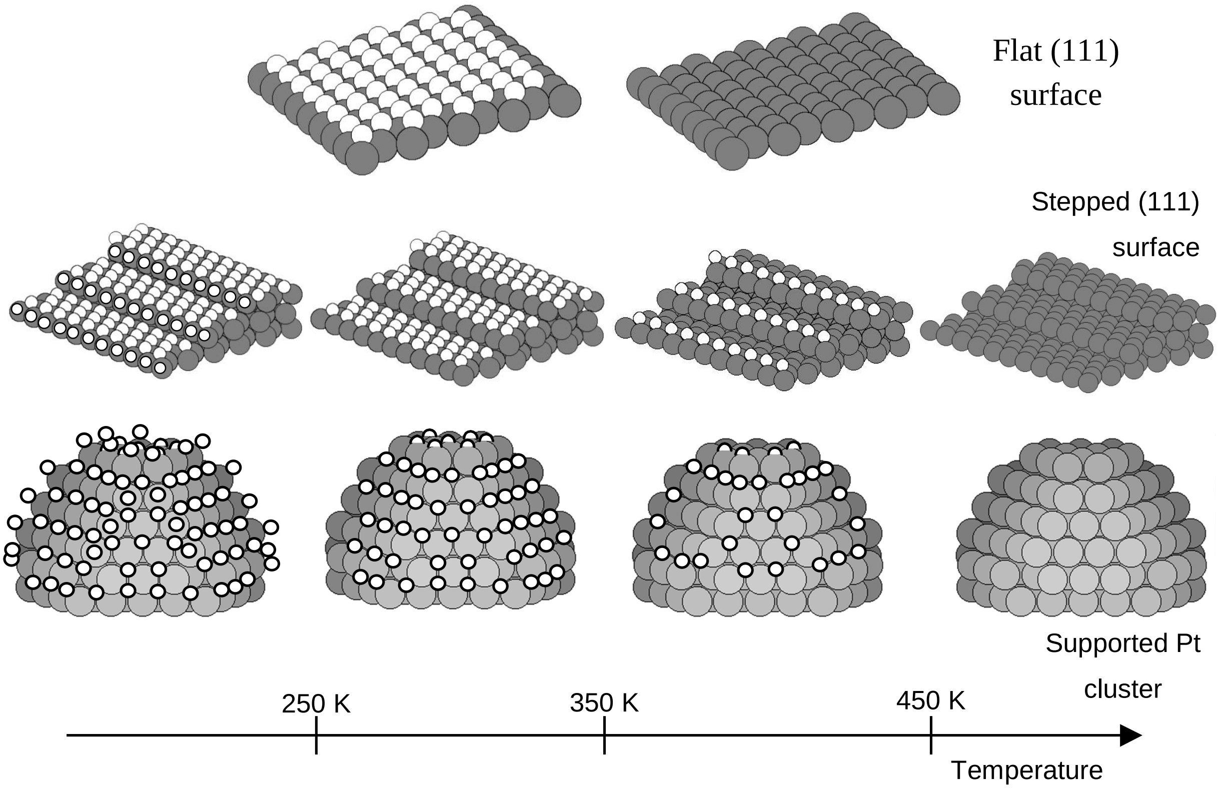

Figure 2: The coverage with H of a flat Pt (111) surface (top), a stepped surface (middle) and a supported Pt cluster (bottom) as a function of temperature. Dark spheres: platinum; white spheres: H.

Most experimental data and theoretical calculations as summarized in Figure 1 suggest that H binds in the 3-fold fcc sites. For example, Olsen *et al.*[20] showed, using DFT, that H adsorbs on the hcp or fcc 3-fold site on a Pt (111) surface rather than on a bridged or atop site, in agreement with published HREELS and IR results. Similar results have been reported by Papoian *et al*[21].

However, all this work has been performed on flat (111) surfaces. Small supported metal particles contain mostly edges and corners, which adsorb H stronger than atoms in a (111) flat surface, and may result in a different preferred adsorption site. Moreover, there are strong indications that the support properties influence the electronic structure of the supported Pt

particles[22-25]. This may result in variations in the Pt-H bond strength and the H adsorption position.

Previous work by our and other groups has shown that the Pt L_3 XANES is sensitive to the adsorption of H[26-29]. This sensitivity was interpreted by our group as being caused by the creation of a chemical bond between Pt and H[30]. The Pt-H anti-bonding state (AS) above the Fermi level was thought to produce a shaperesonance arising from the interference between the resonantly and nonresonantly scattered photoelectron waves.

However, in a recent paper reporting FEFF8[31] results on a Pt_6H_8 cluster, Ankudinov *et al.*[29] pointed out the importance of changes in the L_3 XANES region due to an influence of chemisorbed H on the Pt-Pt multiple scattering paths. When H atoms are adsorbed on the 3-fold hollow sites, the H has a large effect on the Pt-Pt bonding for Pt atoms beneath the H adsorption site. This bond weakening has been called d-electron frustration by Feibelman[32], and Pt-Pt destabilization by Papoian *et al*[21]. Ankudinov *et al.*[29] concluded that this bond destabilization and the accompanying change in the atomic XAFS dominate the Pt-H contribution. This would imply that the H induced changes in the L_3 X-ray absorption data, as interpreted to be originated from a shaperesonance only, is not appropriate.

Nevertheless, XANES data reported by Mojet *et al.*[27] showed a strong influence of the support acid/base properties on hydrogen induced changes in the X-ray absorption data of supported Pt particles. This suggests that H_2 chemisorbs differently on Pt when the acid/base properties of the support are varied. Since Pt particles supported on highly acidic supports are the most active in hydrogenation and hydrogenolysis reactions, it is entirely possible that the difference in the catalytic activity is related to differences in H_2 chemisorption properties.

In this manuscript it will be investigated what the strength and mode of hydrogen adsorption on dispersed Pt particles with an Al_2O_3 support with varying acidity is. Analysis of the Pt ΔL_3 XANES difference spectra (L_3 edge with chemisorbed H minus the L_3 edge in vacuum) shows that the H adsorption position (n-fold vs. atop) depends on the acid/base properties of the support and the coverage with H. These results could be further interpreted with the help of DFT calculations that have been performed on supported Pt_4 clusters, mimicking a true catalyst. These DFT calculations confirm the observed changes in adsorption site as a function of the acid/base property of the support material and the coverage with H.

Methods

Catalyst preparation

Two Al_2O_3 supported Pt catalysts containing 2 wt.% Pt were prepared. Details on the loading of the support with Pt are given elsewhere[4]. The support of one of the Pt/Al_2O_3 catalysts was made alkaline by impregnating it with a KOH solution, yielding a support containing 0.25

wt.% K. This catalyst is further referred to as Pt/K-Al_2O_3. The support of the second catalyst was made acidic by impregnating it with a HCl solution, resulting in a 3.3 wt.% Cl loading. This catalyst is coded Pt/Cl-Al_2O_3.

XAFS data collection and EXAFS Data Analysis

XAFS measurements were performed at the European Synchrotron Radiation Facility (Swiss-Norwegian Beamline) in Grenoble, France. Details of the measurements are given elsewhere[4]. In short, the catalysts were reduced in flowing H_2 at 673 K *in situ* and cooled down in H_2 to liquid nitrogen (LN) temperature. At this temperature, the XAFS spectra were recorded. This freshly reduced catalyst is further denoted as 'RED'. Next, the catalysts were evacuated at 323, 373, 423 and 473 K for 30 minutes (all heating rates were 5 K/minute). After the respective evacuations at each temperature, the catalysts were cooled down to LN, and the L_2/L_3 XAFS spectra were collected maintaining a pressure of lower than 10^{-3} Pa. These samples are further referred to as VAC323, VAC373, VAC423 and VAC473, respectively. The L_2 edges are not discussed in this paper. After evacuation at 473 K, (nearly) all H is removed from the Pt surface as suggested by the TPD data summarized in Figure 1. Logically, the H coverage increases in the order VAC473 < VAC423 < VAC373 < VAC323 < RED.

Details on the analysis of the resulting fine structure (EXAFS) are given elsewhere[4]. The fits were performed in R-space (1.6 < R < 3.2 Å, k^2- weighting and 2.5 < k < 14 $Å^{-1}$) using the difference file technique[33]. Two backscatterers were used for the fits, O and Pt. The O backscatterer originates from the oxidic support material[34-36].

Near Edge Analysis of the Pt L_3 absorption edges.

Experiment

The pre-edge subtracted and normalized XAFS spectra for each catalyst after reduction and after the various evacuations were aligned in a fashion reported previously[30]. First, the L_2 edge spectra are aligned at 0.6 of the step heights. Then the EXAFS structure in the L_2 and L_3 spectra are aligned in the region between 50-120 eV beyond the edge using the least-squares method. At these energies, the contribution to the EXAFS of the H atoms is negligible. An example of the quality of alignment is shown Figure 3.

After evacuation at 473 K almost all H is removed from the Pt particles and the L_3 XAFS spectrum obtained after evacuation at 473 K is further called the reference spectrum: μ_{L3}(ref). To obtain the (average) signature of the H atoms that remained adsorbed on the surface after evacuation at a certain temperature T the reference spectrum μ_{L3}(ref) was subtracted from the corresponding spectrum: $\Delta\mu_{ads}(T) = \mu_{L3}(\text{VAC at } T) - \mu_{L3}(\text{ref})$ with T = 323, 373 and 423 K, respectively. The $\Delta\mu_{ads}$ obtained after reduction is called '$\Delta\mu_{ads}$(RED)'. The signature of the

incremental changes induced by desorption and rearrangement of the remaining H after an evacuation procedure at a certain temperature T is reflected by subtracting the spectra of two consecutive evacuation treatments: $\Delta\mu_{inc}(T) = \mu_{L3}(VAC[T-50] - \mu_{L3}(VACT)$.

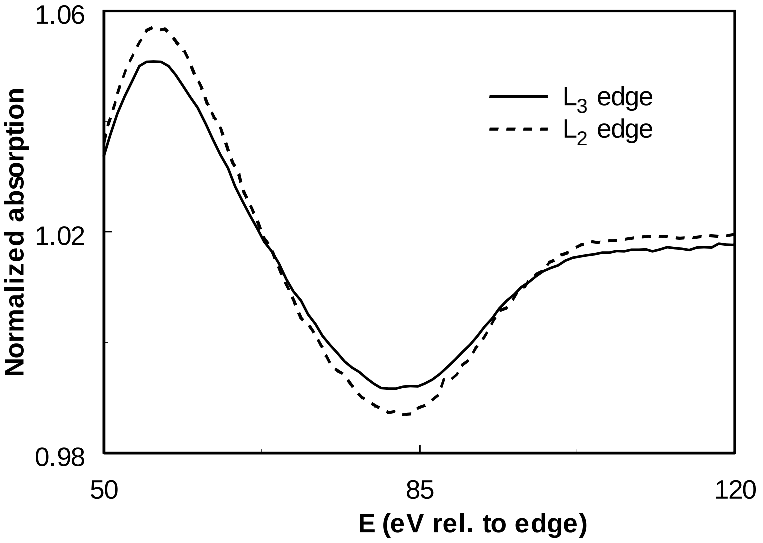

Figure 3: An example of the quality of alignment. The L_3 spectrum (solid line) was aligned on the L_2 spectrum (dashed line), using minimization of the square of the difference between the two spectra. The example is for the freshly reduced Pt/K-Al_2O_3 catalyst.

Theoretical background

It is known that the Pt L_3 X-ray absorption near edge structure (XANES) is sensitive to the adsorption of H[26,28-30,37]. Recently, Ramaker *et al*[38] and Andkudinov[29] have examined the relative contributions to the difference spectrum $\Delta\mu$ of the L_3 edge in the presence of hydrogen and the L_3 edge in vacuum. Since the absorption μ equals $\mu_o(1+\chi)$, the total change, $\Delta\mu = \mu_{L3}(H/Pt)-\mu_{L3}(Pt)$, can be approximately expressed as:

$$\Delta\mu = \mu_{H/Pt} - \mu_{Pt} = \Delta\mu_0 + \bar{\mu}_o \Delta\chi_{Pt-Pt} + \mu_{0,H/Pt}\chi_{Pt-H} \qquad (1)$$

with $\Delta\mu$: the difference spectrum,

$\mu_{H/Pt}$: the L_3 edge spectrum in the presence of H_2,

μ_{Pt} : the L_3 edge spectrum in vacuum,

$\Delta\mu_o$: changes in the atomic L_3 XAFS,

$\bar{\mu}_0$: an effective average of the free atom L_3 X-ray absorptions with and without the presence of H,

$\Delta\chi_{Pt-Pt}$: changes in the Pt-Pt total scattering induced by H_2 chemisorption,

$\mu_{o,H/Pt}$: the free atom L_3 absorption (including atomic XAFS) in the presence of H_2, and

χ_{Pt-H} : the additional Pt-H scattering.

Ankudinov *et al.*[29] showed with FEFF8[31] calculations on octahedral Pt_6 and Pt_6H_8 clusters (H in 3-fold sites) that the first two terms dominate in $\Delta\mu = \mu_{L3}(Pt_6H_8)-\mu_{L3}(Pt_6)$. This indicates that H chemisorption induces changes in the Pt atomic XAFS and the Pt-Pt total scattering (near edge and EXAFS). These changes were previously incorrectly thought to be marginal compared to the Pt-H total scattering $\mu_o\chi_{Pt-H}$ (anti-bonding state AS and Pt-H EXAFS)[27,30]. In contrast, Ramaker *et al.*[38] showed that the experimental $\Delta\mu$ for highly dispersed Pt clusters on acidic supports does indeed result entirely from the last term, the Pt-H scattering. Further FEFF8 calculations showed that the choice of the H adsorption site is crucial for the observed changes in $\Delta\mu$. If the H is adsorbed atop and the X-ray absorption spectra are calculated for a Pt_6 and P_6H_6 cluster using FEFF8, then the results lead to entirely different conclusions as drawn by Ankudinov[29]. The results of many previous calculations on small Pt_n clusters (with n=4-6) with H adsorbed in the 3-fold and atop sites are schematically summarized in Figure 4.

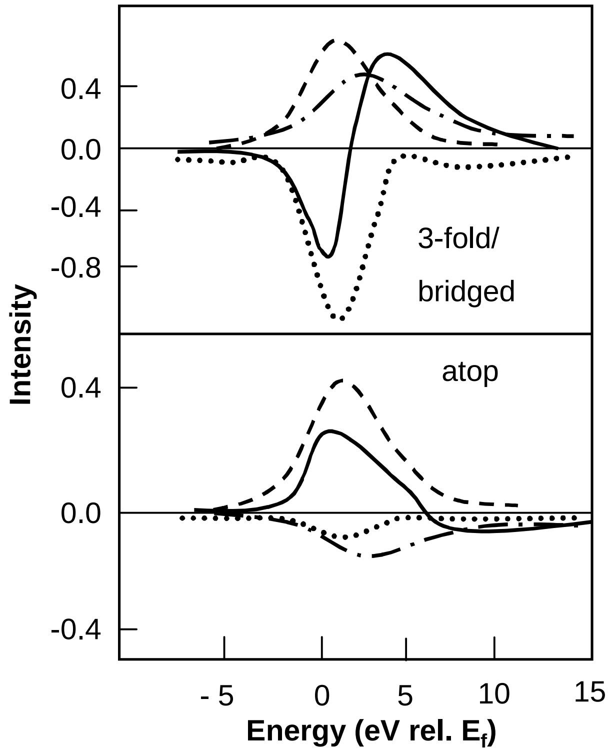

Figure 4: Schematic representation of the signature of $\Delta\mu$ (=μ_{Pt-H} - μ_{Pt}) and its contributions as a function of adsorption site. Solid line: total $\Delta\mu$, with all contributions, dashed line: Pt-H scattering, $\mu_{o,Pt-H}\chi_{Pt-H}$, dotted line: the change in Pt-Pt scattering, $\mu_o\Delta\chi_{Pt-Pt}$, and dashed-dotted line: the change in AXAFS, $\Delta\mu_o$.

Since the H adsorbed in the bridged and 3-fold position yield essentially the same calculated spectral lineshapes for $\Delta\mu$, these sites are further referred to as the n-fold site. Figure 4 shows that when the H is placed in the n-fold position, the change in the Pt-Pt scattering (the $\mu_o\Delta\chi_{Pt-Pt}$ term, the dotted line in Figure 4) is the largest. This originates from a destabilization of the Pt-Pt bonds beneath the H. Thus the Pt-Pt multiple-scattering is strongly reduced in the presence of the H, and this appears as a large negative contribution in the $\mu_o\Delta\chi_{Pt-Pt}$ term. However, when H is adsorbed in the atop position, the change in the Pt-Pt scattering is very small. Surprisingly, the Pt-H scattering (the $\mu_o\chi_{Pt-H}$ term, the dashed line in Figure 4) is nearly independent of the H binding site. As discussed above, this was previously, but incorrectly, suggested to be most sensitive to the Pt-H bond strength). The AXAFS $\Delta\mu_o$ term (dashed-dotted line in Figure 4) is the smallest of the three terms, and appears to change sign upon moving the H from the n-fold to the atop position. Calculations suggest that this may result from a change in the direction of the charge transfer, but the magnitude of this charge transfer is very small for all adsorption sites.

Many FEFF8 calculations on small Pt_n clusters (with n=4-6) with H adsorbed in the 3-fold and atop sites have been performed[29,39]. DFT calculations support the FEFF8 results, showing that the destabilization is not near as severe when the H is bonded in the atop site[21]. All these calculations suggest that one of the critical factors that determine the relative size of the terms describing the variations in $\Delta\mu$ depends strongly on the H adsorption site[38]. The other important terms that determine the overall $\Delta\mu$ include the cluster shape and size, the H coverage, the Pt-H bond distance, the H binding site, the placement of the Fermi level (i.e. whether the cluster is metallic or not), and the choice of potentials in FEFF8 (Hedin-Lundquist or Dirac-Hara).

In short, when H is adsorbed in the 3-fold hollow site or bridged site, the Pt-Pt bond strength is decreased. This results in decreased Pt-Pt XAFS, and, hence, the first 2 terms in equation (1) dominate the difference spectrum $\Delta\mu$. However, if H adsorbs on an atop position on a Pt atom, the surrounding Pt atoms are only marginally influenced by the adsorbed H atoms, and the Pt-H scattering (the 3rd term in equation (1)) dominates $\Delta\mu$. Consequently, the signature of $\Delta\mu$ reflects the adsorption site of H. This introduces an exciting new possibility, namely the prospect of determining the H adsorption site on the Pt particles via the analysis of the XANES data. This has experimentally been confirmed by Teliska *et al*[39]. In an electrochemical cell with a Pt electrode and in the presence of H_2 at very high and intermediate coverage H is known to exist in atop and 3-fold sites, respectively. The experimental $\Delta\mu$ for these Pt electrodes showed the same change of the $\Delta\mu$ signature as was obtained from the FEFF8 calculations.

Density Functional Calculations (DFT)

We have previously reported DFT calculations on supported Pt_4 clusters[23]. A tetrahedral Pt_4 cluster was supported on 3 X_2O molecules to mimic the alumina support. By changing the nature of the X atoms from Na to F, a change in acidity can be simulated. Since F is more electronegative than Na, the oxygen atoms are electron rich in the presence of Na and electron poor in the presence of F, thereby simulating a change in electron richness on the support oxygen atoms going from acidic (X = F) to basic (X = Na) supports. On these supported Pt_4 clusters, a single H atom was attached in a 3-fold and atop site for both supported Pt_4 clusters. The Pt_4 cluster and H atom were allowed to relax their geometry within the restrictions of C(S) symmetry. The cluster and adsorbate positions are depicted in Figure 5. The X_2O molecules were kept at fixed positions. These calculations were repeated with 2 and 3 H atoms in 3-fold, bridged and atop positions.

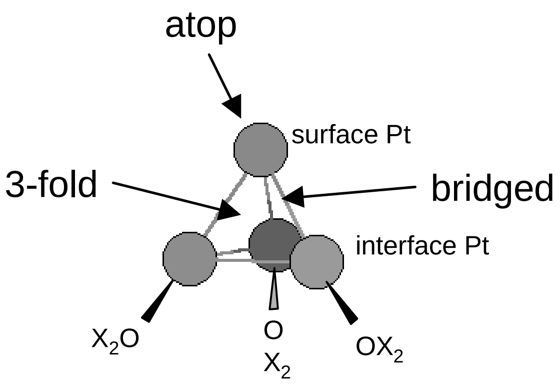

Figure 5: The supported Pt_4 model cluster with X_2O (X=F or Na) molecules mimicking the support.

The DFT calculations were carried out using the Amsterdam Density Functional Package ADF[40]. Details are give elsewhere[23]. The geometry optimizations were carried out in the spin unrestricted mode (the spin state is taken into account) at the GGA (generalized gradient approximation) level including scalar relativistic effects. Olsen *et al.*[20] showed that this level of accuracy provides good agreement with experiments for the interaction of H and platinum.

Results

EXAFS data analysis

In Figure 6A, the raw EXAFS data for the Pt/K-Al_2O_3 catalyst after reduction, evacuation at 323 K and 473 K are shown. The quality of the data is representative for all spectra. The evacuation treatment clearly changes the nodes of the oscillations. The distance between the nodes is smallest after reduction at 673 K and increases when the catalyst is evacuated at a

higher temperature. This indicates a decrease in the Pt-Pt bond length when the Pt/K-Al_2O_3 catalyst is evacuated at higher temperatures.

The Fourier Transform (k^2 weighted, 2.5 < k < 14 Å^{-1}) of the EXAFS data of the reduced (673 K) Pt/K-Al_2O_3 catalysts is shown in Figure 6B with the corresponding best fit. The quality of fit is representative for all data. Data analysis has been performed by multiple shell fitting in R space (1.6 < R < 3.2 Å). The O and Pt backscatterers have been identified using the difference file technique[33]. The variances in imaginary and absolute parts were used to determine the fit quality. The fit results are given in Table 1 (the Pt/K-Al_2O_3 catalyst) and Table 2 (Pt/Cl-Al_2O_3).

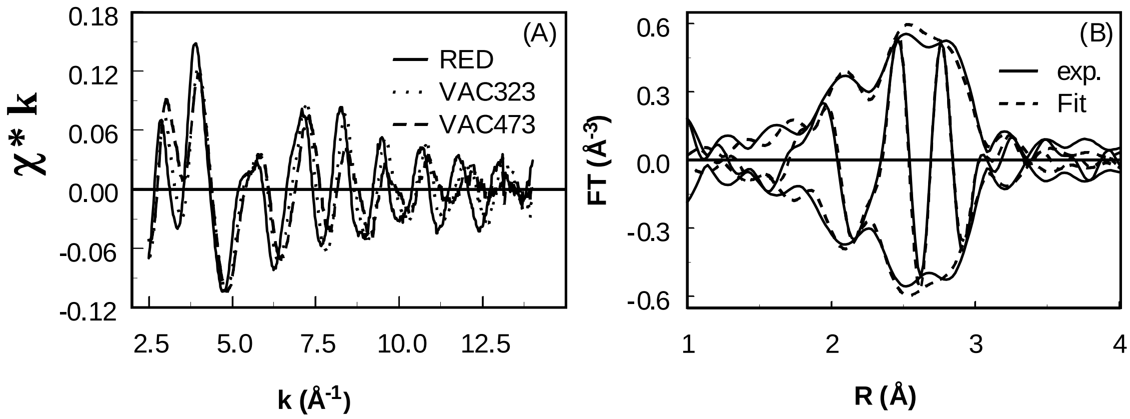

Figure 6: (A) k^1 weighted raw EXAFS spectra of Pt/K-Al_2O_3 after reduction at 673 K (solid line), after evacuation at 323 K (dotted line) and after evacuation at 473 K (dashed line). (B) Fourier transform (k^2, 2.5 < k < 14 Å^{-1}) of the spectrum taken after reduction at 673 K (solid line) and best R-space fit (1.6 < R < 3.2 Å, dashed line).

Table 1: EXAFS fit results for sample Pt/K-Al_2O_3[a].

treatment	scatterer	N (±10%)	R (Å) (± 0.02 Å)	$\Delta\sigma^2$ (x 10^3, ±5%)	E_0 (eV) (±10%)	variance	
						imaginary	absolute
RED	Pt	6.5	2.75	4.1	1.2	0.868	0.308
	O	0.3	2.10	2.0	-8.0		
VAC323	Pt	6.5	2.71	5.6	-0.3	0.414	0.135
	O	0.3	2.10	4.0	-7.3		
VAC373	Pt	6.5	2.71	5.0	-0.2	0.700	0.321
	O	0.4	2.10	4.0	-7.0		
VAC423	Pt	5.7	2.69	5.0	0.1	1.59	0.993
	O	0.5	2.10	4.0	-7.0		
VAC473	Pt	5.4	2.68	6.6	-0.6	2.07	0.632
	O	0.7	2.10	4.0	-2.6		

Table 2: EXAFS fit results for sample Pt/Cl-Al_2O_3[a].

treatment	scatterer	*N* (±10%)	R (Å) (± 0.02 Å)	$\Delta\sigma^2$ (x 10^3, ±5%)	E_0 (eV) (±10%)	variance imaginary	variance absolute
RED	Pt	8.8	2.76	2.5	-0.2	0.527	0.319
	O	n.d.[b]					
VAC323	Pt	7.9	2.74	3.6	-0.5	0.459	0.126
	O	0.2	2.05	5.0	0.0		
VAC373	Pt	7.3	2.73	2.6	-0.2	0.666	0.177
	O	0.3	2.09	4.0	-5.0		
VAC423	Pt	7.8	2.73	3.3	-0.2	0.466	0.139
	O	0.3	2.07	4.0	5.0		
VAC473	Pt	7.7	2.73	3.4	-0.4	0.951	0.429
	O	0.4	2.07	5.0	5.0		

[a] Fits were done in R-space, k^2 weighting, $1.6 < R < 3.2$ Å and $\Delta k = 2.5 – 14$ $Å^{-1}$. The Debye Waller factors ($\Delta\sigma^2$) were multiplied by 10^3 and are relative to the references. Accuracy limits[51] are given between brackets.
[b] This contribution was to small to be fitted.

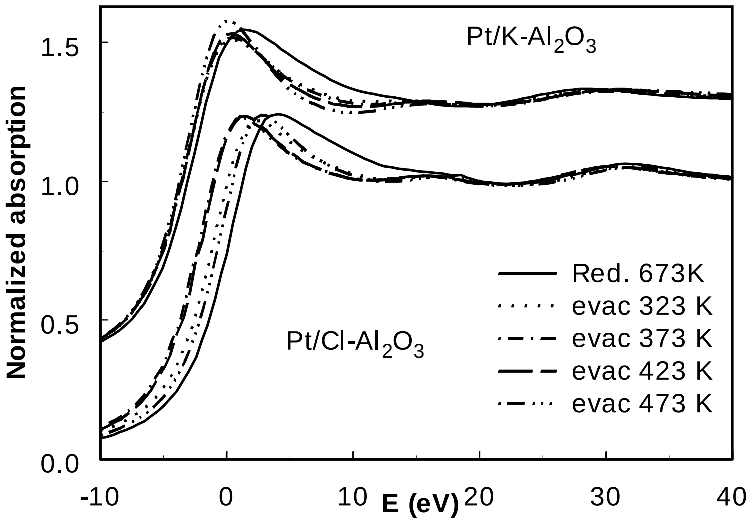

Figure 7: The L_3 edges for both catalysts after the various pretreatments. The spectra of catalyst Pt/K-Al_2O_3 have been shifted upwards by 0.3.

The Pt particle size after reduction for the Pt/K-Al_2O_3 catalyst is smaller than for the Pt/Cl-Al_2O_3 catalyst (coordination number N_{Pt-Pt} 6.5 vs. 8.8). The Pt/K-Al_2O_3 sample shows a larger decrease of the Pt-Pt coordination distance after evacuation at 473 K (Pt/K-Al_2O_3: 2.75 to 2.68 Å; Pt/Cl-Al_2O_3: 2.76 to 2.73 Å). The evacuation treatment leads for both catalysts to a decrease in the Pt-Pt coordination number and an increase in the Pt-O coordination number (see Table 1 and Table 2).

Table 3: Binding energies (kJ/mol) and equilibrium distances (Å) of H with respect to gasphase H_2 as a function of coverage, position and support acidity

Number of H atoms	Pt_4/F_2O		Pt_4/Na_2O		Position[a]	spin
	E_b (kJ/ mol H_2)	R_{Pt-H} (Å)	E_b (kJ/mol H_2)	R_{Pt-H} (Å)		
1 H	-77	1.55	-150	1.59	atop	½
2 H	-71	1.68[b] 1.77[c]	-77	1.74[b] 1.70[c]	bridged	0
3 H	-3	1.75[b] 2.05[c]	+42	1.87[b] 1.80[c]	3-fold	½

[a]: this was the optimal position. When H was placed in another position, the H drifted away.
[b]: distance from the surface Pt atom to the H.
[c]: distance from the interface Pt atom to the H.

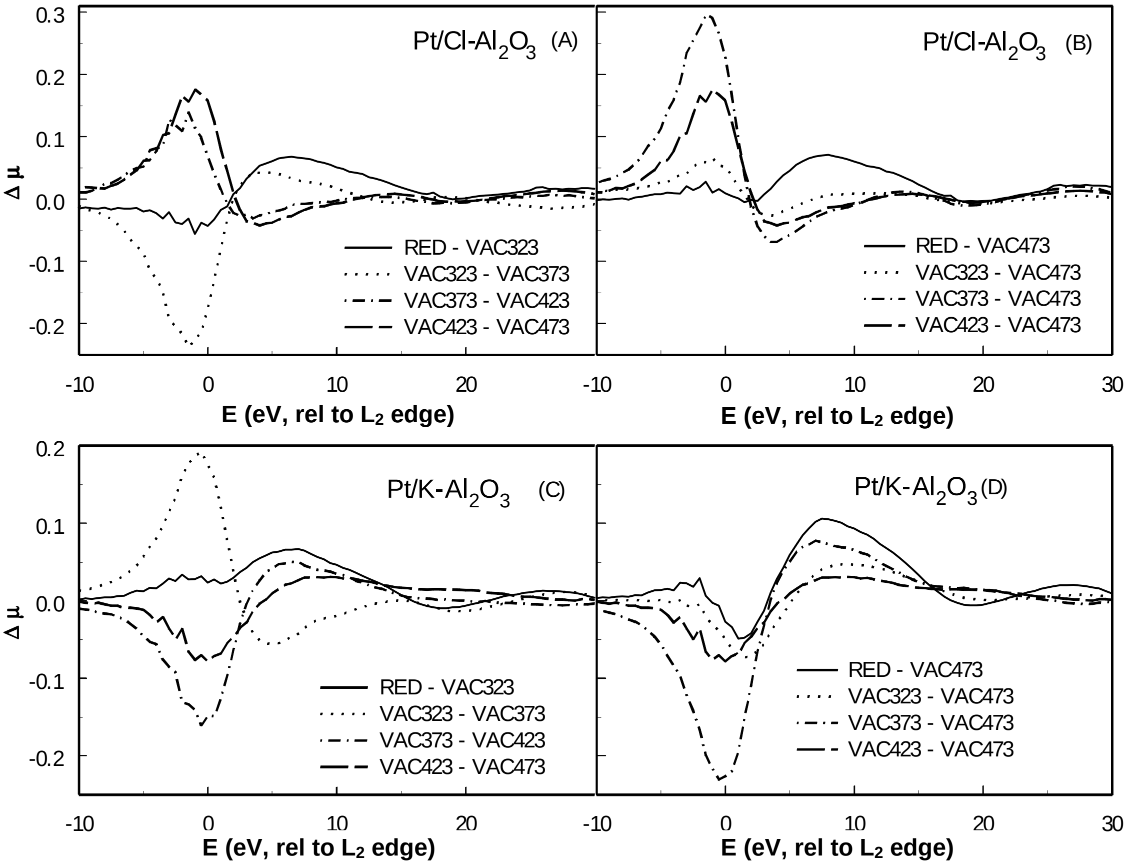

Figure 8: Difference spectra of the XANES region for the L_3 edges for Pt/Cl-Al_2O_3: (A) $\Delta\mu_{inc}(T)$ and (B) $\Delta\mu_{ads}(T)$, and Pt/K-Al_2O_3: (C) $\Delta\mu_{inc}(T)$ and (D) $\Delta\mu_{ads}(T)$.

Near Edge Analysis of the Pt L_3 absorption edges.

The L_3 X-ray absorption edges obtained after the various experiments are shown in Figure 7. The edge position and whiteline intensity are influenced by the amount of H adsorbed on the sample. The $\Delta\mu_{inc}(T)$ and $\Delta\mu_{ads}(T)$ difference spectra, displayed in Figure 8 (A,B: Pt/Cl-Al_2O_3 and C,D: Pt/K-Al_2O_3), show more detailed changes. It can clearly be seen that the difference spectra are strongly influenced by the acid/base properties of the support and by the coverage with H atoms. $\Delta\mu_{ads}(T)$ represents the H that remained on the surface after an evacuation procedure, $\Delta\mu_{inc}(T)$ reflects the effect of H desorption and a possible rearrangement of the remaining H.

DFT calculations

The calculated binding energies of H in the atop and 3-fold sites as a function of coverage and support molecules are given in Table 3. The binding energy E_b is calculated as the difference between molecular H_2 and a clean, supported Pt_4 cluster, in kJ/mol H_2 and with n H atoms on the Pt_4 cluster:

$$E_b = \frac{2}{n} E_{Pt_4-nH\ on\ X_2O} - \frac{2}{n} E_{Pt_4\ on\ X_2O} - E_{H_2} \qquad (2)$$

The required atomic reference energies are obtained according to Baerends *et al*[41]. When only 1 H atom is chemisorbed on the Pt_4 cluster, the most stable position is the atop site. A single H atom in a 3-fold site is unstable with respect to the atop site, so that in the geometry optimization, the H atom simply moves to the atop site, exactly as was found by Kua and Goddard[42]. The calculated binding energy is clearly also dependent on the acid/base properties of the support. The Pt-H bond for the basic support (3 Na_2O molecules) is –150 kJ/mol stronger than for the acidic support (F_2O, –76.6 kJ/mol). When the H coverage is increased to 3 H atoms on the Pt_4 cluster, the 3-fold sites turned out to be the most favored for H chemisorption. The Pt-H bond distance depends on the adsorption site; 1.55 – 1.60 Å in the case of the atop site, 1.75 – 1.90 Å in the 3-fold. The optimal doublet state is the optimal spin state for the supported Pt_4 clusters with 1 and 3 H atoms, the singlet state is optimal for 2 adsorbed H atoms.

Discussion

Effect of metal particle size and H coverage on the EXAFS region

The average size of Pt particles supported on K-Al_2O_3 is smaller than for the Pt/Cl-Al_2O_3 catalysts. Consequently, the influence of H removal on the contraction of the Pt-Pt distance is largest for the Pt particles on the K-Al_2O_3 support. The Pt-Pt bond length decreases from 2.75 Å after reduction to 2.71 Å after evacuation at 323 K. It decreases even further to 2.68 Å after

evacuation at 473 K. The contraction of the first shell Pt-Pt coordination is due to the increase of the dehybridisation of the s,p,d orbitals after H_2 desorption. Chemisorption of H tends to cancel the effect of the dehybridisation. In addition the Pt-O coordination number increases from 0.3 to 0.8 with increasing temperature of evacuation. The increase in Pt-O coordination can be explained by an increase in the metal-support interface after removal of chemisorbed H. The Pt particle is flattening out onto the support in order to minimize the effect of the coordinative unsaturation of the surface Pt atoms. The increase in disorder of the Pt-Pt coordination can also be explained by this change in morphology. The reduction of the Pt-Pt bond length and flattening of the particle induced by H desorption are well known phenomena for supported metal particles[4,43]. The EXAFS results for Pt/Cl-Al_2O_3 show similar trends, but due to the larger size of the Pt particles the effects due to the desorption of H are smaller.

Effect of H coverage on the XANES region

The effects of H desorption on the $\Delta\mu_{inc}$ and $\Delta\mu_{ads}$ difference spectra (see Figure 8) depend strongly on the surface coverage with chemisorbed H and the acid/base properties of the support. The $\Delta\mu_{ads}$ for the as prepared reduced samples have small maxima at –2 and 8 eV. It does not compare with the lineshape of H adsorbed in an atop or n-fold position (Figure 4). The lack of a clear signature and the double, small maximum indicate that a combination of both atop and 3-fold H is adsorbed on the Pt cluster. Moreover, the overall amplitude is small, since the contributions of atop and 3-fold are canceling each other out. This is as expected since all adsorption sites should contain H at this level of H coverage. Heating to 323K should remove the weakly bonded H, according to Figure 1. The $\Delta\mu_{inc}$(red) lineshapes for both supports do are similar to the $\Delta\mu_{ads}$(red) lineshapes. This indicates that the weakly bonded H exists in both atop and n-fold sites, exactly similar to that found from the TPD data for the other polycrystalline samples in Figure 1.

The data become very different upon further heating, implying that most of the weakly adsorbed H is removed upon heating to 373K. The signature of the $\Delta\mu_{inc}(373) = \mu_{L3}$ (VAC323) - μ_{L3} (VAC373) data resembles H in the n-fold position (Figure 4), showing that heating to 373K removes n-fold H in the acidic case. In the basic case, however, the $\Delta\mu_{inc}(373)$ signature shows that atop H disappears from the Pt surface. Indeed, the signature that resembles the H that is left on the surface at 373K, $\Delta\mu_{ads}(373) = \mu_{L3}$ (VAC373) - μ_{L3} (VAC473), shows primarily the signature of atop H in the acidic case, and of n-fold H in the basic case. At even higher temperatures, the $\Delta\mu_{ads}$ simply reflect the remaining occupied H sites, and $\Delta\mu_{inc}$ the removal of H from those same sites with increasing temperature. These signatures indicate that in the case of an acidic support at lower coverage of H (higher temperature of desorption) the H is adsorbed in the atop position, and in the case of the basic support it is adsorbed in the n-fold position.

In summary, the signature of the L_3 XANES difference data strongly suggest that at full H coverage both atop and n-fold Pt sites are occupied independent of the acid/base properties of the support. The weakly bound H is probably in the 3-fold Pt sites on the flat (111) faces and perhaps near the edges in the atop Pt sites, exactly as found previously from TPD and spectroscopic data. However the Pt absorption sites of the strongly bound H detected after removal of the weakly bound H are very dependent on the support, with atop H preferred for acidic supports, and n-fold preferred for basic supports. These results are summarized in Figure 1, which shows that the situation for the strongly bound H on Pt particles supported on basic supports is very similar to that found for stepped single crystal Pt surfaces. This is not a surprise, since one would expect that the chemisorption process of H on small Pt clusters on basic supports is somewhat similar to that of the larger Pt crystal surfaces with steps: it has been shown earlier[23,25] that the Pt 5d band is shifted to higher energy and is broadened when the support basicity is increased, which resembles more the valence band of bulk platinum. In addition, it has been shown that the average number of Pt atoms per Pt particle for which the insulator-to-conductor transition takes place is decreased by increasing the support basicity[22,44]. This implies also that Pt particles on basic supports behave more like metallic Pt. Thus, only acidic supports appear to introduce the large change in the Pt chemisorption properties towards strongly bonded H, namely to make the atop sites more stable. The variation in the mode of H adsorption on Pt particles as a function of acid/base properties of the support will have significant implications for catalysis. This will be discussed in forthcoming papers .

DFT calculations

The DFT calculations, as summarized in Table 3, show that regardless of the acid/base properties of the support, the first H atom preferentially adsorbs on the atop site. This preference for the atop site on Pt was also suggested by the results of Olsen *et al.*[20] and Kua and Goddard[42]. However, in the case of a basic support (Na_2O), the Pt-H bond energy is larger than for an acidic support (F_2O). The bond energies of –77 to –150 kJ/mol (for 1 H_2 molecule) that are found are somewhat higher than found in other studies for Pt (111) surfaces (~ -80 kJ/mol)[20]. This can be attributed to the highly unsaturated Pt atoms in the case of the Pt_4 cluster under study. However, the observed small Pt-H bond length of 1.55- 1.60 Å for the atop position[21] is in good agreement with other theoretical results reported in the literature.

Regardless of the acid/base properties of the support, at higher coverage (3 H atoms on a Pt_4 cluster), the H atoms should preferentially adsorb in the n-fold positions, according to the DFT results. However, the large difference between the Pt_{int}-H distance of 2.05 Å and Pt_{surf}-H distance of 1.75 Å in the case of the acidic F_2O support molecules indicates that the H atoms are 'reluctant' to move into the full 3-fold position even at this coverage. On the basic Na_2O support molecules, the Pt_{surf}-H and Pt_{int}-H are more similar, 1.80 and 1.87 Å respectively.

This indicates that the H adsorption position for Pt on a basic support (Na_2O) is much closer to 3-fold symmetry than for Pt on the acidic support (F_2O) . The bond lengths in the range of 1.75 - 1.90 Å as obtained for H adsorbed in 3-fold hollow sites is in agreement with experiment and calculations presented in the literature for Pt (111) surfaces[21,32,45].

However, our DFT bond energy for 3H on Pt_4/Na_2O with H in the 3-fold sites is positive, indicating that a clean Pt_4/Na_2O cluster plus 1½ H_2 molecules is more stable than the 3H chemisorbed on Pt_4/Na_2O cluster. In fact, 3 H atoms on a supported Pt_4 cluster is a very high coverage. Only one of the four Pt atoms is a true surface atom; the other 3 atoms are interfacial atoms bonded to the Na_2O or F_2O support molecules. Following the concept of 'conservation of bond order'[46], these interface Pt atoms will bond only weakly to new H adsorbates. The Pt-Na_2O bond is stronger than the Pt_4-F_2O bond (see chapter 8 of this thesis), and, therefore it is not surprising that our calculated adsorption energy for 3H on Pt_4/Na_2O is positive.

Experimentally, H/Pt ratios larger than 1 are commonly found in highly dispersed Pt in supported metal catalysts[47,48]. These high H/Pt values are a strong indication that at high coverage H can adsorb on both atop and 3-fold hollow sites simultaneously[19]. These experimental chemisorption data in combination with the ADF calculations on a supported Pt_4 cluster together with the above discussed $\Delta\mu$ L_3 difference spectra confirm that both atop and 3-fold hollow sites have to be taken into account in describing the H chemisorption process on the surface of supported Pt particles.

General description of hydrogen chemisorption on supported Pt particles

The DFT calculations indicate that at low coverage H adsorbs in atop sites much stronger to Pt clusters on basic supports than on acidic supports. With increasing coverage, the Pt-H bond strength decreases and the difference in bond strength between basic and acidic supports also decreases. At the highest coverage of 3 H atoms on the Pt_4 cluster, the acidic Pt_4H_3/F_2O cluster is even more stable than the basic Pt_4H_3/Na_2O cluster. The results from DFT calculations as summarized in Table 3 are plotted in Figure 9 and give some insights into the situation of supported Pt particles.

Upon reduction of a supported Pt catalyst in a H_2 atmosphere, effectively any H_2 with an exothermic binding enthalpy is adsorbed on the catalyst at low temperature. This results in a particular H coverage, as is illustrated in Figure 9 for the supported H_nPt_4 cluster. When this catalyst is evacuated at higher temperature, *e.g.* 330 K, some H is removed. The binding energy of H on Pt(111) has been estimated both from experimental TPD data and from theory to be approximately 70-77 kJ/mol[21], and this H is all removed by 325K. As is indicated in Figure 9, after this initial heating in vacuum, the change in coverage is much larger for Pt on the acidic support. This suggests that the fraction of weakly bonded H is greater on an acidic

support compared to a basic support, or conversely that the fraction of strongly bonded H is greater on basic supports than on acidic supports.

If the H coverage indeed depends on the support acidity, this should also be reflected by experiments. In order to check this, a series of Pt/LTL catalysts were investigated. The acidity of these LTL zeolites was varied by varying the K content from K/Al=0.47 (most acidic) to 1.53 (most basic). Experimental details are given elsewhere[27,49]. The final metal catalysts all have similar particle sizes, as was determined from EXAFS and electron microscopy. In addition, standard H_2 chemisorption experiments have been performed on these catalysts (details elsewhere[4]) in order to determine the metal dispersion. In these experiments, the H_2 that desorbs below approximately 323 K is regarded as weakly adsorbed H, whereas the H_2 that desorbs above this temperature is considered to be strongly adsorbed H, exactly as is illustrated in Figure 1. In Figure 10, the ratio of the strongly adsorbed H to the total adsorbed H (strong plus weak) as a function of the K/Al ratio is given. As can be seen, the relative amount of strongly adsorbed H increases with increasing basicity (K/Al ratio) of the support. These experiments confirm what we find from the DFT calculations.

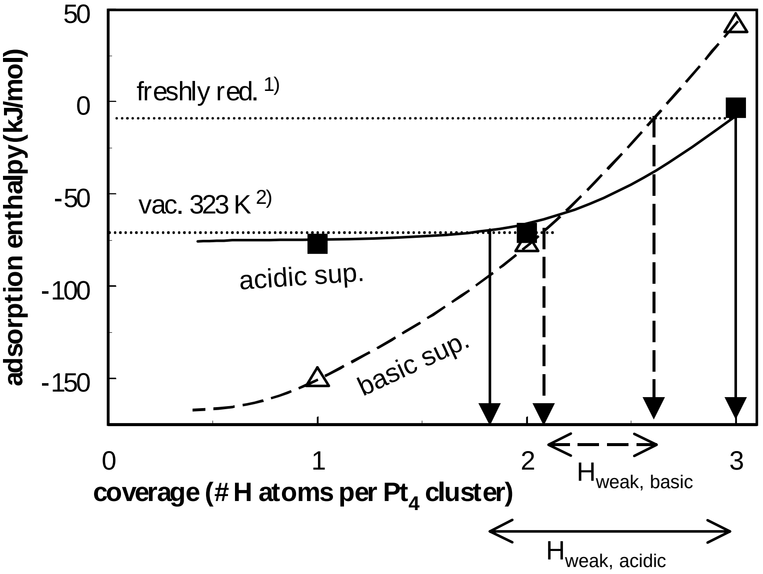

Figure 9: The H_2 adsorption energy as calculated by ADF vs H coverage (H_n/Pt_4 cluster) for the acidic and basic supports (acidic: solid squares and solid lines, basic: open triangles and dashed lines). [1)] In a H_2 atmosphere at low temperature, all H_2 that has a exothermic (negative) adsorption enthalpy binds to the Pt, and the predicted coverage (H/Pt_4) is shown on the x-axis. [2)] Upon evacuation at high T (eg. 323 K), only strongly adsorbed H_2 with a large exothermic adsorption enthalpy (< -75 kJ/mol) remains on the surface. The amount of weakly adsorbed H_2 is relatively small for basic supports.

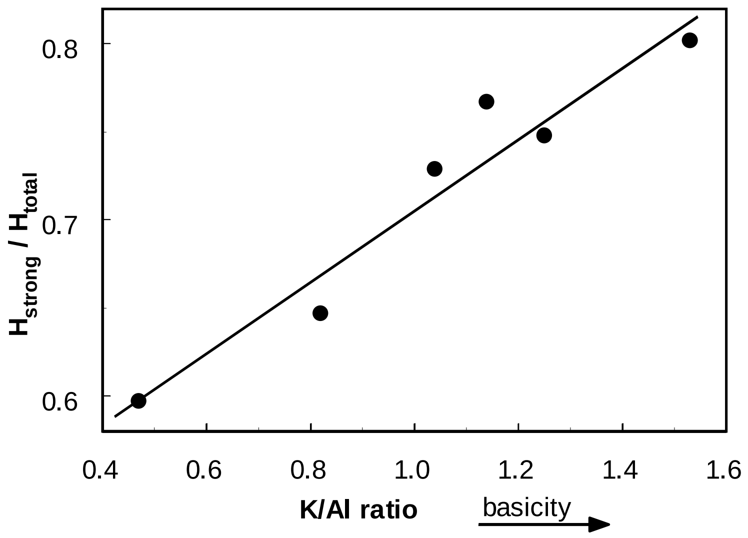

Figure 10: The amount of strongly adsorbed H relative to the total amount of H adsorbed as a function of support basicity.

The Δμ signatures and DFT calculations indicate the existence of atop H at low coverage, especially in the case of acidic supports. Atop H has never been seen spectroscopically on Pt, except at very high coverage in an electrochemical cell[39] and on Pt black at low temperatures[17], but never at temperatures greater than 330K. Although atop H has been seen via HREELS on Ir (111) it has not been seen on Pt(111) at any coverage or temperature. However, Kua and Goddard[42] have suggested that at very low coverage (below 1/7 monolayer [ML]) H may in fact prefer the atop sites on Pt (111), since it can then maximize its overlap with 3 interstitial bond orbitals (IBO). At coverage above this level, the H clearly prefers the 3-fold fcc sites on Pt(111) where it can maximize its overlap with one IBO, and not have to share with other H.

However at very low coverage the H also prefers to be delocalized on the surface to minimize the vibrational zero point energy. The delocalized H exists on Pt (111) surfaces because the difference in energy between 3-fold fcc and bridged sites is small, and the energy barrier is marginal. This delocalized/localized (dl/l) transition on Pt(111) occurs at a coverage greater than 0.5 ML. Indeed Christman[50] was unable to observe a LEED pattern until 0.8 ML of H was absorbed on the surface. Since the atop/3-fold (a/3f) transition occurs at lower coverage (~ 0.15) than the Dl/l (0.5-0.8) transition, localized atop H does not exist on Pt(111).

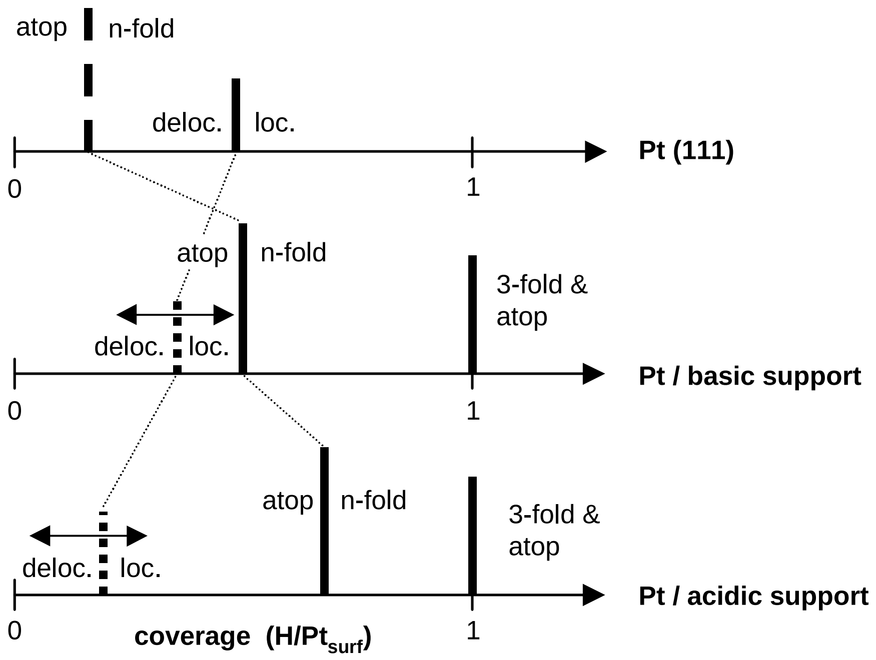

Figure 11: Schematic showing the transitions from atop to 3-fold and delocalized to localized H as a function of coverage and support material. Solid vertical lines indicated transition regions as suggested from experimental data, dashed vertical lines possible transition regions, but not experimentally verified. Short horizontal arrows indicated large uncertainty where predicted transition might occur.

The relative coverage for which the a/nf (atop/n-fold) and dl/l transitions are expected on supported Pt clusters will be different than on Pt(111). Since the most strongly bonded H is delocalized, we suggest that even on small particles H adsorbed at low coverage might be delocalized. On small particles, however, the sites are more heterogeneous since the coordination of the Pt atoms is irregular and depend on the position in the particle. Consequently, there are less sites (*e.g.* a series of adjacent 3-folf fcc sites) where H can be delocalized and it is expected that the dl/l transition occurs at lower coverage compared to Pt (111) surfaces. This delocalized H is invisible in the XANES data, but its effects on the Pt cluster and the water double layer in an electrochemical cell have been confirmed by Teliska *et al*[39]. Further, the dl/l transition occurs at higher coverage on basic supports, as suggested in Figure 11. Since the $\Delta\mu$ signatures for low coverage indicated atop H for Pt on acidic supports and n-fold H for Pt/basic supports, H apparently localizes into atop sites on acidic supports, and into n-fold sites on basic supports. Furthermore, the DFT calculations show that H is adsorbed in the 3-fold site at higher coverage, regardless of the support. The $\Delta\mu$ signatures and all literature discussed showed that H is adsorbed in both atop and 3-fold sites at even higher coverage.

We do not observe delocalized H on the supported Pt clusters. We note that even if the dl/l transition does not exist on small clusters, the coverage must be much smaller on basic supports to observe the atop H, and then the signal might be too small to observe at all. Thus it is possible, though not likely, that even at 473K we have not yet reached the a/nf transition, preventing the observation of atop H on the basic supports.

Conclusions

Hydrogen adsorption on Pt/Cl-Al_2O_3 and Pt/K-Al_2O_3 has been studied utilizing Pt $L_{2,3}$ XANES data. Both the effects of hydrogen coverage and support acid/base properties were investigated. The preferred H absorption site can be ascertained from the signature of the Pt ΔL_3 XANES difference spectra: L_3 edge measured in the presence of chemisorbed hydrogen minus L_3 edge taken in vacuum. Based upon this signature, it was found that at low coverage hydrogen prefers to adsorb in the 3-fold hollow sites near edges for Pt particles supported on basic supports. However, when Pt is supported on acidic carriers, the hydrogen prefers at low coverage to adsorb on the edge atop sites.

This difference in adsorption site can be understood with the help of density functional calculations. The DFT calculations for H_n/Pt_4 clusters show that at low coverage, hydrogen prefers the atop sites, with the adsorption energy much lower for Pt on acidic supports compared to basic supports. At higher coverage, the difference in adsorption energy between the basic and acidic supports is much smaller and the hydrogens adsorb in the 3-fold hollow site. Consequently, the hydrogen coverage at low temperatures is similar for basic and acidic supports, but very different at high temperatures. This was confirmed by H_2 chemisorption experiments involving a series of Pt/LTL catalysts with different support acidities.

Reference list

1. R. A. Dalla Betta and M. Boudart, *Proc 5th Int Con Cat* (1973), 1329-1341.
2. A. de Mallmann and D. Barthomeuf, *J. Chim. Phys.*, **87** (1990), 535-538.
3. H. Yasuda and S. Y. Y. Sato, *Catal. Today,* **50** (1999), 63-71.
4. M. K. Oudenhuijzen, J. H. Bitter and D. C. Koningsberger, *J. Phys. Chem. B,* **105** (2001), 4616-4622.
5. J. J. F. Scholten, A. P. Pijpers and A. M. L. Hustings, *Catal. Rev. - Sci. Eng.,* **27** (1985), 151-206.
6. Z. Paál and P. G. Menon, *Catal. Rev. - Sci. Eng.,* **25** (1983), 229-324.
7. J. H. Sinfelt, Y. L. Lam, J. A. Cusumano and A. E. Barnett, *J. Catal.,* **42** (1976), 227-237.
8. J. H. Sinfelt and G. H. Via, *J. Catal.,* **56** (1979), 1-11.
9. C. J. Hagedorn, M. J. Weiss and W. H. Weinberg, *Phys. Rev. B,* **60** (1999), R14016 - R14018.
10. S. M. Davis and G. A. Somorjai, *Surf. Sci.,* **91** (1980), 73-91.
11. C. S. Ko and R. J. Gorte, *Surf. Sci.,* **161** (1985), 597-607.
12. K. Christmann and G. Ertl, *Surf. Sci.,* **60** (1976), 365-384.

13. K. E. Lu and R. R. Rye, *Surf. Sci.,* **45** (1974), 677-695.
14. H. Wang, R. G. Tobin, D. K. Lambert, G. B. Fisher and C. L. Dimaggio, *Surf. Sci.,* **330** (1995), 173-181.
15. H. Wang, R. G. Tobin and D. K. Lambert, *J. Chem. Phys.,* **101** (1994), 4277-4285.
16. V. D. Thomas, J. W. Schwank and J. L. Gland, *Surf. Sci.,* **in press** (2001).
17. S. Tsuchiya, Y. Amenomiya and R. J. Cvetanovic, *J. Catal.,* **19** (1970), 245-255.
18. M. J. Puska and R. M. Nieminen, *Surf. Sci.,* **157** (1985), 413-435.
19. A. Renouprez and H. Jobic, *J. Catal.,* **113** (1988), 509-516.
20. R. A. Olsen, G. J. Kroes and E. J. Baerends, *J. Chem. Phys.,* **111** (1999), 11155-11163.
21. G. Papoian, J. K. Nørskov and R. Hoffmann, *J. Am. Chem. Soc.,* **122** (2000), 4129-4144.
22. Chapter 7 of this thesis.
23. Chapter 8 of this thesis.
24. D. C. Koningsberger, J. de Graaf, B. L. Mojet, D. E. Ramaker and J. T. Miller, *Appl. Catal. A: General,* **191** (2000), 205-220.
25. D. E. Ramaker, J. de Graaf, J. A. R. Van Veen and D. C. Koningsberger, *J. Catal.,* **203** (2001), 7-17.
26. S. N. Reifsnyder, M. M. Otten, D. E. Sayers and H. H. Lamb, *J. Phys. Chem. B,* **101** (1997), 4972-4977.
27. B. L. Mojet, D. E. Ramaker, J. T. Miller and D. C. Koningsberger, *Catal. Lett.,* **62** (1999), 15-20.
28. K. Asakura, T. Kubota, N. Ichikuni and Y. Iwasawa, *Stud. Surf. Sci. Catal.,* **101** (1996), 911-919.
29. A. L. Ankudinov, J. J. Rehr, J. Low and S. R. Bare, *Phys. Rev. Letters,* **86** (2001), 1642-1645.
30. D. E. Ramaker, B. L. Mojet, M. T. Garriga Oostenbrink, J. T. Miller and D. C. Koningsberger, *Phys. Chem. Chem. Phys.,* **1** (1999), 2293-2302.
31. A. L. Ankudinov, B. Ravel, J. J. Rehr and S. D. Conradson, *Phys. Rev. B,* **58** (1998), 7565-7576.
32. P. J. Feibelman and D. R. Hamann, *Surf. Sci.,* **182** (1987), 411-422.
33. D. C. Koningsberger, B. L. Mojet, G. E. van Dorssen and D. E. Ramaker, *Top. Catal.,* **10** (2000), 143-155.
34. M. Vaarkamp, J. T. Miller, F. S. Modica and D. C. Koningsberger, *J. Catal.,* **163** (1996), 294-305.
35. M. Vaarkamp, F. S. Modica, J. T. Miller and D. C. Koningsberger, *J. Catal.,* **144** (1993), 611-626.
36. J. B. A. D. Van Zon, D. C. Koningsberger, H. F. J. Van 't Blik, R. Prins and D. E. Sayers, *J. Chem. Phys.,* **80** (1984), 3914.
37. T. Kubota, K. Asakura, N. Ichikuni and Y. Iwasawa, *Chem. Phys. Lett.,* **256** (1996), 445-448.
38. D. E. Ramaker and D. C. Koningsberger, *Phys. Rev. Letters,* **submitted** (2002).
39. M. L. Teliska, W. E. O'Grady and D. E. Ramaker, **to be published** (2002).
40. Amsterdam Density Functional Package ADF 2000.02, Department of Theoretical Chemistry, Vrije Universiteit, Amsterdam. http://www.scm.com.
41. E. J. Baerends, V. Branchadell and M. Sodupe, *Chem. Phys. Lett.,* **265** (1997), 481-489.

42. J. Kua and W. A. Goddard III, *J. Phys. Chem. B,* **102** (1998), 9481-9491.
43. B. Delley, D. E. Ellis, A. J. Freeman, E. J. Baerends and D. Post, *Phys. Rev. B,* **27** (1983), 2132-2144.
44. D. E. Ramaker, M. K. Oudenhuijzen and D. C. Koningsberger, *J. Chem. Phys.* (submitted).
45. A. M. Baró, H. Ibach and H. D. Bruchmann, *Surf. Sci.,* **88** (1979), 384-398.
46. E. Shustorovich, *Adv. Catal.,* **37** (1990), 101-163.
47. B. J. Kip, F. B. M. Duivenvoorden, D. C. Koningsberger and R. Prins, *J. Catal.,* **105** (1987), 26-38.
48. J. de Graaf, A. J. van Dillen, K. P. de Jong and D. C. Koningsberger, *J. Catal.,* **203** (2001), 307-321.
49. Chapter 4 of this thesis.
50. K. Christmann, *Surf. Sci. Reports,* **9** (1988), 1-163.
51. G. G. Li, F. Bridges and C. H. Booth, *Phys. Rev. B,* **52** (1995), 6332.

7

Observation of Strong Support Effects on the Insulator to Metal Transition of Supported Pt Clusters as Observed by X-ray Absorption Spectroscopy

Abstract

The development of a new *in situ* probe of metallic character in supported metal clusters utilizing X-ray absorption spectroscopy is described. A very strong support effect on the metal-insulator transition with cluster size in supported Pt clusters is found. Pt particles with basic supports show metallic screening for sizes as small as 6Å. In contrast, with acidic supports the Pt particles do not show metallic behavior below 10Å.

Introduction

There is great interest in deepening our understanding of metal atom clusters, particularly in the solid state[1]. Such clusters are of fundamental interest because they span the range from the very small molecular clusters having quantized states to the relatively large microcrystalline clusters having quasi-continuous bands. They constitute new types of nanoscale materials with unique properties. The evolution of the electronic structure with cluster size is of particular interest; *e.g.*, when does the cluster become metallic[2]? One of the problems in studies of the insulator-metal transition in these materials is finding some definitive experimental probe. Different experimental probes may measure different aspects of the electronic structure through the transition, causing different conclusions to be reached as to its onset[3]. A clear understanding of the transition, if successfully exploited, could pave the way for precise control of nanoscale properties and thus lead to a broader range of material applications, such as in novel catalysts, gas sensors, electronic materials, etc. If these applications are to be realized however, the effect of the interaction of a nanoscale cluster with its supporting substrate or surroundings must also be quantified[4]. Thus, the experimental probe must be applicable *in situ* under general conditions.

The range of probes for such metal-insulator transitions is very broad with each probe having its own strengths and weakness as summarized recently by Dowben[3]:

Direct conductivity measurements are difficult to apply to free clusters, and even to two-dimensional systems.

- Spectroscopic measurements, such as electron energy loss spectroscopy (EELS), infrared (IR) and Raman spectroscopy, can probe the very small energy excitations across the Fermi level (E_f) or band gap by changes in the peak shape such as via the Drude tail in photoemission. However, such lines-shape changes can also be caused by a number of experimental effects making these measurements difficult.
- Measurements of the dielectric response from the optical properties and plasmon losses have similar problems.
- Work function and ionization potential measurements, although in widespread use for this purpose, may not be a good measure of the metallicity.
- Because of these problems, observations of the screening of the core-hole and the creation of excitons in core level excitation has become a favored technique for observing the metal-insulator transition; the most utilized here has been core-level X-ray photoelectron spectroscopy (XPS)[5].

This paper describes the development of a new probe of metallic character utilizing core-level X-ray absorption spectroscopy (XAS), which has several important advantages over XPS:

- Because of its very nature (photons in and photons out using transmission or fluorescence yield mode), XAS can be applied *in situ* under general conditions, as opposed to XPS, which requires ultra-high vacuum (UHV) conditions.

- Further, the XAS data yields simultaneous the extended X-ray absorption fine structure (EXAFS), which provides simultaneously information about the cluster size.
- Finally, the final state of the XAS excitation in the near edge region as studied here does not change the charge on the cluster, so that the interaction with the support or surroundings is not different from the initial state. In contrast, XPS leaves a positive charge on the cluster which requires a separation of the contributions arising from screening by the cluster itself and that arising from polarization by the support[6]. This separation can be difficult.

The XAS technique developed here will show that the support can critically alter the metallicity of the cluster, but the effect observed is a direct effect existing already in the ground state. Although the technique is applied here in UHV conditions, it can in principle be used under *in situ* conditions.

Experimental methods

Sample preparation and data collection

The newly developed technique is applied to Pt clusters supported on high surface area alumina or silica (denoted as Cl-Al_2O_3 or K-SiO_2) modified by doping with promoters such as Cl or K to alter the acidity/alkalinity of the support. Data for Pt dispersed in zeolite LTL with various K^+ contents has also been utilized[7]. It has been shown elsewhere that this cation exchange induces profound changes in the acid/base properties of the zeolitic support[8] and, related to that, different catalytic properties of the supported clusters[7,9]. The preparation of these samples has been described previously[7,9,10,a].

The samples (typically 120-150 mg) were pressed into self-supporting wafers and placed in an *in situ* stainless steel cell with controlled atmosphere[11]. The samples were dried in flowing He for 1 hr at 423 K and reduced for 1 hr in H_2 at 623 K. Finally, the hydrogen was pumped off the Pt surface by evacuating for 1 hr at 473 K. After the evacuation, the samples were cooled down to liquid nitrogen temperature, at which temperature the spectra were recorded. During the cooling down and spectrum recording at liquid nitrogen temperatures, a vacuum better than 5 x 10^{-3} Pa was maintained.

---

[a] The Al_2O_3 support (pseudobohemite, Criterion) was impregnated with a solution of H_2PtCl_6 (2 wt% Pt), dried, calcined at different temperatures and further reduced at 623 K. The silica support was prepared by ion-exchange of SiO_2 microspheres (Davison grade 644, 284 m^2/g, 1.12 cc/g) with an amount of KOH followed by calcination at 400°C. Pt was added by incipient wetness impregnation using an aqueous solution of $Pt(NH_3)_4(NO_3)_2$ followed by calcination at 225°C. The acidity of the LTL zeolite was varied by impregnating a commercial K-LTL zeolite with KNO_3 or exchanging it with NH_4NO_3 to give different K/Al ratios. Pt (1wt%) was added as described above followed by drying at 120°C.

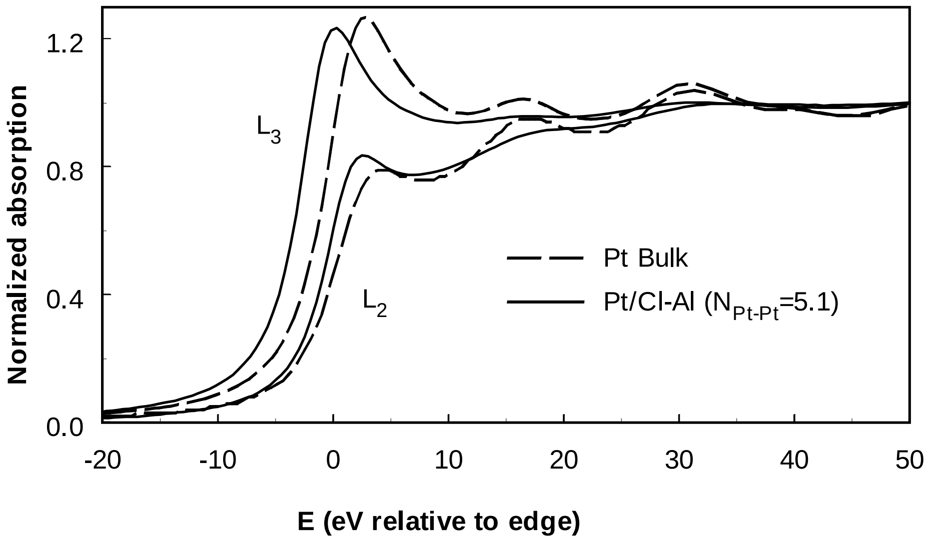

Figure 1: L_3 and L_2 edges (aligned as described in the text) for Pt (N = 5.1)/Cl-Al_2O_3 (solid line) and for bulk Pt (dotted line).

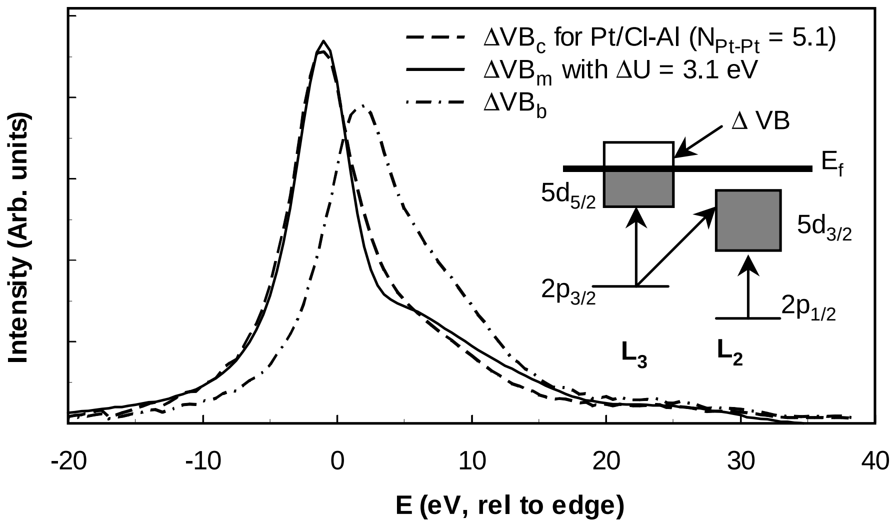

Figure 2: Comparison of ΔVB_{bulk}, $\Delta VB_{cluster}$, and the ΔVB_{model}, where ΔVB_{model} was obtained using eq. 1 with an optimal ΔU value of 3.1 eV. Here ΔVB_{bulk} and $\Delta VB_{cluster}$ have been area normalized. Insert: Illustration of the spin-orbital coupling effects in the X-ray absorption $L_{2,3}$ edge spectra and 5d valence band. The energy scale is non-linear, *i.e.* that for the 2p and 5d levels are different.

The XAS spectra of the Pt/LTL and Pt/K-SiO_2 samples were taken at the SRS laboratories (station 9.2) in Daresbury, UK, the spectra of the Pt/Cl-Al_2O_3 samples were taken at the ESRF (BM 29) in Grenoble, France and at the HASYLAB (X1.1) in Hamburg, Germany. These measurements were done in transmission mode using ion chambers filled with Ar to have an

X-ray absorbance of 20% in the first and 80% in the second ion chamber. The monochromator was detuned to 50% maximum intensity to avoid higher harmonics present in the beam.

Data analysis methods

The method described here to analyze the screening effects in the various Pt catalysts uses lineshape changes in the whitelines, not changes in the absolute energy of the X-ray absorption edge. Therefore, the L_3 spectra of the Pt catalysts are aligned carefully on the EXAFS oscillations at higher energy of the accompanying L_2 spectra. An example of the L_2 and L_3 edges for one of the $Cl\text{-}Al_2O_3$ samples is shown in Figure 1.

At higher energy, the EXAFS oscillations are influenced only by the geometry around the X-ray absorber atom, not final state effects. The much smaller whiteline intensity near the edge in the L_2 data compared to the L_3 in transition metal samples is well known and arises from spin-orbit interactions in the Pt 5d state, and the preferred selection rules as illustrated in the insert of Figure 2[12]. The $5d_{5/2}$ –$5d_{3/2}$ spin-orbital splitting is ~ 1.5-2.5 eV in Pt. The L_3 edge reflects the empty levels of both the $d_{5/2}$ and $d_{3/2}$ bands weighted as $d_{5/2}/d_{3/2} \approx 6$ (Figure 2); however, the L_2 edge reflects only the $d_{3/2}$ level. The symbol ΔVB is utilized to indicate the difference in the empty valence band in the L_3 minus that in the L_2. The difference, ΔVB, between the L_3 and L_2 data isolates the whiteline intensity as shown in Figure 2, and provides a spectral measure of the valence-band 5d empty density of states (DOS), which is modified by the presence of the core-hole consistent with the final-state rule[13-15].

Figure 2 also compares the ΔVB obtained for bulk Pt with that for a Pt cluster supported on alumina with coordination number N = 5 (approximately 7 Å diameter) as obtained by analysis of the EXAFS data. The difference in line shape here reveals that the core-hole electron attraction U in the cluster is different than it is in the bulk. Because of metallic screening, U is near zero in bulk Pt. A reasonable average measure of this U in the cluster can be obtained by modifying the bulk lineshape, ΔVB_b by utilizing the Anderson Z+1 impurity model[16,17],

$$\Delta VB_{model}(E) = \frac{\Delta VB_{bulk}(E)}{[1 - \Delta U \bullet I(E)]^2 + [\pi \bullet \Delta U \bullet \Delta VB_{bulk}(E)]^2} \qquad (1)$$

with *ΔVB_{model}*

with	ΔVB_{model}	: the modeled ΔVB at energy E (it is the distorted ΔVB_{bulk}),
	ΔVB_{bulk}	: the bulk ΔVB, obtained from a Pt foil.
	ΔU	: the core-hole – electron attraction in the cluster, relative to the bulk (U≈0), where ΔU (ΔU represents the core-hole electron attraction) is chosen such that ΔVB_{model} is closest to the ΔVB of the measured cluster, $\Delta VB_{cluster}$, and
	$I(E)$	: the Hilbert transform:

$$I(E) = \int_{\varepsilon=-\infty}^{\varepsilon=+\infty} \frac{\Delta VB_{bulk}(\varepsilon)}{E-\varepsilon} d\varepsilon \qquad (2)$$

with $I(E)$ the Hilbert transform at energy E, and in practice the integral is calculated for -40 eV to +40 eV around the absorption edge.

Results

Figure 3 plots the changes in ΔU and the ratio of the integrated areas, R = $A(\Delta VB_{cluster})/A(\Delta VB_{bulk})$ with cluster size for the acidic and basic supports. The cluster size is determined from the experimental Pt-Pt coordination number N_{PtPt} obtained from the EXAFS. Model calculations assuming spherical clusters with FCC packing[18,19] then allow us to give the approximate particle diameters, the total number of atoms Z_{total}, and dispersion ($Z_{surface}/Z_{total}$). Note the very non-linear scale in diameter on this linear coordination number axis. These scales show that for N<7.5, the dispersion is near one meaning that most of the atoms are surface atoms.

Figure 3 shows that ΔU and R vary dramatically with cluster size and support acidity. Note first that ΔU goes to zero and R approaches 1 for the large clusters as expected, since the electronic structure in the larger clusters must eventually resemble that in the bulk (the apparent increase in ΔU around N = 7 on basic supports will be discussed elsewhere[20]).

Discussion

Validity of the impurity model

The Anderson Z+1 impurity model[16,17] was used to obtain a measure of the core-hole electron attraction U (Equation 1). The Z+1 impurity model chosen here assumes that the impurity states (5d orbitals on atom with core-hole) are largely decoupled from the other host states, in contrast to the Clogston-Wolf model, which assumes that the impurity-host hybridization matrix element is unchanged from the host-host[21]. The former is used for two reasons: it is sufficiently valid since we are interested only in the relative changes in ΔU with respect to bulk Pt, and it is more convenient.

Figure 2 shows excellent agreement between the model ΔVB_{model} and that for the cluster $\Delta VB_{cluster}$ utilizing a ΔU of 3.1 eV. Note that the small shoulder in the experimental $\Delta VB_{cluster}$ is nicely reproduced in the model. The ΔVB_{bulk} and $\Delta VB_{cluster}$ have been area normalized here and Equation 1 preserves this normalization. The total integrated area $A(\Delta VB_{cluster})$ before normalization is NOT a direct measure of the difference in number of holes in the two spin-orbit valence bands, $h_{5/2}$-$h_{3/2}$, as one might expect. We will show below, however, that it reflects on the nature of the screening of the core-hole.

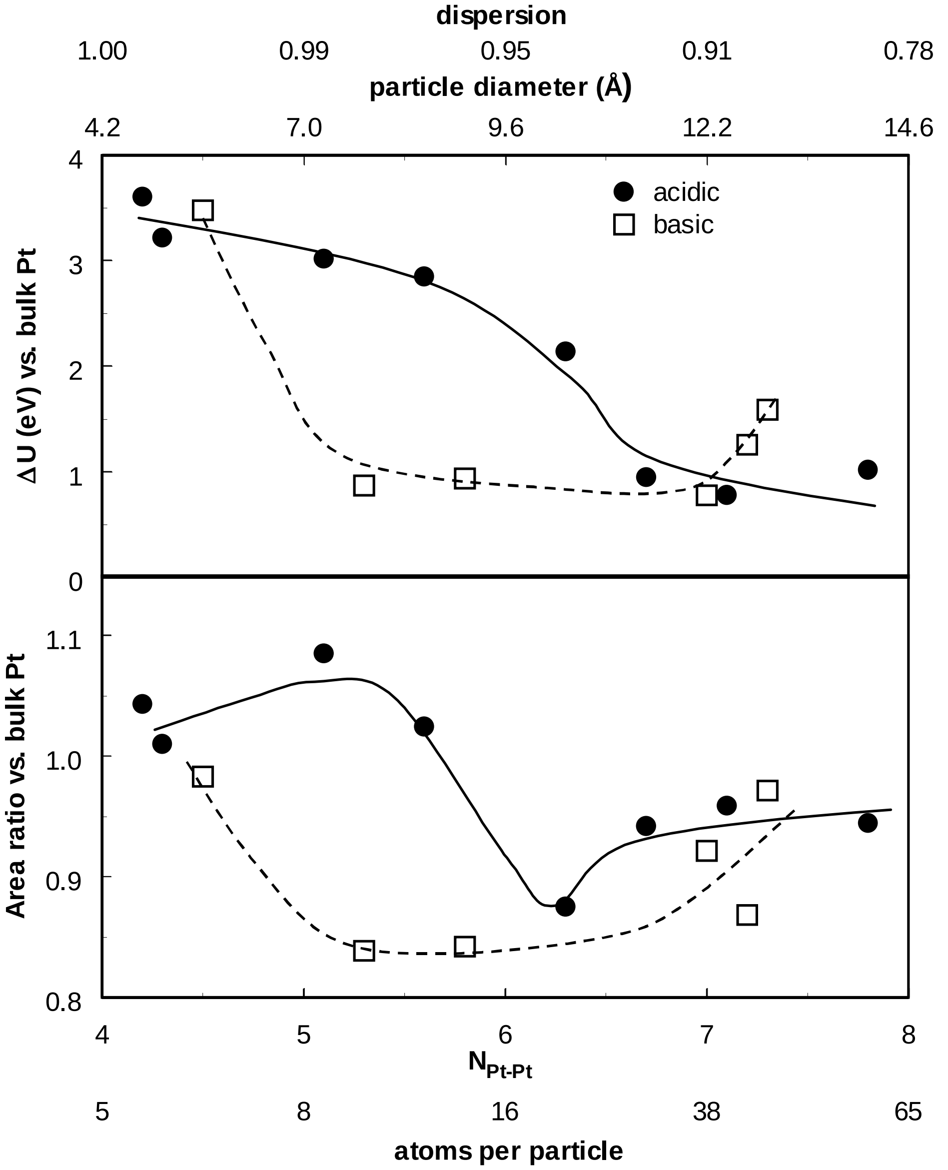

Figure 3: Plot of ΔU and the area ratio R = $\Delta VB_c/\Delta VB_b$ as a function of the Pt-Pt coordination number N, as obtained from the EXAFS analysis. Also shown is the estimated dispersion, cluster diameter and number of atoms/particle as estimated assuming spherical clusters and FCC packing. Data are shown for the acidic supports (LTL[K/Al=0.63] zeolite and Cl-Al_2O_3, SiO_2) and for the basic supports (LTL [K/Al=1.25] zeolite and K-Al_2O_3, K-SiO_2).

The different dynamic screening mechanisms

A core-hole is dynamically screened by a series of processes. This dynamic screening, as discussed extensively by Mahan[22,23], Gadzuk[24], von Barth and Grossman[13-15], and others[25-28], depends on the time scale over which the effective potential was changed. The various

processes are schematically shown in Figure 4. For slow, nearly adiabatic changes (such as that examined here near threshold), the entire system is in the ground state of the potential determined by the instantaneous charge density. Thus initially (10^{-16} sec), the relaxation occurs by inter-atomic charge transfer (ICT) from neighboring atoms to the atom with the core-hole. Some time later (10^{-14} sec) the screening is accomplished by 5d electron-hole pair excitations at E_f, which facilitates the non-local electron hopping or metallic screening. Such metallic screening is generally much more efficient in a metal, so if the latter occurs, the initial ICT screening is reversed and the effective core-hole electron attraction is reduced to zero. In the absence of either of these relaxation mechanisms (*e.g.* in a small cluster or molecule), valence-valence-valence (VVV) Auger processes may allow for rearrangement of charge in the cluster MOs[24]. But, such VVV Auger processes are even slower (10^{-11} sec) than the CVV Auger process (10^{-13} sec) that determines the lifetime of the Pt L_3 core-hole. Thus, in this sense the XAS does not reflect the completely adiabatic case, since the final VVV processes do not get a chance to occur in the absence of CT and metallic screening.

Both the ICT and metallic screening mechanisms depend critically on the DOS near E_f. Frölich[29] and Kubo[30] pointed out long ago that a cluster presents metallic behavior when the average spacing between the electronic levels becomes smaller than kT (k is Boltzman's constant) and the discrete energy levels begin to form a quasi-continuous band. Formulated in terms of the DOS, the transition to metallic behavior occurs when the DOS within 0-0.1 eV of E_f exceeds 1/kT (or approx. 40 states/(eV-cluster))[31]. In contrast, the ICT process depends on the DOS within 0-3 eV of E_f.

Variation in ΔU reflects onset of metallic screening

The sharp drop in the core-hole electron attraction U compared to the bulk value (ΔU, Figure 3) around N = 4.5 and 6.5 for the basic and acidic supports respectively is obviously due to the onset of the insulator to metal transition. The size of ΔU (≈ 3.5 eV) for the very small clusters is consistent with previous estimates of U(5d5d) ≈ 3-6 eV for the nearly filled 5d band transition metals when efficient metallic screening is shut off[32]. Most interesting is the large difference in the behavior of the core-hole electron attraction for the basic vs. acidic supports. This difference dramatically reveals the importance of the support in determining the nature and onset of the metal-insulator transition. It provides direct experimental evidence for a metal-support interaction.

Variation in the area ratio, R, reflects onset of ICT screening

While ΔU, as expected, drops off monotonically with onset of metallic character, the area ratio R drops much more sharply and at slightly lower values of N. This difference is most significant for the acidic supports (Figure 3). The area ratio R reveals much more clearly the changes in ICT screening with cluster size, as demonstrated by the following theoretical calculations.

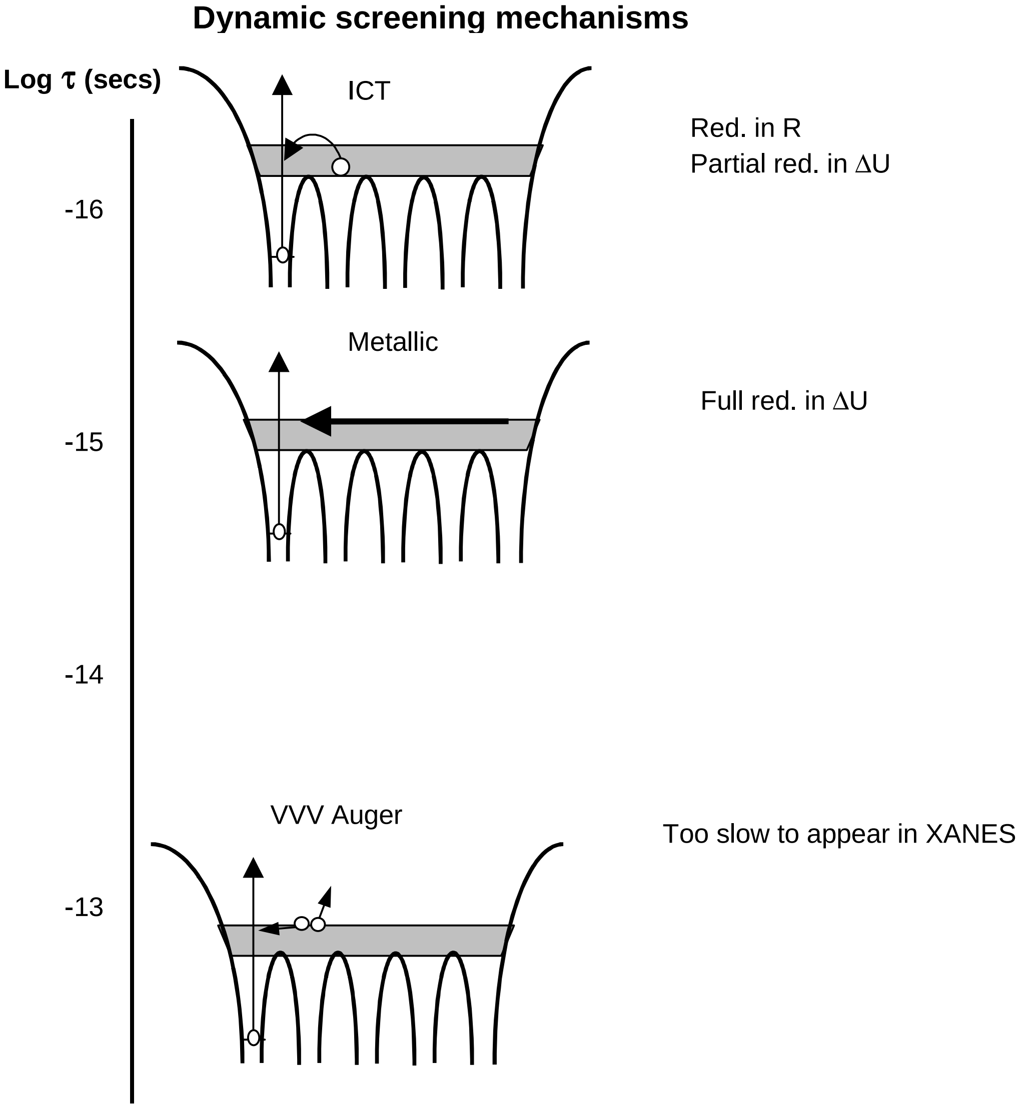

Figure 4: A schematic illustration of the various screening processes and the time scale on which they occur.

Figure 5 shows DOS from self-consistent field, full multiple scattering calculations as implemented in the FEFF8 code[33] on the supported Pt_{10} cluster illustrated. The support is mimicked by the 3 water molecules as shown; the O atoms represent the O atoms in the support, and the H atoms effectively terminate the cluster and represent the Si or Al atoms such as that in a zeolite. The DOS are shown from calculations with and without a core-hole on the 3 different site symmetries (surface, edge, and center).

Notice first that the magnitude of the unoccupied DOS increases significantly with the coordination number (4, 5 or 9) of the Pt site. The DOS for each core-hole site have been shifted by the energy indicated (ΔE_F in Figure 5) to give best alignment with the no-hole calculation. This energy shift represents the increase in binding energy of the Pt 5d band on the absorber atom, or the extent to which the core-hole remains unscreened. Notice also the

sharp reduction in this shift with the increase in the magnitude of the ICT screening charge as indicated by the shade areas.

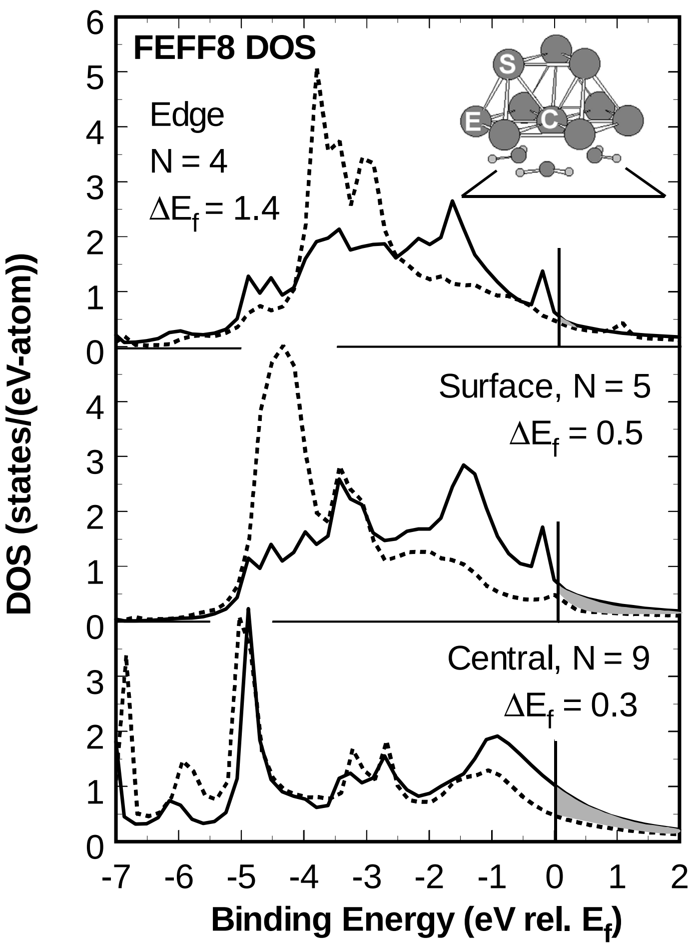

Figure 5: Pt d DOS obtained from a FEFF8 calculation for a Pt_{10}(3,7) cluster on a support mimicked by three water molecules as shown. The DOS are shown for the edge (E), center (C), and surface (S) atoms without (solid line) and with (dotted line) the core-hole. The DOS obtained with the core-hole have been aligned by the amount (ΔE_f) indicated for each case reflecting the magnitude of the shift of the Fermi level on the absorber atom. The shaded areas indicate the screening charge. The coordination number N of each site is also given.

Figure 6 shows calculated ΔVB, at the 3 different sites on the Pt_{10} cluster, obtained by taking the difference $\mu(L_3)$-$\mu(L_2)$ from FEFF8 exactly as ΔVB is obtained experimentally. Thus these theoretical results should directly mimic the experimental results, and show the variation in R with coordination number. Because the theoretical μ equals $\mu_o(1+\chi) = \mu_o + \mu_o\chi$, we can even separate the theoretical ΔVB into two different contributions $\Delta\mu_o$ and $\Delta\mu_o\chi$. The calculated ΔVB and its two contributions for the 3 different sites are shown, assuming

metallic screening (no core-hole) and with ICT screening (with core-hole). In each instance E_f was shifted downward by the amounts indicated by ΔE_F in Figure 5, since in the absence of the VVV decay process, the 'effective' E_f is indeed shifted downward on the absorber atom by these amounts.

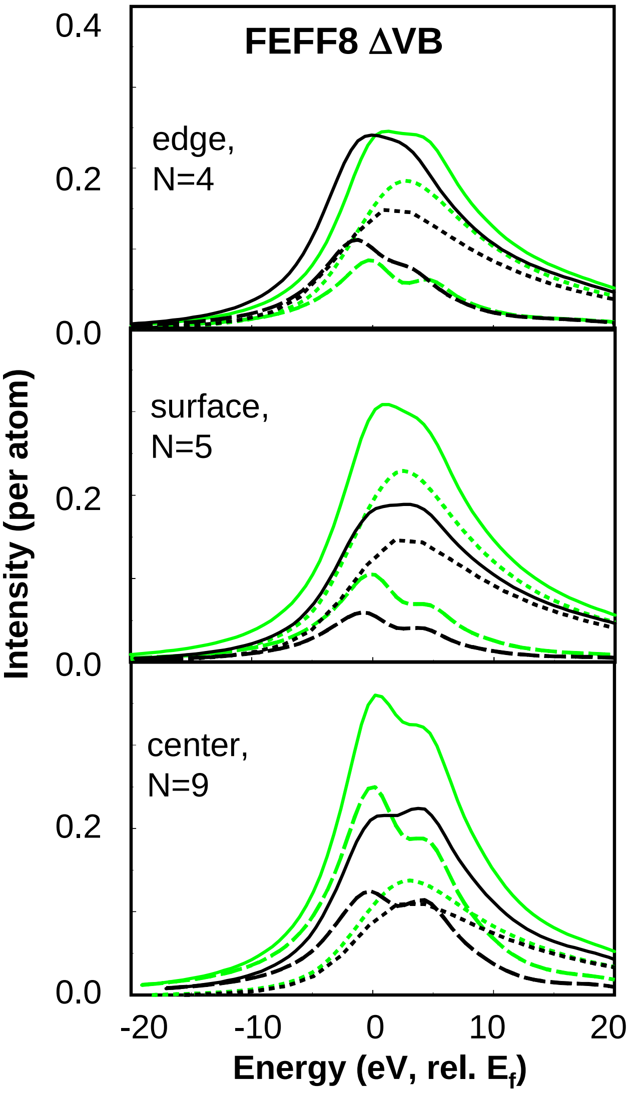

Figure 6: The calculated ΔVB (solid lines) from FEFF8 for the same 3 sites on the Pt_{10} cluster indicated in Figure 4, obtained with (dark) and without (light) the core-hole. Also shown are the components $\Delta\mu_o$ (dotted lines) and $\Delta\mu_o\chi$ (dashed lines).

The increase of the ΔVB intensity with N assuming full metallic screening (no core-hole, light solid line in Figure 6), reflects the increase in empty DOS with N. However, the ICT screened ΔVB (with core-hole) does not show this increase, indeed now ΔVB is largest for the edge (N=4) sites. The reduction in ΔVB intensity upon introduction of the core-hole occurs because the ICT significantly reduces the unoccupied DOS on the absorber atom. This reduction is much greater for the larger coordination sites, obviously because the ICT is much greater.

When the ICT is nearly negligible, the unscreened ΔVB is actually slightly larger than the screened case, exactly as is indicated in the experiment by the area ratios larger than unity for the small clusters on acidic supports (Figure 3B). Also, the theoretical ΔVB shifts to lower energy with decreasing N, reflecting an increased U, just as indicated in the experimental data by the large ΔU for the small clusters (Figure 3A).

Although the calculated results show the proper trends in R, the magnitudes in R are not predicted accurately. Figure 5 shows that the unoccupied DOS changes by about 10-50% upon introduction of the core-hole. Figure 6 shows that the intensity of the calculated ΔVB changes by around 30-45% upon introduction of the core-hole, reflecting this change in final state hole count, $h_{5/2}$-$h_{3/2}$. However, the experimental R ratio changes by only about 10-15%, a factor of 3 smaller. We give two possible reasons:

- First, the theoretical calculations reveal that the amount of ICT screening and, hence, ΔU varies dramatically at the different sites even on the same cluster. Of course the experiment effectively averages over these different sites in a cluster, and the average change will be smaller than at a specific site where ICT screening is large.
- Second, the large reduction in the experimental R range is more likely a direct reflection of the dynamic screening mechanisms. Many of the dynamic screening effects mentioned above can be approximated by utilization of the 'orthogonalized' final state rule[13-15,25-28], which states that the spectral lineshape is best approximated by the final state (i.e., in XAS the metallic or ICT screened core-hole state), but the intensity is determined by the projection of this final state onto the initial no core-hole state. The remaining intensity appears as shake-off or shake-up satellites, which usually blend into the background in XAS. This projection will decrease the magnitude of the intensity variations in ΔVB, but this is not included in FEFF8. Thus, FEFF8 over-estimates the magnitude of the variations in R with N, but correctly predicts the trends.

The variation in the separate contributions, $\Delta\mu_o$ and $\Delta\mu_o\chi$, to ΔVB is also interesting. In general $\Delta\mu_o\chi$ peaks at lower energies than $\Delta\mu_o$. At smaller N, $\Delta\mu_o > \Delta\mu_o\chi$, and the reverse is true at larger N. Figure 6 shows that $\Delta\mu_o$ generally decreases upon introduction of the core-hole, and its absolute value in the presence of the core-hole is nearly constant. This is consistent with the nature of μ_o reflecting the atomic potential, and absorption to the continuum, and not directly the valence band DOS. In contrast, $\Delta\mu_o\chi$ nearly reflects the final-state hole count, $h_{5/2}$-$h_{3/2}$, in the valence band, either in the presence or absence of the core-hole. Further, $\Delta\mu_o\chi$ primarily shifts to lower energy upon introduction of the core-hole at low N, when all screening is shut off, simply reflecting the shift in the unoccupied DOS as shown in Figure 5.

The experimental drop in R occurs at smaller values of N than the drop in ΔU in Figure 3. The theoretical results reveal that the dip in the experimental R around N = 4.5 (basic supports) or N = 5.5-6.5 on acidic supports occurs in the region of ICT screening. Below these values of

N, negligible screening occurs, and above 4.8 (6.5 acidic) metallic screening dominates. Thus the sharp R drop is reflecting the onset of ICT screening, whereas the monotonical drop in U reflects the onset of metallic screening.

Effect of support acidity on ΔU and R

The very important differences evident in the ΔU and R behavior between the basic and acidic supports can easily be understood. As the acidity of the support increases, the electron richness of the support O atoms decreases[7,34,35]. This decreased O electron richness shifts the 5d orbitals to lower energy (higher binding energy), causing a higher work function. Feibelmann and Hamann[36] first suggested such a change in the work function from theoretical calculations. This shift in the 5d band was confirmed experimentally utilizing 'atomic' EXAFS and further theoretical calculations[7,34,35,37]. This can easily be modeled with the cluster illustrated in Figure 5, by increasing the support oxygen ionic charge by small levels, say 0.05 e^-/ O atom. Such a calculation shows the 5d DOS shifts by nearly 1 eV, but the shift is not uniform. The central atom DOS on the cluster in Figure 5 moves to higher binding energy while the edge atom DOS moves to lower, since only the more interior atoms experience the full increased work function. Thus charge will move from the surface to the interior of the cluster, exactly as suggested previously[36]. The calculation here reflects charge rearrangement from the edge to the central atom, suggesting that one can generalize the phenomenon and indicate that charge moves from lower to higher coordinated atoms with increased support acidity. This will have the effect of decreasing the net DOS at E_f. Tong *et al*. have experimentally verified this using NMR studies that show the local DOS at E_f could indeed be changed by the degree and nature of the ion exchange in the support[38], and the direction of the charge rearrangement was exactly as indicated above. The decreased DOS at E_f on acidic supports versus a higher DOS on basic supports (reverse charge movement) means the insulator-metal transition will occur at larger cluster sizes on acidic supports, exactly as seen in Figure 3.

The experimentally observed insulator-metal transition on both acidic and basic supports occurs in clusters where most of the atoms are surface atoms (the dispersion is near one). Therefore the support primarily induces charge rearrangement between edge sites and flat areas for these cluster sizes. The DOS at E_f around N = 7 will be dictated by the flat areas. Figure 5 shows that the DOS at E_f is around 1.0 state/(eV-atom) on the central atom, meaning that as the number of atoms goes significantly below 40, the DOS at E_f indeed drops below the required 40 states/(eV-cluster) for metallic conductivity, just where the metallic screening is lost on acidic supports. On basic supports, the DOS at edge sites will dictate the transition at very low N, since the flat areas are now absent. The DOS at edge sites is less than 0.5 states/(eV-atom), consistent with the transition on basic supports occurring around 10 atoms/particle.

Conclusions

In summary, this paper reports the development of a novel probe for assessing the metallic character of supported nanoscale metal clusters, and the changing mechanisms for core-hole screening. The ability to perform *in situ* studies utilizing XAS simultaneously with a determination of the cluster size from EXAFS, makes this a powerful technique. The neutral XAS final state, as utilized here, enables a determination of the metallic character expected in the ground state and hence a direct determination of the effects of the support. Dramatic changes in both R and U reveal the charge re-arrangements occurring with cluster size and support acidity.

Reference list

1. H. Haberland: *Clusters of Atoms and Molecules I: Theory, Experiment and Clusters of Atoms*, Springer Series in Chemical Physics, Springer Verlag, Berlin, 1995, Vol. 52.
2. P. P. Edwards, R. L. Johnston, C. N. R. Rao, D. P. Tunstall and F. Hensel, *Phil. Trans. R. Soc. Lon.,* **A356** (1998), 5.
3. P. A. Dowben, *Phil. Trans. R. Soc. Lon.,* **A356** (1998), 267.
4. M. R. C. Hunt and R. E. Palmer, *Phil. Trans. R. Soc. Lon.*, **A356** (1998), 231.
5. W. Eberhardt, P. Fayet, D. M. Cox, Z. Fu, A. Kaldor, R. Sherwood and D. Sonderiker, *Phys. Rev. Letters,* **64** (1990), 780.
6. G. K. Wertheim and S. B. Di Cenzo, *Phys. Rev. B,* **37** (1988), 844.
7. B. L. Mojet, J. T. Miller, D. E. Ramaker and D. C. Koningsberger, *J. Catal.,* **186** (1999), 373-386.
8. G. N. Vayssilov and N. Rösch, *J. Catal.,* **186** (1999), 423-432.
9. Chapter 4 of this thesis.
10. D. C. Koningsberger, M. K. Oudenhuijzen, D. E. Ramaker and J. T. Miller, *Stud. Surf. Sci. Catal.,* **130A** (2000), 317-322.
11. M. Vaarkamp, B. L. Mojet, F. S. Modica, J. T. Miller and D. C. Koningsberger, *J. Phys. Chem.,* **99** (1995), 16067.
12. L. F. Mattheiss and R. E. Dietz, *Phys. Rev. B*, **22** (1980), 1663-1676.
13. E. Von Barth and G. Grossman, *Phys. Rev. B*, **25** (1982), 5150.
14. E. Von Barth and G. Grossman, *Phys. Scr.,* **21** (1980), 580.
15. E. Von Barth and G. Grossman, *Solid State Commun.,* **32** (1979), 645.
16. P. W. Anderson, *Phys. Rev.,* **124** (1961), 41.
17. E. N. Economou: *Green' s Functions in Quantum Physics*, Springer Series in Solid-State Sciences, Springer Verlag, Berlin, 1979, Vol. 7.
18. J. de Graaf, Ph.D., Utrecht University, Ridderkerk, 2001.
19. J. de Graaf, A. J. van Dillen, K. P. de Jong and D. C. Koningsberger, *J. Catal.,* **203** (2001), 307-321.
20. D. E. Ramaker and D. C. Koningsberger, **to be published**.
21. P. A. Wolff, *Phys. Rev.,* **124** (1961), 1030.
22. G. D. Mahan, *Phys. Rev. B,* **17** (1980), 187.
23. G. D. Mahan, *Solid State Phys.,* **29** (1974), 75.

24. J. W. Gadzuk, *J. Electron Spectrosc.Rel. Phenom.*, **11** (1977), 255.
25. L. C. Davis and L. A. Feldkamp, *Phys. Rev. B,* **23** (1981), 4269.
26. Grebennikov, Y. A. Babanov and O. B. Sokolov, *Phys. Status Solidi,* **80** (1977), 73.
27. K. Schonhammer and O. Gunnarsson, *Phys. Rev. B,* **22** (1980), 3710.
28. K. Schonhammer and O. Gunnarsson, *Solid State Commun.,* **23** (1977), 691.
29. H. Fröhlich, *Physica,* **4** (1937), 406.
30. R. Kubo, *J. Phys. Soc. Jap.,* **17** (1962), 975.
31. J. A. Alonso, *Chem. Rev.,* **100** (2000), 637-677.
32. D. E. Ramaker, *Solid State and Mater. Sci.,* **17** (1991), 187.
33. A. L. Ankudinov, B. Ravel, J. J. Rehr and S. D. Conradson, *Phys. Rev. B,* **58** (1998), 7565-7576.
34. Chapter 8 of this thesis.
35. N. López, *J. Chem. Phys.,* **114** (2001), 2355-2361.
36. P. J. Feibelman and D. R. Hamann, *Surf. Sci.,* **149** (1985), 48.
37. D. E. Ramaker, B. L. Mojet, D. C. Koningsberger and W. E. O'Grady, *J. Phys.: Condens. Matter,* **10** (1998), 8753-8770.
38. Y. Y. Tong, P. Mérlaudau, A. J. Renouprez and J. J. van der Klink, *J. Phys. Chem. B,* **101** (1997), 10155.

8

Influence of the Support Acid/Base Properties on the Density of States of Pt particles

Theory versus experiment

Abstract

X-ray absorption experiments on supported Pt catalysts indicate that increased support alkalinity induces an increased whiteline intensity of the Pt L_2 and L_3 X-ray absorption edges. Density functional theory (DFT) shows that the origin of this support effect is due to a rehybridization of the Pt valence band. The Madelung potential of a basic support rehybridizes the filled part of the valence band towards an increased amount of anti-bonding $6sp^*$ character, and consequently the empty part obtains more 5d character. Furthermore, DFT calculations reveal that the metal-support interaction consists of three additional effects. First, the Madelung potential of the support polarizes the Pt particles and second, it shifts the complete valence band to higher energies for basic supports and to lower energies for acidic supports. Third, the bonding between metal and support is strong as long as the support is non-inert. This bonding has a large impact on the metal 6sp states. For acidic supports the Pt 6sp orbitals are geometrically located at the interface between the metal and support. If the support is basic, then the Pt 6sp orbitals are located more at the metal surface. Since reactants like hydrogen or alkanes chemisorb partly via the 6sp orbitals, the metal-support interaction can have large implications for the catalytic properties of supported Pt particles.

Introduction

Supported noble metal catalysts are widely used in commercially important reactions, including hydrogenation, naphtha reforming and isomerization reactions[1]. It has been well established that the nature of the support influences the rate of hydrogenation and hydrogenolysis reactions on catalytically active metal particles[2,3]. Several explanations have been given for this support effect on the catalytic performance. Besides the formation of metal-proton adducts[4,5] on Brønsted acidic supports, a support material can have two effects on the supported cluster. First, it can act as a ligand for the Pt cluster. A ligand can result in a rehybridization of the orbitals within the metal particle, and electrons may be transferred between the support and metal[3,6,7]. Second, if the support material is partly ionic, the series of alternating charges produces an electric field: the Madelung potential. This electric field can polarize the metal particle, and the polarization will alter the valence electron distribution within the metal particle[8,9]. In addition, nearby cations can polarize the metal particles[10]. Several experimental papers reported an influence of the support material on the electronic structure of the metal particle[11-15]. The electronic structure will probably influence the chemisorption of reactants and therefore the catalytic properties of the metal particles.

Utilizing surface science techniques and theoretical calculations, there has been an overwhelming amount of work reported for the chemisorption of reactants (CO, CH_x, H_2, ..) on ideal (111) surfaces[16-21]. From this work, it is well known that the metal sp band is important for the chemisorption of adsorbates. Nørskov *et al.*[18] use the concept that the metal sp states are important for the chemisorption, but for the transition metals the sp states are essentially the same along a transition metal row in the periodic table. The consequence is that it are the changes in the d-states that are responsible for the changes in the chemisorption of adsorbates on the various transition metals. Kua and Goddard[19,22] developed the concept of an interstitial bonding orbital (IBO) to explain the chemisorption of hydrocarbons and hydrogen on metal surfaces. The IBO is constructed primarily of the metal s and p orbitals, 6s and 6p in the case of Pt. Each Pt_4 tetrahedron shares an IBO in the center, and the IBO is dominant in the chemisorption of reactants[19].

However, the above mentioned work on the chemisorption of reactants is for (111) metal surfaces, and in the ‘real world’ of catalysis, the metal particles are preferably highly dispersed, with particles containing 5-500 atoms, and these particles have a considerable amount of edges, steps and low-coordinated surface sites. Furthermore, as has been mentioned above the electronic structure of these metal particles are influenced by the acid/base properties of the support material.

Relatively few studies have focused on influence of the acid/base properties of the support on the chemisorption of reactants on supported metal clusters. A NMR study by Tong *et al.*[23] showed that the stretching frequency of CO chemisorbed on zeolite supported Pt particles correlates with the surface local density of states (LDOS) of the Pt. The LDOS also showed a correlation with the faujasite framework acidity, but an explanation of this correlation is lacking. Several infrared studies on similar supported Pt catalysts show that the mode of CO

chemisorption shifts from linear to bridged sites[12,24,25]. Several density functional theory (DFT) studies reproduce that the chemisorption of CO on Pt is influenced by the support acidity[26-29]. However, all of these DFT studies offer explanations in terms of donation and backdonation of electrons between metal and adsorbate (the Blyholder model[30]). They do not provide any insight how the electronic structure of the metal particles is influenced by the support properties. A theoretical study that presents a basis for understanding the influence of the acid/properties of the support on the electronic structure of the metal particles is missing.

Recent work by our group[14] has shown that the electronic basis of the metal-support interaction is not only a shift of the metal valence d-orbitals to higher binding energy with decreasing electron richness on the support oxygens (*i.e.* increasing support acidity), but also a charge rearrangement or transfer from within the metal particles to the metal support interface. This charge rearrangement was experimentally observed with atomic X-ray Absorption Fine Structure (AXAFS) spectroscopy. The AXAFS intensity was shown to be sensitive for the Madelung potential of the support and to correlate with the catalytic activities for the hydrogenation of tetralin and hydrogenolysis of neopentane[14]. Ramaker *et al.* applied the concept of the IBO in order to explain the with AXAFS observed charge rearrangement within supported Pt particles[14]. They suggested that the IBO shifts towards the interface region for Pt on acidic supports, and this would influence the chemisorption characteristics of the catalyst. The influence of a support material was also observed in a study on the transition from insulator to metallic in metal particles[15]. This transition follows the observed screening of the core-hole, which is reflected in the difference between the Pt L_2 and L_3 X-ray absorption edges and is influenced strongly by the electron richness of the support material.

The electronic properties of the metal particles are influenced by the acid/base properties of the support via the oxygen atom. Therefore, it is important to define clearly the terms of basicity (or alkalinity) and acidity with respect to oxidic support materials. The definition of a Lewis acid is 'a substance that acts as an electron acceptor', whereas a Lewis base is able to donate electrons. A basic, oxidic support is then defined as a support material with electron rich surface oxygen atoms. An example of a basic support is MgO. In the series MgO → SrO → BaO, the ionicity is increased towards BaO[28]. Hence, an increased ionicity in a support material leads higher electron richness for the support oxygen atoms and to increased basicity. Zeolites in the protonic form are generally regarded as acidic. Also an increase of the acidity by decreasing the Si/Al ratio in zeolites, replacing charge compensating Na^+ by H^+ or La^{3+}, and incorporating Al_2O_3 in a SiO_2-matrix lead to a decrease of the electron richness of the support oxygen atoms. It seems obvious that any study aimed at understanding the fundamental basis of the origin of the metal-support interaction should focus on unraveling of the influence of the electron richness of the support on the electronic properties of the metal particles.

This paper provides a theoretical basis for understanding the metal support interaction. X-ray absorption spectroscopy (XAS) experiments are carried out in order to probe the empty part of the density of d states (DOS) of supported Pt particles. Small Pt particles on 3 different

support materials, a hydrotalcite (HT) and three LTL zeolites with various K^+ contents have been investigated with XAFS spectroscopy. The supports increase in acidity in the order HT < LTL [K/Al=1.53] < LTL [K/Al=1.04] < LTL [K/Al=0.82]. DFT is used to interpret the observed effects and to determine the changes in the filled part of the DOS induced by the electron richness of the support oxygen atoms. Theoretically, the small Pt particles are mimicked by using a Pt_4 tetrahedron in the DFT calculations. The influence of the support under the Pt_4 cluster is introduced in the calculations in two ways: first, by placing X_2O molecules (X=Na, H or F) underneath the Pt_4 cluster, and second: by using a series of pointcharges that simulate the Madelung potential of a support (Figure 1). DFT calculations are used to optimize the geometry of the Pt_4 and $Pt_4/3{\bullet}X_2O$ clusters. These optimized structures are also used as input for the ab initio full multiple scattering program FEFF8[31], which calculates the X-ray absorption near edge structure and the local DOS. This paper will focus on understanding the influence of the electron richness of the support oxygen atoms on the electronic structure of the supported metal particles. Future research will deal with the support induced change in the chemisorption of adsorbates on the Pt metal particles.

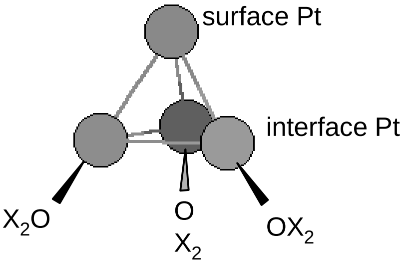

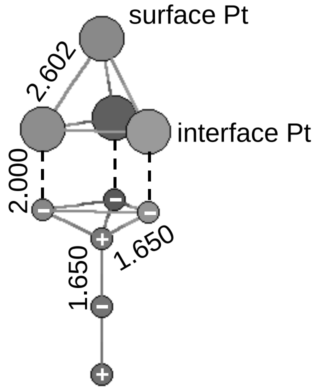

Figure 1: Schematic picture of the Pt_4 cluster supported (left) on 3 X_2O molecules (X=Na, H, F), and (right) a cluster where the support is mimicked by pointcharges in a Si_2O_4 arrangement.

Experimental Methods

Catalyst preparation

The acid/base properties of LTL zeolite was varied by changing the K^+ loading. The K^+ content of a K-LTL zeolite was increased by impregnation with KNO_3 (aq), followed by calcination at 225°C. The K^+ content was decreased by exchanging the K-LTL zeolite with NH_4NO_3, followed by calcination. After calcination the K is present in the form of K^+ and K_2O. The obtained zeolites were analyzed for K and Al contents. The catalysts are designated Pt/LTL [*.**] with *.** representing the K/Al ratio. An increasing K/Al ratio results in an increased electron-richness on the support oxygen atoms (corresponding to an increasing basicity of the support)[32]. Platinum was added by incipient wetness impregnation with an

aqueous $Pt(NH_3)_4(NO_3)_2$ solution, resulting in a 1 wt.% Pt/LTL catalyst. The impregnation was followed by drying the zeolite at 150°C for 1 hour in a high He flow. Subsequently, the catalyst was calcined in a high O_2 flow at 275°C (LTL [1.04] and LTL [0.82]) or 350°C (LTL [1.53]) with a slow heating rate of 0.2 °C/minute. The samples were cooled down in He to 100°C and reduced in H_2 at 350°C (1°C/min). After passivation the catalysts were stored in air for further use.

Hydrotalcite was also used as support. A hydrotalcite is regarded as a very basic support. It consists of platelets in a brucite structure, with Mg^{2+} ions octahedrally coordinated by O atoms. Part of the Mg^{2+} ions are isomorphically exchanged for Al^{3+} ions, creating a positive charge on the framework. Between the platelets, this positive charge is compensated with CO_3^- or OH^- ions. The OH^- ions located at the edge of the platelets are active in basic catalysis.

The hydrotalcite (HT) support was prepared and activated with a Mg/Al ratio of 3.0 according to Roelofs *et al*[33]. The activation procedure consists of a calcination in N_2 at 450°C, followed by a rehydration of the hydrotalcite in H_2O, during which the hydrotalcite structure is restored. During the rehydration procedure, H_2PtCl_6 was added to the hydrotalcite support. The OH^- at the edges of the HT platelets can than be replaced by the $PtCl_6^{4-}$ precursor. The now ion exchanged hydrotalcite was filtrated and dried in N_2 at 80°C for 18 hours, followed by drying at 200°C (heating rate 2°C/min) for 1 hour and a reduction in H_2 at 200°C for 1 hour. At this temperature the hydrotalcite stays largely intact[34]. Moreover, the reduction of the Pt complex is complete[35], as is also indicated by the fact that it can reversibly adsorb H_2 in H_2 chemisorption experiments. The reduced sample was passivated and stored in air for further use. The resulting catalyst is designated as Pt/HT [IE].

A second batch of the hydrotalcite was activated, rehydrated, filtrated and then impregnated with an aqueous $Pt(NH_3)_4(NO_3)_2$ solution. The resulting catalyst precursor was also dried in N_2 at 80°C for 18 hours, followed by drying at 200°C (2°C/min) for 1 hour. The sample was directly reduced in H_2 at 200°C for 1 hour, passivated and stored in air. The resulting catalyst is denoted as Pt/HT [IM]. The resulting Pt particles in both Pt/HT catalysts will be located at the edges of the platelets, near the OH^- ions, and they will experience the support material as basic.

The Pt particle size of all catalysts was determined by H_2 chemisorption. Details of H_2 chemisorption are given elsewhere[36].

XAFS data collection

XAFS measurements were performed at the HASYLAB synchrotron (beamline X1.1) in Hamburg, Germany. The measurements were done in transmission mode using ion chambers filled with a mixture of Ar and N_2 to have an absorption of 20% in the first and an absorption of 80% in the second ion chamber. The monochromator was detuned to 50% at maximum intensity to avoid higher harmonics present in the X-ray beam.

The catalyst sample (100-160 mg, resulting in a total absorption of 2.5 after the Pt L_3 edge) was pressed in a self-supporting wafer and mounted in a stainless steel *in situ* cell equipped

with Be-windows[37]. Both the Pt L_2 and L_3 edge XAFS spectra were recorded in transmission at liquid nitrogen temperature .

The sample was *in situ* dried at 150°C for 1 hour (heating rate 10°C/min) in He and subsequently rereduced at 200°C (the hydrotalcite catalysts) or 350°C (the LTL catalysts) for 1 hour (5°C/min) in flowing H_2 and cooled down in a H_2 atmosphere. XAFS data at both the L_2 and L_3 edge were collected in H_2 at liquid nitrogen (LN) temperature. Subsequently, the sample was evacuated at 35°C and 200°C (all heating rates were 5°C/min) for 30 and 60 minutes, respectively, maintaining a pressure of $P < 10^{-3}$ Pa. After each evacuation the $L_{2/3}$ XAFS data were measured at LN temperature while maintaining a pressure below 10^{-3} Pa.

EXAFS data analysis

The background of the XAS spectra was subtracted using standard procedures[38,38]. Data analysis was performed by multiple shell fitting in R-space (1.6<R<3.2 Å) by applying a k^2 weighted Fourier transform from k = 2.5 to k = 14 $Å^{-1}$. The commercially available data analysis package XDAP[39] was used. The variances between the imaginary and absolute parts of the Fourier transform of the data and the fit were used to determine the fit quality[38]. Different backscatterers were identified by applying the difference-file technique[38] using phase-corrected Fourier transforms. Data for the Pt-Pt and Pt-O phase shifts and backscattering amplitudes were generated by the FEFF7 code[40]. The reference data were calibrated with experimental spectra of Pt-foil and $Na_2Pt(OH)_6$[41]. The references are reliable for k>2.5 $Å^{-1}$.

Computational Methods

The Pt_4/X_2O model cluster

The starting point of the DFT calculations was a tetragonal Pt_4 cluster, which was geometrically optimized maintaining T_D symmetry. To mimic the support three X_2O molecules were placed underneath the Pt_4. The oxygen atoms are in direct contact with the Pt_4 cluster. A schematic representation of the cluster is shown in Figure 1. Changes in acidity of the support were simulated by changing the nature of atom X from F (highly electronegative, resulting in a low electron richness on the oxygen atom: acidic support) via H (neutral support) to Na (low electronegativity, resulting in a high electron richness on the oxygen atom: basic support). The mimicked support acidity (F_2O) and basicity (Na_2O) are probably more extreme than the acid/base properties of experimental supports, but this allows to obtain a clear understanding of the trends that are observed. The geometrically optimized Pt_4/X_2O clusters were also used for real space full multiple scattering calculations. The electric field of a support was also mimicked by using a clean Pt_4 cluster supported on a series of point charges. The number of point charges used was limited due to computational problems. The geometry of the point charges resembles part of a SiO_2 network, with tetrahedrally coordinated Si atoms and oxygen atoms on the corners of the tetrahedron represented by pointcharges. The geometry of the cluster supported on point charges is shown in Figure 1.

An increasing ionicity of a support results in an increased electron richness of the surface oxygen atoms, giving a basic support. This was simulated by increasing the magnitude of the point charges. The negative charges were varied from –0.01 (simulating a covalent support) to –2.00 (ionic support). The positive charges were twice as large in magnitude, *i.e.* if the negative charges are –0.20, the positive charges are +0.40. The total charge was 0.

Density Functional Theory

The DFT calculations have been performed using the Amsterdam Density Functional Package ADF[42]. This package uses the Kohn-Sham approach to the density-functional theory. Slater-type orbitals are used to represent the atomic orbitals. All basis sets consisted of triple-ζ quality, extended with two polarization functions. The density functional was calculated using the Vosko-Wilk-Nussair approximation of the local density approximation (LDA), and using the Becke gradient correction[43] and Perdew correlation term[44] for the generalized gradient approximation (GGA). To enhance computational efficiency, several atomic core shells of the Pt atoms were frozen up to and including the Pt 4d level. Relativistic effects were accounted for using the ZORA approximation[45,46]. Initially, the geometry optimizations were carried out in the spin restricted mode, followed by spin unrestricted calculations (spin α and spin β may be spatially different and may have different electron occupations). The numerical integration precision applied was set to 5.5 significant digits. The applied criterions for the geometry optimization were 1 x 10^{-3} Hartree for the changes in energy, 1 x 10^{-4} Hartree/Å for changes in the energy gradients and 1 x 10^{-2} Å for changes in the Cartesian coordinates.

Real space full multiple scattering calculations

The FEFF8 code[31] was used to perform self-consistent full multiple scattering calculations. FEFF8 implements self-consistent field potentials for the determination of the Fermi-level and the charge transfer. Full multiple scattering (FMS) calculations are used to calculate the X-ray Absorption Near-Edge Structure (XANES) and the local density of states.

The calculations were performed using the Hedin-Lundquist exchange correlation potential. When X-ray absorption spectra are calculated, a core-hole has to be present in order to mimic the photon absorption process. The calculations were performed both with and without complete core-hole screening. The optimal geometry for the clusters as derived from the ADF calculations was used as input for the FEFF8 calculations.

Two different types of Pt atoms can be distinguished in the supported Pt_4 cluster: Pt_{surf} and Pt_{int}. The theoretical X-ray spectrum of the supported cluster (μ) was obtained by calculating $\mu(Pt_{surf})$ and $\mu(Pt_{int})$ followed by averaging: $\mu = ¼\ \mu(Pt_{surf}) + ¾\ \mu(Pt_{int})$. Since the number of oxygen atoms in close contact with the metal particles may be different for experiment and the model Pt_4 cluster, the average X-ray absorption spectrum of the supported Pt_4 cluster was calculated including the effect of the support on the electronic structure but excluding the scattering against oxygen and fluorine or sodium neighbors. This was done by performing calculations with various radii for the FMS calculations around an absorbing atom. For the Pt_{surf} atom the FMS calculation was carried out with a radius of 3 Å, which includes the Pt_{inf}

atoms and excludes the support X_2O atoms. In order to isolate for the Pt_{int} the contribution of the scattering against the oxygen and fluor or sodium neighbors first a FMS calculation with a radius of 2.4 Å was performed leading to a $\mu(Pt_{int})$ that only includes the scattering against the X_2O support molecules. When a radius of 3 Å is chosen, both the neighboring Pt atoms and the X_2O atoms are taken into account for the $\mu(Pt_{int})$ calculation. By subtracting the two obtained theoretical spectra, a $\mu(Pt_{int})$ contribution is obtained including the contribution of the neighboring Pt and excluding the contribution of the support X_2O atoms.

Results

Particle Sizes

As is shown in Table 1 and Table 2, both H_2 chemisorption and the EXAFS Pt-Pt coordination number indicate some variations in the final metal particle size after reduction. The Pt/LTL [1.04], Pt/LTL [1.53] and Pt/HT [IE] have similar particle sizes and Pt/HT [IM] show somewhat larger particles. The EXAFS analysis after evacuation at 200°C (Table 2) showed a similar trend.

Table 1: Results for H_2 chemisorption and EXAFS.

	H/Pt		
Catalyst	total	strong	weak
Pt/HT [IE]	0.62	0.09	0.53
Pt/HT [IM]	0.39	0.25	0.14
Pt/LTL [1.53]	0.97	0.69	0.28
Pt/LTL [1.04]	1.06	0.59	0.47
Pt/LTL [0.82]	1.18	0.76	0.41

Both after reduction and evacuation at 200°C, the Pt/HT [IE] and the Pt/LTL catalysts show a long Pt-O bond length (~2.55-2.75 Å). The O neighbor originates from the oxidic support[47]. The long Pt-O distances indicate the presence of interfacial hydrogen[48]. The Pt/HT [IM] shows a small Pt-O distance of 2.02 - 2.06 Å in all cases.

The Pt/HT [*] catalysts show a decrease in the Pt-Pt coordination number after evacuation. This indicates a change in morphology of the Pt particles after desorption of hydrogen. The decrease of $N_{Pt\text{-}Pt}$ can be explained by a flattening of the Pt particles. In contrast, the neutral catalyst, Pt/LTL [1.04] shows only minor changes in the morphology after evacuation and the catalysts Pt/LTL [0.82] and [1.53] show an increase in the Pt-Pt coordination number.

X-ray absorption edge structures

In Figure 2A, the L_3 X-ray absorption edges for the evacuated supported Pt catalysts are shown. For reference purposes, also the L_3 edges for Pt^0 (Pt-foil) and Pt^{2+} ($Pt^{2+}[NH_3]_4[NO^-_3]_2$) are shown. The whiteline of Pt^{2+} has clearly a higher intensity than all other metallic Pt edges. In Figure 2B, only the L_3 edges for the catalysts are displayed. The intensities decrease in the order HT [IM] ≥ HT [IE] > LTL [1.53] > LTL [1.04] > LTL [0.82], in line with the expected

increase in electron richness of the oxygen atoms (increasing basicity) of the support materials. The L_2 edges (Figure 2C) show the same order in intensity as the L_3 edges, with the Pt/HT catalysts having the highest whiteline intensity. The two Pt/HT catalysts have different particle sizes, but show almost the same whiteline intensity. Also, the L_3 edge positions show a spread of a few eV. This spread is smaller for the L_2 edges.

Table 2: R-space fit (k^2 weighted, Δk= 2.5-14.5 Å^{-1}, ΔR=1.6-3.2 Å) parameters[a] of EXAFS spectra after reduction and evacuation at 200°C .

Catalyst,	1st Pt shell				O shell				variances (%)	
Pt/	N	$\Delta\sigma^{2\,b}$	R	E_0	N	$\Delta\sigma^{2\,b}$	R	E_0	im.	abs.
HT[IE] H_2	5.2	5.9	2.68	5.5	0.7 0.4	4.0 4.0	2.76 2.01	-9.5 -10.0	0.804	0.248
HT[IE] vac	4.3	3.8	2.63	4.1	1.1	4.0	2.67	0.5	1.50	0.626
HT[IM] H_2	6.4	3.6	2.75	1.9	0.4	4.0	2.02	-10.0	0.749	0.205
HT[IM] vac	5.7	5.5	2.74	0.1	0.6	4.0	2.06	-10.0	2.76	1.37
LTL[1.53] H_2	4.1	2.3	2.74	3.8	1.4 0.4	4.0 4.0	2.68 1.99	-5.8 -6.5	0.353	0.162
LTL[1.53] vac	5.4	7.1	2.73	0.0	0.8	4.0	2.56	3.2	0.843	0.499
LTL[1.04] H_2	4.9	4.2	2.73	2.5	0.7 0.5	4.0 4.0	2.69 2.12	-5.8 -10.0	1.27	0.506
LTL[1.04] vac	4.6	4.3	2.64	5.3	0.9 0.4	4.0 4.0	2.73 2.07	-9.4 3.1	0.920	0.291
LTL [0.82] H_2	5.5	3.5	2.74	0.1	1.5	4.0	2.61	4.9	0.739	0.234
LTL [0.82] vac	6.2	8.9	2.64	7.9	1.4	3.0	2.65	-10.0	2.73	0.968

[a] errors in fits: R ± 1%, N ± 10%, $\Delta\sigma^2$ ± 5%, E_0 ± 5%
[b] Debye-Waller factor, * 10^{-3}

DFT calculations

The unsupported Pt_4 cluster

As a starting point for all calculations, the geometry of the unsupported tetragonal Pt_4 cluster was optimized. The Pt-Pt equilibrium distance was found to be 2.60 Å. This bond length is considerably smaller than the bulk value of 2.77Å, as is generally found for small clusters[22,36,49,50]. The groundstate state of the cluster, which is a triplet state[22], resulted in a binding energy of –1191 kJ/mol as compared to the individual atoms in the gas phase. This value is in excellent agreement with reported values in literature[49]. The atomic reference energies were obtained according to Baerends *et al*[51].

In Figure 3 the gross population density of states (GPDOS) around the Fermi level for this Pt_4 cluster is shown. Some features are apparent in this GPDOS. Around –10 eV, a band constructed of ca. 50% 5d and 50% 6s and 6p orbitals is visible. This band is referred to as the 'interstitial bonding orbital' (IBO) by Kua and Goddard[22]. Above this IBO, the 5d band is visible with several maxima in the GPDOS up to the Fermi-level at –4.3 eV. In the same region, also the 6s DOS shows some intensity. It is well known that the s and d valence

electrons mix substantially[49,50,52]. Above the Fermi level, several antibonding combinations of the 6s and 6p orbitals (IBO* orbitals[22]) are present, containing a small amount of 5d character. At higher energies, E ≥ 2.5 eV, the higher, unoccupied orbitals (7s, 7p, ..) are visible.

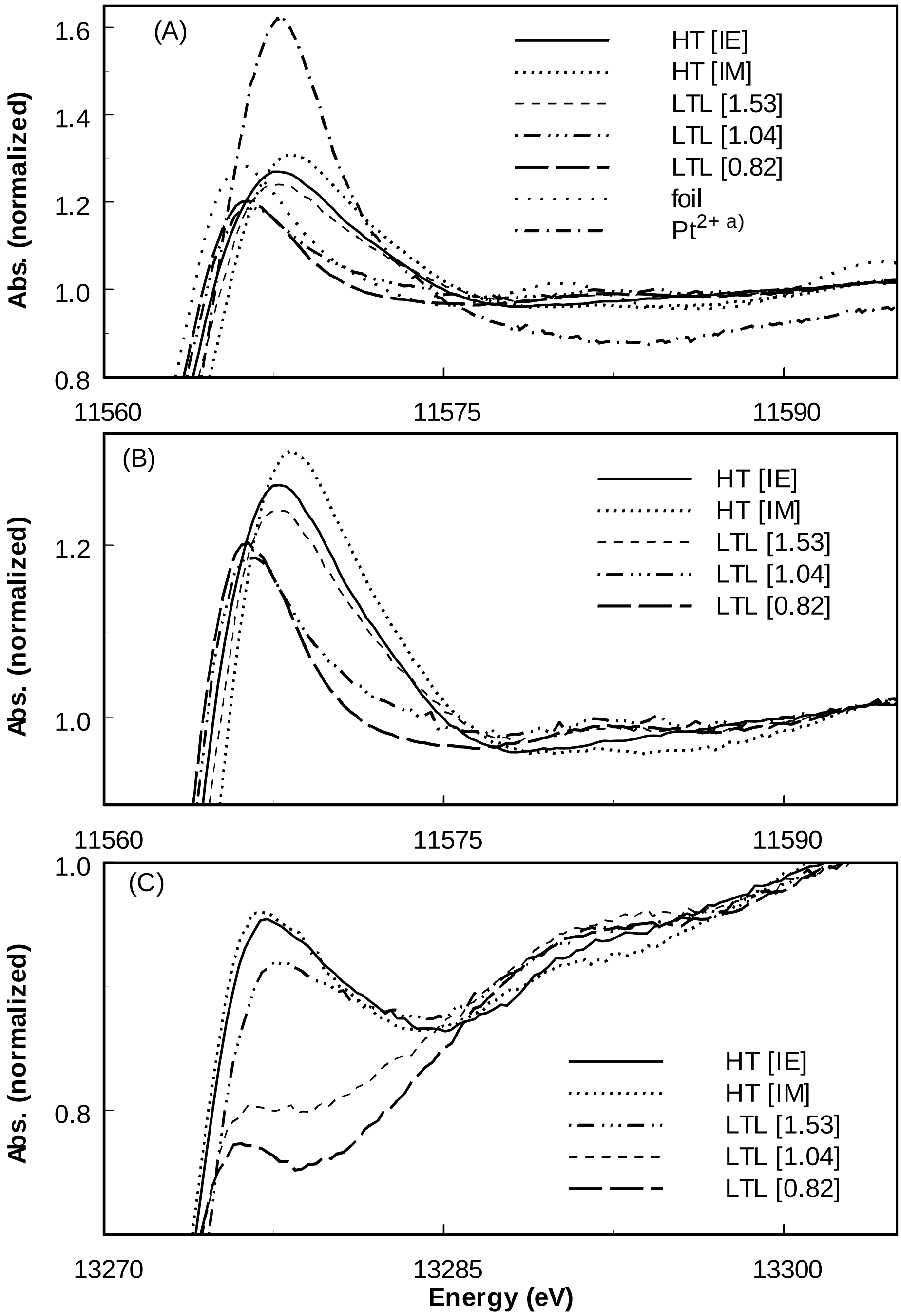

Figure 2: (A), (B) L_3 and (C) L_2 X-ray absorption edges. In (A) the L_3 edge for Pt^0 (Pt foil) and Pt^{2+} ($Pt^{2+}[NH_3]_4[NO_3^-]_2$) are also given for reference.

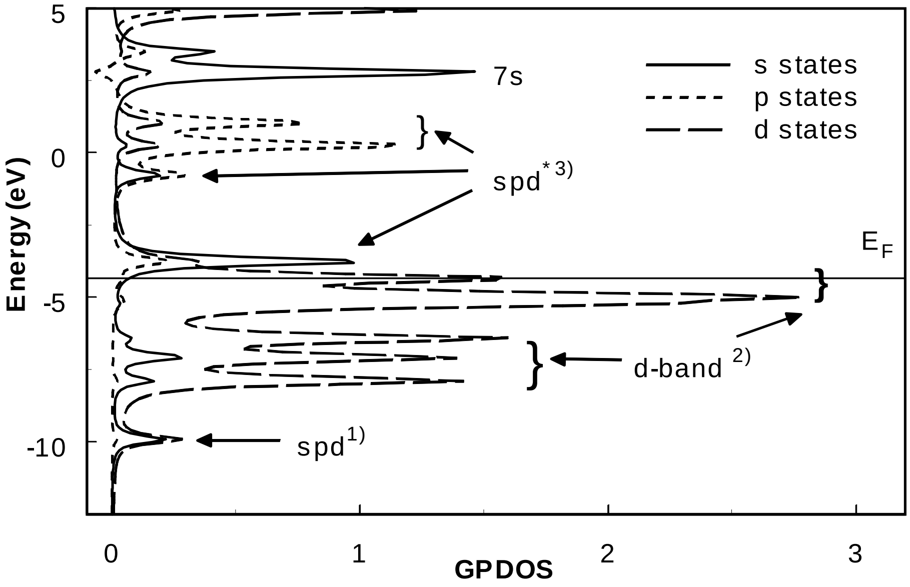

Figure 3: The gross population density of states (GPDOS) calculated for a clean, tetrahedral Pt_4 cluster. [1)] The interstitial bonding orbital (IBO) constituted mainly of 6s and 6p orbitals, mixed with 5d orbitals[22], [2)] the d-band includes a small amount of mixing with 6s and 6p orbitals, [3)] anti bonding combination of 6s, 6p and a small amount of 5d orbitals.

Supported Pt_4 clusters

The geometry parameters obtained after geometry-optimizations of the Pt_4/X_2O clusters are given in Table 3 and Figure 4 . For Pt_4/Na_2O and Pt_4/H_2O, the distance between two interface atoms(which are the Pt atoms connected to the oxygen of a X_2O molecule) is considerably longer (approximately 2.7 Å) than the distance between an interface atom and the surface atom (approximately 2.5Å). For Pt_4/F_2O, these distances are both small (2.51 and 2.56 Å, respectively). The Pt-O distance is ~0.3 Å longer in the case of the Pt_4/H_2O cluster compared to the two other clusters.

Table 3: Coordination distances for the different $Pt_4(X_2O)_3$ clusters after optimization of the geometry

Support (3 X_2O)	Distance (Å)			
	Pt_{int}[a] – Pt_{int}	Pt_{int} – Pt_{surf}	Pt_{int} - O	O - X (Na,H,F)
Na_2O	2.70	2.55	1.95	2.14
H_2O	2.73	2.51	2.22	0.98
F_2O	2.51	2.56	1.90	1.77
unsupported	2.60			

[a] Pt_{int}: An interface Pt atom, Pt_{surf}: A surface Pt atom. See Figure 7.

Table 4: The influence of the support on a Pt_4 cluster. The support is mimicked by 3 X_2O molecules, with X=Na, H, F.

(X_2O)	Pt_4-X_2O bond energy (kJ/mol)[a]	Fermi level (eV)[b]	Hirshfeld charges on				
			X in X_2O	O	Pt_{int}	Pt_{surf}	Pt_4 cluster
Na_2O	-287	-2.3	+0.33	-0.51	-0.11	-0.16	-0.48
H_2O	-38	-3.3	+0.17	-0.19	-0.14	-0.04	-0.45
F_2O	-170	-7.4	-0.17	-0.04	+0.32	+0.15	1.11

[a] The bond energy is per Pt_4-X_2O bond.
[b] The Fermi-level for the free Pt_4 cluster is at –4.3 eV.

Table 5: The effect of a series of point charges on a Pt_4 cluster.

ionicity[a]	Hirshfeld charges on		# 6s electrons	# 5d electrons
	Pt_{int}	Pt_{surf}		
0.01	-0.010	*+0.031*	0.71	9.07
0.10	0.004	-0.011	0.71	9.07
0.20	0.018	-0.054	0.70	9.08
0.50	0.056	-0.168	0.72	9.05
1.00	0.109	-0.328	0.87	8.89
1.50	0.170	-0.511	1.09	8.70
2.00	0.228	-0.685	1.35	8.51

[a] The point charges are constructed of a series of points with increasing charge separation, in a Si_2O_4 arrangement. The value given is the charge on the O positions, the charge on the Si position is of the opposite sign and twice as large (*e.g.*, if the charge on the oxygen position is –0.1, the charge on the Si position is +0.2.

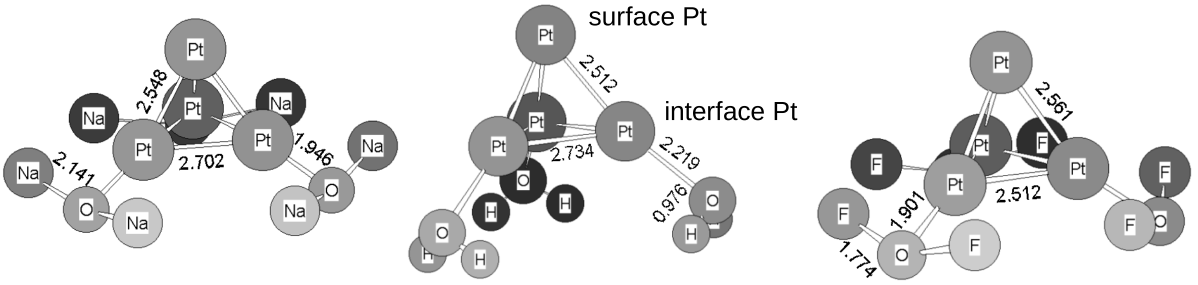

Figure 4: The $Pt_4(X_2O)_3$ (with X=F, H and Na) models after optimization of the geometry. The numbers show the bond length in Å.

The bond energy for an individual Pt-X_2O bond was also calculated (see Table 4). This bond energy is lowest for Pt/H_2O: –38 kJ/mol. For the Na_2O and F_2O supported clusters, these bond energies are considerably higher, with the highest bond energy for the Pt-Na_2O bond (-287 kJ/mol).

In addition to changes in bond energy, a significant amount of charge transfer between the X_2O molecules and Pt_4 clusters occurs (Table 4). A Hirshfeld charge analysis[53,54] of the

individual atoms shows that the total charge of the Pt_4 cluster increases from –0.48 (atomic units, an electron has a charge of –1.0) for the Pt_4/Na_2O cluster to +1.11 for the Pt_4/F_2O cluster. The clusters are also polarized by the presence of the support X_2O under the clusters. For Pt_4/Na_2O, the surface atom is more negative (-0.16) than the interface atoms (-0.11). Also Pt_4/F_2O shows a smaller charge on the surface atom (+0.15) than the interface atoms (+0.32).

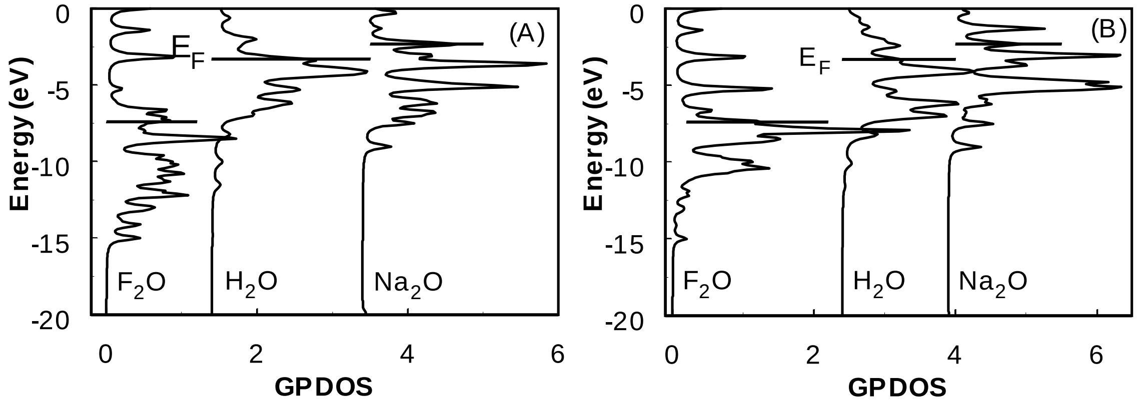

Figure 5: The GPDOS near the Fermi-level for a Pt_4 cluster supported on X_2O with X=F, H and Na for (A) the interface Pt atoms and (B) the surface Pt atoms.

In Figure 5 the GPDOS within the Pt_4 cluster for the different clusters is shown. Going from Na_2O → H_2O → F_2O, the complete GPDOS is shifted upwards, along with the Fermi level. This is similar for both the interface and the surface Pt atoms. However, compared to the interface atoms, the GPDOS for the surface atoms is more contracted (it expands over a smaller energy range). The interface Pt of the Pt_4/Na_2O cluster shows a negative GPDOS at 2.5 eV. A negative GPDOS indicates a negative overlap between symmetry-optimized combinations of fragment orbitals.

The GPDOS for the different clusters is shown in more detail in Figure 6. The GPDOS of the support oxygen atoms and Pt_{int} atoms on the Pt_4/Na_2O and Pt_4/F_2O clusters show considerable overlap, which is not the case for the Pt_4/H_2O cluster. In general, the shape of the DOS for the different clusters varies significantly. The isolated s-density of states of the Pt_{int} atoms is shown in Figure 7. This figure shows that below the Fermi-level the s-density of states of Pt_{int} is higher in the case of the basic Na_2O support compared to the F_2O support.

Pt_4 supported on a series of point charges

In addition to the use of various X_2O molecules, the electric field induced by the support is mimicked with a series of point charges. The geometry of these clusters is shown in Figure 1. The DFT calculations show that by increasing the magnitude of the point charges the cluster becomes more polarized (see Table 5). The complete cluster is neutral. The polarization of the cluster leads to a negatively charged Pt_{surf} with a positively charged Pt_{int}. The Fermi level of the unsupported cluster was positioned at –4.3 eV. The complete DOS was shifted to higher energies with increasing negative point charges. The Fermi level gradually increased from –4.3 eV to +2.2 eV for the cluster supported on the point charges with the highest magnitude (4

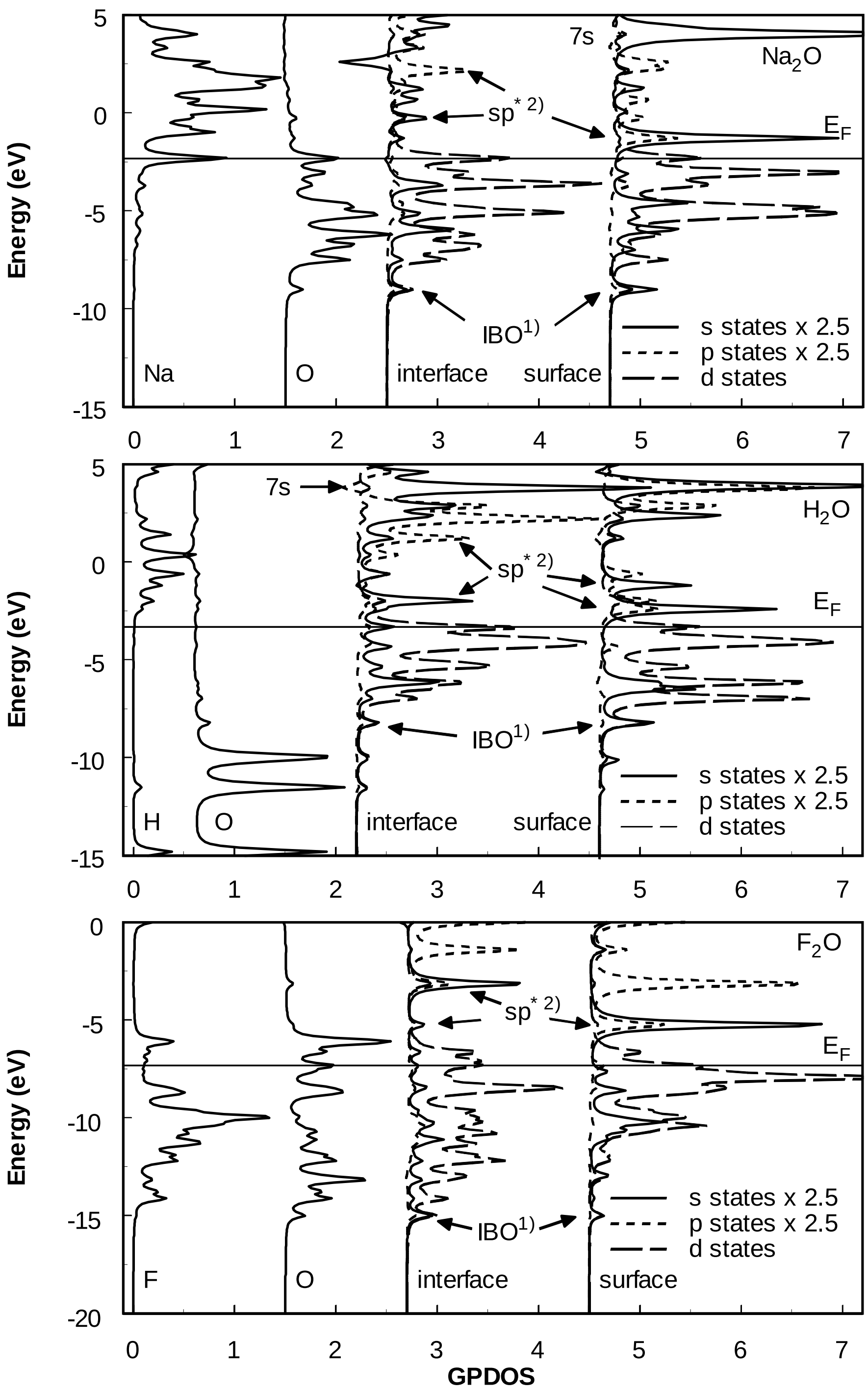

Figure 6: The GPDOS for the oxygen, Pt_{int} and Pt_{surf} atoms, as calculated with ADF for the Pt_4/Na_2O (top picture), Pt_4/H_2O (middle) and Pt_4/F_2O (bottom) clusters. The Pt 6s and 6p states were magnified by a factor of 2.5. The horizontal line represents the Fermi level E_F. [1] IBO = interstitial bonding orbital: a bonding combination of 6s and 6p orbitals. [2] an antibonding combination of 6s and 6p orbitals, mixed with small amounts of 5d and O 2p orbitals.

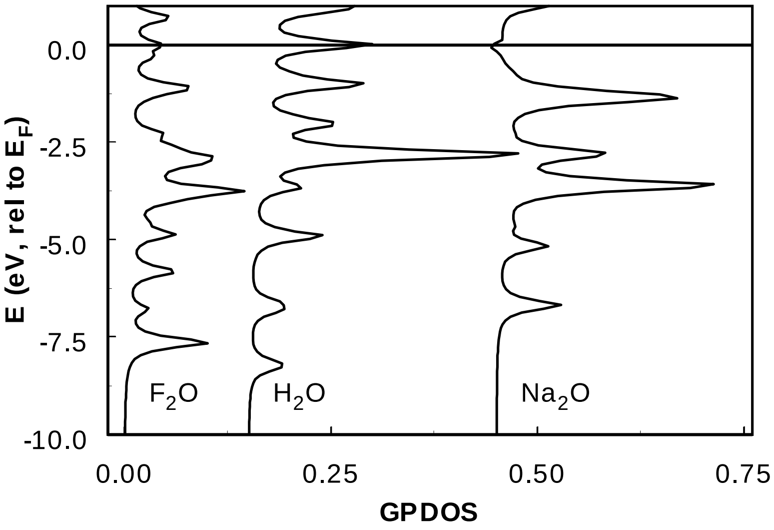

Figure 7: The s GPDOS for the interface Pt atoms. The energy is relative to the Fermi level.

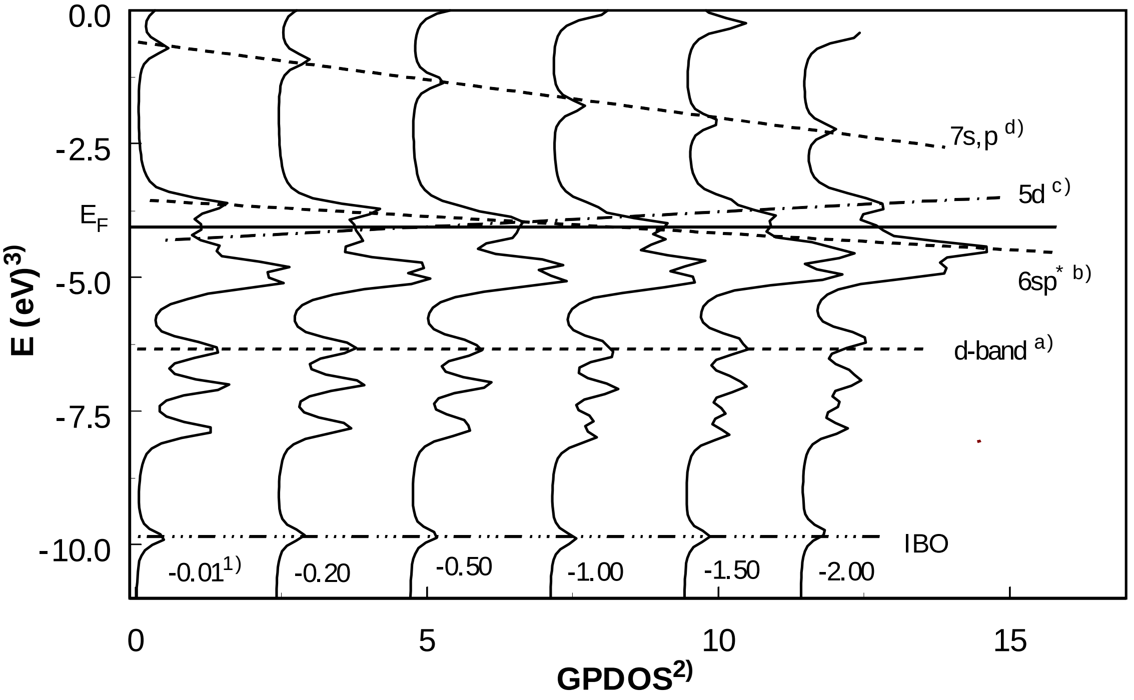

Figure 8: The influence of a series of pointcharges in a Si_2O_4 arrangement under the Pt_4 cluster on the Pt interface GPDOS around the Fermi level. [a]: a pure d-band is unaffected, [b]: the 6s6p anti bonding combiantion is sucked down below the Fermi level, [c]: a filled d-band is pushed up beyond the Fermi level and [d]: also higher combinations of s and p orbitals (7s, 7p) are sucked down. [1] For an explanation of the charges, see table 5. [2] For reasons of clarity, the GPDOS has been shifted to higher values for the consecutive graphs. [3] All graphs have been aligned on the Fermi levels.

x –2.0 and 2 x +4.0). The GPDOS as a function of increasing point charges is displayed in Figure 8. The GPDOS calculated for each point charge magnitude is aligned on the Fermi level of the unsupported cluster. Several antibonding combinations (6sp*) shift down below the Fermi level, and several 5d states become empty by moving above the Fermi level. The IBO is always located at approximately –10 eV (6 eV below E_F), and does not seem to be influenced by the presence of the point charges.

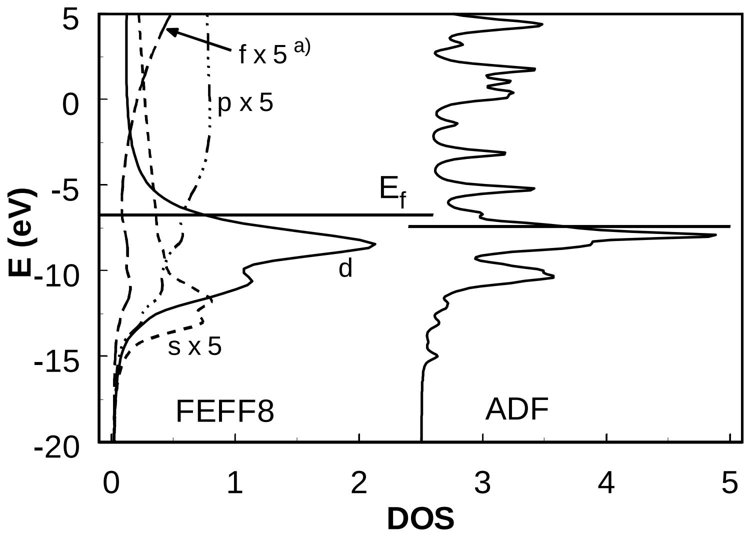

Figure 9: A comparison between the DOS calculated with FEFF8 and ADF for the surface atom of the $Pt_4/3•F_2O$ cluster. a): the DOS for the orbitals with s, p and f momentum have been magnified with a factor 5.

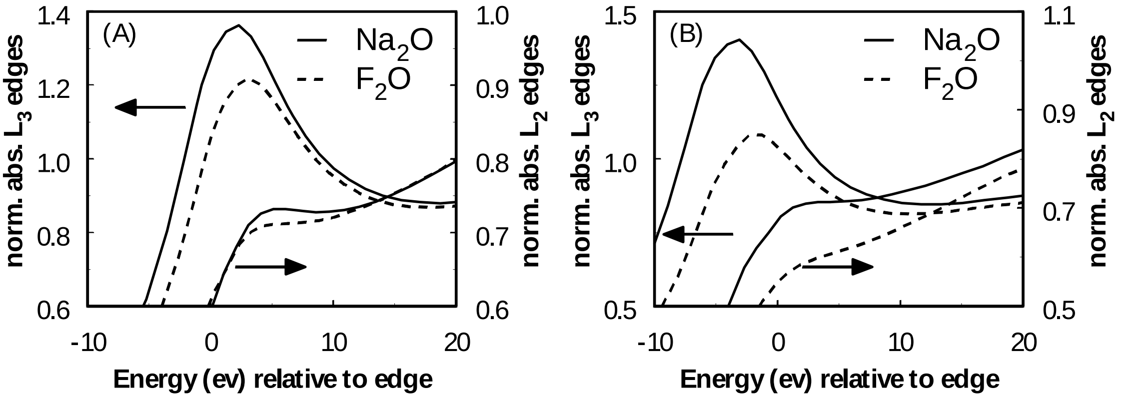

Figure 10: The L_2 and L_3 whitelines with (A) and without (B) complete core-hole screening, as calculated with the FEFF8 code. Solid line: $Pt_4/3•Na_2O$ cluster, dashed line: $Pt_4/3•F_2O$ cluster.

Full multiple scattering calculations

The DOS as calculated with FEFF8 for Pt_{surf} in the Pt_4/F_2O cluster is shown in Figure 9. The DOS for the orbitals with s, p and f momentum has been magnified with a factor 5. It can be seen that in Figure 9 that the DOS for Pt_{surf} calculated with FEFF8 reproduces the gross features of the GPDOS as obtained for Pt_{surf} with the DFT calculations.

The Pt L_2 and L_3 X-ray absorption edges for Pt/Na_2O and Pt/F_2O were calculated in the presence of a core-hole, with and without full core-hole screening (see Figure 10). As mentioned before, the scattering against the O, Na and F neighbors was not included in the FEFF8 calculation. It can be seen in Figure 10 that the intensity of the Pt L_2 and L_3 edges for Pt/Na_2O are higher than for Pt/F_2O. This means that the trends for the theoretically obtained L_2 and L_3 edges follow the same trend as the experimental data: highest edge intensity for Pt on basic supports with electron rich oxygen atoms.

Discussion

X-ray absorption edge structures

The reduced supported Pt catalysts after evacuation show a variation in the intensity of whiteline of the L_2 and L_3 X-ray absorption edges. This variation is induced by the support, and not by a particle size effect. The latter can also induce changes in the whiteline intensity[55,56], but cannot account for the observed changes. This is apparent when the two Pt/HT catalysts are compared (Figure 2): they have different particles size, but the changes in the whiteline intensity are marginal compared to the effect of the support on the whiteline. The whiteline intensities correlate to the electron richness on the support oxygen atoms, and are in the order HT [IE] ≈ HT [IM] > LTL [1.54] > LTL [1.04] > LTL [0.82].

There are several factors that can influence the whiteline intensity. Basically, the whiteline is determined by the final state empty DOS and by the core-hole attraction. It has been well established in older literature that the whiteline intensity is related to the number of holes in the 5d band[57,58]. Good examples of this phenomenon are a comparison between a Pt^0 and a Pt^{2+} species and the differences between the Pt L_2 and L_3 edge (see also Figure 2). A Pt^{2+} species will have a large number of holes in the 5d band, and consequently shows a large whiteline intensity. Similarly the L_2 edge consists of the $2p_{1/2} \rightarrow 5d_{3/2}$ transition and the L_3 edge reflects mainly the $2p_{3/2} \rightarrow 5d_{5/2}$ transition. Due to spin-orbit coupling, the $5d_{3/2}$ band is several eV higher in energy than the $5d_{5/2}$ band. This results in a higher, almost complete filling of the $5d_{3/2}$ band, whereas the $5d_{5/2}$ band is partially empty. This is reflected in a higher whiteline intensity for the L_3 edge. It is clear that the amount of d-holes can influence the whiteline, but the question is which factors in the catalytic samples can induce such changes the number of 5d holes.

The first possibility is the presence of an adsorbate on the Pt particles. An adsorbate will create an antibonding state with d character[20], and this antibonding state can act as an extra empty state above the Fermi level. Hence, it will be reflected in the whiteline[59-62]. Two

different types of adsorbates can be distinguished, (i) a gasphase adsorbate chemisorbed on the Pt surface and (ii) support atoms in the metal-support interface. The changes in the whiteline intensity were observed after reduction at elevated temperatures and evacuation at 200°C for 1 hour. At these temperatures, adsorbates like hydrogen are removed from the metal surface. Thus, an adsorbate on the Pt surface cannot account for the observed variation in the whiteline intensity. A support material can also create an empty antibonding state that is reflected in the whiteline. This has actually been reported in the work of Boyanov[63]. Moreover, an adsorbate can – in general – rehybridize the Pt valence orbitals, which will lead to different whiteline intensities. The influence of the support material viewed as an adsorbate is studied in more detail in the following paragraphs.

Another possibility for supported metallic clusters is a different filling of the d-band, achieved by (i) charge transfer from the metal cluster to the oxidic support or (ii) a rearrangement of the electrons within the Pt clusters. If a charge transfer would be responsible for the observed changes in the whiteline intensity, the order in which the whiteline intensities decrease is opposite to what would be expected. An acidic support has electron-poor oxygen atoms, and these electron-poor oxygen atoms would draw the electrons from the Pt particles away, as is observed with DFT (Table 4). This will resulting in less filling of the Pt 5d band – and, hence, a higher whiteline intensity. This is in contradiction to what is observed experimentally. Also other work dedicated to the support effects on Pt clusters discards the possibility of a charge transfer[63].

The effect of possibility (ii), an electron rearrangement, is far from straightforward. A rearrangement can exist of flowing of electrons to geometric different locations, or for example a rehybridization of the valence electrons. A rearrangement could be due to the electric field of the support. A rearrangement may lead to different electron configuration, for example a transition from $6s^1\ 5d^9$ to $6s^{1.2}\ 5d^{8.8}$. With such an electron rearrangement, the L_2 and L_3 whiteline would increase in intensity. In principle, the transition $2p \rightarrow 6s$ is also possible, and this transition is indeed reflected in the $L_{2,3}$ whitelines. However, the contribution to the $L_{2,3}$ whiteline of the $2p \rightarrow 6s$ transition is negligible compared to the $2p \rightarrow 5d$ transition. An electron rearrangement may also influence the core-hole screening in the final state[15].

From the experimental X-ray absorption data it can be concluded that the variation in both the L_2 and L_3 whiteline intensity correlates with the support alkalinity. This variation cannot be due to particle size effects. Charge transfer and the presence of a gasphase adsorbate are also excluded as possible causes. Two causes for the observed changes in the whiteline intensity are left: an electron rearrangement induced by the support, and atoms of the support material viewed as adsorbates. These two causes and the influence of the support on the part of the valence band below the Fermi level (undetectable with XAFS spectroscopy) will be discussed in the next sections using the results of the DFT and ab initio FMS calculations.

DFT

Unsupported Pt_4 cluster

The Pt-Pt bond length of 2.60 Å for the Pt_4 cluster with T_D symmetry, as was obtained with DFT, resembles nicely the experimental Pt-Pt bond length for small, clean Pt clusters (see *e.g.* Table 2). Also the features found in the density of states (Figure 3) reproduce results given in literature. The bonding combination of the 6s and 6p orbitals that is visible at –10 eV was also described by Kua and Goddard[22], which they called the 'interstitial bonding orbital' (IBO). They show that Pt atoms share an IBO in the center of every tetrahedron. These IBO's are suggested to play an important role in the bonding of molecules on the metal surface[19]. The antibonding combinations of these 6s and 6p orbitals are also distinctly present, above the Fermi-level. The 5d band extents from ~-8 eV to the Fermi-level at –4.3 eV. The Fermi-level 'cuts' through the highest 5d orbital, indicating they are not completely filled. This illustrates that the ground state for a Pt-tetrahedron is a multiplet state[22].

The 6s,p orbitals are present over a large energy range, on both sides of the 5d band. This shows that the 5d band is more contracted than the 6s,p band. This was also shown by Nørskov *et al.* in work on Pt slabs[21]. In their work, it was found that the bonding combinations of the 6s,p states are located at an energy higher than the bottom of the 5d band, whereas for the small clusters investigated here the bonding combination of the 6s,p states is located below the 5d band. This is most probably a result of the higher coordination of Pt atoms in slabs compared to small clusters. The larger the number of neighbors, the more the 5d band is broadened.

Supported Pt_4

The geometry of the Pt_4 clusters changes significantly when the three X_2O molecules are added. The Pt-Pt bond length is clearly influenced by the charges on the Pt atoms. With F_2O as support atoms, the interface Pt atoms are positively charged (see Table 4), and less electrons are shared in a Pt-Pt bond. To compensate for this effect, the atoms move closer to each other (Table 3). The opposite effect is observed for the negatively charged Pt atoms in the Na_2O supported cluster.

The supported clusters become charged and polarized when the X_2O molecules are placed underneath the Pt_4 cluster. In the case of the F_2O molecules, the oxygen atom is electron-poor, and charge flows from the Pt_4 cluster to the F_2O molecules. The oxygen in Na_2O is electron-rich, and, hence, these molecules donate electrons to the Pt_4 tetrahedron. The polarization of the clusters depends also on the X_2O molecules. The dipole is directed towards the interface in the case of the F_2O and Na_2O support, and towards the surface in the case of the Pt_4/H_2O cluster. However, for catalysis applications – catalysis is a surface process – another important parameter is the charge on the surface Pt in addition to the polarization. The charge on the surface Pt is –0.16 for the Pt_4/Na_2O cluster and increases for H_2O (-0.04) and F_2O (+0.15) supported clusters.

From the DFT calculations it is concluded that a basic support leads to negatively charged Pt_4 clusters and an acidic support to positively charged Pt_4 clusters. Both an acidic (F_2O) and basic (Na_2O) support result in a polarization of the Pt_4 clusters that is directed in the same direction: the interface.

The nature of the supporting X_2O molecules also has a profound effect on the DOS. The complete DOS (Figure 5) is shifted by several eV, along with the Fermi level. The Fermi level is shifted from –4.3 eV (clean cluster) to –7.4 eV for the Pt_4/F_2O cluster and to –2.3 eV for the Pt_4/Na_2O cluster. Shifts in the d-band were also experimentally observed in AXAFS studies[9,14].

More detailed information about the influence of the support X_2O on the Pt DOS can be obtained from Figure 6. For the Pt_4/F_2O cluster, the DOS of Pt_{int} shows some intensity just above the Fermi-level. These are empty d states. At –2.5 eV there are several distinct antibonding combinations of the Pt 6s and 6p orbitals. Compared to the clean cluster (Figure 3), these antibonding 6s and 6p combinations are shifted to higher energy with respect to the Fermi level. At higher energies the higher, unoccupied orbitals (7s, 7p, ..) are visible. The presence of 3 Na_2O molecules under the Pt_4 cluster has an opposite effect. Compared to the clean Pt_4 cluster, the complete DOS including all 5d and 6s,p orbitals of both the Pt_{int} and Pt_{surf} atoms is shifted upwards by several eV. The Fermi level is placed at –2.3 eV. The antibonding combinations of the 6s and 6p are sucked down relative to the Fermi level, and are mixed with the d-band. The antibonding combination with the lowest energy is even partially filled. This effect is emphasized in Figure 7, where the isolated Pt 6s DOS for the interface Pt atoms on the different support is shown. Clearly, the 6s DOS below the Fermi level is increased when the basic Na_2O support is employed. Effectively, this results in a different electron configuration for different supports, with an increased number of 6s electrons and a decreased amount of 5d electrons for a more basic support. This decreased amount of 5d electrons automatically results in an increased amount of empty d-states. This will lead to an increase in the $L_{2,3}$ whitelines for basic supports, as was observed experimentally. It is difficult to give quantitative numbers of this rehybridization because in these small clusters the charge transfer from metal to support and vice versa plays an important role.

For both types of support, acidic or basic, no antibonding combination between the orbitals of the X_2O and Pt_4 fragments was observed above the Fermi-level. This is most likely because the bonding combination has a lot of X_2O character, and the antibonding combination a lot of Pt character (Figure 11). This makes it difficult to see an antibonding combination. However, both the acidic and the basic support bond strongly to the Pt_4 clusters and they will both have antibonding states. Therefore, the difference in the whiteline intensity for Pt particles with acidic and basic supports cannot be due to the creation of extra antibonding states. This is in contrast to what has been proposed in the work of Boyanov *et al*[63]. They also report a variation in the whiteline with support materials of various acidities. In their work, this is

attributed to the creation of antibonding states. DFT shows no evidence to support these conclusions.

When 3 H_2O molecules are placed below the Pt_4 cluster, this leads to a different bonding with the Pt_4 cluster than in the case of the Na_2O and F_2O molecules. First, the bond energy is an order of magnitude lower for the H_2O molecules (Table 4). Second, with of the Na_2O and F_2O molecules, the oxygen shows some DOS in the energy range of the Pt 5d band (Figure 6). This indicates some mixing of the Na_2O and F_2O molecular orbitals with the Pt 5d band. In the case of the H_2O molecules, this does not seem to occur. The DOS of the oxygen or hydrogen atoms do not show any intensity in the region of the Pt 5d band. This shows that limited mixing between the Pt 5d band and the H_2O molecular orbitals occurs. This clearly illustrates the different nature for the Pt_4 – H_2O bonding compared to the Pt_4 – Na_2O or – F_2O bonding. This is also reflected in the long Pt-H_2O distance (Table 3). The observation that H_2O shows no interaction with the Pt_4 cluster, indicates that H_2O is relatively inert. Of course this could be expected, since H_2O exists in abundance and Na_2O or F_2O are uncommon molecules. Therefore, H_2O reflects an inert support material like SiO_2. Experimentally, it is known that it is difficult to make highly dispersed Pt on SiO_2. This has to do with the inertness of the support material, and it is simulated in the case of the Pt_4/H_2O cluster. The current results show that interaction between the support and the Pt occurs as long as the support is non-inert, regardless whether it is basic or acidic.

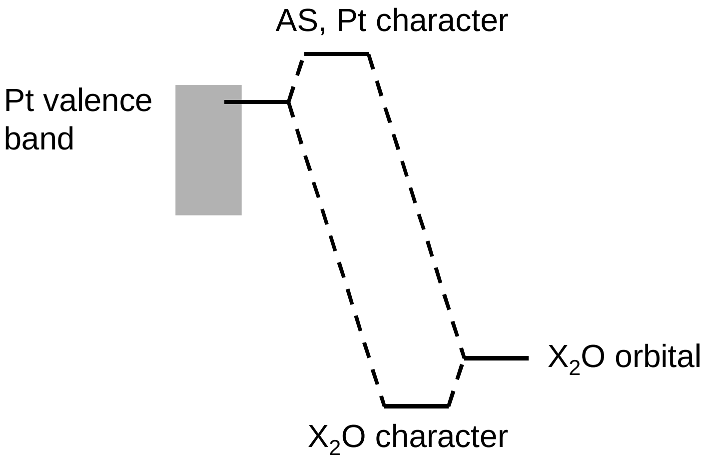

Figure 11: A schematic representation of the interaction between the Pt valence band and the X_2O valence orbital. The bonding combination has a lot of X_2O character, the antibonding state (AS) Pt character.

Clearly, the bonding of a support to the Pt cluster influences the metal valence orbitals. At this point, it is not clear whether the rehybridization is influenced by the Pt-support bond or by the Madelung potential of the support. However, above it is shown that the Pt_4-support bond strength goes through a minimum going from acidic to basic supports, with the minimum for neutral, inert support materials. If the variations in the whiteline intensity would be due to a rehybridization within the metal cluster caused by the creation of a metal-support bond, it is to be expected that the whiteline intensity follows the bond strength: low intensity for Pt on a

neutral support and high intensity for both a basic and an acidic supports. Since the whiteline intensities follow the trend in acidity (acidic < neutral < basic), it is unlikely that the variations in the whiteline intensity are caused by a rehybridization resulting from the cluster-support bonding properties. Thus, the observed rehybridization is caused by the Madelung potential of the support.

The DFT calculations lead to the conclusion that with increasing electron richness of the support oxygen atoms the Pt DOS together with the Fermi level moves to higher energy. On a basic support, the empty 6s,p combinations are shifted below the Fermi level and become filled, resulting in extra empty d-states. This explains the experimentally observed increase in intensity of the Pt $L_{2,3}$ X-ray absorption edges for basic supports. DFT shows no evidence for the creation of extra antibonding states that can explain such an increase. In addition, it was shown that the metal–support interaction is strong, as long as the support is not inert.

The interstitial bonding orbital

Kua and Goddard showed that the IBO is dominant for the chemisorption of adsorbates[19,22,64]. The use of DFT gives a reliable tool for determining the effect of the support material on the IBO. It was already observed that the IBO shifts along with the complete DOS to higher energy with increasing electron richness of the support oxygen atoms (which corresponds to a higher basicity of the support).

For the Pt_4/F_2O and the Pt_4/Na_2O clusters both Pt_{int} and Pt_{surf} show some intensity for the IBO (Figure 6). However, for the F_2O support the IBO for Pt_{surf} is smaller than for Pt_{int}, and the reverse is true for the Na_2O support. The ratio of the intensity in the DOS at the energy of the IBO, $DOS_{IBO,surface\ Pt}/(DOS_{IBO,surface\ Pt} + 3*DOS_{IBO,interface\ Pt})$, is a measure for the geometric location of the interstitial bonding orbital. If this ratio is 0.25, then the IBO is equally shared by all 4 atoms. For the Pt_4/F_2O cluster, this ratio $DOS_{IBO,surface\ Pt}/(DOS_{IBO,surface\ Pt} + 3*DOS_{IBO,interface\ Pt}) = 0.09$, indicating that only 9% of the IBO is located on Pt_{surf} and for 91% on the 3 Pt_{int} atoms. This shows that for the Pt_4/F_2O cluster the IBO is not only shifted to lower energy, but also geometrically towards the interface region. When the same principle is applied to Pt_4/Na_2O, it is found that the IBO is geometrically located for approximately 28% at the surface atom and for 72% on the interface atoms. The results are given in Table 6. These shifts in the location of the IBO were also suggested –without evidence- in earlier work[14]. These changes will have a large effect on the chemisorption of reactants, and, hence, on the catalytic properties. The adsorption energy and probably also the adsorption geometry will be influenced by these changes. This is the focus of forthcoming papers[65].

Table 6: The effect of the support on the interstitial bonding orbital.

Cluster	Position (eV)	Location (%)	
		3 interface Pt atoms	Surface Pt
Pt_4 free	-9.9	75	25
$Pt_4(F_2O)_3$	-15.0	91	9
$Pt_4(Na_2O)_3$	-9.0	72	28

Pt_4 placed on point charges

The effect of the Madelung potential of a support material on the metal cluster has been investigated using a series of point charges in a SiO_2 configuration below the Pt_4 cluster (Figure 1). The variations in the charges below the Pt_4 cluster were varied from –0.01 to –2.00 to imitate the oxygen sites and from +0.02 to +4.00 to mimic the Si sites. For comparison, a real support like SiO_2 has charges of approximately –1.2 for the oxygen site and +2.4 for the Si site[66], zeolites are a little more covalent with Mulliken charges around –1.0 for the oxygen positions[32,67]. Increasing the magnitudes of the point charges resembles an increase in electron richness of the support oxygen atoms, thereby increasing the basicity of a support[28].

The effect of the series of point charges is a heterogeneous electric field, that induces a polarization of the Pt_4 cluster. The surface Pt atom is increasingly negatively charged for an increased charge separation in the point charges directly under the Pt_4 cluster (Table 5). Not only the polarization but also the increased electron richness of the Pt surface atoms is of extreme importance from a catalysis point of view, since catalysis is a surface process.

By increasing the ionicity of the support (resulting in a simulation of more electron rich surface oxygen atoms, and more basic supports) below the Pt cluster, the complete DOS is shifted to higher energies. However, compared to low lying d-orbitals, which shift along with the Fermi-level, the shift for antibonding 6s,p orbitals is less pronounced. The result is that the antibonding combinations of the 6s and 6p orbitals end up below the Fermi level, mix with d orbitals and become filled. This is shown in Figure 8. The filling of the 6s and 6p orbitals result in a lower occupation of orbitals with d character. An increase in empty d states will result directly in an increased whiteline intensity as is observed experimentally.

The origin of the different influence of an increased Madelung potential on the s, p and d states close to or above the Fermi level lies probably in the delocalized nature of the empty s and p states. In contrast to the d states, s and p orbitals are very diffuse. The Madelung potential is strongest near the metal-support interface and the potential decreases with $1/r^2$ (with r= the distance from a certain point to a point charge). Due to the delocalized nature of s and p orbitals, these orbitals will be less influenced than the localized d orbitals. The result is that the filled d states are pushed above the empty s and p states. This rehybridization of the Pt valence band is basically similar to what was observed with the X_2O molecules as a support. As a consequence, Pt electrons rearrange from 5d to $6sp^*$. An increased number of d-holes will result in i) an increase of the whiteline intensity, as was seen experimentally, and ii) clusters with more metallic character with respect to screening of the core-hole, as was observed earlier[15].

Similar to what happens with point charges, also X_2O leads to a Madelung potential and indeed, in some respects, the series of point charges has the same influence on the Pt_4 clusters as the X_2O molecules. For both simulations of the support, it was seen that a basic support leads to a rehybridization with more filled $6sp^*$ and empty 5d states, to a polarization of the particle and to a shift of the complete DOS to higher energies.

Full multiple scattering calculations

An example of the DOS resulting from the FMS calculations is shown in Figure 9. A comparison between the DOS as calculated with ADF and FEFF8 reveals that below the Fermi level both methods result in the same features. Both methods result in a similar splitting of the d-band, and both methods calculate the presence of an interstitial orbital containing s and p character below the 5d band. Above the Fermi level, the features calculated with FEFF8 are broadened by the life time broadening incorporated in X-ray absorption spectroscopy. Therefore, the DOS above the Fermi level is very broad, and no distinct features are visible. All the antibonding combinations of the 6s, 6p and at higher energies the 7s orbitals are broadened by the FMS calculations to a very broad, low intensity band. This broadening and resulting low intensity of the empty 6s explains why the 2p → 6s transition does not contribute significantly to the whiteline intensity. Moreover, the 6s and 6p antibonding states have some p-character, which makes the transition less likely. The result is that the whiteline is determined almost exclusively by the empty d states.

The X-ray absorption edge (Figure 10) as calculated with FEFF8 shows a higher L_2 and L_3 whiteline for the Pt_4/Na_2O cluster. This is visible for both complete screening of the core-hole and in the presence of the core-hole. The higher whiteline for the Pt_4/Na_2O cluster is rather remarkable, since the Pt_4 cluster on the F_2O molecules is positively charged, and on the Na_2O molecules negatively charged. As explained previously, when electrons are extracted from the Pt cluster, this would lead to a higher whiteline. Apparently, the charge transfer is not the dominating factor for the observed differences in the whiteline.

It seems obvious that a different electron structure will lead to a different screening of the core-hole. A different screening would be the result of a transition from insulator to metal. Although some differences in the whitelines are visible when complete screening is turned on and of, in both situations the whitelines are higher for the basic cluster. Clearly, differences in screening cannot explain the observed differences in the whiteline intensity. The different screening probabilities can best be studied by analyzing the difference between the Pt L_2 and L_3 edges[68].

Conclusions

The X-ray absorption experiments on the Pt L_2 and L_3 edges of supported Pt particles indicated that an increase in the electron richness of the support oxygen atoms, which is associated with an increased basicity of the support, leads to an increased number of 5d holes. DFT (ADF code) and full multiple scattering calculations (FEFF8 code) were carried out on a $Pt_4/3{\bullet}X_2O$ cluster with X = F, H, and Na to mimic changes on the electron richness of the support oxygen atoms. The influence of the support was also simulated by the presence of a series of point charges. The origin of the interaction between support and metal particle consists of a combination of several effects. First, the electric field of the support (the Madelung potential) creates a polarization within the metal particle. Second, the complete Pt DOS is shifted to higher energies with increasing basicity of the support. Third, the Madelung

potentials results in a rehybridization of the orbitals close to, or above the Fermi level. For a basic support, some 6s,p* are sucked below the Fermi level whereas 5d states are pushed above the Fermi level. This results in a different electron configuration, with extra empty d-holes as seen experimentally.

Fourth, a bond is formed between the support and metal particle, mainly via the interstitial bond orbital of the metal particle. For a basic support with electron rich support oxygen atoms, electrons are donated to the Pt particle and the IBO is geometrically located at the surface of the metal particle. The opposite occurs for acidic supports, where Pt particles becomes positively charged and the IBO is geometrically located at the metal-support interface region. Since reactants will adsorb on the metal via this IBO, the different geometrical locations will have large effects on the catalytic properties of a supported Pt catalyst.

Acknowledgements

Jules Roelofs is acknowledged for his help and discussions concerning the synthesis of hydrotalcites. The EXAFS team is acknowledged for their help performing the EXAFS measurements in at beamline X1.1 at the HASYLAB in Hamburg. All work was supported by the Dutch science foundation NWO. The EXAFS work was also supported by the IHP-Contract HPRI-CT-1999-00040 of the European Commission.

Reference list

1. B. C. Gates, *Chem. Rev.*, **95** (1995), 511-522.
2. R. A. Dalla Betta and M. Boudart, *Proc 5th Int Con Cat* (1973), 1329-1341.
3. A. de Mallmann and D. Barthomeuf, *J. Chim. Phys.*, **87** (1990), 535-538.
4. Z. Karpinski, S. N. Gandhi and W. M. H. Sachtler, *J. Catal.*, **141** (1993), 337-346.
5. Z. Zhang, T. T. Wong and W. M. H. Sachtler, *J. Catal.*, **128** (1991), 13-22.
6. G. Larsen and G. L. Haller, *Catal. Lett.*, **3** (1989), 103-110.
7. A. M. Ferrari and G. Pacchioni, *J. Phys. Chem.*, **100** (1996), 9032-9037.
8. B. L. Mojet, J. T. Miller, D. E. Ramaker and D. C. Koningsberger, *J. Catal.*, **186** (1999), 373-386.
9. D. E. Ramaker, G. E. van Dorssen, B. L. Mojet and D. C. Koningsberger, *Top. Catal.*, **10** (2000), 157-165.
10. A. P. J. Jansen and R. A. van Santen, *J. Chem. Phys.*, **94** (1990), 6764.
11. A. Yu. Stakheev and L. M. Kustov, *Appl. Catal. A: General*, **188** (1999), 3-35.
12. A. Yu. Stakheev, E. S. Shapiro, N. I. Jaeger and G. Schulz-Ekloff, *Catal. Lett.*, **32** (1995), 147-158.
13. B. I. Boyanov and T. I. Morisson, *J. Phys. Chem.*, **100** (1996).
14. D. E. Ramaker, J. de Graaf, J. A. R. Van Veen and D. C. Koningsberger, *J. Catal.*, **203** (2001), 7-17.
15. D. E. Ramaker, M. K. Oudenhuijzen and D. C. Koningsberger, *J. Chem. Phys.* (submitted).
16. G. A. Somorjai, *J. Mol. Catal. A*, **107** (1996), 39-53.
17. P. Cernota, K. Rider, H. A. Yoon, M. Salmeron and G. A. Somorjai, *Surf. Sci.*, **445** (2000), 249-255.

18. A. Ruban, B. Hammer, P. Stoltze, H. L. Skriver and J. K. Nørskov, *J. Mol. Catal. A,* **115** (1997), 421-429.
19. J. Kua and W. A. Goddard III, *J. Phys. Chem. B,* **102** (1998), 9492-9500.
20. B. Hammer and J. K. Nørskov, *Nature,* **376** (1995), 238-240.
21. G. Papoian, J. K. Nørskov and R. Hoffmann, *J. Am. Chem. Soc.,* **122** (2000), 4129-4144.
22. J. Kua and W. A. Goddard III, *J. Phys. Chem. B,* **102** (1998), 9481-9491.
23. Y. Y. Tong, J. Billy, A. J. Renouprez and J. J. van der Klink, *J. Am. Chem. Soc.,* **119** (1997), 3929-3934.
24. A. de Mallmann and D. Barthomeuf, *Stud. Surf. Sci. Catal.,* **46** (1989), 429.
25. G. S. Lane, J. T. Miller, F. S. Modica and M. K. Barr, **0** 465-477.
26. A. L. Yakovlev, K. M. Neyman, G. M. Zhidomirov and N. Rösch, *J. Phys. Chem.,* **100** (1996), 3482-3487.
27. C. Hippe, R. Lamber, G. Schulz-Ekloff and U. Schubert, *Catal. Lett.,* **43** (1997), 195-199.
28. N. López, *J. Chem. Phys.,* **114** (2001), 2355-2361.
29. M. T. M. Koper, R. A. van Santen, S. A. Wasileski and M. J. Weaver, *J. Chem. Phys.,* **113** (2000), 4392-4407.
30. G. Blyholder, *J. Phys. Chem.,* **68** (1964), 2772.
31. A. L. Ankudinov, B. Ravel, J. J. Rehr and S. D. Conradson, *Phys. Rev. B,* **58** (1998), 7565-7576.
32. N. O. Gonzales, A. K. Chakraborty and A. T. Bell, *Catal. Lett.,* **50** (1998), 135-139.
33. J. C. A. A. Roelofs, A. J. van Dillen and K. P. de Jong, *Catal. Today,* **60** (2000), 297-303.
34. J. A. van Bokhoven, J. C. A. A. Roelofs, K. P. de Jong and D. C. Koningsberger, *Chem. Eur. J.,* **7** (2001), 1258-1265.
35. K. Kinoshita, K. Routsis and J. A. S. Bett, *Thermochim. Acta,* **10** (1974), 109-17.
36. M. K. Oudenhuijzen, J. H. Bitter and D. C. Koningsberger, *J. Phys. Chem. B,* **105** (2001), 4616-4622.
37. M. Vaarkamp, B. L. Mojet, F. S. Modica, J. T. Miller and D. C. Koningsberger, *J. Phys. Chem.,* **99** (1995), 16067.
38. D. C. Koningsberger, B. L. Mojet, G. E. van Dorssen and D. E. Ramaker, *Top. Catal.,* **10** (2000), 143-155.
39. M. Vaarkamp, J. C. Linders and D. C. Koningsberger, *Physica B,* **208** (1995), 159-160.
40. S. I. Zabinsky, J. J. Rehr, A. L. Ankudinov, R. C. Albers and M. J. Eller, *Phys. Rev. B,* **52** (1995), 2995-3009.
41. G. E. van Dorssen, Ph.D., *thesis*, Utrecht University, Utrecht, 1999.
42. Amsterdam Density Functional Package ADF 2000.02, Department of Theoretical Chemistry, Vrije Universiteit, Amsterdam. http://www.scm.com.
43. A. D. Becke, *J. Chem. Phys.,* **85** (1986), 7184-7187.
44. J. P. Perdew, *Phys. Rev. B,* **33** (1986), 8822-8824.
45. P. H. T. Philipsen, E. Van Lenthe, J. G. Snijders and E. J. Baerends, *Phys. Rev. B,* **56** (1997), 13556.
46. E. Van Lenthe, E. J. Baerends and J. G. Snijders, *J. Chem. Phys.,* **101** (1994), 9783.
47. J. B. A. D. Van Zon, D. C. Koningsberger, H. F. J. Van 't Blik, R. Prins and D. E. Sayers, *J. Chem. Phys.,* **80** (1984), 3914.
48. M. Vaarkamp, F. S. Modica, J. T. Miller and D. C. Koningsberger, *J. Catal.,* **144** (1993), 611-626.

49. D. Majumdar, D. Dai and K. Balasubramanian, *J. Chem. Phys.,* **113** (2000), 7928-7938.
50. D. Majumdar, D. Dai and K. Balasubramanian, *J. Chem. Phys.,* **113** (2000), 7919-7927.
51. E. J. Baerends, V. Branchadell and M. Sodupe, *Chem. Phys. Lett.,* **265** (1997), 481-489.
52. J. A. Alonso, *Chem. Rev.,* **100** (2000), 637-677.
53. F. L. Hirshfeld, *Theoret. Chim. Acta,* **44** (1977), 129.
54. K. B. Wiberg and P. R. Rablen, *J. Comp. Chem.,* **14** (1993), 1504.
55. Ichikuni, N.; Iwasawa, Y. *Catal. Lett.* **1993**, *20*87-95.
56. D. Bazin, D. E. Sayers, J. J. Rehr and C. Mottet, *J. Phys. Chem. B,* **101** (1997), 5332-5336.
57. L. F. Mattheiss and R. E. Dietz, *Phys. Rev. B,* **22** (1980), 1663-1676.
58. F. W. Lytle, *J. Catal.,* **43** (1976), 376-379.
59. S. N. Reifsnyder, M. M. Otten, D. E. Sayers and H. H. Lamb, *J. Phys. Chem. B,* **101** (1997), 4972-4977.
60. K. Asakura, T. Kubota, N. Ichikuni and Y. Iwasawa, *Stud. Surf. Sci. Catal.,* **101** (1996), 911-919.
61. D. E. Ramaker, B. L. Mojet, M. T. Garriga Oostenbrink, J. T. Miller and D. C. Koningsberger, *Phys. Chem. Chem. Phys.,* **1** (1999), 2293-2302.
62. D. C. Koningsberger, M. K. Oudenhuijzen, J. H. Bitter and D. E. Ramaker, *Top. Catal.,* **10** (2000), 167-177.
63. B. I. Boyanov and T. I. Morisson, *J. Phys. Chem.,* **100** (1996), 16318-16326.
64. J. Kua, F. Faglioni and W. A. Goddard III, *J. Am. Chem. Soc.,* **122** (2000), 2309-2321.
65. Chapter 9 of this thesis.
66. R. P. Gupta, *Phys. Rev. B,* **32** (1985), 8278-8292.
67. R. A. van Santen and G. J. Kramer, *Chem. Rev.,* **95** (1995), 637-660.
68. Chapter 7 of this thesis.

9

Influence of Support Alkalinity on Pt Particle Adsorbate Bonding

Implications for alkane hydrogenolysis

Abstract

The influence of the acid/base properties of the support on the adsorption of H and CH_x (x=2,3) on supported Pt particles is investigated using density functional theory (DFT). The DFT results show that the support acidity has a large impact on the Pt 6s,p states. On basic supports, the 6s,p states are pushed towards the surface of a metal cluster, whereas on acidic supports they are attracted towards the metal-support interface. In addition, the DFT calculations reveal that the importance of the 6s,p states for the Pt adsorbate bonding increases in the order Pt-CH_2 < Pt-CH_3 < Pt-H. Consequently, the Pt-H bond strength is strongly affected by changes in the support acidity while the difference for the Pt-CH_x bond strength is much smaller. Due to the stronger Pt-H bond on basic supports, the H coverage with strongly bonded hydrogen on Pt particles with a basic support is higher than on acidic supports.

The support induced changes in hydrogenolysis reactions of alkanes can be explained to a large extent by support induced changes in the Pt-H bond strength and hydrogen adsorption site on Pt. This can easily explain the well-known compensation effect found in the kinetics of the hydrogenolysis of alkanes catalyzed by supported metal catalysts.

Introduction

Supported noble metal catalysts are widely used in commercially important reactions, including hydrogenation, naphtha reforming and isomerization reactions[1]. The first report of enhanced reaction rates with specific supports was made by Dalla Batta and Boudart[2]. Since then, it has been well established that the nature of the support influences the rate of hydrogenation and hydrogenolysis reactions on catalytically active metal particles[2-8]. For example, in the conversion of neopentane ($C\text{-}(CH_3)_4$) it has been observed that the rate of hydrogenolysis is several orders of magnitude higher when Pt particles are supported on an acidic support compared to a basic support. In addition, the inhibition by hydrogen of the hydrogenolysis of alkanes is much stronger for basic supports: the order in H_2 ranges from –2.5 (basic support) to –1.5 (acidic)[7,9-11].

Although the effect of the support on the catalytic properties of the supported metal particles has been well established, the nature of this metal-support interaction has been the subject of much debate. Explanations have involved the formation of metal-proton adducts on Brønsted acidic supports[5,12], electron transfer between support and particle[8,13,14], the polarization of the metal particle by nearby cations[15] and a rehybridization and polarization within the particle by the Madelung potential of the support[16,17].

Recent work by our group revealed that the nature of the metal support interaction involves a change in the electronic properties of the metal cluster, induced by and correlated to the electron richness of the support oxygen atoms[18,19]. X-ray absorption fine structure experiments (L_2 and L_3 near edge structure and Atomic XAFS) and density functional theory (DFT) calculations on supported Pt clusters revealed that the support influences the electronic properties of a metal particle in three separate ways. First, the complete Pt density of states (DOS) near the Fermi level shifts to higher energy (lower binding energy) with increasing electron richness of the support oxygen atoms (electron rich support oxygen atoms are associated with basic supports[19,20]). Second, the Madelung potential of a basic support shifts some 6s and 6p valence states below the Fermi-level where they consequently become filled at the expense of 5d states (*e.g.* rehybridization from $5d^9 6s^1$ to $5d^{8.5} 6s^{1.5}$). Third, the location of the 6s,p bonding orbital (IBO: interstitial bonding orbital[21]) moves from the metal-support interface to the surface of the Pt particles with increasing electron richness of the support oxygen atoms.

It seems obvious that these changes in the DOS within a supported Pt particle will affect the chemisorption of adsorbates like CH_x and H_2 on the surface. Indeed, XAFS, hydrogen chemisorption experiments and DFT calculations showed that on basic supports and at low coverage hydrogen is adsorbed more strongly on the Pt 3-fold hollow sites, while on acidic supports the hydrogen is adsorbed on atop sites with lower adsorption energy[22]. However, an explanation for these different bonding properties has not been given, and it remains unclear how the bonding of hydrocarbons is affected by the changes in the electronic properties of supported metal clusters. The limited amount of work reported regarding the adsorption of CH_x and H on metals mainly focuses on Pt (111) flat surfaces[21,23-25]. These flat surfaces are

very small in the case of highly dispersed metal particles, which mainly consist of edge and step sites. However, theoretical work has suggested that the metal s-p states are very important for hydrogen chemisorption, while the d states are more important for chemisorbed CH_x fragments[21,23-25].

As mentioned above, the support has three effects on the electronic structure of supported Pt particles. An increasing electron richness of the support oxygen atoms results in: (i) a shift in the total density of states to higher energy, (ii) rearrangement of the s-p states within the particle from the particle-support interface to the particle surface and (iii) rehybridization of the valence band to more 6sp and less 5d character. A crucial question to answer is how these change in s,p and d-states influences the chemisorption of H and CH_x on the Pt particles.

This paper will focus on answering the above raised question. In order to find these answers, DFT calculations with the ADF package[26] on supported Pt_4 clusters are performed. CH_3, CH_2 and H fragments are adsorbed on the Pt_4 clusters. Since it is computationally expensive to simulate a complete support matrix, the Pt_4 clusters are placed on three X_2O molecules to mimic the support. The change of the electron richness of the O atom in 'real' supports from electron rich (basic support) to electron poor (acidic support)[19,20] is simulated by varying the nature of the *X* atom. F_2O (F is very electronegative, therefore giving an electron poor oxygen atom) represents an acidic support while Na_2O (Na is less electronegative than oxygen, thus giving electron rich oxygen atoms) mimics a basic support. It was shown earlier that these support molecules reproduce the electronic phenomena within the Pt cluster as observed with the use of L_2 and L_3 X-ray absorption edges surprisingly well[19].

The results of this work will show that the support acid/base properties has the largest influence on the adsorption of H, while the effect of the support on CH_3 and CH_2 adsorption is much smaller. These new results can explain several support-induced changes in the catalytic properties of supported Pt catalysts. These changes are mainly driven by the strength of the Pt-H bond.

Computational Methods

The DFT calculations reported here have been performed using the Amsterdam Density Functional Package ADF[26]. This package uses the Kohn-Sham approach to the density-functional theory. Slater-type orbitals are used to represent the atomic orbitals. All basis sets consist of triple-ζ quality, extended with two polarization functions. The density functional was calculated using the Vosko-Wilk-Nussair approximation of the local density approximation (LDA), and using the Becke gradient correction[27] and Perdew correlation term[28] for the generalized gradient approximation (GGA). To enhance computational efficiency, several atomic core shells of the Pt atoms were frozen up to and including the Pt 4d level. Relativistic effects were accounted for using the ZORA approximation[29,30]. The geometry optimizations that were performed were carried out in the spin-restricted mode including scalar relativistic effects, thereby excluding spin-orbit effects. This level of accuracy has been reported to agree well with experimental data[31]. The numerical integration

precision applied was set to 5.5 significant digits. The applied criterions for the geometry optimization were 1 x 10^{-3} Hartree for the changes in energy, 1 x 10^{-4} Hartree/Å for changes in the energy gradients and 1 x 10^{-2} Å for changes in the Cartesian coordinates.

The clusters that were investigated consist of a Pt_4 tetrahedron supported by 3 X_2O molecules, with X = Na or F. The global geometry is shown in Figure 1. The geometry of the clean Pt_4/X_2O was optimized within the boundaries of C_{3v} symmetry. Details are given elsewhere[19].

A H atom, and CH_3 or CH_2 fragments were placed in the atop, bridged or 3-fold site (see Figure 1). The Pt_4 cluster with adsorbate was allowed to relax its geometry within the limits of C_s symmetry, however, the coordinates of the X_2O molecules were fixed in order to represent the rigid nature of a real support.

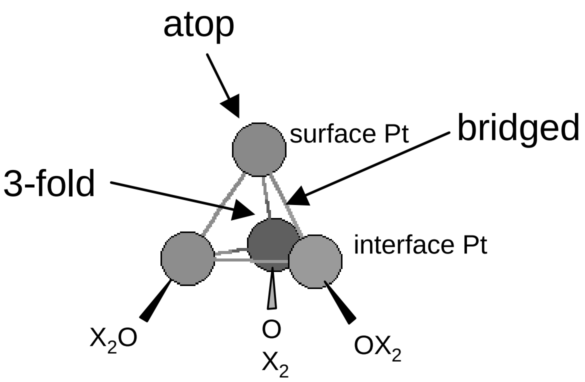

Figure 1: The Pt_4/X_2O cluster with 3 different adsorption sites.

The bond energy is calculated in two ways. The 'heat of adsorption', E_{ads}, reflects the decomposition of the gas phase molecule into fragments followed by adsorption of these fragments onto the Pt cluster. The gas phase molecule was either H_2 or CH_4.

Thus, E_{ads} for H_2 is calculated by taking the difference in the total energy of Pt_4-H/X_2O and H_2 + Pt_4/X_2O:

$$E_{ads,H2} = 2 * E_{Pt4\text{-}H/X2O} - 2 * E_{Pt4/X2O} - E_{H2} \quad (1)$$

The total energy of a cluster was determined relative to the atomic reference energies according to Baerends *et al*[32].

In calculating the adsorption energy of CH_n it was assumed that the hydrogen fragment adsorbs on a clean cluster, and thus the adsorption energy E_{ads} is given by:

$$E_{ads,CHn} = E_{Pt4\text{-}CHn/X2O} + (4\text{-}n) * E_{Pt4\text{-}H/X2O} - (5\text{-} n) * E_{Pt4/X2O} - E_{CH4} \quad (2)$$

The 'intrinsic bond energy' reflects the energy required to remove a fragment adsorbed on the Pt_4 cluster to the gas phase. It is given for hydrogen bonded on Pt_4 by:

$$E_{int,H} = E_{Pt4\text{-}H/X2O} - E_H - E_{Pt4/X2O} \quad (3)$$

and for a CH_n fragment bonded on Pt_4:

$$E_{int,CHn} = E_{Pt4\text{-}CHn/X2O} - E_{CHn} - E_{Pt4/X2O}\ (CH_n \text{ bonding}) \quad (4)$$

Results

Hydrogen adsorption

The H was placed on the supported Pt_4 clusters in either the 3-fold hollow, bridged, or atop site, and the geometry was optimized. Regardless of the support (Na_2O vs. F_2O), when starting in the 3-fold hollow site the hydrogen drifts to the atop site after geometry optimization. Moreover, hydrogen in the atop site is more stable than the bridged site by as much as 200 kJ/mol H_2 (Table 1). Clearly, hydrogen on these small cluster is most stable in the atop site. However, in earlier work[22] it was shown that under typical experimental conditions (~ 400 – 600 K, with a coverage of approximately ¼ monolayer of hydrogen) the hydrogen adsorption position strongly depends in the support material. When Pt is placed on a basic support, H prefers the 3-fold hollow site or bridged site at relatively low coverage. However, when Pt is placed on an acidic support, H prefers the atop position even up to relatively high H coverage.

The hydrogen in the atop site is found to be tilted towards the interface, and this tilt is largest in the case of the acidic support: compare Figure 2A with B. The Pt-H bond length is 1.55 Å for adsorption in the atop position on the Pt_4/F_2O cluster, with Pt-Pt bond lengths varying from 2.49 to 2.59 Å. For Pt_4/Na_2O, the Pt-H bond length is 1.59 Å, and the Pt-Pt bond lengths range from 2.56 – 2.59 Å.

The heat of adsorption, E_{ads} and intrinsic bond energy E_{int} for Pt-H are given in Table 1. E_{ads} is 70 kJ/(mol H_2) more exothermic in the case of the basic support compared to the acidic support. Analogous to the heat of adsorption, the intrinsic bond strength is increased by 35 kJ/(mol H) for the basic supported.

Table 1: The heat of adsorption (E_{ads}) and intrinsic bond energy (E_{int}) for the adsorption of H_2 and CH_n in the atop, bridged (br.) and 3-fold hollow site (3-f.) on Pt_4/F_2O or Pt_4/Na_2O.

Adsorbate		E_{ads} (kJ/mol)		E_{int} (kJ/mol)	
		Pt_4/F_2O	Pt_4/Na_2O	Pt_4/F_2O	Pt_4/Na_2O
H[1]	atop	–106.0	-175.2	-375.8	-410.4
	br.	+105.4	-14.8	-270.1	-330.2
	3-f.	unstable[2]			
CH_3	atop	-59.7	-110.1	-303.8	-319.5
	br.	unstable[2]			
	3-f.	unstable[2]			
CH_2	atop	+1.6	-86.7	-553.4	-572.5
	br.	-49.6	-105.7	-604.6	-591.5
	3-f.	+23.2	unstable[2]	-531.8	unstable[2]

[1]: The adsorption energy E_{ads} for H_2 is in kJ per mol H_2, the intrinsic energy E_{int} is in kJ per mol H.

[2]: The adsorbed fragment drifted to the most stable position during the geometry optimization.

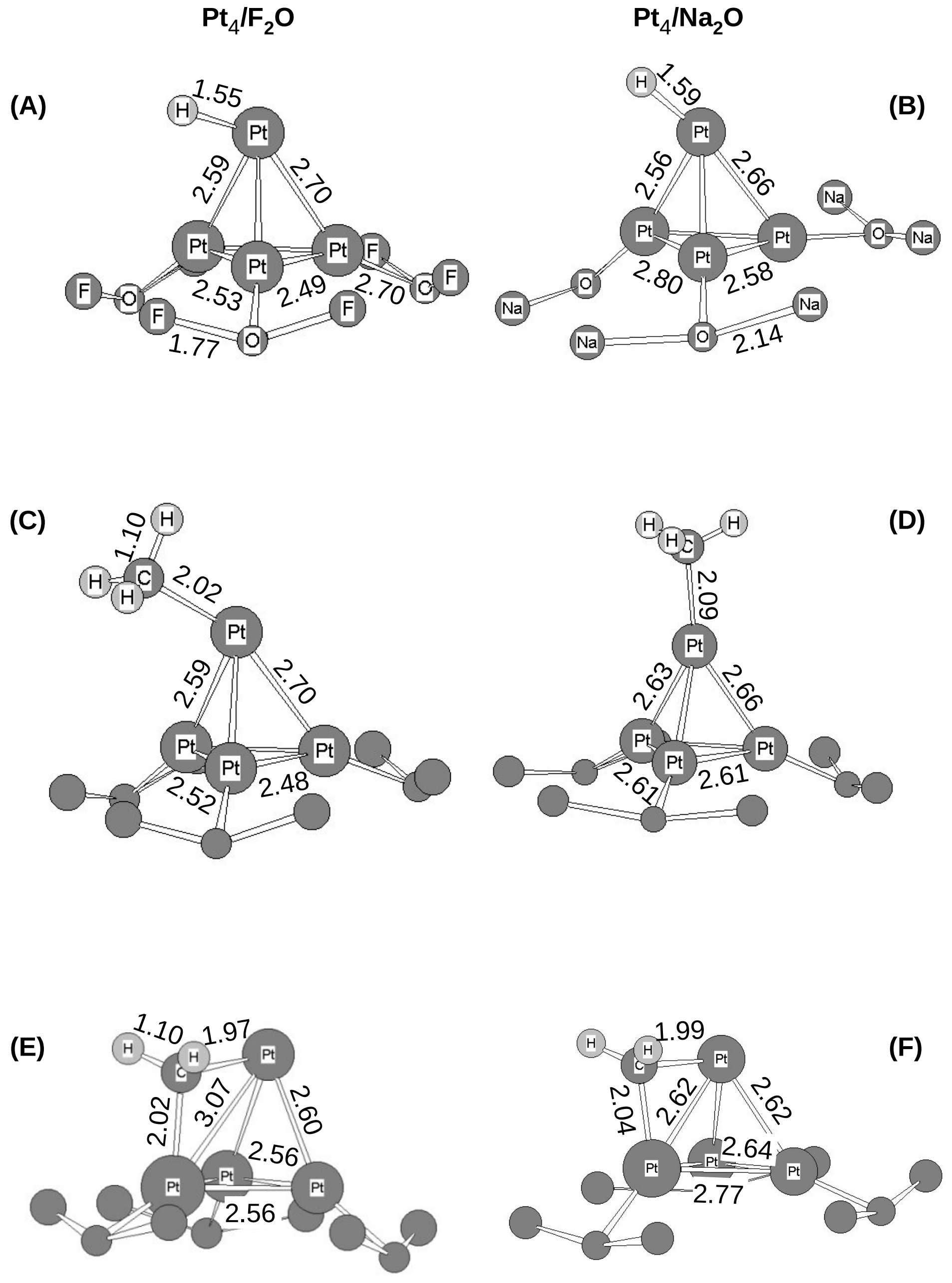

Figure 2: The optimized geometries of a Pt_4 cluster. Hydrogen adsorbed in the atop position: (A) F_2O and (B) Na_2O support. CH_3 adsorbed atop: (C) F_2O and (D) Na_2O support. CH_2 adsorbed in the bridged position: (E) F_2O and (F) Na_2O support. The C-H bond length was not affected by the support, the Pt-O and O-X bond lengths were unaffected by the adsorbate. The bondlengths are given in Å.

The gross population density of states (GPDOS) for the H and $Pt_{surface}$ atoms for the Pt_4/F_2O and Pt_4/Na_2O clusters are shown in Figure 3 and Figure 4, respectively. Several observations can be made: The H 1s state is split into multiple peaks, with maxima aligning with peaks in the Pt 6s,p DOS. The Pt 5d band does not take significant part in the H bonding, since most of

its DOS does not overlap with the maxima in the H 1s DOS. Above the Fermi-level, the H 1s - Pt 6s,p anti-bonding state (AS) is clearly visible. Compared with the acidic F_2O support, the H 1s overlaps more with the Pt 6s,p states and less with the Pt 5d states on the Na_2O support. Moreover, there are clearly more Pt 6sp states below the Fermi level in the Na_2O case.

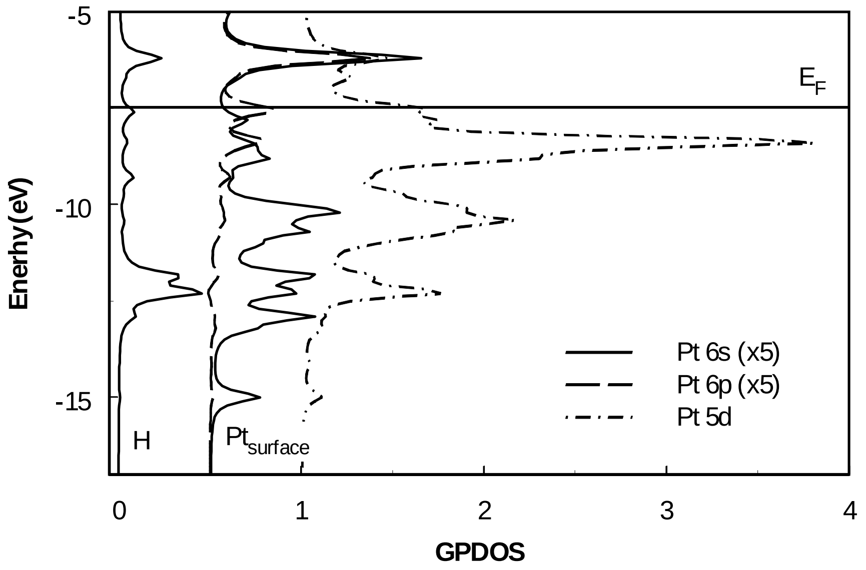

Figure 3: The H 1s GPDOS and the surface Pt atom 5d,6s-p GPDOS for hydrogen adsorbed in the atop position on a Pt_4/F_2O cluster. The Pt 6s and 6p GPDOS is magnified by a factor of 5. E_F is the Fermi level.

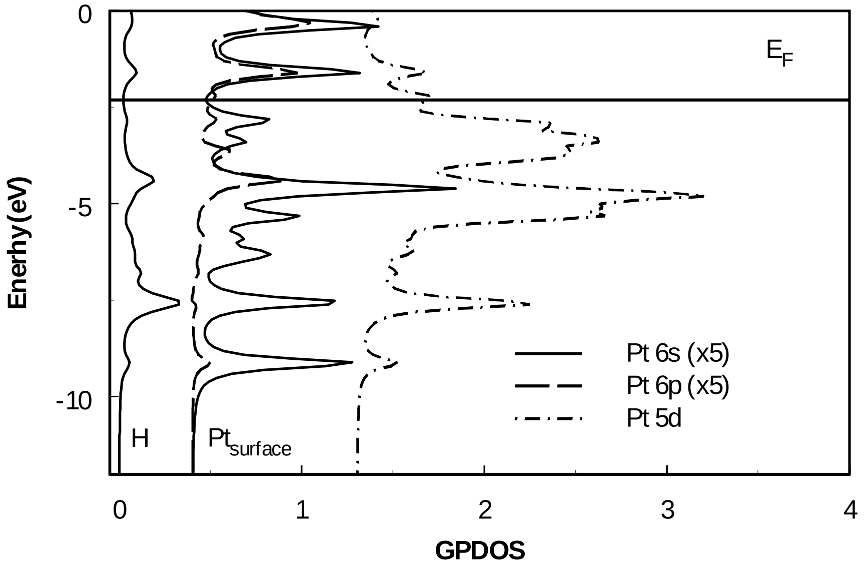

Figure 4: The H 1s GPDOS and the surface Pt atom 5d,6s-p GPDOS for hydrogen adsorbed in the atop position on a Pt_4/Na_2O cluster. The Pt 6s and 6p GPDOS is magnified by a factor of 5. E_F is the Fermi level.

CH_3 adsorption

The most favorable adsorption site for CH_3 on the supported Pt_4 cluster is the atop position. If CH_3 was placed in another adsorption site initially, it drifted to the atop position during the geometry optimization. The optimized geometries for CH_3 adsorbed on the Pt_4/F_2O and Pt_4/Na_2O cluster are shown in Figure 2C and D. The Pt-C bond length for the Pt_4/F_2O (and Pt_4/Na_2O) cluster is 2.02 Å (2.09 Å) and the Pt-Pt bond lengths range between 2.48 and 2.70 Å (2.61 and 2.66 Å). The CH_3 adsorbate is tilted towards the interface with the F_2O support, but nearly perfectly in the atop geometry for the Na_2O support.

The intrinsic bond energy E_{int} for Pt-CH_3 is smaller for the acidic support (Table 1), just as was observed for the Pt-H bond; however, the difference is much smaller for CH_3: 16 kJ/(mol CH_3) vs. 35 kJ/(mol H). The heat of adsorption for CH_3 is 50 kJ/mol smaller in the case of an acidic support compared to a basic support.

The GPDOS for CH_3 adsorbed in the atop position on the Pt_4/F_2O cluster is shown in Figure 5. Since no extra information is obtained from the results for the Pt_4/Na_2O cluster, these results are omitted. For the Pt_4/F_2O cluster, the DOS show maxima at approximately –12 eV for both the H 1s and C 2s,p states. These maxima represent the C-H bond involving the C $2p_z$ orbital. This C-H bonding orbital is degenerate with some Pt 5d states, indicating that some mixing between those orbitals occurs. The overlap between the C 2s and H 1s orbital is located at lower energy and is not shown in Figure 5. At ~ -11 eV, a second, smaller peak in the C 2p DOS is visible, corresponding to a peak in the Pt 6s,p states. The H 1s shows no intensity at that energy. Just above the Fermi level another maximum in the C 2p and Pt 6s,p states is visible, showing the antibonding state.

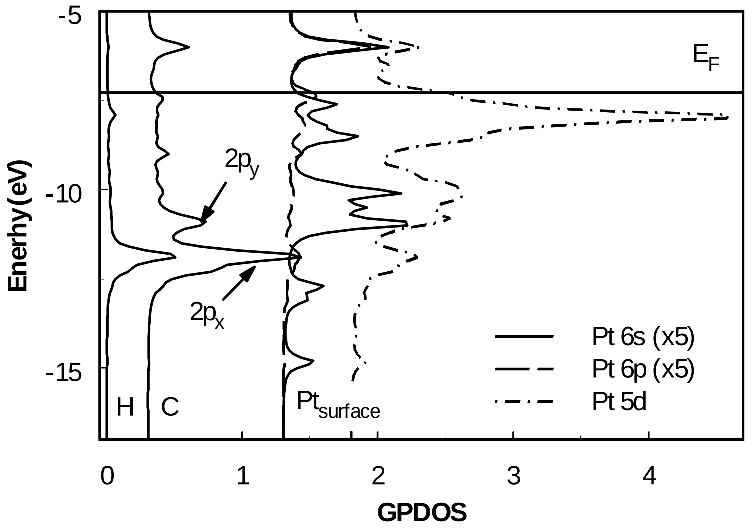

Figure 5: The H 1s GPDOS, C 2s,2p GPDOS and the surface Pt atom 5d,6s-p GPDOS for CH_3 adsorbed in the atop position on a Pt_4/F_2O cluster. The Pt 6s and 6p GPDOS is magnified by a factor of 5. E_F is the Fermi level.

CH_2 adsorption

The favored adsorption site for the CH_2 fragment is the bridged site for both supports. The optimized geometries are shown in Figure 2E and F. The two hydrogen atoms are eclipsed with respect to the two Pt atoms bonded to the carbon. In other words, CH_2 shows a tetrahedral coordination together with the two Pt atoms,. The $Pt_{interface}$-C bond lengths are 2.02 and 2.04 Å and the $Pt_{surface}$-C are 1.97 and 1.99 Å for Pt_4/F_2O and Pt_4/Na_2O, respectively. The Pt-Pt bond length between the 2 Pt atoms cluster that bond to the CH_2 decreases from 3.07 to 2.62 Å for Pt_4/F_2O and Pt_4/Na_2O, respectively.

The other adsorption positions, the 3 fold hollow site and the atop site, are less stable by 50-70 kJ/mol (Table 1). If CH_2 is initially placed in the 3-fold site for the Pt_4/Na_2O cluster, it drifts towards the atop position during the geometry optimization. Due to symmetry restrictions (the symmetry is C_s), the CH_2 fragment cannot move to the bridged site.

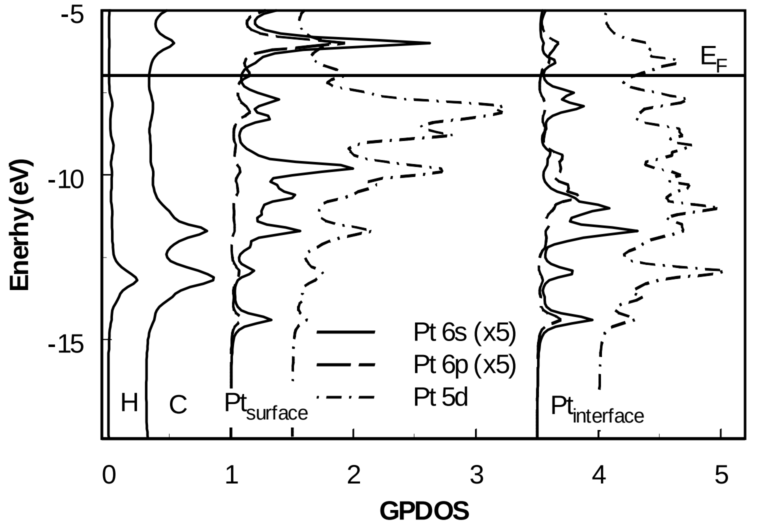

Figure 6: The H 1s GPDOS, C 2s,2p GPDOS and the surface and interface Pt atom 5d,6s-p GPDOS for CH_2 adsorbed in the bridged position on a Pt_4/F_2O cluster. The Pt 6s and 6p GPDOS is magnified by a factor of 5. E_F is the Fermi level.

The intrinsic bond energy of CH_2 in the bridged position is lower by 13 kJ/mol in the case of the acidic F_2O support (-605 kJ/mol vs. -592 kJ/mol). This is the reverse order to that found for the adsorption of H and CH_3, which were adsorbed more strongly on the basic supported Pt_4 cluster. In contrast, the heat of adsorption, which includes the adsorption of 2 hydrogen atoms, is lowest in the case of the basic support (-105.7 kJ/mol compared to -49.6 kJ/mol).

Figure 6 shows the GPDOS for the CH_2 adsorbed on a Pt_4/F_2O cluster in the bridged position. The results for the Pt_4/Na_2O cluster are omitted here since no extra information is obtained from these DOS. Only the H 1s, C 2s,p and Pt 5d 6s,p DOS of the Pt atoms attached to the CH_2 are shown (Figure 6). At ~ -13 eV the C 2p and H 1s DOS show simultaneously a maximum, representing the C-H bond. The Pt states peak at a little higher energy, indicating that the mixing between the C-H bond and Pt states is limited. At –12 eV, the C 2s,p states

show a second maximum in the DOS. The Pt 5d and 6s,p DOS for both the surface and the interface atoms peak at the same position. Compared to CH_3 adsorption (Figure 5), the relative intensity of the Pt 6s,p states is decreased significantly. Just above the Fermi level at – 6 eV, the C 2p and Pt 6s,p states reveal an anti-bonding state.

Discussion

Hydrogen adsorption

The Pt-H bond lengths with H in the atop position (1.56 and 1.59 Å for the F_2O and Na_2O supports respectively) are in good agreement with the value of 1.57 Å reported by Papoian *et al*[25]. The Pt-Pt bond lengths, which are between 2.49 and 2.59 Å, are low compared to the bulk value of 2.77 Å. However, it is well known that due to the increasing de-hybridization of the Pt valence orbitals for decreasing Pt particle sizes the Pt-Pt bond strength and consequently the Pt-Pt coordination distance decrease for small clusters[21,33]. Thus, our calculations clearly reproduce the geometries that have been found in the literature. In general, the favored adsorption position for hydrogen on flat Pt (111) surfaces is the 3-fold site[25,34]. However, for small clusters the first hydrogen that adsorbs is known to go into the atop position[21,22,35].

The bond energies that are found (-100 to -170 kJ/mol H_2) for H adsorption here are larger than is generally found for H/Pt (111) (-70 to -100 kJ/mol)[25,31]. The higher adsorption energy for hydrogen on small clusters compared to adsorption on Pt (111) surfaces agrees with temperature programmed desorption studies that show that all hydrogen desorbs below 300-350 K from Pt (111) surfaces[36-38], whereas hydrogen remains on the surface up to 450 K for stepped edges[36,39,40] or highly dispersed particles[22,41,42].

The origin of the large difference in the adsorption energy for basic and acidic supports lies in the relatively large contribution of Pt 6s,p states to Pt-H bonding. As can be seen in the DOS for the Pt_4/F_2O cluster (Figure 3), the maxima of the H 1s DOS align to a large extent with the Pt 6s,p peaks. This suggests that hydrogen bonding on Pt mainly occurs via the Pt 6s,p states. This has also been reported previously in the literature. Kua and Goddard[21] performed generalized valence bond calculations on a series of Pt clusters of variable size, and showed that hydrogen mainly binds via the so-called ‘interstitial bonding orbital’ (IBO). When bulk Pt is involved, Pt atoms share one IBO in each tetrahedron. In fact, this IBO is the bonding combination of the Pt 6s and 6p orbitals in a Pt_4 tetrahedron. Although others do not use the IBO terminology, it is generally found that the Pt 6 s,p states play a significant role in the bonding of H on Pt[25]. The specific symmetry properties of the Pt 6s,p orbitals are very beneficial for Pt-H bonding.

In an earlier paper, it was shown that the location of the IBO within the Pt particle shifts from the metal-support interface to the Pt surface with increasing electron richness of the support oxygen atoms (more basic support)[18,19]. In addition, some anti-bonding 6sp states are shifted below the Fermi-level and become populated at the cost of the Pt 5d. This can also be seen when the H DOS on Pt_4/F_2O (Figure 3) and Pt_4/Na_2O (Figure 4) are compared. There are

clearly more Pt 6sp states below the Fermi level for Na_2O, and they are at lower energy relative to the Fermi-level. These 6s,p states overlap strongly with the H 1s orbital. Effectively, with increasing electronrichness, the Pt valence band rehybridizes and obtains more 6s,p character, *e.g.* from $5d^9 6s^1$ to $5d^{8.8} 6s^{1.2}$.

These results show that the changes in the Pt-H bond strength are correlated with changes in the Pt 6s,p states. When the IBO moves towards the metal-support interface, as is the case for the acidic support[18,19], it can no longer participate in the Pt-H bond. The IBO is located below the 5d band at –15 eV in the Pt_4/F_2O cluster, and at that energy the H 1s DOS shows no intensity, revealing a lack of bonding between the hydrogen and the IBO. However, on the Na_2O support, the IBO is located at the surface[18,19]. Therefore, the IBO can participate in the Pt-H bond and this is indeed shown in Figure 4 for the H and $Pt_{surface}$ DOS of Pt_4/Na_2O. In this cluster, the IBO is located at –9 eV, and the H 1s orbital shows a small peak at this energy. Since sp states are mixed with the 5d band to a greater extent on the basic Na_2O support, the altered symmetry of the 5d - 6sp orbital (they become more sp like) improves the overlap with H 1s, and consequently the Pt-H bond is strengthened.

The shift of the sp states towards the interface with the acidic cluster can also explains the remarkable difference between the H in the atop position adsorbed at the Pt_4/Na_2O and at the Pt_4/F_2O cluster. H is tilted much more towards the interface region in the case of the acidic F_2O support (Figure 2). Since the Pt 6s,p states are very important in the Pt-H bonding, the hydrogen atom tries to 'follow' the metal sp states. Therefore, the Pt 6s,p states do not only determine the Pt-H bond energy, but also influence the geometry.

CH_3 adsorption

The optimized geometries for CH_3 adsorbed in the atop site show similar features to the H adsorbed in the atop position. The Pt-C bond lengths of 2.03 (acidic cluster) and 2.09 Å (basic) are similar to values reported in literature[23-25]. The favored atop adsorption position is also well known for the adsorption of CH_3 fragments. CH_n fragments generally tend to maintain the tetrahedral geometry, *i.e.* CH_3 adsorbs in an atop position, CH_2 in the bridged position and CH in the 3-fold hollow site[23-25,43].

We find intrinsic bond energies E_{int} for adsorption of CH_3 and H of -304 kJ/mol (F_2O support) to -320 kJ/mol (Na_2O). This is larger than the values reported in literature (-200 kJ/mol[43]) for CH_3 adsorption on Pt (111) surfaces. This difference is caused by the coordinatively unsaturated nature of the Pt atoms in a Pt cluster compared to a flat (111) surface. In addition, the calculations reported here do not fully account for the spin properties, and therefore the true atomic groundstate and true bond energy are not calculated. The trends that are observed, however, are not spin-related and can be calculated reliably without using the computationally expensive calculations including spin-orbit effects. Although E_{int} is only lower by 16 kJ/mol for the basic support, the heat of adsorption E_{ads} is lower by 50 kJ/mol. This large drop in E_{ads} reflects the much larger change (35 kJ/mol) in Pt-H bond strength going from acidic to basic supports.

When the DOS for CH_3 vs. H adsorbed on Pt_4/F_2O (Figure 5 and Figure 3) are compared, some interesting differences are seen. The C 2p states show some overlap with the Pt 6s,p states, but the degree of overlap is much smaller for Pt-CH_3 than for Pt-H. However, the Pt-CH_3 bond involves more Pt 5d states than the Pt-H bond. This means that the Pt 6s,p states are more important for the Pt-H bonding and that the Pt 5d states are more essential for the chemisorption of CH_3 on Pt.

The Pt 6s and 6p orbitals are very diffuse, whereas the Pt 5d states are more localized orbitals with specific geometries. Due to their delocalized nature, the Pt 6s,p states will have more interaction with the support than the localized Pt 5d states. Consequently, the Pt 6s,p states are affected the most, even though the Pt 5d states are shifted to lower binding energies for basic supports. Since the Pt 6s and p states are more important for chemisorption of H than for CH_3 adsorption, it can be concluded that the influence of the support is less important for the chemisorption of CH_3.

CH_2 adsorption

As expected, CH_2 preferentially adsorbs in the bridged position where it can complete the carbon's tetrahedral geometry (Figure 2E and F). The Pt-C bond length of ~ 2.00 Å is in agreement with the work of Kua and Goddard[23,24], but it is much smaller than the 2.3 Å reported by Paul[43] for the adsorption of CH_2 in the bridged position on Pd (111). In the case of the Pt_4/F_2O cluster, the adsorption of CH_2 leads to a large elongation of the Pt-Pt bond length to 3.07 Å between the Pt atoms forming the bridge. This elongation suggests that the CH_2 is adsorbed very strongly, since it weakens the Pt-Pt bond to a large extent. This elongation is not observed for the Pt_4/Na_2O cluster. In agreement with these observations, the intrinsic bond energy E_{int} is more negative (more exothermic) by 13 kJ/mol for the Pt_4/F_2O cluster compared to the Pt_4/Na_2O cluster. However, the heat of adsorption E_{ads} is more negative in the case of the Na_2O support. This again is caused by the larger difference in the Pt-H bond strength, since during the dissociative adsorption of CH_4 as CH_2,

$$CH_4 \rightarrow CH_2 + 2\ H,$$

two hydrogen atoms are adsorbed on the Pt_4 cluster. This means that the dissociative adsorption of CH_4 is more exothermic for adsorption on the Pt_4/Na_2O cluster than it is on the Pt_4/F_2O cluster, although the intrinsic Pt-CH_2 bond strengths are in the reverse order. Clearly, the change in the CH_2 heat of adsorption is governed by the hydrogen intrinsic adsorption energy.

A comparison of the DOS of CH_2 in the bridged position (Figure 6) with the DOS of CH_3 on the atop position (Figure 5) on the Pt_4/F_2O cluster, it is clear that the CH_2 adsorption involves even less Pt 6s,p states and more Pt 5d states than the CH_3. Therefore, the adsorption of CH_2 is mainly determined by the influence of the support acidity on the d-band. On acidic supports, the d-band is shifted to lower energies, which is beneficial for the overlap of the C 2p and Pt 5d band when CH_2 is adsorbed.

The importance of the Pt 5d states for the bonding of CH_x fragments is in agreement with results reported by Nørskov *et al*[44]. They show that the adsorption energy correlates with the energy of the d-band center across a transition metal series. The diffuse metal sp states effectively are the same across a transition metal series, and only changes in the d-band are reflected in the adsorption energies.

Influence of the support acid/base properties on the adsorbate bonding

When the DOS for adsorption of H, CH_3 and CH_2 in their optimal positions are compared, the importance of the Pt 6s,p states in the bonding increases in the order CH_2 < CH_3 < H. The high importance of the metal-d orbitals in the M-CH_n bond with highly unsaturated C atoms (*e.g.* n=0) was observed earlier[43]. Since the influence of the support acid/base properties is the largest on the delocalized Pt 6s,p states, the consequence is that the influence of the support is largest when the binding of Pt with adsorbates is dictated by the metal sp states. This is the case for H adsorption. The Pt 6s,p states are the least important in the bridged adsorption of CH_2 and in this case the changes in the Pt 5d states dominate the changes in the bond strength. It is now possible to derive a relationship between the type of Pt-Ads (with Ads: = CH_2, CH_3 and H) bonding and the Pt-Ads bond energy. The importance of the Pt sp, respectively d states in a particular Pt-Ads bonding become clear if the acid/base properties of the support are used as parameter. In Figure 7 E_{int} relative to the averaged E_{int} (whereby the averaged E_{int} is set at zero) is plotted as a function of the type of Pt-Ads bonding. It can clearly be seen that for the Pt-CH_2 bonding the Pt 5d states and for the Pt-H bonding the Pt 6sp states are the most important.

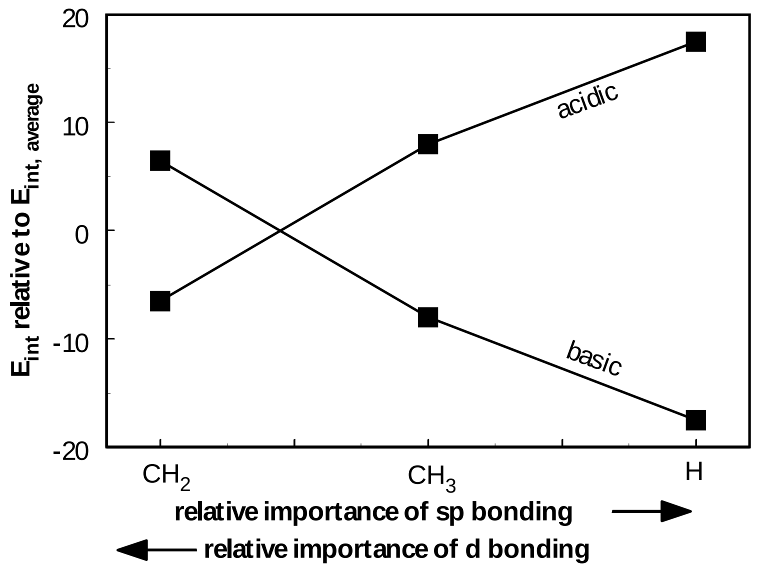

Figure 7: The relative intrinsic bond energy as a function of the type of Pt-adsorbate bonding with the acid/base properties of the support as independent parameter. The average E_{int} is set to zero for each adsorbate.

Implications for alkane hydrogenolysis catalyzed by Pt

It is generally observed that the reaction rate for alkane hydrogenolysis is first order in the alkane partial pressure, whereas the order in the hydrogen partial pressure is very negative[45]. In addition, it is observed that the apparent activation energy E_{app} is correlated with the order in P_{H2}. For example, in ethane hydrogenolysis, for a very negative order of -2.5 in P_{H2} a very high E_{app} (225 kJ/mol) is measured, and a moderately negative order of -1.5 leads to a lower E_{app} (175 kJ/mol)[46]. The same results are found for the conversion of neopentane (2,2-dimethylbutane) to iso-pentane (isomerization) or iso-butane and methane (hydrogenolysis)[9-11,47].

In addition to the correlation between the order in P_{H2} and E_{app}, the compensation effect is regularly observed for hydrogenolysis reactions[48-50]. The compensation effect denotes a linear relationship between the apparent activation energy and the pre-exponential factor. This relationship is also called the Constable-Cremer relation[51]:

$$\ln A_{app} = mE_{app} + c \tag{5}$$

Although the occurrence of a compensation effect is a widely accepted phenomenon, the reasons for this compensation effect are still under debate. One mechanism that can account for the compensation effect involves changes in the surface coverage or binding energies of the reactants[48]. These changes can alter the kinetic parameters, even if the true activation energy remains constant. The influence of the adsorption of the reactants on the observed activation energy E_{app} is expressed by the Temkin equation[52]:

$$E_{app} = E_{true} + \Sigma\, n\, \Delta H, \tag{6}$$

with E_{true} : the true, intrinsic activation energy and

$\Sigma n \Delta H$: the sum of all the relevant adsorption enthalpies multiplied by the order *n* of that reactant.

The results presented in this paper provide a simple explanation for the compensation effect. Neopentane ($C\text{-}(CH_3)_4$) is chosen as a specific example since neopentane can only adsorb via one of the methyl groups, and therefore its adsorption can be approximated by CH_3 adsorption, which has been considered in this paper. Other, more straight alkanes like n-hexane can adsorb in a variety of geometries, which complicates the picture.

Neopentane conversion

The conversion of neopentane to iso-pentane (isomerization) or iso-butane and methane (hydrogenolysis) is known to be first-order in the partial pressure of neopentane. However, the reaction is inhibited by hydrogen and negative orders from –1.5 to –2.5 have been reported[9-11,47]. Moreover, with increasing negative order in hydrogen partial pressure the apparent activation energy E_{app} also increases[9,10,47]. This correlation between E_{app} and the order in H_2 has been found for a number of supported metal-catalysts. When the conversion of neopentane ($C\text{-}(CH_3)_4$) is performed over Pt on an acidic support, the reaction rates are

several order of magnitudes higher than on basic supports. In addition, the observed negative order in H_2 is only –1.5 for acidic supports and –2.5 for basic supports[9].

The lower order in H_2 observed for basic supports can be intuitively understood in light of recently reported results. Neopentane experiments are typically performed around 523 K. In earlier work we have shown that hydrogen adsorbs in the Pt fcc 3-fold hollow or bridged sites on basic supports at high coverage, but in the Pt atop site on acidic supports but with relatively lower coverage at 523 K[22]. A Pt atom on a (111) surface is surrounded by 3 fcc sites. Before neopentane can adsorb, some adsorbed H must first be removed from the Pt surface. Thus, for a basic support the three hydrogen atoms in the surrounding fcc sites must be desorbed, but on a acidic support only the one hydrogen atom in the atop site needs to be removed. Consequently, 1 extra H_2 molecule has to be formed on basic supports, which means that the order in H_2 has to be lower by 1 compared to acidic support. This is exactly what is observed: the order in H_2 is –1.5 for acidic supports but –2.5 for basic supports.

Even though the adsorption sites are different, the adsorption enthalpy is similar for the different supports. The adsorption enthalpy is a function of coverage, as indicated by e.g. the broad TPD profile[22,36,37]. The coverage dependency of the H_2 adsorption enthalpy means that hydrogen is adsorbed *until* the adsorption energy ΔG is greater than 0. Assuming an adsorption entropy of ΔS_{ads} = -85 J mol^{-1} K^{-1} for the dissociative adsorption of hydrogen[53], a ΔH_{ads} < -45 kJ/mol is required at 523 K in order to make $\Delta G_{ads} = \Delta H_{ads} - T\Delta S_{ads}$ smaller than 0. Since the Pt particles are very small in typical catalysts, it is likely that many particles are completely covered by H that is adsorbed even more strongly. Therefore, the value of -45 kJ/mol is an upper limit and the actual values may be much lower. Based on these thermodynamic arguments and our calculated H adsorption enthalpies, we conclude that the minimum hydrogen adsorption enthalpy is similar for both basic and acidic supports, but the *coverage* is very different. The Pt on basic supports has much greater coverage.

Neopentane adsorbs dissociatively on the Pt surface. A C-H bond is broken and a Pt-C and Pt-H bond are formed. The cleavage of the neopentane C-H bond is not influenced by the support. Moreover, as argued above, the adsorption enthalpy of H_2 is > 45 kJ/mol regardless of the support, and on a basic support an additional H_2 molecule is formed prior to the adsorption of neopentane. Thus, according to equation (6) the difference in E_{app} between the basic and acidic support is given by the sum of the difference in the intrinsic Pt-C bond energy (16 kJ/mol lower for the basic support) and the H_2 desorption enthalpy limit at the reaction temperature:

$$\Delta E_{app} = \Delta H_{int,\ Pt\text{-}C} - \Delta H_{ads,H2} \geq -16 - (-45) \geq 29 \text{ kJ/mol} \qquad (7)$$

This value is of the same magnitude as the experimentally observed difference between a basic and acidic Y zeolite, which is around 47 kJ/mol[7].

The different number of desorbing hydrogen molecules is also reflected in the pre-exponential factor ln A_{app}[7]:

$$\ln A_{app} = \ln A_{true} + \ln\left(P_{neo} P_{H2}^{n}\right) + \sum_{n} \frac{\Delta S_n}{R} \qquad (8)$$

with A_{true} : the true pre-exponential factor,
P_{neo} : the partial pressure of neopentane,
P_{H2} : the partial pressure of H_2,
n : the order in H_2,
ΔS : the entropy-change, and
R : the gas constant, 8.3145 J K^{-1} mol^{-1}.

The gain in entropy from desorption of two H atoms on Pt as a H_2 molecule for a basic support is approximately 85 J mol^{-1} K^{-1} [53]. Since typical conditions are P_{H2} = 0.99 bar, with P_{neo} = 0.01, an increase in the order in H_2 has no effect on the pressure-term in equation 8. Thus the change in the pre-exponential factor for the conversion of neopentane on an acidic versus a basic support is given by

$$\Delta \ln A_{app} = \Delta n * \Delta S_{H2\ desorption}/R = 1 * 85/8.3145 = 10.2 \qquad (9)$$

This is similar to the difference in ln A_{app} of 6 - 12 reported in literature[7,9-11,47].
It can be concluded that the experimentally observed changes in activity and H_2 order for neopentane conversion with support alkalinity can be quantitatively explained by the calculations reported here. The changes in E_{app} and $\ln A_{app}$ arise from the change in n. Hence, $\ln A_{app}$ and E_{app} are linearly related explaining the compensation effect. These results indicate that the observed variations in hydrogenolysis activity are driven by the adsorption of hydrogen rather than related to the adsorption of the hydrocarbons. This is in agreement to the report of Bond et al.[48], who argue that the dominant cause of the compensation effect are changes in the surface coverage. The low reaction order of –2.5 in H_2 for hydrogenolysis over Pt particles on a basic support reflects the previously reported[22] different binding sites for H under the reaction conditions: in the 3-fold site for basic supports and in the atop site for acidic supports.

Conclusions

DFT results show that the importance of the Pt 6s,p states in the chemisorption bond increases in the order CH_2 < CH_3 < H. The Pt 6s and 6p states are influenced strongly by the support acid/base properties, thereby influencing the bonding of the adsorbates for which the Pt 6s,p states are important . On acidic supports, the sp states are moved toward the metal – support interface, and consequently the adsorbate bond energies are decreased. However, on basic supports the Pt 6s,p states are located at the surface of the Pt cluster and are readily available for the bonding to adsorbates. Consequently, the Pt-adsorbate bond strength is increased on a basic support. When the Pt 6s,p orbitals are less important in the chemisorption, as is the case for CH_2 bonding, the 5d band dictates the bond energy. In this case the Pt-adsorbate bond is stronger for acidic supports than for basic supports.

These new results can explain the compensation effect and the negative order in the partial pressure of hydrogen found for the hydrogenolysis of neopentane catalyzed by supported Pt particles. The kinetics of the catalytic reaction is driven by the mode of the adsorption of hydrogen on the Pt surface.

Reference list

1. B. C. Gates, *Chem. Rev.*, **95** (1995), 511-522.
2. R. A. Dalla Betta and M. Boudart, *Proc 5th Int Con Cat* (1973), 1329-1341.
3. Z. Xu, F. S. Xiao, S. K. Purnell, O. Alexeev, S. Kawi, S. E. Deutsch and J. T. Miller, *Nature*, **372** (1994), 346-348.
4. P. Reyes, I. Concha, M. E. König and J. L. G. Fierro, *Appl. Catal. A: General*, **103** (1993), 5-16.
5. Z. Karpinski, S. N. Gandhi and W. M. H. Sachtler, *J. Catal.*, **141** (1993), 337-346.
6. S. T. Homeyer, Z. Karpinski and W. M. H. Sachtler, *J. Catal.*, **123** (1990), 60-73.
7. J. de Graaf, Ph.D., Utrecht University, Ridderkerk, 2001.
8. A. de Mallmann and D. Barthomeuf, *J. Chim. Phys.*, **87** (1990), 535-538.
9. G. C. Bond, *Catal. Today*, **17** (1993), 399.
10. F. G. Gault, *Adv. Catal.*, **30** (1981).
11. K. Foger and J. R. Anderson, *J. Catal.*, **54** (1978), 318-335.
12. Z. Zhang, T. T. Wong and W. M. H. Sachtler, *J. Catal.*, **128** (1991), 13-22.
13. G. Larsen and G. L. Haller, *Catal. Lett.*, **3** (1989), 103-110.
14. A. M. Ferrari and G. Pacchioni, *J. Phys. Chem.*, **100** (1996), 9032-9037.
15. A. P. J. Jansen and R. A. van Santen, *J. Chem. Phys.*, **94** (1990), 6764.
16. B. L. Mojet, J. T. Miller, D. E. Ramaker and D. C. Koningsberger, *J. Catal.*, **186** (1999), 373-386.
17. D. E. Ramaker, G. E. van Dorssen, B. L. Mojet and D. C. Koningsberger, *Top. Catal.*, **10** (2000), 157-165.
18. D. E. Ramaker, J. de Graaf, J. A. R. Van Veen and D. C. Koningsberger, *J. Catal.*, **203** (2001), 7-17.
19. Chapter 8 of this thesis.
20. N. López, *J. Chem. Phys.*, **114** (2001), 2355-2361.
21. J. Kua and W. A. Goddard III, *J. Phys. Chem. B*, **102** (1998), 9481-9491.
22. Chapter 6 of this thesis.
23. J. Kua, F. Faglioni and W. A. Goddard III, *J. Am. Chem. Soc.*, **122** (2000), 2309-2321.
24. J. Kua and W. A. Goddard III, *J. Phys. Chem. B*, **102** (1998), 9492-9500.
25. G. Papoian, J. K. Nørskov and R. Hoffmann, *J. Am. Chem. Soc.*, **122** (2000), 4129-4144.
26. Amsterdam Density Functional Package ADF 2000.02, Department of Theoretical Chemistry, Vrije Universiteit, Amsterdam. http://www.scm.com.
27. A. D. Becke, *J. Chem. Phys.*, **85** (1986), 7184-7187.
28. J. P. Perdew, *Phys. Rev. B*, **33** (1986), 8822-8824.
29. P. H. T. Philipsen, E. Van Lenthe, J. G. Snijders and E. J. Baerends, *Phys. Rev. B*, **56** (1997), 13556.
30. E. Van Lenthe, E. J. Baerends and J. G. Snijders, *J. Chem. Phys.*, **101** (1994), 9783.
31. R. A. Olsen, G. J. Kroes and E. J. Baerends, *J. Chem. Phys.*, **111** (1999), 11155-11163.
32. E. J. Baerends, V. Branchadell and M. Sodupe, *Chem. Phys. Lett.*, **265** (1997), 481-489.

33. L. Yang and A. E. DePristo, *J. Catal.*, **149** (1994), 223-228.
34. A. Renouprez and H. Jobic, *J. Catal.*, **113** (1988), 509-516.
35. A. L. Ankudinov, J. J. Rehr, J. Low and S. R. Bare, *Phys. Rev. Letters,* **86** (2001), 1642-1645.
36. S. M. Davis and G. A. Somorjai, *Surf. Sci.,* **91** (1980), 73-91.
37. C. S. Ko and R. J. Gorte, *Surf. Sci.,* **161** (1985), 597-607.
38. K. Christmann and G. Ertl, *Surf. Sci.,* **60** (1976), 365-384.
39. H. Wang, R. G. Tobin, D. K. Lambert, G. B. Fisher and C. L. Dimaggio, *Surf. Sci.,* **330** (1995), 173-181.
40. H. Wang, R. G. Tobin and D. K. Lambert, *J. Chem. Phys.,* **101** (1994), 4277-4285.
41. V. D. Thomas, J. W. Schwank and J. L. Gland, *Surf. Sci.,* **in press** (2001).
42. S. Tsuchiya, Y. Amenomiya and R. J. Cvetanovic, *J. Catal.,* **19** (1970), 245-255.
43. J.-F. Paul and P. Sautet, *J. Phys. Chem. B*, **102** (1998), 1578-1585.
44. A. Ruban, B. Hammer, P. Stoltze, H. L. Skriver and J. K. Nørskov, *J. Mol. Catal. A*, **115** (1997), 421-429.
45. J. H. Sinfelt, *Catal. Rev.,* **3** (1969), 175-205.
46. G. A. Martin, R. Dutartre, S. Yuan, C. Márquez-Alvarez and C. Mirodatos, *J. Catal.,* **177** (1998), 105-112.
47. P. V. Menacherry and G. L. Haller, *J. Catal.*, **167** (1997), 425.
48. G. C. Bond, M. A. Keane, H. Kral and J. A. Lercher, *Catal. Rev. - Sci. Eng.,* **42** (2000), 323-383.
49. A. K. Galwey, *Thermochim. Acta*, **294** (1997), 205-219.
50. A. Wootsch and Z. Paál, *J. Catal.*, **205** (2002), 86-96.
51. F. H. Constable, *Proc. Roy. Soc. (London) A*, **108** (1925), 355.
52. M. Temkin, *Acta Physicochim. URSS,* **3** (1935), 312.
53. S. G. Podzolkin, R. M. Watwe, Q. Yan, J. J. de Pablo and J. A. Dumesic, *J. Phys. Chem. B,* **105** (2001), 8550-8562.

Summary

It is well known in literature that for many metal-catalyzed reactions the support influences the catalytic properties of the metal particles. For example, it has been well established that the reaction rates of hydrogenation and hydrogenolysis reactions of hydrocarbons over supported Pt catalysts are improved when the Pt particles are supported on acidic supports. It has also been observed that the electronic properties of the supported Pt particles depend on the acid/base properties of the support. However, the nature of this interaction between metal and support that leads to altered electronic properties is poorly understood. Moreover, there is no understanding on how the support-induced changes in the electronic properties affect the catalytic properties. The goal of the research performed during the Ph.D. project described in this thesis was to understand the nature of the metal-support interaction and to relate the support-induced changes in catalytic properties to the changes in electronic properties. The work in this thesis has provided important insights in finding answers to these questions.

Chapter 2 aims at understanding which processes take place during the pretreatment of $Pt(NH_3)_4(NO_3)_2$ impregnated on SiO_2. The ultimate goal was (i) to understand how a certain metal particle size and particle size distribution is obtained and (ii) based upon these insights to prepare a supported metal catalyst with a narrow particle size distribution.
Using the combination of mass spectrometry, *in situ* QEXAFS, HRTEM and hydrogen chemisorption, the reactions taking place during different pretreatments of the catalyst precursor $[Pt^{2+}(NH_3)_4](NO_3^-)_2$ impregnated on a high surface area SiO_2 (400 m^2/g) were elucidated. Direct reduction in hydrogen leads to the formation of Pt metal particles in the temperature range of 150-200°C in a fast process. The reduction is accompanied by sintering of the platinum particles, leading to relatively large particles with an average particle size of approximately 14-16 Å. Autoreduction in helium leads to multiple steps in the reduction. Around 210°C and 240°C, NO_x released due to the decomposition of NH_4NO_3, formed during heating up to 180-200°C, reduce the catalyst precursor at a high rate. At higher temperatures, the reduction continues slowly through an autoreduction of the $Pt(NH_3)_x^{2+}$ complex. The slow reduction rate suggests a non-mobile species. Accordingly, the final metal-particle size is small with particles of 10-12 Å. The particle size distribution after autoreduction is considerably smaller than after direct reduction. Calcination proceeds via a similar decomposition of NH_4NO_3 as autoreduction, but the atoms are immediately oxidized to Pt-O. Reduction following the calcination results in large particles. The key to obtain small particles with a relatively narrow size distribution is to avoid the formation of mobile species. With impregnated $[Pt^{2+}(NH_3)_4](NO_3^-)_2$, this is best achieved by autoreduction.

In **Chapter 3**, the attention was focused on using a catalytic test reaction, the exchange of hydrogen for deuterium (H/D exchange) in cyclopentane (CP). The H/D exchange of CP is a promising test reaction for studying support effects in heterogeneously metal catalyzed reactions. In order to employ this test reaction, a full understanding of the H/D exchange mechanism is essential. However, a clear insight in the observed kinetics and selectivities is

lacking in the literature. In this chapter, a kinetic model that adequately describes the observed activity and orders in CP and D_2 is developed. It is shown that the selectivity is determined in a series of reactions after the rate-determining step. To understand the observed selectivities a Monte-Carlo model is developed which accurately simulates the observed exchange patterns and reveals the relative contributions of four competitive intermediates. One intermediate (a π-bonded η^2-cyclopentene) can rotate in a non-activated mechanism via an allylic intermediate. The model reveals that the number of rotations which each intermediate experiences, can be as high as ~20, even if only 5 D atoms are observed in the product. This number of rotations is a better measure of the H/D exchange than the conventional 'multiplicity'. The H/D exchange of CP together with these insights can now be applied to investigate in detail the influence of the support on the catalytic properties of supported metal particles.

In **Chapter 4** the H/D exchange of cyclopentane was measured for Pt catalysts with supports of various acidity. With the earlier developed Monte-Carlo model the contributions of the various possible intermediates in the H/D exchange can directly be measured. It was shown that the activity and the selectivity in the H/D exchange over the supported Pt catalysts strongly depend on the support acid/base properties. The activities of the various catalysts show a compensation effect. The compensation effect can directly be correlated to the contribution of the various exchange mechanisms, which proceed via different intermediates. The contribution of each intermediate depends on the electronic properties of the Pt particles, which in turn depend on the support acidity. This shows that the compensation effect is caused by support induced changes in the adsorption modes of cyclopentane.

Hydrogen is a common reactant in the hydrogenolysis and hydrogenation reactions that show a support effect on the activity. The mode of chemisorption and the bondstrength of hydrogen on the surface of supported Pt particles is studied in chapter 5 and chapter 6.

A long-standing problem in the research of hydrogen chemisorption on supported Pt catalysts is the unclarity about the difference in nature of the Pt-H bonding for weakly and strongly bonded hydrogen. Based on Pt-Pt EXAFS and a newly developed XANES analysis of the Pt L_2 and L_3 edges it is shown in **chapter 5** that both types of hydrogen are truly chemisorbed species. The EXAFS analysis shows a similar contraction of the Pt-Pt bond irrespective of the removal of weakly or strongly bound hydrogen indicating a similar nature for both interactions. Moreover, the analysis of the L_2 and L_3 X-ray absorption edges shows unambiguously the presence of a Pt-H anti-bonding state for both the weakly and strongly bonded hydrogen. This is a clear indication for chemisorption of hydrogen for both types of hydrogen. The Pt-H EXAFS shows a smaller Pt-H bond-length in the case of strongly adsorbed, which is in correlation with the expected strength of the Pt-H bond.

The analysis of the L_2 and L_3 X-ray absorption edges that was used in chapter 5 turned out to be more complex in later studies. The changes in the Pt L_3 X-ray absorption edge induced by the adsorption of hydrogen are also sensitive to the mode of adsorption of hydrogen on the Pt

surface. This more complex interpretation is used in **chapter 6**, where hydrogen chemisorption on supported Pt catalysts was studied utilizing Pt L_3 XANES data. The Pt L_3 edge is sensitive to the H adsorption position. Both hydrogen coverage and support effects were investigated. It is found for Pt on basic supports that H is adsorbed in the Pt 3-fold hollow sites near cluster edges at high temperatures. However, in the case of acidic supports, the H appears to adsorb at the Pt cluster edge atop sites. This difference in adsorption site is supported by density functional theory (DFT) calculations on H_n/Pt_4 clusters, which show that at low coverage, H prefers the atop sites. However, the adsorption energy in this atop position is much lower for Pt on acidic supports compared to basic supports. At higher coverage, the H prefers the 3-fold hollow sites with approximately equal bond strength on both acidic and basic supports. The DFT calculations therefore suggest that the fraction of strongly bonded H is much larger in basic supports. Due to the higher coverage this H exists in the 3-fold sites. On basic supports a greater fraction of strongly bonded H is found with the DFT calculations. This is confirmed by H_2 chemisorption experiments involving a series of Pt/LTL catalysts with different support acidities. This is the first reported finding that hydrogen, at high temperature catalytic reaction conditions, changes its dominant adsorption site as the support acid/base properties are varied.

The influence of the acid-base properties of the support on the electronic properties of the supported metal particles was investigated in chapter 7 and 8.
One of the changes between small metal particles and bulk metal is the change in conductivity: bulk metal is a conductor, small particles are insulators. In **chapter 7** the development of a new *in situ* probe of metallic character in supported metal clusters utilizing X-ray absorption spectroscopy is described. A very strong support effect on the metal-insulator transition with cluster size in supported Pt clusters is found. Pt particles with basic supports show metallic screening for sizes as small as 6Å. In contrast, with acidic supports the Pt particles do not show metallic behavior below 10Å.
X-ray absorption experiments on supported Pt catalysts performed in **chapter 8** indicate that increased support alkalinity induces an increased whiteline intensity of the Pt L_2 and L_3 X-ray absorption edges. Density functional theory (DFT) shows that the origin of this support effect is due to a rehybridization of the Pt valence band. The Madelung potential of a basic support rehybridizes the filled part of the valence band towards an increased amount of anti-bonding $6sp^*$ character, and consequently the empty part obtains more 5d character. Furthermore, DFT calculations reveal that the metal-support interaction consists of three additional effects. First, the Madelung potential of the support polarizes the Pt particles and second, it shifts the complete valence band to higher energies for basic supports and to lower energies for acidic supports. Third, the bonding between metal and support is strong as long as the support is non-inert. This bonding has a large impact on the metal 6sp states. For acidic supports the Pt 6sp orbitals are geometrically located at the interface between the metal and support. If the support is basic, then the Pt 6sp orbitals are located more at the metal surface. Since reactants

like hydrogen or alkanes chemisorb partly via the 6sp orbitals, the metal-support interaction can have large implications for the catalytic properties of supported Pt particles.

The changes in the electronic properties of the supported metal particles were connected to the chemisorption of reactants in **chapter 9**, where the influence of the acid/base properties of the support on the adsorption of H and CH_x (x=2,3) on supported Pt particles is investigated using density functional theory (DFT). As mentioned above, the DFT results show that the support acidity has a large impact on the location within the metal particle of the Pt 6s,p states. In addition, the DFT calculations reveal that the importance of the 6s,p states for the Pt adsorbate bonding increases in the order $Pt\text{-}CH_2 < Pt\text{-}CH_3 < Pt\text{-}H$. Consequently, the Pt-H bond strength is strongly affected by changes in the support acidity while the difference for the Pt-CH_x bond strength is much smaller. Due to the stronger Pt-H bond on basic supports, the H coverage with strongly bonded hydrogen on Pt particles with a basic support is higher than on acidic supports.
The support induced changes in hydrogenolysis reactions of alkanes can be explained to a large extent by support induced changes in the Pt-H bond strength and hydrogen adsorption site on Pt. This can easily explain the well-known compensation effect found in the kinetics of the hydrogenolysis of alkanes catalyzed by supported metal catalysts.

Samenvatting

Bij veel metaal-gekatalyseerde reacties beïnvloedt de drager, die dient om de metaaldeeltjes hoog gedispergeerd te houden, de katalytische eigenschappen van de metaaldeeltjes. Zo wordt bijvoorbeeld in het algemeen gevonden dat de reactiesnelheden in de hydrogenolyse en hydrogenering van koolwaterstoffen over een platina katalysator aanzienlijk verhoogd worden als de platina deeltjes worden afgezet op zure dragers. Naast de katalytische eigenschappen hangen ook de elektronische eigenschappen van de gedragen metaaldeeltjes af van de zuur/base eigenschappen van het drager materiaal. Deze invloed van de drager op de metaaldeeltjes wordt aangeduid met 'metaal-drager interactie'. Hoewel deze interactie algemeen bekend en geaccepteerd is, is het onderwerp van discussie *hoe* deze metaal-drager interactie de elektronische eigenschappen beïnvloedt. Bovendien is het ook onduidelijk hoe de katalytische eigenschappen samenhangen met de veranderingen in de elektronische eigenschappen van de gedragen metaaldeeltjes. Het doel van het promotieonderzoek dat is beschreven in dit manuscript was een begrip te krijgen van hoe de aard van de metaal-drager interactie is, en om de relatie tussen veranderingen in de elektronische eigenschappen en katalytische eigenschappen te begrijpen. Het in dit proefschrift beschreven werk heeft geleid tot belangrijke inzichten tot het beantwoorden van deze vragen.

Hoofdstuk 2 is gericht op het begrijpen welke processen plaatsvinden tijdens de voorbehandeling van een katalysator precursor, $Pt(NH_3)_4(NO_3)_2$ geïmpregneerd op SiO_2. Het uiteindelijke doel was (i) begrijpen hoe een bepaalde deeltjesgrootte en deeltjesgrootte verdeling tot stand komt en (ii) om op basis hiervan in staat te zijn een gedragen metaalkatalysator te maken met een smalle deeltjesgrootte verdeling.
Met behulp van de combinatie van massa spectrometrie, *in situ* QEXAFS, HRTEM en H_2 chemisorptie werd opgehelderd welke reacties plaatsvinden tijdens verschillende voorbehandelingen van de katalysator precursor ($Pt(NH_3)_4(NO_3)_2$ geïmpregneerd op SiO_2). Direkte reductie in waterstof leidt tot leidt tot de vorming van metaaldeeltjes via een snel proces in het temperatuurgebied van 150-200°C. Deze reductie gaat gepaard met sintering van de Pt deeltjes. Dit resulteert in relatief grote metaaldeeltjes met een gemiddelde diameter van 14-16 Å. Autoreductie in helium vindt in meerdere stappen plaats. Rond 210 en 240 °C wordt de katalysator precursor gereduceerd door NO_x. NO_x komt vrij door de decompositie van NH_4NO_3, wat is gevormd tijdens het opwarmen tot 180-200 °C. De reductie door NO_x gebeurt relatief snel. Bij hogere temperaturen vindt de reductie plaats via een geleidelijke autoreductie van het $Pt(NH_3)_x^{2+}$ complex zelf. De lage reactiesnelheid van deze autoreductie wijst op een immobiel complex. Deze autoreductie leidt dan ook tot kleine metaaldeeltjes met een gemiddelde diameter van 10-12 Å. De deeltjesgrootte verdeling na autoreductie is aanzienlijk smaller dan na directe reductie. De calcinatie verloopt via een vergelijkbaar proces waarin het uiteenvallen van NH_4NO_3 leidt tot een reductie van het Pt^{2+} complex. Het verschil met autoreductie is dat nu ieder metallisch Pt atoom meteen wordt geoxideerd tot Pt-O. Wanneer het PtO_x wordt gereduceerd na de calcinatie, worden grote metaaldeeltjes verkregen. De

belangrijkste factor in het verkrijgen van kleine deeltjes met een smalle deeltjesgrootte verdeling is het vermijden van mobiele complexen tijdens de reductie. In het geval van geïmpregneerd $Pt(NH_3)_4(NO_3)_2$ gaat dit het best met autoreductie.

In **hoofdstuk 3** wordt de uitvoering van een katalytische testreactie besproken: de uitwisseling van waterstof voor deuterium (H/D exchange) in cyclopentaan (CP). De H/D exchange in CP is een veelbelovende testreactie om dragereffecten in heterogeen gekatalyseerde reacties te bestuderen. Om deze reactie te kunnen gebruiken als testreactie, is een volledig begrip van de reactiemechanismen noodzakelijk. In de bestaande literatuur ontbreekt een goed begrip van de kinetiek en selectiviteiten in de H/D exchange van CP. Daarom werd in dit hoofdstuk een kinetisch model ontwikkeld dat de waargenomen ordes en reactiesnelheden adequaat beschrijft. Het werd aangetoond dat de selectiviteit wordt bepaald in een serie reacties die pas ná de snelheidsbepalende stap plaatsvinden. Om de waargenomen selectiviteiten te begrijpen, werd een Monte-Carlo model ontwikkeld. Dit model simuleert de selectiviteit en geeft ook de relatieve bijdragen tot het eindprodukt van vier verschillende mechanismen. Eén intermediair, π-gebonden η^2-cyclopenteen, kan vrij roteren in een niet-geactiveerd mechanisme via een allylisch intermediair. Het Monte-Carlo model laat zien dat het aantal rotaties voor 1 molekuul kan oplopen tot ongeveer 20, hoewel slechts 5 D atomen in het produkt worden gevonden. Het aantal rotaties is dan ook een betere maat voor de H/D exchange dan de conventionele parameter ‘multipliciteit’. Het nieuw verkregen begrip van de H/D exchange in CP kan nu worden toegepast om de invloed van de drager op de katalytische eigenschappen van het metaal te bestuderen.

In **hoofdstuk 4** wordt de H/D exchange in CP over Pt katalysatoren met dragers van verschillende zuursterktes gemeten. Met behulp van het eerder ontwikkelde Monte-Carlo model konden de bijdragen van de diverse reactiemechanismen worden bepaald. De activiteit en selectiviteit hangt sterk af de zuur/base eigenschappen van de drager. De activiteiten van de verschillende dragers vertonen een compensatie effect. De compensatie hangt direkt samen met de verschillende bijdragen van de diverse reactie mechanismen. De bijdrage van ieder reactiemechanisme hangt af van de elektronische eigenschappen van de metaaldeeltjes, die op hun beurt weer afhangen van de zuurheid van de drager. Hieruit blijkt dat het compensatie effect wordt veroorzaakt door veranderingen in de absorptie toestand van cyclopentaan, die worden veroorzaakt door de drager.

Waterstof is een gemeenschappelijke reactant in de hydrogenolyse en hydrogenering reacties waarvan de reactiesnelheid sterk wordt beïnvloed door de zuurheid van de drager. De manier waarop en sterkte waarmee waterstof op het oppervlak van gedragen Pt deeltjes chemisorbeerd worden bestudeerd in hoofdstukken 5 en 6.

Een oud, terugkerend probleem in het onderzoek naar H_2 chemisorptie op gedragen Pt katalysatoren is de onduidelijkheid over het het verschil in de Pt-H binding bij sterk en zwak gebonden waterstof. Met behulp van Pt-Pt EXAFS en een analyse van de XANES bij de Pt L_2

en L_3 röntgen absorptie edges wordt in **hoofdstuk 5** aangetoond dat beide typen waterstof daadwerkelijk zijn gechemisorbeerd. De EXAFS analyse laat een contractie in de Pt-Pt bindingslengte zien, die onafhankelijk is van het type waterstof (sterk of zwak gebonden). Dit wijst op een vergelijkbare Pt-H binding voor beide types. Bovendien laat de analyse van de L_2 en L_3 edges voor beide types waterstof een duidelijke anti-bindende toestand zien. Dit laat duidelijk zien dat beide types gechemisorbeerd zijn. De Pt-H EXAFS laat een korte Pt-H binding zien in het geval van de sterk gebonden waterstof. Dit is in overeenstemming met de verwachtte bindingsterkte.
De analyse van de L_2 en L_3 edges die in hoofdstuk 5 werd gebruikt bleek later een stuk complexer te zijn dan was voorzien. De veranderingen in de L_3 edge die worden waargenomen als waterstof wordt geadsorbeerd blijken ook gevoelig te zijn voor de absorptie positie van waterstof op Pt. Deze nieuwe interpretatie wordt in **hoofdstuk 6** gebruikt. In dit hoofstuk wordt de chemisorptie van waterstof op Pt bestudeerd met behulp van de Pt L_3 röntgen absorptie edge. Zowel het effect van de bedekkingsgraad met H als het effect van de drager op de chemisorptie van waterstof op Pt werd bestudeerd. In het geval dat Pt is afgezet op basische dragers zit waterstof bij hogere temperaturen geadsorbeerd tussen 3 Pt atomen in. In het geval van zure dragers zit waterstof juist bovenop 1 Pt atoom geadsorbeerd. Dit experimenteel waargenomen verschil in de adsorptie positie wordt ondersteund door ‘Density Functional Theory’ (DFT) berekeningen aan H_n/Pt_4 clusters. Deze berekeningen laten zien dat – bij lage bedekkingsgraad – waterstof bij voorkeur bovenop een Pt atoom zit. De adsorptie energie van H_2 op Pt is echter veel hoger in het geval van een basische drager. Bij hoge bedekkingsgraden zit waterstof bij voorkeur tussen 3 Pt atomen in, en de adsorptie energie is vrijwel gelijk voor zure en basische dragers. Door de hogere adsorptie energie bij lagere bedekking in het geval van een basische drager is de bedekkingsgraad veel hoger, wat leidt tot 3-voudig gebonden waterstof bij hogere temperaturen en basische dragers. Bovendien leidt de hogere adsorptie energie tot een grotere fractie sterk gebonden waterstof bij basische dragers. Dit wordt ook bevestigd door een serie H_2 chemisorptie experimenten aan een serie Pt/LTL katalysatoren waarbij de drager LTL verschillende zuursterktes heeft. Dit is de eerste keer dat wordt gerapporteerd dat waterstof onder katalytische omstandigheden van adsorptie positie verandert onder invloed van de zuur/base eigenschappen van de drager.

De invloed van de zuur/base eigenschappen van de drager op de elektronische eigenshcappen van de gedragen metaal deeltjes werd bestudeerd in hoofdstuk 7 en 8.
Een van de grote verschillen tussen kleine metaaldeeltjes en bulk metaal is het veranderde geleidingsvermogen: bulk metaal is een geleider, maar kleine metaaldeeltjes zijn isolatoren. In **hoofdstuk 7** wordt een experimentele *in situ* techniek ontwikkeld om het metallisch karakter van de gedragen Pt deeltjes te bepalen met behulp van röntgen absorptie spectroscopie. Er werd een sterke invloed van de drager op de deeltjesgrootte waar de overgang van isolator naar geleider plaatsvindt gevonden. Als de Pt deeltjes worden gedragen door basische dragers,

laten ze al metallische eigenschappen zien vanaf 6 Å. Als zure dragers daarentegen worden gebruikt, laten de Pt deeltjes pas boven de 10 Å metallisch karakter zien.
Röntgen absorptie experimenten die werden uitgevoerd op gedragen Pt katalysatoren in **hoofsdtuk 8** laten zien dat een toename van de basiciteit van de drager leidt tot een hogere intensiteit van de Pt L_2 and L_3 whiteline. Deze toegenomen whiteline intensiteit duidt op een toegenomen aantal 5d toestanden in het Pt. DFT berekeningen laten zien dat dit wordt veroorzaakt door een rehybridisatie van de Pt valentieband. De Madelung potentiaal van een basische drager rehybridiseert het gevulde gedeelte van de valentieband tot meer antibindend $6s^*$ karakter. Dientengevolge krijgt het lege gedeelte van de valentieband meer lege 5d toestanden, en deze worden gemeten met de L_2 en L_3 röntgen absorptie edges. Verder laten de DFT berekeningen zien dat de metaal-drager interactie uit nog 3 effecten bestaat. Ten eerste, de Madelung potentiaal van de drager polariseert de Pt deeltjes en ten tweede, de volledige valentie band wordt naar hogere energie geduwd bij basische dragers. Ten derde, de binding tussen de drager en het metaaldeeltje is sterk zolang de drager niet inert is. Deze metaal-drager binding heeft een groot effect op de metallische 6sp toestanden. In het geval van zure dragers bevinden deze zich voornamelijk in het contact vlak van het metaaldeeltje en de drager. Echter, bij basische dragers bevinden de 6sp toestanden zich juist in de buurt van het oppervlak van de metaaldeeltjes. Aangezien de Pt 6sp toestanden deelnemen in de binding van reactanten op het Pt opppervlak, kan dit grote gevolgen hebben voor de katalytische eigenschappen van de metaaldeeltjes.

De veranderingen in de elektronische eigenschappen van de gedragen metaal deeltjes werden in **hoofdstuk 9** gerelateerd aan de chemisorptie van reactanten. In dit hoofdstuk wordt de invloed van de zuur/base eigenschappen van de drager op de adsorptie van H en CH_x (met x=2,3) op gedragen Pt deeltjes onderzocht met behulp van DFT berekeningen. Zoals hierboven gezegd lieten eerdere DFT berekeningen zien dat de drager met name een grote invloed heeft op de positie van de 6sp orbitalen van het Pt. Bovendien laten de DFT berekeningen zien dat de belangrijkheid van deze 6sp orbitalen in de Pt-adsorbaat binding toeneemt in de volgorde $Pt\text{-}CH_2 < Pt\text{-}CH_3 < Pt\text{-}H$. Het gevolg is dat de Pt-H binding veel sterker wordt beïnvloed door veranderingen in de zuursterkte van de drager dan de $Pt\text{-}CH_x$ binding. Door de sterkere Pt-H binding bij basische dragers is de bedekkingsgraad van Pt met waterstof in het geval van sterk gebonden waterstof veel hoger dan bij Pt deeltjes op zure dragers.
De invloed van de drager op de hydrogenolyse van alkanen kan voor een groot deel worden verklaard met de invloed van de drager op de Pt-H binding. De effecten van de drager op de Pt-H binding kunnen het compensatie effect, dat algemeen wordt gevonden in de kinetiek van de hydrogenolyse van alkanen over gedragen metaal katalysatoren, gemakkelijk verklaren.

List of Publications and Presentations

Publications

M.K. Oudenhuijzen, P.J. Kooyman, B. Tappel, J.A. van Bokhoven and D.C. Koningsberger, 'Understanding the Influence of the Pretreatment Procedure on Platinum Particle Size and Particle-size Distribution for SiO_2 Impregnated with $Pt^{2+}(NH_3)_4(NO_3^-)_2$: A Combination of HRTEM, Mass Spectrometry and Quick EXAFS', *J. Catal.*, **205** (2002), 135-146.

M.K. Oudenhuijzen, J.H. Bitter and D.C. Koningsberger, 'The Nature of the Pt-H bonding for strongly and weakly bonded hydrogen on Platinum. A XAFS spectroscopy study of the Pt-H antibonding shaperesonance and Pt-H EXAFS', *J. Phys. Chem. B*, **105** (2001), 4616-4622.

D.C. Koningsberger, M.K. Oudenhuijzen, J.H. Bitter and D.E. Ramaker, 'Study of geometrical and electronic effects induced by hydrogen chemisorption on supported Pt particles. Analysis of Pt-H EXAFS and Pt-H anti-bonding state shape resonances', *Top. Catal.*, **10** (2000), 167-177.

D.C. Koningsberger, M.K. Oudenhuijzen, D.E. Ramaker and J.T. Miller, 'An Atomic XAFS study of the metal-support interaction in $Pt/SiO_2-Al_2O_3$ and $Pt/MgO-Al_2O_3$ catalysts: an increase in ionisation potential of platinum with increasing electronegativity of the support oxygen ions', *Stud. Surf. Sci. Catal.*, **130A** (2000), 317-322.

Poster Presentations

M.K. Oudenhuijzen, B. Tappel, J.A. van Bokhoven and D.C. Koningsberger, 'Pretreatment of impregnated $Pt(NH_3)_4(NO_3)_2$ on SiO_2 studied by Mass Spectrometry', 2^{nd} Netherlands Chemistry and Catalysis Conference, march 2001, Noordwijkerhout, the Netherlands.

M.K. Oudenhuijzen, B. Tappel, J.A. van Bokhoven and D.C. Koningsberger, 'Pretreatment of impregnated $Pt(NH_3)_4(NO_3)_2$ on SiO_2 studied by Mass Spectrometry', NATO workshop 'Catalysis by Unique Metal Ion Structures in Solid Matrices', June 2000, Prague, Czech Republic.

M.K. Oudenhuijzen, J.H. Bitter and D.C. Koningsberger, 'Detection of different types of adsorbed hydrogen on Pt using XAFS spectroscopy', EU Summerschool on Surface Science and Catalysis, august 1999, Dronten, the Netherlands.

Oral Presentations

Keynote speaker at the 17th North-American Catalysis Conference NACS, Toronto (Canada), june 2001, M.K. Oudenhuijzen, B. Tappel, J.A. van Bokhoven and D.C. Koningsberger, 'Understanding the influence of variations in the pretreatment procedure on the particle size and particle size distribution for Pt/SiO_2'

M.K. Oudenhuijzen, J.H. Bitter and D.C. Koningsberger, 'Hydrogen chemisorption on supported Pt catalysts studied by XAFS spectroscopy', 1st Netherlands Chemistry and Catalysis Conference, January 2000, Lunteren, the Netherlands.

Dankwoord

Hoewel het aio zijn soms een eenzame bezigheid is, hebben toch heel veel mensen bijgedragen aan dit boekje. Die wil ik hier allemaal bedanken.

Ten eerste wil ik natuurlijk mijn promotor bedanken. Diek, jouw soms tomeloze enthousiasme kan heel inspirerend zijn. Hierdoor was het een fijne en productieve samenwerking. Hoewel het hard werken was aan het einde, hebben we het toch maar gehaald om het boekje op tijd af te hebben.

Dave, I admire the enormous amount of energy and the passion that you show for science. I don't think you ever get tired of a new scientific problem. Say hello to Beverly from me.

Jeroen, copromotor, bedankt voor de dagelijkse begeleiding, de vruchtbare discussies, alle inhoudelijke input, het bier drinken in Hamburg (…), voor het harde nakijkwerk van alle hoofdstukken, en voor het vertrouwen dat je hebt getoond. Succes in Zürich.

Harry, copromotor van het 1e jaar, ook jouw bijdrage is aanzienlijk geweest. Hoewel niet heel veel van het werk waarbij jij betrokken was in het boekje terecht is gekomen, is toen toch de basis gelegd. Dankjewel.

Jeff, thanks for all the catalysts. They were invaluable.

Patricia, alles bij elkaar heb ik toch aardig wat uurtjes bij jouw TEM gezeten. Bedankt voor de mooie foto's.

Jaap, bedankt voor het op weg helpen met de ADF berekeningen. Dat zelf op te starten was ondoenlijk geweest.

Degenen die misschien nog wel de grootste bijdrage hebben gehad aan dit boekje, zijn de studenten geweest die bij mij hebben gewerkt: Floris van Driel, Bas Tappel (door jouw werk mocht ik naar Canada!) en Stefan van Dommele. Ook scriptieschrijver Laurens wil ik bedanken.

Zo ben ik langzamerhand op de 2e verdieping van het Went terecht gekomen. Ik heb daar altijd met veel plezier gewerkt. Ik wil iedereen, en met name Jan (serieuze werker, maar een harde lacher), Marjolein (de tv vraagbaak en tegenwoordig aio-opperhoofd), Sander (met jou erbij wordt harder en meer gelachen in de koffiepauzes), Tijmen (val je nou op mannen?), Marije (lekker ding), Miekje (de laatste der Mohikanen, ik hoop dat je het leuk blijft vinden op de vakgroep) en Jules (altijd in voor een biertje en praten over sport), bedanken voor al die lol en gezelligheid bij de koffiepauzes, de borrels, de voetbaltoernooien etc.

Fred bedankt voor de hulp met de MS problemen, ook al zijn we er nooit achter gekomen waar die problemen vandaan kwamen.
Ook John wil ik nog bedanken voor alle metingen, gesprekken en wijze raad over computers. Jammer dat ik je niet meer een boekje kan uitreiken. Jouw overlijden heeft mij veel geleerd over de verschillende mensen op de vakgroep.
Een speciaal woordje van dank gaat ook naar de bewoners van N209 door de jaren heen: Ellart, Laurens en Daphne. Jan (de B.koning, alias de Fartman en de man van de Sexpo poster), ik zal jouw lucht niet snel vergeten. Gelukkig waren de discussies met jou leuk en leerzaam.
Eén van de dingen waaraan ik altijd met veel plezier heb meegedaan op de vakgroep was de teammaster. Het gaf altijd veel gespreksstof. Iedereen van San Marco daarvoor bedankt.
Ik ben ook nog op (zaken)reis geweest met een aantal collega's. Marije, je kreunt als geen ander in bed! Jules, ik heb nog nooit zo vast op een rots gezeten. Verder hoop ik ook maar dat ik net zo koelbloedig een vrachtwagen weet te ontwijken als jij. Ook alles EXAFS-mensen (Abdeltif, Ad, Andrea, Gerbrand, Harry, Jan, Jeroen, Laurens, Moniek, Sylvain, Rosmans): hartelijk dank voor al die metingen. Zoals jullie kunnen lezen in dit boekje, heb ik veel met al die metingen gedaan.

Met mijn beide paranimfen heb ik al veel meegemaakt, een promotie kan daar ook nog wel bij.
Iel, paranimfomaan, bedankt voor al je vriendschap door de jaren heen. Ik kan jouw uitgesproken mening altijd erg waarderen, en ik bewonder je trouw aan je vrienden, je zal niet snel iemand laten vallen. Bovendien ben je erg gezellig en een goede vriendin – hopelijk nog vele jaren!
Para-snader, we zijn alweer sinds het 1e jaar scheikunde bevriend. Het zal wennen worden om niet meer vanzelfsprekend met jou te squashen, je iedere dag op de vakgroep te zien en te lachen aan de koffietafel.

Katia, zus, en natuurlijk papa en mama, bedankt voor alles. Pap, mam, jullie hebben me altijd gesteund, zowel in goede als slechte tijden. Hoewel ik altijd wist dat ik op jullie kon rekenenen, en weet dat dat zo zal blijven, beschouw ik dat geenszins als vanzelfsprekend. Ik kan me geen betere ouders wensen.

Martine, lieffie, jij vroeg jezelf af wat jouw bijdrage aan mijn boekje is geweest. Nou, die is er wel degelijk! Jij hebt de tijd van het schrijven gemaakt van een deprimerende tijd achter een beeldscherm tot een tijd waarin ik iedere 5 minuten mijn mail controleer op berichtjes van jou en tot een tijd waarin aan mij wordt gevraagd waarom ik zoveel lach! Ik zó blij dat ik jou heb leren kennen.

Mike Michiel Mikey Mike Monsieur[a]

[a] s.v.p. doorhalen wat van toepassing is

Curriculum Vitae

Michiel Karel Oudenhuijzen werd op 12 juni 1975 geboren in Gouda als zoon van Karel en Addy, en broertje van Katia. In 1987 begon hij aan zijn V.W.O opleiding op het Schaepman college in Dongen, waar hij zijn diploma in 1993 behaalde. In september van hetzelfde jaar begon hij zijn studie Scheikunde aan de universiteit Utrecht. Tijdens zijn studie was Michiel actief in de Utrechtse Scheikundige Studentenvereniging Proton. Hij was o.a. vice-voorzitter in het bestuur 1994-1995. In mei 1998 behaalde hij zijn doctoraal diploma Scheikunde met genoegen. Zijn afstudeerstages hadden als onderwerp 'Luminescentie', 'Moleculaire Dynamica'en 'Heterogene Katalyse'. Sinds juni 1998 is hij verbonden als onderzoeker in opleiding (oio) aan de vakgroep Anorganische Chemie en Heterogene Katalyse van de faculteit Scheikunde, Universiteit Utrecht. Het onderzoek dat sinds die tijd werd uitgevoerd onder supervisie van D.C. Koningsberger heeft geleid tot dit proefschrift.